Variational-based Global-Local approach for a phase-field formulation of a fracturing material

Von der
Fakultät Architektur, Bauingenieurwesen und Umweltwissenschaften
der Technischen Universität Carolo-Wilhelmina
zu Braunschweig

zur Erlangung des Grades eines
Doktoringenieurs (Dr.-Ing.)
genehmigte

Dissertation

von
Nima Noii
geboren am 31.07.1985
aus Teheran

Eingereicht am:	07 October 2020
Disputation am:	11 February 2021
Berichterstatter:	Prof. Dr. Laura De Lorenzis Prof. Dr.-Ing. Peter Wriggers

2021

Variationsbasierte Global-Lokal-Methode für eine Phasenfeldformulierung für ein Bruchmaterial

Von der
Fakultät Architektur, Bauingenieurwesen und Umweltwissenschaften
der Technischen Universität Carolo-Wilhelmina
zu Braunschweig

zur Erlangung des Grades eines
Doktoringenieurs (Dr.-Ing.)
genehmigte

Dissertation

von
Nima Noii
geboren am 31.07.1985
aus Teheran

Eingereicht am:	07 Oktober 2020
Disputation am:	11 Februar 2021
Berichterstatter:	Prof. Dr. Laura De Lorenzis Prof. Dr.-Ing. Peter Wriggers

2021

Acknowledgements

This dissertation is the outcome of my research work that was conducted between 2014 and 2018 at the Institute of Applied Mechanics, Technische Universität Braunschweig. The work is part of the DFG[1] IRTG1627[2] project, a.k.a. ViVaCE (Virtual Materials and their Validation: German-French School of Computational Engineering).

First and foremost, I would like to express my greatest appreciation to my doctoral supervisor, Prof. Dr. Laura De Lorenzis, for her inimitable guidance and limitless support in both research and personal matters. Her deep knowledge, including many excellent years of research experience as a world-renowned professor in the field of computational mechanics, came as a magnificent benefit to my research. Undoubtedly, the achievement of this dissertation would not have been feasible within the time frame of the project had it not been backed by her excellent and careful scientific support. Thank you for mentoring me and for placing trust in me to work on this interesting topic.

Cordially, I am very grateful to my second advisor, Prof. Olivier Allix at LMT[3] ENS Paris-Saclay[4], for his fruitful discussion, giving his time generously, and being very friendly with me. His multifarious expertise in the subject was invaluable and served as a solid basis for my achievement.

Furthermore, I would like to acknowledge Prof. Dr.-Ing. Peter Wriggers and Prof. Dr.-Ing. Dieter Dinkler for generously offering their time, support, and goodwill to review my dissertation for being members of my dissertation committee. Also, I would like to address my thanks to Prof. Dr.-Ing. Manfred Krafczyk for accepting the presidency of the examination board.

I would like to thank all my colleagues at the Institute of Applied Mechanics for the many scientific exchanges and creating such a great and friendly environment. In particular, I wish to express my appreciation to Dr. Tymofiy Gerasimov, who fascinated me with his structured way of thinking within our numerous discussions.

I send my sincere thanks to the IRTG members for all the memorable times during the scientific workshops we spent together. I am especially thankful to Mrs. Dorit Schulte, the VIVACE program coordinator, who is super-efficient at organizing all events.

With all my heart, I believe the great opportunity I have today has resulted from the support of my family in the past and present. I owe a large debt of gratitude to my father, mother, and brother for their love and trust throughout my entire life thus far.

Braunschweig, May 05, 2021 Nima Noii

---

[1] Deutsche Forschungsgemeinschaft

[2] International Research and Training Group IRTG 1627

[3] Laboratoire de Mécanique et Technologie

[4] École normale supérieure Paris-Saclay

Kurzfassung

Unter Bruchmechanik versteht man im Allgemeinen das Untersuchen von Materialversagen, wobei die Beschreibung von Bildung sowie Ausbreitung auftretender Risse in einem Festkörper aufgrund von Verformungsprozessen zum Tragen kommt. Ein Beispiel für diesen Ansatz ist das variationsbasierte Bruchmodell von Francfort und Marigo sowie die damit verbundene regularisierte Formulierung, die allgemein als variationelle Phasenfeldformulierung des Sprödbruchs bezeichnet wird. Diese weit verbreitete Formulierung wird zur Modellierung und Berechnung von Bruchphänomenen in elastischen Festkörpern verwendet. Sie führt zu einem neuartigen Simulationswerkzeug, welches eine effiziente Beschreibung komplizierter Bruchphänomene für industrielle Anwendungen ermöglicht. Die größte Herausforderung besteht darin, ein Gerüst zu beschreiben, welches für eine industrielle Anwendung geeignet ist.

In dieser Arbeit wird die Adaption Global-Lokaler Ansätze bei der Modellierung von Rissen mithilfe der Phasenfeld-Methode untersucht. Eine erfolgreiche Ausweitung des Global-Lokalen Ansatzes auf dieses Methode würde den Weg für eine breite Akzeptanz der Phasenfeld-Methode für industrielle Anwendungen ebnen. Der Global-Lokale Ansatz wird zunächst verwendet, um kleine Verformungen abzubilden. Es werden zwei verschiedene Arten der Global-Lokalen Formulierung unterschieden: eine mit Dirichlet-Neumann-Rand-bedingungen ($g/l-1$) und eine mit Robin-Randbedingungen ($g/l-2$). Der erste Typ ist stark nicht-intensiv, was Berechnungen mit Legacy-Codes ermöglicht wodurch weniger Implementierungsaufwand notwendig ist. Aufgrund des extremen Unterschieds in der Steifigkeit zwischen der lokal zu analysierenden Zone und seiner tatsächlichen Reaktion bei umfangreichen Rissen sind die Robustheit, Genauigkeit und Effizienz des iterativen Fixpunkt-Algorithmus die Hauptschwierigkeiten, welche den Kern der Methode bildet. Diese Probleme werden in dieser Dissertation behandelt. Wir untersuchen die Konvergenz, wenn der Global-Local-Algorithmus verwendet wird, und zeigen, dass die erhaltenen Ergebnisse identisch mit der Referenzlösung sind. Wir verwenden auch in dem Aktualisierungsverfahren der Lösung Entspannungs- sowie Beschleunigungstechniken wie die Aitken Δ^2-Methode, Symmetric Rank One- und der Broyden-Methode und zeigen, dass die Konvergenz erheblich verbessert werden kann. Die Robin-Randbedingung $g/l-2$, hat den Vorteil, eine höhere Recheneffizienz zu besitzen. Im Gegensatz zu den Dirichlet-Randbedingungen auf lokaler Ebene führen die Robin-Randbedingungen nicht zu einer steifen lokalen Reaktion. Insbesondere in einem Erweichungsbereich erfordern diese daher keine ßusätzliche Arbeit"wie Entspannungs- sowie Beschleunigungsverfahren.

Die effiziente Global-Lokale Formulierung wird sowohl für $g/l-1$ als auch für $g/l-2$ auf grosse Verformungen ausgeweitet. Um die Diskretisierung mit Finiten Elementen an der Schnittstelle zwischen der globalen und der lokalen Domain zu bewältigen, wird die Global-Lokale Formulierung weiter ausgedehnt auf nicht konforme Diskretisierungen. Der Hauptvorteil sind mehr Regelmäßigkeit an der Schnittstelle und Adaption der lokalen Domäne ohne Berücksichtigung des globalen Diskretisierungsraums. Zu diesem Zweck werden die Mortarmethode, die duale Mortarmethode und der lokalisierte Mortarmethode angewendet. Um die Effektivität des vorgeschlagenen Modells zu demonstrieren, werden mehrere numerische Beispiele durchgeführt.

Abstract

Fracture mechanics is generally aimed at investigating material failure by describing the nucleation and propagation of the cracks in a solid body due to the deformation process. An example of these approaches is the variational-based model of fracture by Francfort and Marigo as well as the related regularised formulation, commonly referred to as variational phase-field formulation of brittle fracture. This formulation is widely used for modelling and computing fracture phenomena in elastic solids, and leads to novel simulation tool for efficiently describing the complicated fracture phenomena for industrial applications. Despite this, the use of phase-field fracture approaches for structures of industrial complexity has been the subject of limited investigations. Thus, the main challenge here is to propose a framework suitable for an industrial application.

This work is aimed at investigating the adoption of Global-Local approaches while modelling fracture using the phase-field framework. A successful extension of the Global-Local approach to this setting would pave the way for the wide adoption of phase-field modelling of fracture cases with legacy codes for industrial applications. The proposed framework for the Global-Local approach is first used to address small deformation. Two different types of the Global-Local formulation are proposed: one equipped with Dirichlet-Neumann-type boundary conditions ($g/l-1$), and one using Robin-type boundary conditions ($g/l-2$). The first type is strongly non-intrusive, which enables computations performed with legacy codes with less implementation effort. Due to the extreme difference in stiffness between the global counterpart of the zone to be analysed locally and its actual response when undergoing extensive cracking, the main issues are the robustness, accuracy, and efficiency of the fixed-point iterative algorithm, which is at the core of the method. These issues are tackled in this dissertation. We investigate the convergence performance when the native Global-Local algorithm is used, and show that the obtained results are identical to the reference phase-field solution. We also equip the Global-Local solution update procedure with relaxation/acceleration techniques, such as Aitken's Δ^2-method, the Symmetric Rank One and Broyden's methods and show that the iterative convergence can be improved significantly. The second type, namely $g/l-2$, has the advantage of computational efficiency. In contrast to the Dirichlet boundary conditions being used in $g/l-1$ within the local level, this does not lead to a stiff local response, particularly in a softening regime, and thus does not require any "extra efforts" such as relaxation/acceleration procedures.

The efficient Global-Local formulation is further extended towards large deformations for both $g/l-1$ and $g/l-2$. Finally, to cope with different finite element discretization at the interface between the global and local domains, the Global-Local formulation is further extended to non-conformal discretizations. The main advantage is to achieve more regularity at the interface and adoption of the local domain without taking into account the global discretization space. For this purpose, the mortar method, the dual mortar method, and localized mortar method are adopted. To demonstrate the performance of the proposed model, several numerical examples are performed.

Contents

Kurzfassung i

Abstract iii

1. Introduction 1
- 1.1. Motivation and state of the art . . . 1
  - 1.1.1. Variational phase-field modeling for brittle fracture . . . 1
  - 1.1.2. Variational Global-Local formulation . . . 3
- 1.2. One-dimensional analysis for the Global-Local formulation . . . 4
- 1.3. Research objective . . . 7
- 1.4. Outline of the dissertation . . . 9

2. Fundamentals of Continuum Mechanics 11
- 2.1. Basic kinematics and deformation . . . 11
- 2.2. Fundamental mappings at the finite strain . . . 12
- 2.3. Strain tensors . . . 14
- 2.4. Spectral decomposition of the strain tensors . . . 15
- 2.5. Stress tensors . . . 16
- 2.6. Physical balance principles of continuum thermodynamics . . . 16
  - 2.6.1. Balance of mass . . . 16
  - 2.6.2. Balance of linear momentum . . . 16
  - 2.6.3. Balance of angular momentum . . . 17
  - 2.6.4. Balance of energy . . . 17
- 2.7. Dissipation and second axiom of thermodynamics . . . 18
- 2.8. Constitutive models . . . 19
  - 2.8.1. Restricted to the small deformation . . . 21

3. Variational Phase-Field Modeling for the Fracturing Material 23
- 3.1. Variational phase-field modeling of brittle fracture at small deformation . . 24
  - 3.1.1. Primary fields of isotropic brittle solids at small strain 24
  - 3.1.2. Variational formulation for the multi-field problem 24
  - 3.1.3. Phase-field approximation of isotropic crack topologies 26
  - 3.1.4. Extension toward a decoupled strain-energy function 27
  - 3.1.5. Euler-Lagrange equations in a strong form 31
  - 3.1.6. Global balance principle of the continuum phase-field 31
  - 3.1.7. Resolving the crack irreversibility constraint 33
- 3.2. Variational phase-field modeling of brittle fracture at finite strain 35
  - 3.2.1. Primary fields of brittle solids at finite strain 35
  - 3.2.2. Variational formulation for the multi-field problem 35
  - 3.2.3. Phase-field approximation of isotropic crack topologies 37
  - 3.2.4. Decoupled strain-energy function through volumetric- and isochoric-based decomposition 38
  - 3.2.5. Extension toward Mooney-Rivlin hyperelastic solid material 39
  - 3.2.6. Euler-Lagrange equations in a strong form 41
  - 3.2.7. Global balance principle of continuum phase-field at finite strain . . 42
  - 3.2.8. Resolving the crack irreversibility constraint 43
- 3.3. Numerical framework for solving multi-field boundary value problems . . . 44
- 3.4. Numerical examples 44
  - 3.4.1. Example 1: Single-edge-notched test at small deformation 45
  - 3.4.2. Example 2: Single-edge-notched test at finite strain 48

4. Global-Local Approach Applied to the Phase-Field Fracture at Small Deformation 53
- 4.1. Non-overlapping domain decomposition formulation 54
- 4.2. Global-Local formulation 58
- 4.3. Variational formulation for the Global-Local coupling system 60
- 4.4. $g/l-1$: Dirichlet-Neumann-type boundary conditions 62
  - 4.4.1. Non-intrusive computational scheme 62
- 4.5. Accuracy/convergence performance of the $g/l-1$ 65
- 4.6. $g/l-1$ via incremental setting augmented with relaxation/ acceleration techniques 66
  - 4.6.1. Necessity of using relaxation/acceleration techniques 66
  - 4.6.2. Symmetric Rank One method 68

  - 4.6.3. Broyden's method 69
  - 4.6.4. Aitken's Δ^2 method 70
- 4.7. $g/l-2$: Robin-type boundary conditions 70
- 4.8. Finite Element Discretization 74
  - 4.8.1. Global-Local with Dirichlet-Neumann-type boundary conditions . . 77
  - 4.8.2. Global-Local with Robin-type boundary conditions 79
  - 4.8.3. Space-discrete linearization of the variational formulation in material configuration 79
- 4.9. Numerical examples 80
  - 4.9.1. Investigating the references and Global-Local results 81
  - 4.9.2. Reference and $g/l-1$ augmented with relaxation techniques 83
  - 4.9.3. Investigating $g/l-1$ results for different global discretization spaces 84
  - 4.9.4. Reference and $g/l-2$ with Robin-type boundary conditions 86

5. Global-Local Approach Applied to the Phase-Field Fracture at Finite Strain 91

- 5.1. Non-overlapping domain decomposition formulation 91
- 5.2. Global-Local formulation 94
- 5.3. Variational formulation for the Global-Local coupling system 96
- 5.4. $g/l-1$: Dirichlet-Neumann-type boundary conditions 98
- 5.5. Accuracy/convergence check 99
- 5.6. $g/l-2$: Robin-type boundary conditions 101
- 5.7. Finite Element Discretization 103
  - 5.7.1. Global-Local with Dirichlet-Neumann-type boundary conditions . . 106
  - 5.7.2. Global-Local with Robin-type boundary conditions 107
  - 5.7.3. Space-discrete linearization of the variational formulation in material configuration 108
- 5.8. Numerical examples 109
  - 5.8.1. Example 1: Penny-shaped pre-cracked test at finite strain 109
  - 5.8.2. Example 2: Debonding test undergoing finite strain 116

6. Global-Local Approach for Non-conforming Finite Element Discretization 121

- 6.1. Non-conforming discrete interfaces between global and local domains . . . 121
  - 6.1.1. Mortar method 122
  - 6.1.2. Mortar method with a dual basis function for the local Lagrange multiplier 123

6.1.3. Numerical integration for non-mortar/mortar integrals 125
6.1.4. Localized mortar method 129
6.1.5. Effect of the type of basis function for the $\boldsymbol{N}_{\lambda}^{L}$ on $\mathbf{L}_L$ 131
6.2. Benchmark numerical problems 131
6.2.1. Contact patch test 131
6.2.2. Two-dimensional elasticity squared problem 132
6.3. Numerical examples 134
6.3.1. Example 1: Tensile test including voids and fibers at small deformation 134
6.3.2. Example 2: I-shaped specimen at finite strain 136

7. Conclusion and Future Research **145**
7.1. Conclusion 145
7.2. Future research 147

A. Derivation of Robin-Type Boundary Conditions **149**

Bibliography **153**

Chapter 1

Introduction

1.1. Motivation and state of the art

The use of phase-field fracture approaches for structures of industrial complexity has been the subject of limited investigations. To move forward in this direction, the present dissertation advocates the use of Global-Local strategies, initially proposed in [45]. When dealing with large structures, fracture phenomena most often only occur in regions of limited extent. Moreover, in the case of brittle fracture, most structures behave elastically. These features are particularly appealing for Global-Local approaches as they make it possible to first compute the global model elastically, and then to determine the critical areas to be reanalyzed, while storing the factorization of the structural stiffness decomposition. The local models are then iteratively substituted within the unchanged global one, which has the advantage of avoiding the reconstruction of the mesh in the whole structure. The main motivation of the Global-Local approach is (*i*) to avoid the modification of the finite element model (FEM) used by engineers; (*ii*) to create a complex global model, which is by far the most time-consuming task; (*iii*) to apply a localized fractured formulation in the domain of interest and not the entire domain; and (*iv*) to use different discretization space for the fractured area and surrounding domain.

1.1.1. Variational phase-field modeling for brittle fracture

The variational approach to fracture by Francfort and Marigo [43] and the related regularized formulation of Bourdin et al. [23, 21, 22, 24], commonly referred to as the phase-field model of (brittle) fracture, is a widely accepted framework for modeling and computing fracture phenomena in elastic solids. The phase-field framework for modeling systems with sharp interfaces, consisting of incorporating a continuous field variable – the so-called order parameter – denoted by s which differentiates between multiple physical phases within a given system through a smooth transition. In the context of fracture, such an order parameter (termed the *crack phase-field*) describes the smooth transition between the fully broken and intact material phases, thereby approximating the sharp

Figure 1.1: Industrial application for the fracture process appearing in large structures. (a) Airplane damaged by impacting the ground surface [10], and (b) bridge damaged in a heavy storm [14].

crack discontinuity, as sketched in Fig. 1.2. The evolution of this field is a result of the external loading which models the fracture process.

The regularized fracture problem is formulated as a multi-field problem $(\boldsymbol{u}, s)$, where $\boldsymbol{u}$ is the displacement field and s is the phase-field. The discontinuities in $\boldsymbol{u}$ are approximated across the lower-dimensional crack topology with s [23]. The resulting, regularized formulation leads to a diffusive transition zone between two phases in the solid, which correspond to the fractured phase (i.e., $s = 0$) and intact phase (i.e., $s = 1$); see Fig. 1.2. The thickness of the transition zone is affected by a regularized parameter known as length-scale (denoted by l). Moreover, the regularized parameter l is related to the element size h. It must be $h \ll l$ [8, 25] to resolve the transition zone.

Therefore, a sufficiently small length-scale is computationally demanding. To date, the focus in such cases has been on local mesh adaptivity and parallel computing; see for instance [85, 58, 59, 28, 27, 9, 125, 86]. Another recent approach is a Global-Local technique in which parts of the domain are solved with a simplified approach [48, 105], which also aims to reduce the computational cost.

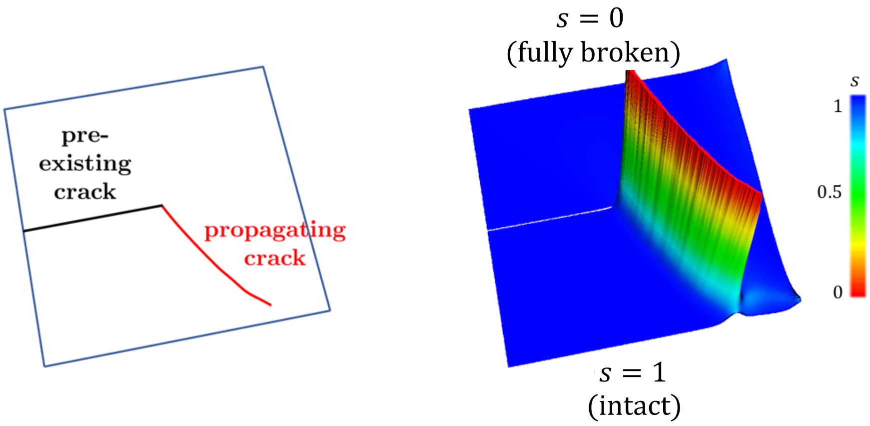

Figure 1.2: Phase-field description of fracture (sketchy): $s \in \mathcal{C}(\mathcal{B}, [0, 1])$ is the crack phase-field. Reprinted from [48].

The computational failure mechanism through phase-field fracture has advantages and shortcomings. The first advantage is a continuum description based on the first physical principles for determining the unknown crack path [43, 23, 94] and computing curvilinear and complex crack patterns. The model allows for nucleation, branching, merging and post-processing of certain quantities such that stress intensity factors become redundant. Therefore, fracture networks in highly heterogeneous media can be treated. The formulation is described in a variational framework which allows finite element discretizations and corresponding analyses. The mathematical model permits any dimension, and thus phase-field fracture applies conveniently to three-dimensional simulations. At the energy level, the formulation is non-convex, constituting a challenge for both the theory and design of numerical algorithms. A second challenge is the computational cost. Various solutions have been proposed thus far, namely staggered approaches (alternating minimization) [21, 27, 28], stabilized staggered techniques [26], quasi-monolithic approaches [58] (possibly with sub-iterations [85]), and fully monolithic approaches [46, 127, 126]. Adaptive mesh refinement was also proposed to reduce the computational cost [27, 58, 9, 125].

A variational phase-field formulation is strongly non-linear and calls for the resolution of small length scales. In fact, the failure behaviour is solely analyzed in a (small) local region, whereas in the surrounding medium, a simplified and linearized system of equations could be solved. Thus, the idea of a multi-scale approach that enables "sending" the non-linearity to a lower (local) scale – while dealing with a linearized problem at an upper (global) one – seems particularly appealing.

1.1.2. Variational Global-Local formulation

The multi-scale family can be classified into two distinct classes denoted as *hierarchical* and *concurrent* multi-scale techniques. These are defined by differentiation of the global characteristic length-scale $\mathfrak{L}_{global}$ with its local domain counterpart $\mathfrak{L}_{local}$. In the hierarchical multi-scale method, the average size of the heterogeneous local domain is much smaller than its global specimen size, that is, $\mathfrak{L}_{local} \ll \mathfrak{L}_{global}$ (see Fig. 1.3a) as it is classified in [90, 42]. This is often denoted as scale separation law, see computational homogenization approaches based on the Hill-Mandel principle, which are outlined for instance in [61, 90] among others. On the other hand, the concurrent multi-scale method implies that $\mathfrak{L}_{local} \equiv \mathfrak{L}_{global}$, see Fig. 1.3b as classified in [80, 42]. Herein, the local periodicity (which underlies the assumption of classical computational homogenization) is not applicable. Then, the full resolution of the non-linear response at the local scale must be taken into account, due to the strain localization effect, as outlined in [41, 1]. These types of materials require a different multi-scale framework in which the non-linear response is consistently projected at the global scale; see for example [91, 88, 136, 56].

In fracture mechanics a multi-scale framework [65, 44, 81, 45, 48], such that the characteristic length of the local scale should be the same order as its global counterpart. This is accomplished by introducing a Global-Local approach based on the idea of a *history-dependent algorithm* at the nodal level; see [91] and the references cited therein. This approaches emanates from the concurrent multi-scale method, which results in an algorithm in which the boundary value problem of one scale is solved based on the given information from another scale (as a history variable). Accordingly, the history-dependent algorithm contains both *upscaling* and *downscaling* steps. In the upscaling step, a global response is achieved while the lower scale information is retained, representing a *local-*

global-transition procedure. However in the downscaling step, a *re-localization/re-meshing* of the coarse domain is performed at the local level, see [62, 30], and thereafter a non-linear boundary value problem is solved; based on the information passed from the global scale, representing *a global-local-transition* procedure.

A departing point towards *a Global-Local approach* applied to the variational phase-field fracture formulation is the domain decomposition method [51]. Global-local approaches have also been applied to quite a large number of situations, such as the computation of the propagation of cracks in a sound model using the extended finite element method (XFEM) [112]; the computation of the assembly of plates introducing realistic non-linear 3D modeling of connectors [53], the extension to non-linear domain decomposition methods [36]; and explicit dynamics [16, 17] with an application for the prediction of delamination under impact using ABAQUS [18]. Alternative strategies can be derived from the Partition of Unity Method [113, 72].

Global-Local approaches easily allow for different spatial discretizations for the global and local domains. This enables computations performed with legacy codes for industrial applications in more efficient settings. In this regard, a flexible choice of the discretization scheme can be employed on each domain independently; e.g. the FEM [135], Isogeometric Analysis (IGA) [66] and the Virtual Element Method (VEM) [134]. A typical application using a simplified Glocal-Local model was presented in [129]. Therein, a (phase-field) fracture model (computed with deal.II [12] in C++) was employed as a local problem using finite elements. The local setting was then coupled to a reservoir simulator (IPARS [123] based on Fortran) for computing the global problem. For this global problem, different discretization schemes – mainly based on finite differences for subsurface fluid flow – were adopted.

1.2. One-dimensional analysis for the Global-Local formulation

This section provides a brief illustrative one-dimensional analysis for the Global-Local formulation. Detailed theoretical variational formulation for the Global-Local framework at small and large deformations are provided in Chapters 4 and 5, respectively.

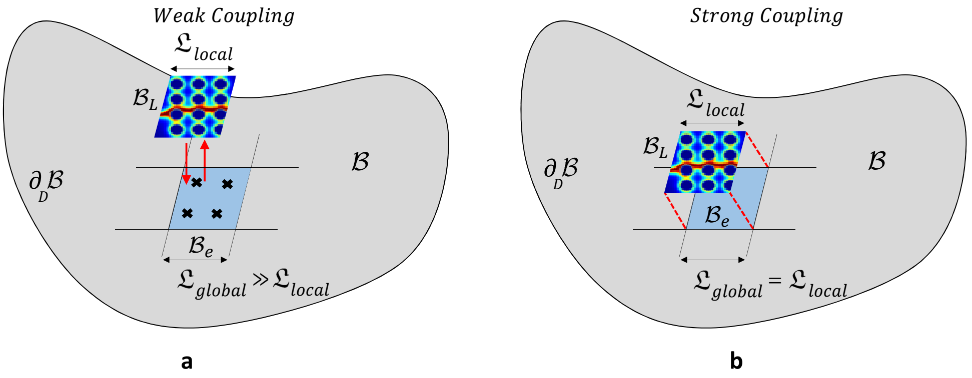

Figure 1.3: Classification of the multi-scale framework based on the global and local characteristic length-scales. (a) Hierarchical multi-scale model with $\mathfrak{L}_{local} \ll \mathfrak{L}_{global}$, and (b) concurrent multi-scale model with. $\mathfrak{L}_{local} \equiv \mathfrak{L}_{global}$

The energy functional $\mathcal{E}(u)$ for linear elasticity is given by

$$\mathcal{E}(u) = \int_{\mathcal{B}} \frac{1}{2} E(x)(u')^2 \mathrm{d}x - \int_{\partial_N \mathcal{B}} \bar{\tau} \cdot u \, \mathrm{d}a, \tag{1.1}$$

where $\bar{\tau}$ is the applied traction at the Neumann boundary and E is Young's modulus. Let us now consider one-dimensional boundary value problem (BVP) that is shown in Fig. 1.4a. We depict this as *a reference* BVP such that its discretized setting includes three elements and four nodal points with a length of $8L$, see Fig. 1.4. The cross-sectional area A is used as an identical unit area through the entire bar. Hence, (1.1) can be rewritten as

$$\mathcal{E}(u) = \int_0^{8L} \frac{1}{2} E(x)(u')^2 A \mathrm{d}x - \int_{\partial_N \mathcal{B}} \bar{\tau} \cdot u \, \mathrm{d}a. \tag{1.2}$$

The function $E(x)$ is shown in Fig. 1.4, hence we have

- $E(x) = E_1$ for $0 \leq x \leq L$
- $E(x) = E_2$ for $L < x \leq 2L$
- $E(x) = E_3$ for $2L < x \leq 8L$

The minimization of the given one-dimensional linear elasticity (1.2) leads to the Euler-Lagrange equation given by

$$\mathcal{E}_u(u; \delta u_G) := \int_0^{8L} E(x) u' \delta u' \, \mathrm{d}x - \int_{\partial_N \mathcal{B}} \bar{\tau} \cdot \delta u \, \mathrm{d}a = 0, \tag{R}$$

where $\mathcal{E}_u$ is the directional derivative of the energy functional $\mathcal{E}$ with respect to the displacement u. Here, $\delta u \in H_0^1(0, 8L)$ is an arbitrary test function. We now aim to resolve (**R**) using the efficient Global-Local formulation. To this end, the corresponding global BVP is given in Fig. 1.4b. We depict this as *a global* BVP such that its discretized setting includes two elements and three nodal points with a length of $8L$. Here, a homogenized Young's modulus E_3 is considered for the entire global domain, thus $E_G = E_3$ at $0 \leq x \leq 8L$. Accordingly, a local BVP is given in Fig. 1.4d. We refer to this as *a local* BVP such that its discretized setting includes two elements and three nodal points with a length of $2L$. Coarse representation of the local domain within the global level is the so-called *fictitious* domain; see Fig. 1.4c. Without a theoretical explanation, a global variational equation is defined to find $u_G \in H_0^1(0, 8L)$ through

$$\widetilde{\mathcal{E}}_{u_G}(u_G; \delta u_G) := \underbrace{\int_0^{8L} E u'_G \delta u'_G \, \mathrm{d}x - \int_{\Gamma_{N,G}} \bar{\tau} \cdot \delta u_G \, \mathrm{d}a}_{\text{standard terms}} \underbrace{- \int_{\Gamma_G} \lambda_\Gamma \cdot \delta u_G \, \mathrm{d}a}_{\text{jump term}} = 0. \tag{G}$$

Here, λ_Γ means the interface residual for measuring the discrepancy between global and local solutions at the interface (i.e., global nodal point 2), which in turn enters the global scale problem as a source term, thereby enabling an update of the global solution.

An interface residual quantity as a traction jump between the fictitious and local domains takes the following form

$$\lambda_\Gamma(x) = \lambda_F(x) - \lambda_L(x) \quad \text{at} \quad x_G = 2L,$$

where $(\lambda_F, \lambda_L) \in L_2$ are given fictitious and local traction quantities at the global level through the previous solution field. To ensure displacement continuity between global and local domains, the resulting global displacement field at the interface, called u_Γ, is imposed on the local BVP; hence we have a constrained local BVP to find $(u_L, \lambda_L) \in (H^1_0(0, 2L), L_2)$ using

$$\begin{cases} \widetilde{\mathcal{E}}_{u_L}(u_L, \lambda_L; \delta u_L) := \displaystyle\int_0^{2L} E(x) u'_L \delta u'_L \, \mathrm{d}x - \int_{\Gamma_G} \lambda_L \cdot \delta u_L \, \mathrm{d}a = 0, \\ \widetilde{\mathcal{E}}_{\lambda_L}(u_L, \lambda_L; \delta \lambda_L) := u_\Gamma - u_L^3 = 0 \end{cases} \tag{L}$$

Two BVPs, namely (G) and (L) have to be solved in an iterative manner such that convergence is ensured. Convergence is achieved when both displacement and traction continuity along the interface are held, see Section 4.5. To evaluate the Global-Local formulation, the BVP given in Fig. 1.4 is considered. We set $A = 1\ m^2$, $L = 1\ m$, and $(E_2, E_3) = (2E_1, 3E_1)$ with $E_1 = 10$. The resulting displacement distribution for the reference, global and local BVPs are provided in Fig. 1.5 for different iterations. After 15 iterations, the Global-Local formulation indeed recovers the displacement solutions identical to the reference one.

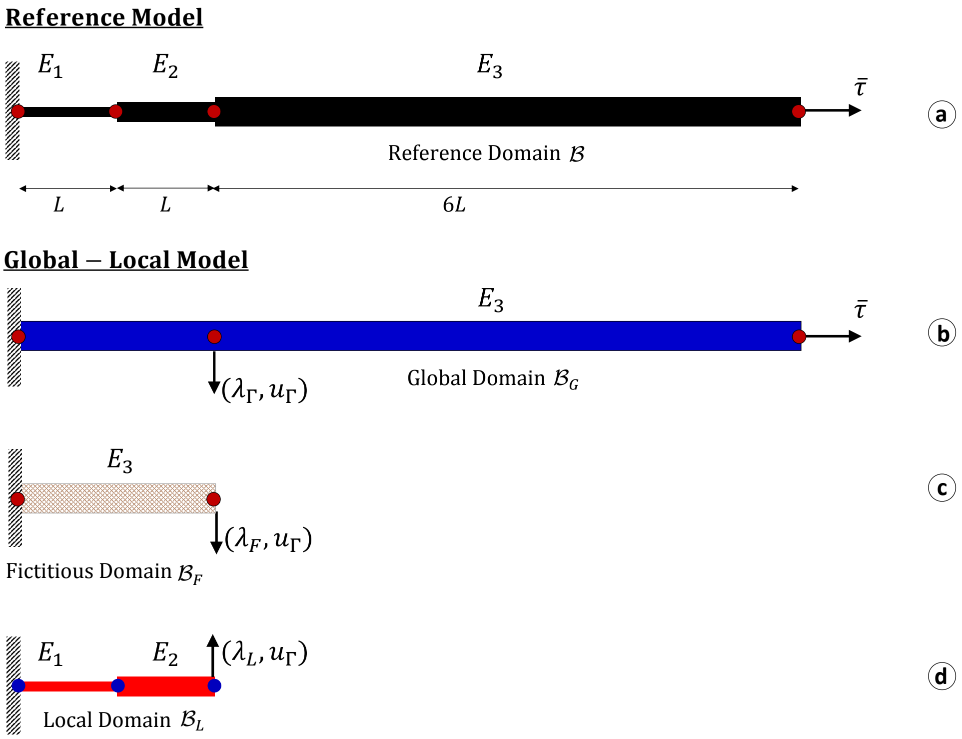

Figure 1.4: Geometry, loading setup, and discretization for the one-dimensional bar. (a) Reference domain, (b) global domain, (c) fictitious domain, and (d) local domain. Nodal points due to the discretization are depicted for each geometry.

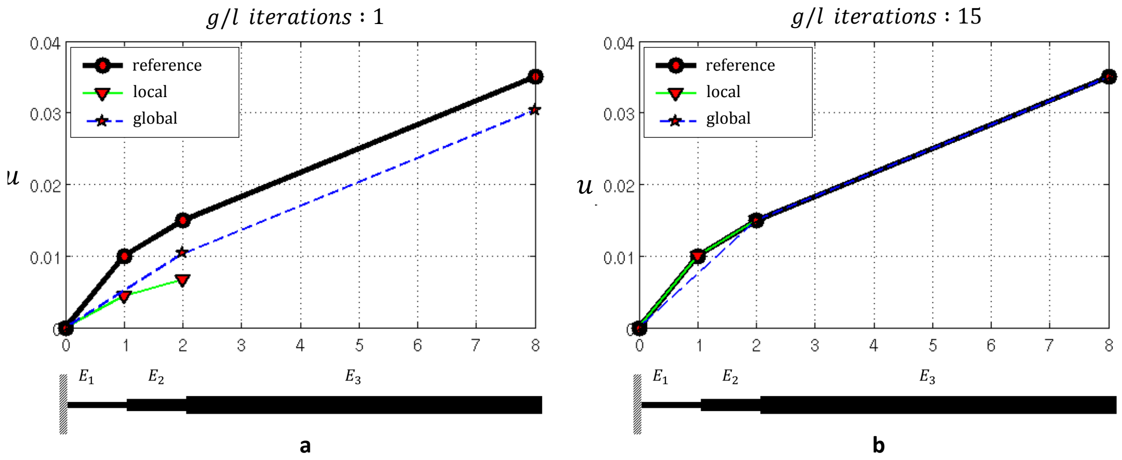

Figure 1.5: Displacement distribution along the bar: reference, global and local solutions. (a) Global-Local solutions at the first iteration, and (b) Global-Local solutions at the 15^{th} iteration.

Figure 1.6 depicts the convergence behavior of the Global-local iterative procedure for the one-dimensional BVP given in Fig 1.4. Here, we set TOL $= 10^{-12}$, and after 39 iterations we reach convergence.

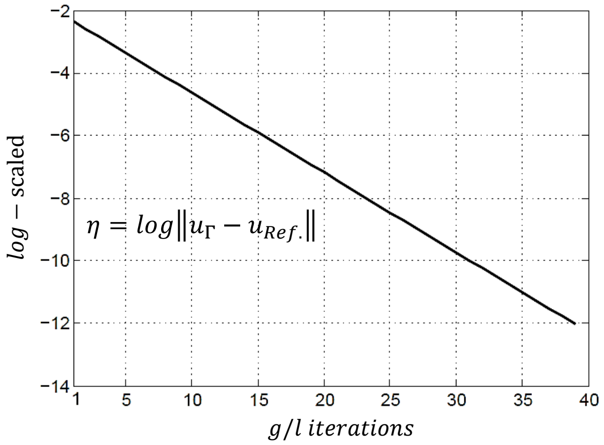

Figure 1.6: Convergence behavior of the Global-Local formulation for the one-dimensional BVP.

1.3. Research objective

In the following, we describe in more detail our main goals. In this dissertation, the Global-Local approach is employed as a computational framework for solving fracture mechanics problems as it was first formulated in [48]. Therein, the following assumptions were made [42, 57]:

i. The nonlinear behavior (e.g., fracture) is embedded at the local scale and linear behavior is assumed at the global scale.

ii. The global level is free from geometrical imperfections and hence heterogeneities exist *only* at the local level.

iii. At the local level, we consider a divergence-free assumption for the stress state, such that it is free from any external imposed load.

The first goal of this contribution is to design an efficient Global-Local framework for the fracturing material undergoing small deformation, while modeling fracture using the variational phase-field formulation. Additionally, it aims to introduce relaxation/acceleration techniques, because of the extreme difference in stiffness between the global counterpart of the zone that is re-analyzed locally and its actual response when undergoing extensive cracking.

The next goal is to use the Global-Local scheme to analyze fracture processes towards large strain formulation. Hence, two different types of Global-Local formulation are aimed to be carefully derived for the materials that tends toward large deformation, like polymers. The first type is formulated based on the Dirichlet-Neumann-type boundary condition [45], while the second one is formulated through the Robin-type boundary conditions which are prescribed to the local and global levels [44, 83, 82].

The final goal of this dissertation is to use the Global-Local scheme to deal with non-matching grids at the interface. This is particularly interesting for cases related to practical field problems, as mentioned in [129, 49], where possibly various programming codes may need to be coupled. To this end, different non-conforming finite element discretization techniques are further discussed. These include the mortar method [15, 131, 76], the dual mortar method [133, 132], and the localized mortar method [109, 120]. In fact, using non-conforming finite element discretization along the interface provides sufficient regularity of the underlying meshes. Consequently, different meshes for the global and local domains can be employed that allow for a very flexible discretization and mesh generation.

In summary, this dissertation comprises the following:

- A variational phase-field formulation in small and finite deformation of brittle fracture.
- A Global-Local approach for the phase-field fracture problem for capturing the full local resolution at the global level.
- A Global-Local scheme with Dirichlet-Neumann-type boundary conditions;
- An introduction to relaxation techniques for the Global-Local method to achieve stabilization and acceleration.
- A Global-Local scheme with Robin-type boundary conditions between the local and the global domains.
- An extension of the Global-Local formulation toward the large deformation settings.
- The extension to a non-matching finite element discretization.

1.4. Outline of the dissertation

The reminder of the dissertation is structured as follows. In **Chapter 2**, the fundamental governing equations in continuum mechanics are provided. In particular, a solid body undergoing large deformation is discussed. **Chapter 3** outlines the variational phase-field formulation of brittle fracture. The variational phase-field fracture model formulated here is used as a departure point for the next chapter. This chapter concludes with some numerical analysis. **Chapter 4** investigates the adoption of Global-Local approaches while modeling fracture using the phase-field framework at small deformation. Relaxation/acceleration techniques are formulated for the Global-Local solution update, in which the convergence performance is further investigated. We introduce Robin-type boundary conditions to relax the stiff local response at the global scale and enhance its stabilization. This chapter is substantiated with numerical tests. In **Chapter 5**, the efficient Global-Local formulation derived in Chapter 4 is further extended towards large defamation. The main objective here is to introduce an adoption of the variational phase-field fracture formulation within legacy codes when the finite strain response is observed. The resulting framework is algorithmically described in detail, and furthermore numerical examples are provided. In **Chapter 6** we aim to cope with different finite element discretization at the interface between the global and local domains. Hence, the Global-Local formulation is extended to non-conforming discretization. To do so, the mortar method, the dual mortar method, and the localized mortar method are further explained. Numerical examples finalize this chapter. **Chapter 7** concludes the dissertation with some remarks and the main results. Subsequently, ideas for future research are discussed.

Chapter 2

Fundamentals of Continuum Mechanics

Continuum theory in mechanics aims to illustrate the mechanical behavior of the material as well to formulate its response consistently. Here, the distribution of the solid material within the body is assumed to be continuous, such as density, stiffness, pressure, and velocity. In this chapter, the fundamentals of continuum mechanics of the solid body are given. We outline the basic equations for kinematics and deformation, fundamental mappings, balance equations of continuum thermodynamics, dissipation, and the second axiom of thermodynamics as well as governing equations. Comprehensive studies on continuum mechanics are provided, such as those by Truesdell & Noll [122], Bonet & Wood [19], Holzapfel [63], Gurtin et al. [54], Haupt [55] among others.

2.1. Basic kinematics and deformation

Let $\mathcal{B} \in \mathcal{R}^\delta$ be a material body (solid in the reference configuration) that is smooth, open and bounded set, and $\partial\mathcal{B}$ is denoted as its boundary with dimension $\delta = \{2,3\}$ in space and time $t \in \mathcal{T} = [0,T]$. We assume Dirichlet boundary conditions on $\partial_D\mathcal{B}$ and Neumann conditions on $\partial_N\mathcal{B} := \Gamma_N$, where Γ_N denotes the outer domain boundary, as illustrated in Fig. 2.1 . The BVP for the mechanical problem is characterized at material points $\boldsymbol{X} \in \mathcal{B}$ by the deformation map $\boldsymbol{\varphi}(\boldsymbol{X},t)$ of the solid defined as follows:

$$\boldsymbol{\varphi} : \left\{ \begin{array}{l} \mathcal{B} \times \mathcal{T} \to \mathcal{R}^\delta, \\ (\boldsymbol{X},t) \mapsto \boldsymbol{x} = \boldsymbol{\varphi}(\boldsymbol{X},t). \end{array} \right. \tag{2.1}$$

As visualized in Fig. 2.1, $\boldsymbol{\varphi}(\boldsymbol{X},t)$ maps at time $t \in \mathcal{T}$ referential points $\boldsymbol{X} \in \mathcal{B}$ of the reference configuration $\mathcal{B} \subset \mathcal{R}^\delta$ onto points $\boldsymbol{x} \in \mathcal{B}^t$ of the current configuration $\mathcal{B}^t \subset \mathcal{R}^\delta$ with $\delta \in \{2,3\}$. Thus, a mapping between material and spatial points is uniquely described by

$$\boldsymbol{x}(\boldsymbol{X},t) = \boldsymbol{\mathcal{X}}(\boldsymbol{\mathcal{X}}_{\mathbf{0}}^{-\mathbf{1}}(\mathrm{X},t)) = \boldsymbol{\varphi}(\mathrm{X},t). \tag{2.2}$$

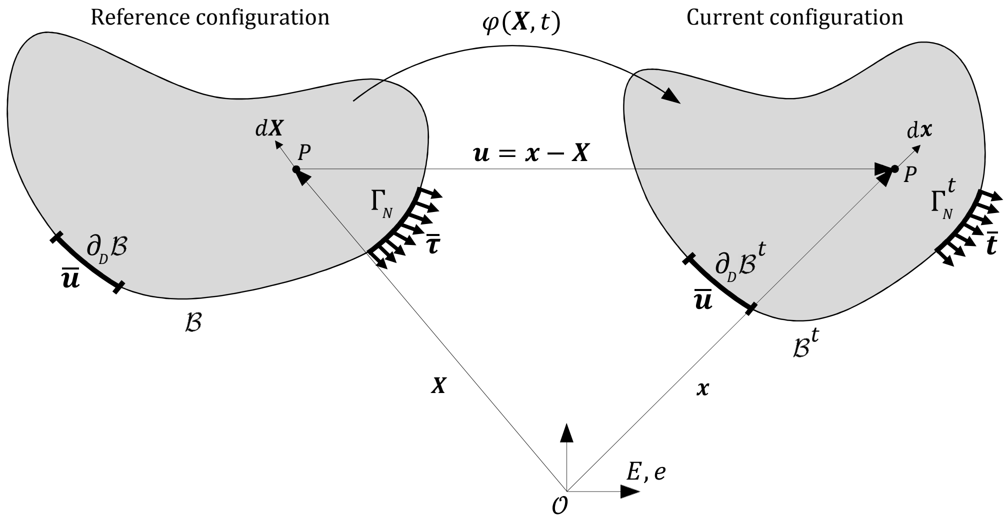

Figure 2.1: Setup of the notation for the configuration and motion of the continuum body $\boldsymbol{\varphi}(\mathbf{X}, t)$. The initial position $\boldsymbol{X}$ in the undeformed configuration $\mathcal{B}$ toward the current position $\boldsymbol{x}$ in the spatial configuration $\mathcal{B}^t$ for the solid material undergoing finite strain.

Following Fig. 2.1, the displacement vector $\boldsymbol{u}(\boldsymbol{x}, t)$ in the spatial description is defined based on the motion of point P at time t from the referential position $\boldsymbol{X}$ towards $\boldsymbol{x}$ using

$$\boldsymbol{u}(\boldsymbol{x}, t) = \boldsymbol{\varphi}(\boldsymbol{X}, t) - \boldsymbol{X} = \boldsymbol{x} - \boldsymbol{X}(\boldsymbol{x}, t). \tag{2.3}$$

2.2. Fundamental mappings at the finite strain

In this section, the fundamental mapping at the finite strain of the continuum thermomechanics are formulated. Accordingly, the strain measurement of the arbitrary point in the continuum body for the material and spatial configuration are provided.

Deformation gradient. To determine a deformation in the neighborhood of the material point, a linear mapping between infinitesimal material line element $d\boldsymbol{X}$ and its corresponding spatial components $d\boldsymbol{x}$ is mapped using the deformation gradient indicated by $\boldsymbol{F}(\boldsymbol{X}, t)$:

$$d\boldsymbol{x} = \boldsymbol{F} d\mathbf{X}, \quad \text{and} \quad d\mathbf{X} = \boldsymbol{F}^{-1} d\boldsymbol{x}, \tag{2.4}$$

which results in

$$\boldsymbol{F} = \frac{\partial \boldsymbol{\varphi}(\mathbf{X}, t)}{\partial \mathbf{X}} = \frac{\partial \boldsymbol{x}(\mathbf{X}, t)}{\partial \mathbf{X}} = \boldsymbol{I} + \boldsymbol{H}. \tag{2.5}$$

Here, a second-order displacement gradient $\boldsymbol{H}$ in the material description is defined as

$$\boldsymbol{H} := \frac{\partial \boldsymbol{u}}{\partial \boldsymbol{x}} = \boldsymbol{F}(\boldsymbol{X}, t) - \boldsymbol{I}. \tag{2.6}$$

Deformation gradient $\boldsymbol{F}$ is the fundamental quantity in the continuum thermodynamics for the body that undergoes large strain. This is a non-singular and unsymmetrical two-point tensor which is written in index notation through:

$$\boldsymbol{F} = F_{iI}\mathbf{e}_i \otimes \mathbf{E}_I. \tag{2.7}$$

Another fundamental inequality constraint applied to the continuum body is Jacobian formulated through determinant of $\boldsymbol{F}$ by

$$J(\boldsymbol{X}, t) := det[\boldsymbol{F}] > 0 \qquad \forall\, \boldsymbol{X} \in \mathcal{B}. \tag{2.8}$$

The Jacobian positivity implies the impenetrability of matter within the body, since the infinitesimal volume element has a non-negative value [63]. Hence, penetrable deformations have to be excluded thus leading to the necessary and sufficient condition of a strictly positive Jacobian $J > 0$. The consistency condition for the non-motion state, namely $\boldsymbol{F} = \boldsymbol{I}$, implies $J(\boldsymbol{X}, t) = det[\boldsymbol{I}] = 1$, meaning a volume-preserving state.

The material time derivative of the two-point deformation gradient tensor indicated by $\dot{\boldsymbol{F}}$ is defined as follows:

$$\dot{\boldsymbol{F}} = \frac{\partial \dot{\boldsymbol{x}}}{\partial \boldsymbol{X}} = \frac{\partial \boldsymbol{V}(\boldsymbol{X}, t)}{\partial \boldsymbol{X}} = \mathrm{Grad}\, \boldsymbol{V}(\boldsymbol{X}, t). \tag{2.9}$$

The spatial velocity gradient $\boldsymbol{l}(\boldsymbol{x}, t)$, which is the derivative of spatial velocity vector $\boldsymbol{v}(\boldsymbol{x}, t)$ with respect to the current coordinate, reads by

$$\boldsymbol{l}(\boldsymbol{x}, t) = \frac{\partial \boldsymbol{v}(\boldsymbol{x}, t)}{\partial \boldsymbol{x}} = \frac{\partial \dot{\boldsymbol{x}}}{\partial \boldsymbol{x}} = \dot{\boldsymbol{F}}.\boldsymbol{F}^{-1}. \tag{2.10}$$

Thus, $\dot{\boldsymbol{F}} = \boldsymbol{l}\boldsymbol{F}$ is multiplicatively decomposed into the spatial velocity gradient $\boldsymbol{l}(\boldsymbol{x}, t)$ and material velocity gradient $\boldsymbol{F}^{-1}$. The symmetrical part of the material velocity gradient is further denoted by $\boldsymbol{d}(\boldsymbol{x}, t)$ and that is

$$\boldsymbol{d}(\boldsymbol{x}, t) = \frac{1}{2}(\boldsymbol{l} + \boldsymbol{l}^T) = \frac{1}{2}(\mathrm{grad}\, \boldsymbol{v} + \mathrm{grad}^T \boldsymbol{v}). \tag{2.11}$$

Normal and area map. The infinitesimal surface element in the material configuration, denoted by $d\boldsymbol{A}$, is mapped onto its counterpart within spatial configuration $d\boldsymbol{a}$ as follows:

$$d\boldsymbol{a} = \mathrm{cof}[\boldsymbol{F}]d\boldsymbol{A} \quad \text{with} \quad \mathrm{cof}[\boldsymbol{F}] = J\boldsymbol{F}^{-T}, \tag{2.12}$$

which is known as a Nanson's formula.

Volume map. The infinitesimal volume element in the material configuration, denoted by dV, is mapped onto its counterpart within spatial configuration dv as follows:

$$\mathrm{d}v = J(\boldsymbol{X}, t)dV > 0. \tag{2.13}$$

Here, the determinant of the deformation gradient $\boldsymbol{F}$ states the volume ratio between infinitesimal material (dV) and spatial volume element (dv). It is trivial that if $J > 1$ then an infinitesimal counterpart of a continuum body is expanded; otherwise, if $J < 1$ it is contracted. If $J = 1$, we have a volume-preserving process that is known as an isochoric state; that is $dv = dV$.

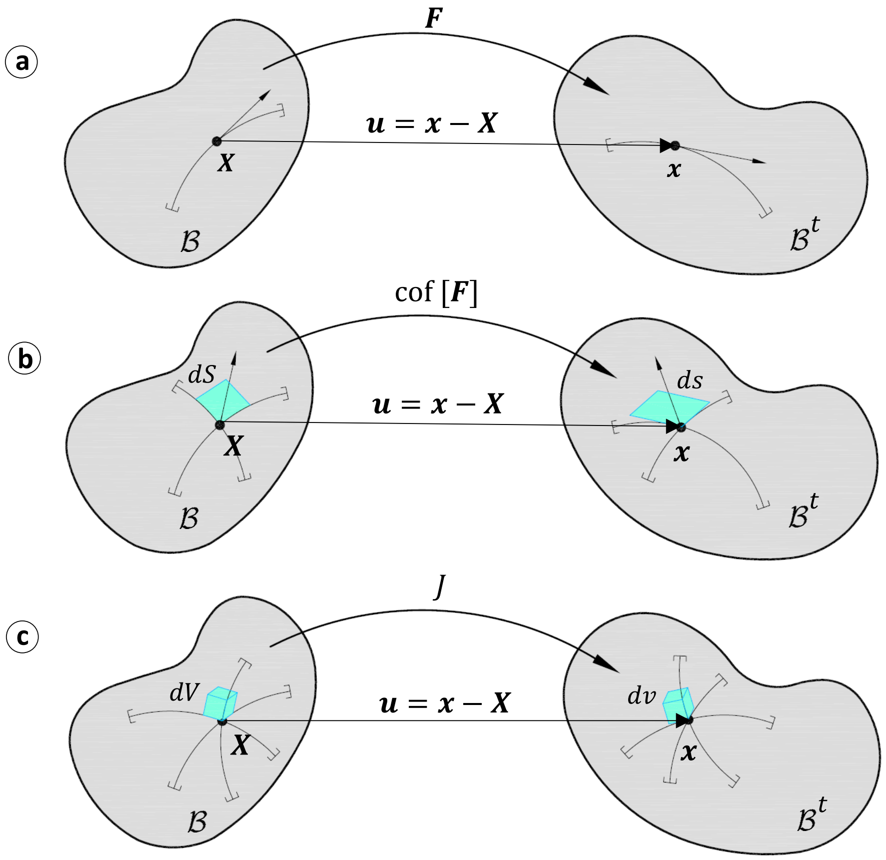

Figure 2.2: Fundamental mappings at finite strain. (a) Deformation mapping between initial position $\mathbf{X}$ toward current position $\boldsymbol{x}$ with $d\boldsymbol{x} = \boldsymbol{F}d\mathbf{X}$, (b) Nanson's formula for the mapping of areas $d\boldsymbol{a} = \mathrm{cof}[\boldsymbol{F}]d\boldsymbol{A}$, and (c) the volume map via the Jacobian $\mathrm{d}v = J(\boldsymbol{X}, t)dV$.

2.3. Strain tensors

Beyond the demand on the deformation map of being one-to-one, in the following, different strain tensors which are formulated at the reference and current configurations will be discussed. Let $\boldsymbol{g}$, $\boldsymbol{G} \in Sym_{+}$ be the standard metrics of the current and reference configuration $\mathcal{B}$ and $\mathcal{B}^t$. Then, the *right* and *left Cauchy-Green tensors* are as follows:

$$\boldsymbol{C} := \varphi^{\star}(\boldsymbol{g}) = \boldsymbol{F}^T\boldsymbol{g}\boldsymbol{F} \quad \text{and} \quad \boldsymbol{c} := \varphi_{\star}(\boldsymbol{G}) = \boldsymbol{F}^{-T}\boldsymbol{G}\boldsymbol{F}^{-1}. \tag{2.14}$$

Here, $\varphi^{\star}(\boldsymbol{g})$ is a pull-back operation of the current metric $\boldsymbol{g}$ and $\varphi_{\star}(\boldsymbol{G})$ is a push-forward operation of the reference metric $\boldsymbol{G}$; see [63]. Next, we introduce the *Green-Lagrange tensor* and *Almansi strain tensor* at the reference and current configuration, respectively, through

$$\boldsymbol{E} := \frac{1}{2}(\boldsymbol{C} - \boldsymbol{G}) \quad \text{and} \quad \boldsymbol{e} := \frac{1}{2}(\boldsymbol{g} - \boldsymbol{c})\,. \tag{2.15}$$

From (2.6), the strain measure (2.7) is formulated as a function of the displacement gradient, and thus (2.15) can be re-written as

$$\begin{aligned}
&\mathbf{E} = \frac{1}{2}(\text{Grad } \mathbf{u} + \text{Grad}^T \ \mathbf{u} + \text{Grad}^T\mathbf{u} \text{ Grad } \mathbf{u}), \quad \mathbf{E} = E_{IJ}\mathbf{E}_I \otimes \mathbf{E}_J, \\
&\mathbf{e} = \frac{1}{2}(\text{grad } \boldsymbol{u} - \text{grad}^T\boldsymbol{u} + \text{grad}^T\mathbf{u} \text{ grad } \mathbf{u}), \quad \mathbf{e} = e_{ij}\mathbf{e}_i \otimes \mathbf{e}_j.
\end{aligned} \tag{2.16}$$

The last terms of $\mathbf{E}$ and $\mathbf{e}$ in (2.16), i.e., "$\frac{1}{2}\text{Grad}^T\mathbf{u}$ Grad $\mathbf{u}$" and "$\frac{1}{2}\text{grad}^T\mathbf{u}$ grad $\mathbf{u}$", are quadratic terms and result in a non-linear response for the Green-Lagrange and Almansi strain tensors. These quadratic terms affect the strain tensors only when Grad$\mathbf{u}$ or grad$\mathbf{u}$ is large. In the linear elasticity framework, the strain is assumed to be small, meaning that the norm of the displacement gradient is bounded by a small number ϵ, i.e., $||\nabla\boldsymbol{u}|| < \epsilon$. Thus, the quadratic term becomes a small value, and it is neglected. The resulting linear strain tensor denoted by $\boldsymbol{\varepsilon}$ is written as follows:

$$\boldsymbol{\varepsilon} = \frac{1}{2}(\text{grad } \ \mathbf{u} + \text{grad}^T\boldsymbol{u}), \quad \boldsymbol{\varepsilon} = \varepsilon_{ij}\mathbf{e}_i \otimes \mathbf{e}_j. \tag{2.17}$$

2.4. Spectral decomposition of the strain tensors

A unique polar decomposition for any point $\boldsymbol{X}$ in the undeformed configuration of the continuum body $\mathcal{B}$ can be described using

$$\boldsymbol{F} = \boldsymbol{R}\boldsymbol{U} = \boldsymbol{v}\boldsymbol{R} \quad \text{s.t.} \ \ \boldsymbol{R}^T\boldsymbol{R} = \boldsymbol{I}. \tag{2.18}$$

Here, $\mathbf{R}$ denotes a proper orthogonal rotation tensor. Furthermore, the right stretch tensor $\boldsymbol{U}$ and the left stretch tensor $\boldsymbol{v}$ are unique, symmetric, and positive definite tensors. These quantities describe a local stretching or contraction of the assumed line surface along their mutually orthogonal eigenvectors. Let $\{\boldsymbol{N}_i\}$ and $\{\boldsymbol{n}_i\}$ for $i = 2, 3$ be the orthogonal and normalized sets of material and spatial eigenvectors, respectively. $\{\boldsymbol{N}_i\}$ and $\{\boldsymbol{n}_i\}$ are also named principal referential and spatial directions. Accordingly, spectral decomposition for the strain tensors reads as follows:

$$\boldsymbol{U} = \sum_{i=1}^{3} \lambda_i \mathbf{N}_i \otimes \mathbf{N}_i \quad \text{and} \quad \boldsymbol{V} = \sum_{i=1}^{3} \lambda_i \mathbf{n}_i \otimes \mathbf{n}_i, \tag{2.19}$$

and hence for the right and left Cauchy-Green tensor, we have

$$\boldsymbol{C} := \boldsymbol{U}^2 = \sum_{i=1}^{3} \lambda_i^2 \mathbf{N}_i \otimes \mathbf{N}_i \quad \text{and} \quad \boldsymbol{b} := \boldsymbol{V}^2 = \sum_{i=1}^{3} \lambda_i^2 \mathbf{n}_i \otimes \mathbf{n}_i. \tag{2.20}$$

Here, $\{\lambda_i\}$ are the real eigenvalues for the $\boldsymbol{U}$ and $\boldsymbol{V}$ and are the so-called principal stretches. The two-point tensors $\boldsymbol{F}$ and $\boldsymbol{R}$ can be written based on the principal stretches and principal directions which take the following spectral decomposition form:

$$\mathbf{R} = \sum_{i=1}^{3} \mathbf{n}_i \otimes \mathbf{N}_i \quad \text{and} \quad \mathbf{F} = \sum_{i=1}^{3} \lambda_i \mathbf{n}_i \otimes \mathbf{N}_i. \tag{2.21}$$

2.5. Stress tensors

Consider a part $\mathcal{P} \subset \mathcal{B}$ cut out of the reference configuration $\mathcal{B}$ and its spatial counterpart $\mathcal{P}^t \subset \mathcal{B}^t$, with boundaries $\partial\mathcal{P}$ and $\partial\mathcal{P}^t$, respectively. The traction vector $\boldsymbol{t}$ acts on the surface element $d\boldsymbol{a} \subset \partial\mathcal{P}^t$ in the deformed configuration. Integrated over $\partial\mathcal{P}^t$, this represents the force that the rest of the body $\mathcal{B}^t \setminus \mathcal{P}^t$ exerts on $\mathcal{P}^t$ through $\partial\mathcal{P}^t$. Cauchy's stress theorem defines the traction as depending linearly on the outward surface normal

$$\boldsymbol{t}(\boldsymbol{x}, t; \boldsymbol{n}) = \boldsymbol{\sigma}(\boldsymbol{x}, t)\boldsymbol{n}, \tag{2.22}$$

through the *Cauchy stress tensor* $\boldsymbol{\sigma}$. The identity $\boldsymbol{\tau} dA = \boldsymbol{t} da$ by scaling the (true) spatial force $\boldsymbol{t} da$ using the reference area element dA induces the definition of the *first Piola-Kirchhoff* or *nominal stress tensor* $\boldsymbol{P}$ through

$$\boldsymbol{P} d\boldsymbol{A} = \boldsymbol{\sigma} d\boldsymbol{a} \quad \text{with} \quad \boldsymbol{P} := (J\boldsymbol{\sigma})\boldsymbol{F}^{-T} \ , \tag{2.23}$$

where the area mapping (2.12) is used. Finally, we can define the *the second Piola-Kirchhoff stress tensor* through a complete pull-back of the Cauchy stress tensor, by:

$$\boldsymbol{S} := J\boldsymbol{F}^{-1}\boldsymbol{\sigma}\boldsymbol{F}^{-T} \, . \tag{2.24}$$

2.6. Physical balance principles of continuum thermodynamics

2.6.1. Balance of mass

The balance of mass results in the constant total mass m during the deformation of continuum body $\mathcal{B}$ within a closed system; thus $m(\mathcal{B}) = m(\mathcal{B}^t)$. The mass density shown by $\rho_0 = \rho_0(\boldsymbol{X})$ in the reference configuration as well as $\rho = \rho(\boldsymbol{x}, t)$ in the current configuration yields the following identity:

$$m = \int_{\mathcal{B}} \rho_0 \mathrm{d}V = \int_{\mathcal{B}^t} \rho \mathrm{d}v \ , \tag{2.25}$$

Using the volume map formulation, namely $\mathrm{d}v = J\mathrm{d}V$, (2.25) results in the material and spatial local forms of the conservation of mass by

$$J\rho(\boldsymbol{x}, t) = \rho_0(\boldsymbol{X}) \quad \text{and} \quad \dot{\rho} + \rho \,\mathrm{div}[\dot{\boldsymbol{x}}] = 0 \ , \tag{2.26}$$

whereas, the time derivative of J is used which is given by

$$\dot{J} = \frac{\partial \det \boldsymbol{F}}{\partial \boldsymbol{F}} : \frac{d\boldsymbol{F}}{dt} = J \,\mathrm{div}[\dot{\boldsymbol{x}}] \ . \tag{2.27}$$

2.6.2. Balance of linear momentum

The conservation of linear momentum states that the changes of linear momentum $L_{\mathcal{B}^t}$ over time results from the sum of all forces $F_{\mathcal{B}^t}$ acting on the deformed body $\mathcal{B}^t$. To do so, the linear momentum denoted by $\boldsymbol{L}_{\mathcal{B}^t}$ of a body is defined as follows:

$$\boldsymbol{L}_{\mathcal{B}^t} = \int_{\mathcal{B}^t} \rho \dot{\boldsymbol{x}} dv \ . \tag{2.28}$$

By definition, the balance of linear momentum is equal to the imposed surface traction denoted by $\boldsymbol{t}(\boldsymbol{x}, t)$ and also a mass specific body force shown by $\boldsymbol{b}(\boldsymbol{x}, t)$ to the body. The global form for the balance of linear momentum results in

$$\frac{d}{dt}\boldsymbol{L}_{\mathcal{B}^t} = \frac{d}{dt}\int_{\mathcal{B}^t} \rho \dot{\boldsymbol{x}} J dV = \int_{\partial \mathcal{B}^t} \mathbf{t} da + \int_{\mathcal{B}^t} \rho \mathbf{b} dv. \tag{2.29}$$

Using Cauchy's stress theorem, divergence theorem and the conservation of mass (2.26) results in spatial local form through

$$\operatorname{div}[\boldsymbol{\sigma}] + \bar{\boldsymbol{b}} = \rho \dot{\boldsymbol{v}} \ . \tag{2.30}$$

Additionally, the material local form of the linear balance of momentum is given by

$$\operatorname{Div}[\boldsymbol{P}] + \bar{\boldsymbol{B}} = \rho_0 \dot{\boldsymbol{V}} \ . \tag{2.31}$$

2.6.3. Balance of angular momentum

The conservation of angular momentum of continuum body $\mathcal{B}$ makes the balance between the changes of angular momentum $\boldsymbol{J}_{\mathcal{B}^t}$, and the resultant momentum force which is acting on body $\mathcal{B}$ at the fixed position. To do so, let $\boldsymbol{x}_0$ be the fixed reference point in the current space, then the angular momentum denoted by $\boldsymbol{J}_{\mathcal{B}^t}$ of a body is defined as follows:

$$\boldsymbol{J}_{\mathcal{B}^t} = \int_{\mathcal{B}^t} \rho(\boldsymbol{x} - \boldsymbol{x}_0) \times \boldsymbol{v} dv. \tag{2.32}$$

Accordingly, the change of angular momentum in the global form is written as,

$$\frac{d}{dt}\boldsymbol{J}_{\mathcal{B}^t} = \frac{d}{dt}\int_{\mathcal{B}^t} (\boldsymbol{x} - \boldsymbol{x}_0) \times \rho \boldsymbol{v} dv = \int_{\partial \mathcal{B}^t} (\boldsymbol{x} - \boldsymbol{x}_0) \times \mathbf{t} da + \int_{\mathcal{B}^t} \rho(\boldsymbol{x} - \boldsymbol{x}_0) \times \mathbf{b} dv. \tag{2.33}$$

Subsequently, the local angular momentum for the material and spatial formulation yields the following form,

$$(\boldsymbol{F}\boldsymbol{P}^T)^T = \boldsymbol{F}\boldsymbol{P}^T \quad \text{and} \quad \boldsymbol{\sigma}^T = \boldsymbol{\sigma}. \tag{2.34}$$

Equation (2.34) explains the symmetry of the stress tensor for the material configuration, which results in the symmetry condition for the Cauchy stress tensor in spatial configuration.

2.6.4. Balance of energy

The conservation of energy of the deformed body $\mathcal{B}^t$ describes the change of internal energy in a body. The kinetic energy of the continuum body for the spatial configuration is

$$K_{\mathcal{B}^t} = \int_{\mathcal{B}^t} \frac{1}{2} \rho \dot{\boldsymbol{x}} . \dot{\boldsymbol{x}} dv \ . \tag{2.35}$$

The internal energy denoted by $\mathcal{E}(t)$, of a continuum body $\mathcal{B}$, is occupying internal elastic strain and thermal energies which is given by

$$\mathcal{E}(t) = \int_{\mathcal{B}^t} e_c dv \ . \tag{2.36}$$

Here, e_c is the current internal energy per unit volume of the body. We further introduce the mechanical power $P_{\mathcal{B}^t}$ and thermal power $Q_{\mathcal{B}^t}$ in the spatial form through

$$P_{\mathcal{B}^t} = \int_{\mathcal{B}^t} \boldsymbol{b}.\boldsymbol{v} dv + \int_{\partial\mathcal{B}^t} \boldsymbol{t}.\boldsymbol{v} da \quad \text{and} \quad Q_{\mathcal{B}^t} = \int_{\mathcal{B}^t} r dv - \int_{\partial\mathcal{B}^t} \boldsymbol{q}.\boldsymbol{n} da \ . \tag{2.37}$$

Here, $\boldsymbol{q}$ is the external heat flux applied to the continuum body $\mathcal{B}^t$ on the Neumann boundary, r is the external heat sources injected in the body, and $\boldsymbol{n}$ is the outward unit normal in the spatial configuration. Accordingly, the global form of energy conservation yields equality between the total energy, namely kinetic energy, and the internal energy, with the total external power, namely the mechanical power and the thermal power. Hence, the global form of energy balance in the spatial form is written as follows:

$$\frac{d}{dt}[\mathcal{E}(t) + K_{\mathcal{B}^t}] = P_{\mathcal{B}^t} + Q_{\mathcal{B}^t} \ . \tag{2.38}$$

Using the symmetric part of the spatial velocity gradient in (2.10) as well as Cauchy stress theorem, divergence theorem, and the balance of linear momentum, the local form of the energy balance in the spatial form, reads

$$\dot{e}_c = \boldsymbol{\sigma} : \boldsymbol{d} + r - div[\boldsymbol{q}] \ . \tag{2.39}$$

Accordingly, the kinetic energy of the continuum body in the material form is

$$K_{\mathcal{B}} = \int_{\mathcal{B}} \frac{1}{2} \rho_0 \dot{\boldsymbol{X}}.\dot{\boldsymbol{X}} dV \ . \tag{2.40}$$

The mechanical power $P_{\mathcal{B}}$ and the thermal power $Q_{\mathcal{B}}$ in the material form are further defined using

$$P_{\mathcal{B}} = \int_{\mathcal{B}} \boldsymbol{B}.\boldsymbol{V} dV + \int_{\partial\mathcal{B}} \boldsymbol{T}.\boldsymbol{V} dA \quad \text{and} \quad Q_{\mathcal{B}} = \int_{\mathcal{B}} R dV - \int_{\partial\mathcal{B}} \boldsymbol{Q}.\boldsymbol{N} dA \ . \tag{2.41}$$

Using these definitions, the local form of the energy balance in the material form is

$$\dot{e} = \boldsymbol{P} : \dot{\boldsymbol{F}} + R - Div[\boldsymbol{Q}] \ , \tag{2.42}$$

where the identity $e(\boldsymbol{X}, t) = J e_c(\boldsymbol{x}, t)$ is used.

2.7. Dissipation and second axiom of thermodynamics

The second axiom of thermodynamics or entropy inequality describes the direction-dependency of energy transfer to the body. This inequality condition possesses a major restriction that is applied to constitutive models. The second axiom of thermodynamics postulates that the change of entropy of the continuum body, denoted as η, is strictly lower than the rate of entropy input; therefore

$$\frac{d}{dt} \int_{\mathcal{B}^t} \rho\eta dv \geq \int_{\mathcal{B}^t} \rho \frac{r}{\Theta} dv - \int_{\partial\mathcal{B}^t} \frac{1}{\Theta} \boldsymbol{q}.\boldsymbol{n} da \ . \tag{2.43}$$

The local versions of (2.43) in the material and spatial descriptions, at any point of the body at all times, is the so-called internal dissipation [63] denoted by $\mathcal{D}_0$ and $\mathcal{D}$, respectively, take the following forms:

$$\mathcal{D}_0 := \mathcal{D}_0(\boldsymbol{X}, t) \geq 0 \quad \text{and} \quad \mathcal{D} := \mathcal{D}(\boldsymbol{x}, t) \geq 0 \ . \tag{2.44}$$

The non-negative inequality condition for dissipation in (2.44) holds for an irreversible process, and the equality condition holds for a reversible process. By means of the HELMHOLTZ FREE ENERGY function, namely $\psi = e - \Theta\eta$, together with divergence theorem, and energy conservation, the local form of the material dissipation inequality states:

$$\mathcal{D}_0(\boldsymbol{X}, t) = \boldsymbol{P} : \dot{\boldsymbol{F}} - \rho(\dot{\psi} + \eta\dot{\Theta}) - \frac{1}{\Theta}\boldsymbol{Q}.Grad\Theta \geq 0 \;, \tag{2.45}$$

and spatial dissipation inequality is given through

$$\mathcal{D}(\boldsymbol{x}, t) = \boldsymbol{\sigma} : \mathbf{d} - \rho(\dot{\psi} + \eta\dot{\Theta}) - \frac{1}{\Theta}\boldsymbol{q}.grad\Theta \geq 0 \;. \tag{2.46}$$

Here, Θ denotes as the absolute temperature that is strictly positive value, i.e., $\Theta > 0$. This is known as CLAUSIUS-DUHEM inequality. The material dissipation is additively decomposed in the so-called material local dissipation $\mathcal{D}_0^{loc}$ and material heat conductivity dissipation $\mathcal{D}_0^{con}$ counterparts, such that $\mathcal{D}_0 = \mathcal{D}_0^{loc} + \mathcal{D}_0^{con}$ holds. Accordingly, the local dissipation additively decomposed through $\mathcal{D} = \mathcal{D}^{loc} + \mathcal{D}^{con}$. The strong condition for Clausius-Duhem inequality results in strict inequality heat condition for each part, namely local and conductivity dissipation. Thus, the material dissipation includes the following parts:

$$\mathcal{D}_0^{loc} = \boldsymbol{P} : \dot{\boldsymbol{F}} - \rho(\dot{\psi} + \eta\dot{\Theta}) \geq 0 \quad \text{and} \quad \mathcal{D}_0^{con} = -\frac{1}{\Theta}\boldsymbol{Q}.Grad\Theta \geq 0 \;. \tag{2.47}$$

Accordingly, for spatial dissipation, we have

$$\mathcal{D}^{loc} = \boldsymbol{\sigma} : \mathbf{d} - \rho(\dot{\psi} + \eta\dot{\Theta}) \geq 0 \quad \text{and} \quad \mathcal{D}^{con} = -\frac{1}{\Theta}\boldsymbol{q}.grad\Theta \geq 0. \tag{2.48}$$

Formulations (2.47) and (2.48) are commonly known as CLAUSIUS-PLANCK inequality, and the following identity between the material and spatial dissipations hold,

$$\mathcal{D}_0^{loc} = J\mathcal{D}^{loc} \quad \text{and} \quad \mathcal{D}_0^{con} = J\mathcal{D}^{con} \;. \tag{2.49}$$

2.8. Constitutive models

The kinematic relations and physical balance principles of continuum thermodynamics provided thus far are not sufficient for resolving the BVPs are given in (2.30) and (2.31). Hence, the necessity of describing unique material behavior leads to the introduction of *governing equations*. Let us define the scalar-valued tensor function as $\Psi := \rho\psi$. Ψ can be classified in terms of the material constituents in the solid body, as:

- *Homogeneous material.* The material constituents are distributed uniformly through the continuum domain, and hence Ψ depends only on the $\boldsymbol{F}$ and *not* on the position of a point within the material; that is $\Psi := \Psi(\boldsymbol{F})$.

- *Heterogeneous material.* The material constituents are not distributed uniformly through the continuum domain, and thus the material is divided into several phases. Thus, Ψ depends on the $\boldsymbol{F}$ and additionally on the position of point $\boldsymbol{X}$ within the domain; that is $\Psi := \Psi(\boldsymbol{F}, \boldsymbol{X})$. These phases are referred to the matrix counterpart, which is surrounded and augmented with fibers with a high stiff response.

The strain density function Ψ is set for the hyperelastic material as a subclass of elastic material, which tends toward a large deformation. We further assume that the material is restricted to the isotropic hyperelastic material. Additionally, the principles of material symmetry and isotropic response leads to the following identity for Ψ:

$$\Psi(\boldsymbol{F}) = \Psi(\boldsymbol{U}) = \Psi(\boldsymbol{V}) = \Psi(\boldsymbol{C}) = \Psi(\boldsymbol{b}) \; . \tag{2.50}$$

In the following, the strain density function is assumed to be dependent on the right Cauchy-Green tensor $\boldsymbol{C}$; namely $\Psi := \Psi(\boldsymbol{C})$.

To describe the scalar-valued tensor function, we further assume $\Psi(\boldsymbol{C})$ is an invariant under rotation. Thus, the elasticity density function $\Psi(\boldsymbol{C})$ may be described based on principal invariants through the so-called *representation theorem for invariants*, see [122, 54]. Hence, we have the following:

$$\Psi(\boldsymbol{C}) := \Psi\big(I_1(\boldsymbol{C}), I_2(\boldsymbol{C}), I_3(\boldsymbol{C})\big) \; , \tag{2.51}$$

with three principal invariants given by

$$I_1(\boldsymbol{C}) = tr(\boldsymbol{C}) = \lambda_1^2 + \lambda_2^2 + \lambda_3^2 \; , \tag{2.52}$$

$$I_2(\boldsymbol{C}) = \frac{1}{2}\big[tr(\boldsymbol{C})^2 - tr(\boldsymbol{C}^2)\big] = \lambda_1^2\lambda_2^2 + \lambda_2^2\lambda_3^2 + \lambda_1^2\lambda_3^2 \; , \tag{2.53}$$

$$I_3(\boldsymbol{C}) = \det \boldsymbol{C} = \lambda_1^2\lambda_2^2\lambda_3^2 = J^2, \tag{2.54}$$

which are valid for the isotropic hyperelastic solid material. Note, the scalar-valued tensor function $\Psi\big(I_1(\boldsymbol{C}), I_2(\boldsymbol{C}), I_3(\boldsymbol{C})\big)$ has to be polyconvex, meaning that it has to be convex in each of its arguments to ensure a well-posed solution for a BVP (i.e., the existence of the global solution, see [11]). Different forms of strain energy density function exist to formulate compressible and incompressible material. For instance, the NEO-HOOKEAN model by TRELOAR [121] for the rubber-like materials considering two material properties. Furthermore, MOONEY [102] and RIVLIN [115] present another type, which includes three material properties and a more general description of the scalar-valued strain energy density function is given by OGDEN [108] which includes six material properties. For a general overview, see [63].

Let us assume the class of perfectly elastic material (i.e., dissipation-free material) together with the isotropic hyperelastic assumption. Thus, using the Clausius-Planck form, we have $\mathcal{D}_0^{loc} = 0$ which results in

$$\mathcal{D}_0^{loc} = \boldsymbol{P} : \dot{\boldsymbol{F}} - \dot{\Psi} = \big(\boldsymbol{P} - \frac{\partial \Psi(\boldsymbol{F})}{\partial \boldsymbol{F}}\big) : \dot{\boldsymbol{F}} = 0 \quad \forall \boldsymbol{X} \in \mathcal{B}. \tag{2.55}$$

Here, the rate of the strain free energy function is replaced by $\dot{\Psi}(\boldsymbol{F}) = \partial_{\boldsymbol{F}}\Psi(\boldsymbol{F}) : \dot{\boldsymbol{F}}$. The identity (2.55) leads to the following constitutive equation

$$\boldsymbol{P}(\boldsymbol{F}) := \frac{\partial \Psi(\boldsymbol{F})}{\partial \boldsymbol{F}} \quad \forall \boldsymbol{X} \in \mathcal{B}. \tag{2.56}$$

Alternatively, an expression for the symmetric second-order Piola-Kirchhoff stress tensor reads:

$$\boldsymbol{S}(\boldsymbol{C}) := 2\frac{\partial \Psi(\boldsymbol{C})}{\partial \boldsymbol{C}} \quad \forall \boldsymbol{X} \in \mathcal{B}. \tag{2.57}$$

Here, the identity $\Big(\partial_{\boldsymbol{F}}\Psi(\boldsymbol{F})\Big)^T = 2\partial_{\boldsymbol{C}}\Psi(\boldsymbol{C})\boldsymbol{F}^T$ is considered.

A representation of the fourth-order elasticity tensor $\mathbb{C}$, which relates the work conjugate pairs of stress $(\boldsymbol{P}(\boldsymbol{F}), \boldsymbol{S}(\boldsymbol{C}))$ and strain $(\boldsymbol{F}, \boldsymbol{C})$ tensors, reads as follows:

$$\mathbb{C}(\boldsymbol{C}) := 2\frac{\partial \boldsymbol{S}(\boldsymbol{C})}{\partial \boldsymbol{C}} = 4\frac{\partial^2\Psi(\boldsymbol{C})}{\partial \boldsymbol{C}\partial \boldsymbol{C}}\ , \quad \text{and} \quad \mathbb{C}(\boldsymbol{F}) := \frac{\partial \boldsymbol{P}(\boldsymbol{F})}{\partial \boldsymbol{F}} = \frac{\partial^2\Psi(\boldsymbol{F})}{\partial \boldsymbol{F}\partial \boldsymbol{F}}\ . \tag{2.58}$$

The fourth-order elasticity tensor $\mathbb{C}(\boldsymbol{C})$ possesses both major and minor symmetries. The major symmetry of $\mathbb{C}(\boldsymbol{C})$ is caused by the existence of strain energy density function Ψ, and the minor symmetry is because of the symmetric representation of the $(\boldsymbol{S}, \boldsymbol{C})$. Notably, the major symmetry of $\mathbb{C}(\boldsymbol{C})$ is identical for the material to be hyperelastic.

2.8.1. Restricted to the small deformation

A Cauchy elastic material is a sub-class of material in which the stress response depends only on the current deformation state and thus $\boldsymbol{F} \approx \boldsymbol{I}$. Therefore, let us assume the class of perfectly elastic material, so we have $\mathcal{D}_0 = 0$ which results in

$$\mathcal{D}^{loc} = \boldsymbol{\sigma} : \boldsymbol{\varepsilon} - \rho\dot{\Psi} = \big(\boldsymbol{\sigma} - \rho\frac{\partial\Psi(\boldsymbol{\varepsilon})}{\partial\boldsymbol{\varepsilon}}\big) : \dot{\boldsymbol{\varepsilon}} = 0 \quad \forall \boldsymbol{x} \in \mathcal{B}, \tag{2.59}$$

whereas, the rate of the strain free energy function is replaced through $\dot{\Psi}(\boldsymbol{\varepsilon}) = \partial_{\boldsymbol{\varepsilon}}\Psi(\boldsymbol{\varepsilon}) : \dot{\boldsymbol{\varepsilon}}$. Herein, the isotropic free-energy function Ψ for Hookean solid that is undergoing small deformation is characterized by the two invariants:

$$I_1(\boldsymbol{\varepsilon}) = tr(\boldsymbol{\varepsilon}), \quad I_2(\boldsymbol{\varepsilon}) = tr(\boldsymbol{\varepsilon}^2). \tag{2.60}$$

The stored elastic energy in a bulk is the so-called strain density function for the isotropic materials reads as follows:

$$\Psi\big(I_1(\boldsymbol{\varepsilon}), I_2(\boldsymbol{\varepsilon})\big) := \frac{\lambda}{2}I_1^2 + \mu I_2, \tag{2.61}$$

where $\lambda > -\frac{2}{3}\mu$, and $\mu > 0$ are the elastic Lamé constants. The identity (2.59) leads to the following constitutive equation

$$\boldsymbol{\sigma}(\boldsymbol{\varepsilon}) := \frac{\partial\Psi(\boldsymbol{\varepsilon})}{\partial\boldsymbol{\varepsilon}} \quad \forall \boldsymbol{x} \in \mathcal{B}\ . \tag{2.62}$$

The fourth-order elasticity tensor $\mathbb{C}$, which relates the work conjugate pairs of stress $\boldsymbol{\sigma}(\boldsymbol{\varepsilon})$ and strain $\boldsymbol{\varepsilon}$ tensors, read as follows:

$$\mathbb{C} := \frac{\partial\boldsymbol{\sigma}(\boldsymbol{\varepsilon})}{\partial\boldsymbol{\varepsilon}} = \frac{\partial^2\Psi(\boldsymbol{\varepsilon})}{\partial\boldsymbol{\varepsilon}\partial\boldsymbol{\varepsilon}}\ . \tag{2.63}$$

The fourth-order elasticity tensor $\mathbb{C}$ at small deformation possesses both major and minor symmetries. A closed-form representation of the fourth-order elasticity tensor for the isotropic material at small deformation (i.e., an identical response in every direction within the solid body) takes the following form,

$$\mathbb{C} = \lambda\boldsymbol{I}\otimes\boldsymbol{I} + 2\mu\mathbb{I} \quad \text{with} \quad \mathbb{C}_{ijkl} = \lambda\delta_{ij}\delta_{kl} + 2\mu\big(\delta_{ik}\delta_{jl} + \delta_{il}\delta_{jk}\big)\ . \tag{2.64}$$

Therein, $\mathbb{I}_{ijkl} := \frac{1}{2}\big(\delta_{ik}\delta_{jl} + \delta_{il}\delta_{jk}\big)$ is the fourth-order symmetric identity tensor. Here, λ and μ are related to Young's modulus E and Poisson's ratio ν through

$$\mu = \frac{E}{2(1+\nu)}\ , \quad \text{and} \quad \lambda = \frac{E\nu}{(1+\nu)(1-2\nu)}\ . \tag{2.65}$$

Chapter 3

Variational Phase-Field Modeling for the Fracturing Material

Fracture mechanics is generally aimed at investigating material failure by describing the nucleation and propagation of the crack state within a solid body caused by the deformation process. To formulate the failure process within complex structures, a numerical method is typically required. Such as these numerical frameworks are based on the variational approaches to fracture [23, 24, 21] and the related regularized formulation or discrete fracture description [101, 111].

Using a variational approach, discontinuities in the displacement field are approximated across the lower-dimensional crack surface by an auxiliary term, the so-called phase-field function [87]. The latter can be viewed as an indicator function, which introduces a diffusive transition zone between the broken and unbroken material. The significant advantage of the variational phase-field formulation [93, 5] over the discrete fracture description is that the numerical implementation requires explicit (in the classical FEM) or implicit (in the extended-FEM) handling of discontinuities [35]. The possibility of avoiding the tedious task of tracking complicated crack surfaces in 3D significantly simplifies the implementation. A further advantage is the ability to simulate complicated processes, including crack initiation (also in the absence of a crack tip singularity), propagation, coalescence, and branching without the need for additional ad-hoc criteria and with very few parameters need to be identified. This feature is particularly attractive for industrial applications, as it minimizes the need for time-consuming and expensive calibration tests. This form the main objective considered in the following chapters. The essential aspects of a phase-field fracture formulation are techniques that must include (*i*) the resolution of the length-scale parameter with respect to spatial discretization, (*ii*) efficient and robust numerical solution procedures, and (*iii*) the enforcement of the irreversibility of crack growth [58, 127].

In this chapter, the variational phase-field formulation of brittle fracture when a solid body undergoes small and large deformations are outlined. Since the fracturing material behaves quite differently for bulk and shear parts, a consistent split for the strain energy density function, into the tension and compression counterparts, are discussed. We conclude this chapter with some remarks and numerical analysis. Here, the set of variational phase-field fracture formulation is used as a departure point for the next three chapters.

3.1. Variational phase-field modeling of brittle fracture at small deformation

3.1.1. Primary fields of isotropic brittle solids at small strain

In the following, let $\mathcal{B} \subset \mathcal{R}^\delta$, $\delta = \{2, 3\}$ be a smooth open and bounded set with $\partial\mathcal{B}$ denoted as its boundary. We assume Dirichlet boundary conditions $\partial_D\mathcal{B}$ and Neumann boundary conditions $\partial_N\mathcal{B} := \Gamma_N \cup \mathcal{C}$, where Γ_N denotes the outer domain boundary and the lower-dimensional fracture $\mathcal{C} \in \mathcal{R}^{\delta-1}$ is the crack boundary, as illustrated in Fig. 3.1. Using a phase-field approach, the fracture surface $\mathcal{C}$ is approximated in $\mathcal{B}_L \subset \mathcal{B} \in \mathbb{R}^\delta$, the so-called *local domain*. The intact region with no fracture is denoted as *the complementary domain* $\mathcal{B}_C := \mathcal{B} \backslash \mathcal{B}_L \subset \mathcal{B} \in \mathbb{R}^\delta$, such that $\mathcal{B}_C \cup \mathcal{B}_L =: \mathcal{B}$ and $\mathcal{B}_C \cap \mathcal{B}_L = \varnothing$. We note that $\mathcal{B}_L$, is the domain in which the smeared crack phase-field is approximated, and its boundary $\partial\mathcal{B}_L$ depends on the choice of the phase-field regularization parameter $l > 0$. This fracture length-scale parameter l is related to the discretization of a domain. In particular, this means that $h = \mathcal{O}(l)$ (see e.g., [20] for the related problem of image segmentation), where h denotes the standard spatial discretization parameter. A simplified numerical analysis on $h = \mathcal{O}(l)$ is provided in [85], and a detailed computational analysis was performed in [125, 59]. Moreover, the loading interval $\mathcal{T} := (t_0, T)$ is discretized using the discrete-time (loading) points

$$0 = t_0 < t_1 < \ldots < t_n < \ldots < t_N = T,$$

with the end time value $T > 0$. For rate-dependent problems, the parameter $t \in \mathcal{T}$ denotes the time, whereas for rate-independent problems it denotes an incremental loading parameter.

A phase-field approach to fracture leads to a multi-field problem that depends on the *deformation field* and the *crack phase-field*

$$\boldsymbol{u} : \left\{ \begin{array}{l} \mathcal{B} \times \mathcal{T} \to \mathcal{R}^\delta \\ (\boldsymbol{x}, t) \mapsto \boldsymbol{u}(\boldsymbol{x}, t) \end{array} \right. \quad \text{and} \quad s : \left\{ \begin{array}{l} \mathcal{B} \times \mathcal{T} \to [0, 1] \\ (\boldsymbol{x}, t) \mapsto s(\boldsymbol{x}, t) \end{array} \right. , \tag{3.1}$$

of a material point $\boldsymbol{x} \in \mathcal{B}$ at time $t \in \mathcal{T}$.

Specifically, we deal with a diffusive formulation that interpolates between the intact (unbroken) region with $s = 1$ and the fully fractured state of the material with $s = 0$ at $\boldsymbol{x} \in \mathcal{B}$. The Neumann condition $\nabla s.\boldsymbol{n} = 0$ is imposed on $\partial\mathcal{B}$ with $\boldsymbol{n}$ being the outward normal to the surface.

3.1.2. Variational formulation for the multi-field problem

In this section, we recapitulate a variational approach to brittle fracture in elastic solids at small strains. The following three invariants characterize the energy stored in a bulk strain density for isotropic materials:

$$I_1(\boldsymbol{\varepsilon}) = tr(\boldsymbol{\varepsilon}) \quad , \quad I_2(\boldsymbol{\varepsilon}) = tr(\boldsymbol{\varepsilon}^2) \quad , \quad I_3(\boldsymbol{\varepsilon}) = tr(\boldsymbol{\varepsilon}^3). \tag{3.2}$$

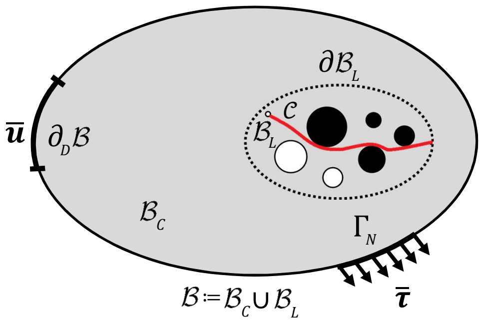

Figure 3.1: Setup of the notation: the unbroken domain denoted by $\mathcal{B}_C$. The smeared crack phase-field $\mathcal{C}$ is approximated in the domain $\mathcal{B}_L$. The whole domain is defined as a close subset as $\mathcal{B} := \mathcal{B}_C \cup \mathcal{B}_L$. The fracture domain boundary is $\partial\mathcal{B}_L$ and the outer boundary of the domain is $\partial\mathcal{B}$.

Let the effective strain density function, $\Psi(\boldsymbol{\varepsilon})$ possess the property of isotropic setting, which has a coordinate-free representation for the material. Thus the following property holds

$$\Psi(\boldsymbol{\varepsilon}) =: \Psi(\boldsymbol{Q}\boldsymbol{\varepsilon}\boldsymbol{Q}^T) \quad \forall \boldsymbol{Q} \in \mathcal{G} \subset \mathcal{O}(3) \ . \tag{3.3}$$

This holds for all orthogonal tensor $\boldsymbol{Q}$, namely $\boldsymbol{Q}^T\boldsymbol{Q} = \boldsymbol{Q}\boldsymbol{Q}^T = \boldsymbol{I}$, which is a subset of the symmetry group $\mathcal{G}$ of the isotropic material. $\boldsymbol{I} = \delta_{ij}$ is the second-order identity tensor. We denote $\Psi(\boldsymbol{\varepsilon})$ as a scalar-valued isotropic tensor function of the symmetric strain tensor $\boldsymbol{\varepsilon}$. Hence, the scalar-valued effective strain density function is invariant in *space and time* between two pairs of points in the given domain under rotation. Thus $\Psi(\boldsymbol{\varepsilon})$ can be represented by the principal invariants of $\boldsymbol{\varepsilon}$ as follows:

$$\Psi(\boldsymbol{\varepsilon}) =: \widetilde{\Psi}\big(I_1(\boldsymbol{\varepsilon}), I_2(\boldsymbol{\varepsilon})\big) := \frac{\lambda}{2} I_1^2 + \mu I_2 \ , \tag{3.4}$$

where $\lambda > -\frac{2}{3}\mu$ and $\mu > 0$ are the elastic Lamé constants. A stress-free condition, (i.e., $\boldsymbol{\varepsilon} = \boldsymbol{0}$) is required $\widetilde{\Psi}\big(I_1(\boldsymbol{0}), I_2(\boldsymbol{0})\big) = 0$.

Using these definitions, to establish a variational-based phase-field approach to brittle fractures, we define the bulk free energy functional, which represents the stored energy in bulk, as follows:

$$\mathcal{E}_{bulk}(\boldsymbol{u}) = \int_{\mathcal{B}_C} \Psi(\boldsymbol{\varepsilon}) \mathrm{d}\boldsymbol{x} - \int_{\partial_N \mathcal{B}_C} \bar{\boldsymbol{\tau}} \cdot \boldsymbol{u} \, \mathrm{d}a \ . \tag{3.5}$$

Here, $\bar{\boldsymbol{\tau}}$ denotes the traction forces on the complementary boundaries $\partial_N\mathcal{B}_C := \Gamma_N \cup \mathcal{C}$. The total energetic functional is based on both the stored bulk energy and fracture dissipation, defined in [43]:

$$\mathcal{E}(\boldsymbol{u}, \mathcal{C}) = \mathcal{E}_{bulk}(\boldsymbol{u}) + G_c \mathcal{H}^{\delta-1}(\mathcal{C}) \, , \tag{3.6}$$

where G_c is Griffith's critical elastic energy release rate and $\mathcal{H}^{\delta-1}$ is a $\delta - 1$ dimensional Hausdorff measure. To determine G_c and other related material properties, a probabilistic inverse technique can be used to identify accurate knowledge regarding the effective unknown parameters; see [69, 106, 107]. For the numerical treatment we regularize (3.6) following [23]. Specifically, the crack energy is approximated through a sequence of elliptic problems, so-called Ambrosio-Tortorelli functionals; see [7, 8]. Therein, $\mathcal{H}^{\delta-1}$ is regularized by the crack phase-field s. Finally, we account for the crack irreversibility constraint meaning that the crack can only grow:

$$\dot{s} \leq 0 \ . \tag{3.7}$$

In the incremental version, this condition reads as follows

$$s \leq s^{old} \ ,$$

where $s := s(t_n)$ and $s^{old} := s(t_{n-1})$. For stating the variational formulations, we now introduce the following spaces:

$$\begin{aligned} \boldsymbol{V} &:= \{\mathbf{H}^1(\mathcal{B})^\delta : \boldsymbol{u} = \bar{\boldsymbol{u}} \text{ on } \partial_D\mathcal{B}\}, \quad W := \mathrm{H}^1(\mathcal{B}), \\ W_{in} &:= \{s \in \mathrm{H}^1(\mathcal{B})^{\delta-1} | \ 0 \leq s \leq s^{old}\}. \end{aligned} \tag{3.8}$$

As typical in problems with inequality constraints (see e.g., [71, 73]), W_{in} is a nonempty, closed, convex, subset of the linear function space W. Due to the inequality constraint in (3.7), W_{in} is no longer a linear space.

3.1.3. Phase-field approximation of isotropic crack topologies

The variational approach of [24] is widely used for fracture failure phenomena in isotropic elastic solids. As a point of departure, in line with [92, 34], we let a regularized macro crack topology of a sharp crack be represented by the exponential function $1 - \exp^{[-|x|/l]}$ satisfying $s(0) = 0$. We define a regularized *isotropic crack surface energy functional* of the solid using

$$G_c\mathcal{H}^{\delta-1}(\mathcal{C}) := G_c \int_{\mathcal{B}} \gamma_l(s, \nabla s)\, \mathrm{s}\boldsymbol{x} \quad \text{with} \quad \gamma_l(s, \nabla s) := \frac{1}{2l}(1-s)^2 + \frac{l}{2}\nabla s.\nabla s, \tag{3.9}$$

in terms of the isotropic crack surface density function per unit volume of the solid γ_l.

Formulation 3.1.1 (Energy functional for the crack phase-field). *Let λ, μ be given with the initial conditions $\boldsymbol{u}_0 = \boldsymbol{u}(\boldsymbol{x}, 0)$ and $s_0 = s(\boldsymbol{x}, 0)$. For the loading increments $n = 1, 2, \dots, N$, find $\boldsymbol{u} := \boldsymbol{u}^n \in V$ and $s := s^n \in W_{in}$ such that the functional*

$$\begin{aligned} \mathcal{E}(\boldsymbol{u}, s) &:= \mathcal{E}_{bulk}(\boldsymbol{u}, s_+) + \ \mathcal{E}_{frac}(s) + \ \mathcal{E}_{ext}(\boldsymbol{u}) \\ &= \int_{\mathcal{B}} w_{bulk}(\boldsymbol{\varepsilon}, s) \mathrm{d}\boldsymbol{x} + \int_{\mathcal{B}} w_{frac}(s, \nabla s)\, \mathrm{d}\boldsymbol{x} - \int_{\partial_N\mathcal{B}} \bar{\boldsymbol{\tau}} \cdot \boldsymbol{u}\, \mathrm{d}a, \end{aligned}$$

is minimized. The elastic bulk density w_{bulk} along with the fracture contribution w_{frac} both define the so-called total pseudo-energy density function as

$$w(\boldsymbol{\varepsilon}, s, \nabla s) = w_{bulk}(\boldsymbol{\varepsilon}, s) + w_{frac}(s, \nabla s), \tag{3.10}$$

$$w_{bulk}(\boldsymbol{\varepsilon}, s) = g(s_+)\Psi(\boldsymbol{\varepsilon}), \tag{3.11}$$

$$w_{frac}(s, \nabla s) = G_c\gamma_l(s, \nabla s). \tag{3.12}$$

Here, the so-called monotonically decreasing quadrature degradation function, namely

$$g(s_+) := (1-\kappa)s_+^2 + \kappa, \tag{3.13}$$

describes the degradation of the solid with the evolving crack phase-field parameter s, including κ, which is a small residual stiffness that is introduced to prevent numerical problems.

Remark 3.1.1. *In the case of elastic cracks, it can be shown that the phase-field satisfies* $0 \leq s \leq 1$. *When additional physics are included, such as a fluid inside the fracture [99] or non-isothermal effects [104], the energy functional must be modified to cope with negative values of* s. *Hence to allow for future extensions, we work in the remainder with* s_+ *rather than* s. *A detailed discussion is provided in [99][Section 3].*

Remark 3.1.2. *The comparison of the bulk energy functional in (3.6) and Formulation (3.1.1) is two-fold. First, the integration is changed from* $\mathcal{B}_C$ *to the entire domain* $\mathcal{B}$ *by the presence of the phase-field function* s. *Second, the presence of* s *in the bulk energy through the degradation function* $g(s)$ *defines the transition state from the unbroken state to the fracture state and hence results in the degradation of the solid material as well as crack propagation.*

Remark 3.1.3. *Following [8, 25, 69], for the variational phase-field formulation, the existence solution for the elasticity partial differential equation (PDE) leads to* $\kappa = ch^{\chi}$ *with* $0 < \chi < 1$ *otherwise;* $||u - u_h||_{H^1}$ *is not in the convergence state. Meanwhile, the well-posedness of the phase-field PDE leads to the* $l = ch^{\beta}$ *with* $0 < \beta < \frac{1}{2}$ *to achieve convergence for* $||s - s_h||_{L^2}$. *However, the inequality condition for* χ *and* β *provides the convergence range, while the optimal convergence rate via the optimum* χ *and* β *remains an open problem in the phase-field community. To summarize, we could address following acceptable range to reach convergence in the phase-field problem, as follows:*

- *Mathematically:* $h \ll \kappa \ll l$ *and* $h = \mathcal{O}(l)$, $h = \mathcal{O}(\kappa)$, $\kappa = \mathcal{O}(l)$.
- *Numerically:* $h \ll l$, $h \ll \kappa$.
- *Practically:* $\kappa \approx 10^{-8}$ *and* $l = 2h$ *or* $l = 4h$.

3.1.4. Extension toward a decoupled strain-energy function

Since the fracturing material behaves quite differently in bulk and shear parts of the domain, in the following section, we employ a consistent split for the strain energy density function (3.4), into *tension* and *compression* counterparts, respectively.

Volumetric- and isochoric-based decomposition. Here, instead of dealing directly with $\boldsymbol{\varepsilon}(\boldsymbol{u})$, we perform additive decomposition of the strain tensor into *volume-changing* (volumetric part) and *volume-preserving* (deviatoric part) counterparts:

$$\boldsymbol{\varepsilon}(\boldsymbol{u}) = \boldsymbol{\varepsilon}^{vol}(\boldsymbol{u}) + \boldsymbol{\varepsilon}^{dev}(\boldsymbol{u}),$$

whereas the volumetric strain is denoted as $\boldsymbol{\varepsilon}^{vol}(\boldsymbol{u}) := \frac{1}{3}(\boldsymbol{\varepsilon}(\boldsymbol{u}) : \boldsymbol{I})\boldsymbol{I}$ and the deviatoric strain is denoted as $\boldsymbol{\varepsilon}^{dev}(\boldsymbol{u}) := \mathbb{P} : \boldsymbol{\varepsilon}$. The fourth-order projection tensor $\mathbb{P} := \mathbb{I} - \frac{1}{3}\boldsymbol{I} \otimes \boldsymbol{I}$ is introduced to map the full strain tensor to its deviatoric counterpart. Therein, $\mathbb{I}_{ijkl} :=$

$\frac{1}{2}\big(\delta_{ik}\delta_{jl}+\delta_{il}\delta_{jk}\big)$ is the fourth-order symmetric identity tensor. Furthermore, $\mathbb{P}$ possesses the major symmetries (i.e., $\mathbb{P}_{ijkl}=\mathbb{P}_{klij}$, and $\mathbb{P}^n=\mathbb{P}$) for any given integer n. Therefore, a decoupled representation of the strain-energy function through the so-called volumetric and deviatoric contribution reads:

$$\Psi(\boldsymbol{\varepsilon}(\boldsymbol{u}))=\Psi(\boldsymbol{\varepsilon}^{vol}(\boldsymbol{u}))+\Psi(\boldsymbol{\varepsilon}^{dev}(\boldsymbol{u}))\ . \tag{3.14}$$

Therein, the volumetric contribution of the strain energy density function reads,

$$\Psi(\boldsymbol{\varepsilon}^{vol}(\boldsymbol{u})):=\frac{\lambda}{2}\big(\boldsymbol{\varepsilon}^{vol}(\boldsymbol{u}):\boldsymbol{I}\big)^2+\mu\boldsymbol{\varepsilon}^{vol}(\boldsymbol{u})^2:\boldsymbol{I}=\frac{K_\delta}{2}(\boldsymbol{\varepsilon}^{vol}(\boldsymbol{u}):\boldsymbol{I})^2, \tag{3.15}$$

where $K_\delta:=\frac{2}{\delta}\mu+\lambda$ is the bulk modulus and $\delta\in\{2,3\}$. The deviatoric contribution of the strain energy density function is as follows:

$$\Psi(\boldsymbol{\varepsilon}^{dev}(\boldsymbol{u})):=\frac{\lambda}{2}\big(\boldsymbol{\varepsilon}^{dev}(\boldsymbol{u}):\boldsymbol{I}\big)^2+\mu\boldsymbol{\varepsilon}^{dev}(\boldsymbol{u})^2:\boldsymbol{I}=\mu\boldsymbol{\varepsilon}^{dev}(\boldsymbol{u})^2:\boldsymbol{I}. \tag{3.16}$$

To show that the equality holds in (3.14) together with (3.15) and (3.16), the identities $\boldsymbol{\varepsilon}^{dev}(\boldsymbol{u}):\boldsymbol{I}=0$, and $\boldsymbol{\varepsilon}^{vol}(\boldsymbol{u}):\boldsymbol{\varepsilon}^{dev}(\boldsymbol{u})=0$ are used. Physically, it is trivial to assume that the degradation induced by the phase-field acts only on the tensile and shear counterpart of the elastic strain density function. Hence, there is no degradation in compression, which also prevents the interpenetration of the crack lips during crack closure; see [92, 5]. Following, [117], it turns out that the modified strain energy density function for the fracturing material becomes,

$$w_{bulk}(\boldsymbol{\varepsilon},s):=g(s_+)\Psi^+\big(\boldsymbol{\varepsilon}(\boldsymbol{u})\big)+\Psi^-\big(\boldsymbol{\varepsilon}(\boldsymbol{u})\big)\ . \tag{3.17}$$

The positive part of the strain energy density function, which is the tensile and deviatoric part of the full strain energy density function, reads

$$\Psi^+(\boldsymbol{\varepsilon}(\boldsymbol{u}))=H^+(\nabla.\boldsymbol{u})\Psi(\boldsymbol{\varepsilon}^{vol}(\boldsymbol{u}))+\Psi(\boldsymbol{\varepsilon}^{dev}(\boldsymbol{u}))\ . \tag{3.18}$$

Therein, $H^+(\nabla.\boldsymbol{u})$ is a *positive Heaviside function* such that if $\nabla.\boldsymbol{u}$ is positive it returns one and otherwise it returns a zero value. Notably, due to identity $\nabla.\boldsymbol{u}=\mathrm{tr}(\boldsymbol{\varepsilon})$, the positive Heaviside function indicates the points in a domain where they are in the tensile state with $H^+(\nabla.\boldsymbol{u})=1$ and the compression state with $H^+(\nabla.\boldsymbol{u})=0$. The negative strain energy density function that is the compression part of the full strain energy density function, is given by:

$$\Psi^-(\boldsymbol{\varepsilon}(\boldsymbol{u}))=\big(1-H^+(\nabla.\boldsymbol{u})\big)\Psi(\boldsymbol{\varepsilon}^{vol}(\boldsymbol{u}))\ . \tag{3.19}$$

The constitutive equation is additively split to purely tensile contribution $\boldsymbol{\sigma}^+(\boldsymbol{\varepsilon})$ and purely compression contribution $\boldsymbol{\sigma}^-(\boldsymbol{\varepsilon})$, reads

$$\boldsymbol{\sigma}(\boldsymbol{\varepsilon},s):=\frac{\partial w_{bulk}(\boldsymbol{\varepsilon},s)}{\partial\boldsymbol{\varepsilon}}=g(s_+)\frac{\partial\widetilde{\Psi}^+}{\partial\boldsymbol{\varepsilon}}+\frac{\partial\widetilde{\Psi}^-}{\partial\boldsymbol{\varepsilon}}=g(s_+)\widetilde{\boldsymbol{\sigma}}^++\widetilde{\boldsymbol{\sigma}}^-, \tag{3.20}$$

therein,

$$\boldsymbol{\sigma}^+(\boldsymbol{\varepsilon})=K_nH^+(\nabla.\boldsymbol{u})(\boldsymbol{\varepsilon}:\boldsymbol{I})\boldsymbol{I}+2\mu\boldsymbol{\varepsilon}^{dev},\quad\text{and}\quad\boldsymbol{\sigma}^-(\boldsymbol{\varepsilon})=K_n\big(1-H^+(\nabla.\boldsymbol{u})\big)(\boldsymbol{\varepsilon}:\boldsymbol{I})\boldsymbol{I}. \tag{3.21}$$

The decoupled representation of the fourth-order elasticity tensor (to relate the work into conjugate pairs of stress and strain tensors) is obtained through the additive decomposition of the stress tensor, reads as follows:

$$\mathbb{C} := \frac{\partial \boldsymbol{\sigma}(\boldsymbol{\varepsilon})}{\partial \boldsymbol{\varepsilon}} = g(s_+)\frac{\partial \boldsymbol{\sigma}^+(\boldsymbol{\varepsilon})}{\partial \boldsymbol{\varepsilon}} + \frac{\partial \boldsymbol{\sigma}^-(\boldsymbol{\varepsilon})}{\partial \boldsymbol{\varepsilon}} =: g(s_+)\widetilde{\mathbb{C}}^+ + \widetilde{\mathbb{C}}^-, \tag{3.22}$$

with

$$\widetilde{\mathbb{C}}^+ = K_n H^+(\nabla.\boldsymbol{u})\boldsymbol{I}\otimes\boldsymbol{I} + 2\mu\mathbb{P}, \quad \text{and} \quad \mathbb{C}^- = K_n\big(1 - H^+(\nabla.\boldsymbol{u})\big)\boldsymbol{I}\otimes\boldsymbol{I}\ ,$$

where the identity $\partial_{\boldsymbol{\varepsilon}}\boldsymbol{\varepsilon}^{dev}(\boldsymbol{u}) =: \mathbb{P}$ is used.

Eigenvalue-based decomposition. Next, we formulate the variational phase-field modeling through eigenvalue-based decomposition of the strain tensor into the $\Psi\big(I_1(\boldsymbol{\varepsilon})\ , I_2(\boldsymbol{\varepsilon})\big)$ [92]. Hence, instead of dealing directly with $\boldsymbol{\varepsilon}(\boldsymbol{u})$, we perform additive decomposition of the strain tensor, as follows:

$$\boldsymbol{\varepsilon}(\boldsymbol{u}) = \boldsymbol{\varepsilon}^+(\boldsymbol{u}) + \boldsymbol{\varepsilon}^-(\boldsymbol{u}) \quad \text{with} \quad \boldsymbol{\varepsilon}^\pm(\boldsymbol{u}) := \sum_{i=1}^{\delta}\langle\varepsilon_i\rangle^\pm \mathbf{N}_i\otimes\mathbf{N}_i\ ,$$

with tension $\boldsymbol{\varepsilon}^+$ and compression $\boldsymbol{\varepsilon}^-$ strains. Here, $\langle x\rangle_\pm := \frac{x\pm|x|}{2}$ is a ramp function of $\mathcal{R}_\pm$ expressed by the Macauley bracket. $\{\varepsilon_i\}$ are the principal strains and $\{\mathbf{N}_i\}$ are the principal strain directions. The tension/compression fourth-order projection tensor is defined as

$$\mathbb{P}^\pm_{\boldsymbol{\varepsilon}} := \frac{\partial \boldsymbol{\varepsilon}^\pm}{\partial \boldsymbol{\varepsilon}} = \frac{\partial\big(\sum_{i=1}^{\delta}\langle\varepsilon_i\rangle^\pm \mathbf{N}_i\otimes\mathbf{N}_i\big)}{\partial \boldsymbol{\varepsilon}}\ . \tag{3.23}$$

In fact, $\mathbb{P}^\pm_{\boldsymbol{\varepsilon}}$ projects the total strain into its positive and negative parts accordingly; that is $\boldsymbol{\varepsilon}^\pm = \mathbb{P}^\pm_{\boldsymbol{\varepsilon}} : \boldsymbol{\varepsilon}$. Thus, a decoupled representation of the strain-energy function into the so-called tension and compression contribution is given as follows:

$$\Psi\big(I_1(\boldsymbol{\varepsilon}), I_2(\boldsymbol{\varepsilon})\big) := \underbrace{\widetilde{\Psi}^+\big(I_1^+(\boldsymbol{\varepsilon}), I_2^+(\boldsymbol{\varepsilon})\big)}_{\text{tension term}} + \underbrace{\widetilde{\Psi}^-\big(I_1^-(\boldsymbol{\varepsilon}), I_2^-(\boldsymbol{\varepsilon})\big)}_{\text{compression term}}. \tag{3.24}$$

Herein, the positive and negative principal invariants are

$$I_1^\pm(\boldsymbol{\varepsilon}) := \langle I_1(\boldsymbol{\varepsilon})\rangle_\pm, \quad I_2^\pm(\boldsymbol{\varepsilon}) := I_2(\boldsymbol{\varepsilon}^\pm)\ . \tag{3.25}$$

The bulk work density function for the fracturing material becomes,

$$w_{bulk}(\boldsymbol{\varepsilon}, s) := g(s_+)\Big[\widetilde{\Psi}^+(I_1^+, I_2^+)\Big] + \widetilde{\Psi}^-(I_1^-, I_2^-)\ . \tag{3.26}$$

Next, the constitutive stress response corresponding to (3.26) reads as follows:

$$\boldsymbol{\sigma}(\boldsymbol{\varepsilon}, s) := \frac{\partial w_{bulk}(\boldsymbol{\varepsilon}, s)}{\partial \boldsymbol{\varepsilon}} = g(s_+)\frac{\partial \widetilde{\Psi}^+}{\partial \boldsymbol{\varepsilon}} + \frac{\partial \widetilde{\Psi}^-}{\partial \boldsymbol{\varepsilon}} = g(s_+)\widetilde{\boldsymbol{\sigma}}^+ + \widetilde{\boldsymbol{\sigma}}^-, \tag{3.27}$$

with

$$\widetilde{\boldsymbol{\sigma}}^\pm := \lambda I_1^\pm(\boldsymbol{\varepsilon})\mathbf{I} + 2\mu\boldsymbol{\varepsilon}_\pm\ . \tag{3.28}$$

The related counterparts of the standard fourth-order elasticity tensor $\mathbb{C}$ reads

$$\mathbb{C} := \frac{\partial \boldsymbol{\sigma}(\boldsymbol{\varepsilon})}{\partial \boldsymbol{\varepsilon}} = g(s_+)\frac{\partial \boldsymbol{\sigma}^+(\boldsymbol{\varepsilon})}{\partial \boldsymbol{\varepsilon}} + \frac{\partial \boldsymbol{\sigma}^-(\boldsymbol{\varepsilon})}{\partial \boldsymbol{\varepsilon}} =: g(s_+)\widetilde{\mathbb{C}}^+ + \widetilde{\mathbb{C}}^-, \tag{3.29}$$

with

$$\widetilde{\mathbb{C}}^\pm(\boldsymbol{\varepsilon}) := \frac{\partial \boldsymbol{\sigma}^\pm_{\boldsymbol{\varepsilon}}}{\partial \boldsymbol{\varepsilon}} = \lambda H^\pm(I_1^\pm(\boldsymbol{\varepsilon}))\mathbb{J} + 2\mu\mathbb{P}^\pm(\boldsymbol{\varepsilon})\ . \tag{3.30}$$

Here, H^+ is the standard Heaviside function, $H^- := 1 - H^+$, and $\mathbb{J} := \mathbf{I} \otimes \mathbf{I}$ is the fourth-order symmetric identity tensor.

Formulation 3.1.2 (Energy functional for the crack phase-field)**.** *Let λ, μ be given with the initial conditions $\boldsymbol{u}_0 = \boldsymbol{u}(\boldsymbol{x}, 0)$ and $s_0 = s(\boldsymbol{x}, 0)$. For the loading increments $n = 1, 2, \ldots, N$, find $\boldsymbol{u} := \boldsymbol{u}^n \in V$ and $s := s^n \in W_{in}$ such that the functional*

$$\mathcal{E}(\boldsymbol{u}, s) = \underbrace{\int_{\mathcal{B}} \big[g(s_+)\widetilde{\Psi}^+ + \widetilde{\Psi}^-\big]\mathrm{d}\boldsymbol{x}}_{\textit{deformation term}} + G_c \underbrace{\int_{\mathcal{B}} \gamma_l \mathrm{d}\boldsymbol{x}}_{\textit{fracture term}} - \underbrace{\int_{\partial_N \mathcal{B}} \bar{\boldsymbol{\tau}} \cdot \boldsymbol{u}\, \mathrm{d}a}_{\textit{external load}},$$

is minimized.

The minimization problem for the given energy functional of the crack phase-field in Formulation (3.1.2) takes the following compact form:

$$\boxed{\{\boldsymbol{u}, s\} = \arg\{ \min_{\boldsymbol{u} \in \mathbf{V}} \min_{d \in W_{in}} [\ \mathcal{E}(\boldsymbol{u}, s)\ ]\ \}.} \tag{3.31}$$

The stationary points of the energy functional in Formulation (3.1.2) are characterized by the first-order necessary conditions, namely the so-called Euler-Lagrange equations, which are obtained by differentiation with respect to $\boldsymbol{u}$ and s.

Formulation 3.1.3 (Euler-Lagrange equations)**.** *Let λ, μ be given with the initial conditions $\boldsymbol{u}_0 = \boldsymbol{u}(\boldsymbol{x}, 0)$ and $s_0 = s(\boldsymbol{x}, 0)$. For the loading increments $n = 1, 2, \ldots, N$, find $\boldsymbol{u} := \boldsymbol{u}^n \in V$ and $s := s^n \in W_{in}$:*

$$\begin{aligned}
\mathcal{E}_{\boldsymbol{u}}(\boldsymbol{u}, s; \delta\boldsymbol{u}) &= \int_{\mathcal{B}} g(s_+)\widetilde{\boldsymbol{\sigma}}^+_{\boldsymbol{\varepsilon}}(\boldsymbol{u}) : \boldsymbol{\varepsilon}(\delta\boldsymbol{u})\mathrm{d}\boldsymbol{x} + \int_{\mathcal{B}} \widetilde{\boldsymbol{\sigma}}^-(\boldsymbol{u}) : \boldsymbol{\varepsilon}(\delta\boldsymbol{u})\mathrm{d}\boldsymbol{x} \\
&\quad - \int_{\partial_N \mathcal{B}} \bar{\boldsymbol{\tau}} \cdot \delta\boldsymbol{u}\, \mathrm{d}a = 0 \quad \forall \delta\boldsymbol{u} \in V, \\
\mathcal{E}_s(\boldsymbol{u}, s; \delta s - s) &= (1 - \kappa) \int_{\mathcal{B}} s_+ \big[\widetilde{\boldsymbol{\sigma}}^+(\boldsymbol{u})\big] : \boldsymbol{\varepsilon}(\boldsymbol{u}).(\delta s - s)\mathrm{d}\boldsymbol{x} \\
&\qquad + G_c \int_{\mathcal{B}} \Big(\frac{1}{l}(s - 1).(\delta s - s) + l\nabla s.\nabla(\delta s - s)\Big)\, \mathrm{d}\boldsymbol{x} \\
&\qquad \geq 0 \quad \forall \delta s \in W \cap L^\infty.
\end{aligned} \tag{3.32}$$

Here, $\mathcal{E}_{\boldsymbol{u}}$ and $\mathcal{E}_s$ are the directional derivatives of the energy functional with respect to $\boldsymbol{u}$ and s, respectively. Furthermore, $\delta\boldsymbol{u} \in \{\mathbf{H}^1(\mathcal{B})^\delta : \delta\boldsymbol{u} = \mathbf{0}$ on $\partial_D\mathcal{B}\}$ is the deformation test function and $\delta s \in H^1(\mathcal{B})$ is the phase-field test function.

3.1.5. Euler-Lagrange equations in a strong form

To complete our derivations, the strong forms of Formulation (3.1.3) are provided. Using integration by parts, we obtain a quasi-stationary elliptic system for the displacements and the phase-field variable, where the latter one is subject to an inequality constraint in time and thus needs to be augmented with a complementary condition:

Formulation 3.1.4 (Strong form of the Euler-Lagrange equations)**.** *Let* λ, μ *be given with the initial conditions* $\boldsymbol{u}_0 = \boldsymbol{u}(\boldsymbol{x}, 0)$ *and* $s_0 = s(\boldsymbol{x}, 0)$. *For the loading increments* $n = 1, 2, \dots, N$, *we solve a displacement equation where we seek* $\boldsymbol{u} := \boldsymbol{u}^n : \mathcal{B} \to \mathbb{R}^\delta$ *such that*

$$\begin{aligned} -\operatorname{div}(\boldsymbol{\sigma}) &= \boldsymbol{0} \quad \text{in } \mathcal{B}, && (3.33)\\ \boldsymbol{u} &= \bar{\boldsymbol{u}} \quad \text{on } \partial_D\mathcal{B}, && (3.34)\\ \boldsymbol{\sigma}\cdot\boldsymbol{n} &= \bar{\boldsymbol{\tau}} \quad \text{on } \partial_N\mathcal{B}, && (3.35) \end{aligned}$$

in terms of the stress tensor $\boldsymbol{\sigma}$ *defined in (3.27) and the given displacement field* $\bar{\boldsymbol{u}}$. *The phase-field system consists of four parts: the PDE, the inequality constraint, a compatibility condition (in fracture mechanics called Rice condition [114]) along with the Neumann-type boundary conditions. Find* $s := s^n : \mathcal{B} \to [0, 1]$ *such that*

$$\begin{aligned} -\Big(2(1-\kappa)s_+\big[\widetilde{\Psi}^+\big] - \frac{G_c}{l}(1-s) - G_c l\delta s\Big) &\geq 0 \quad \text{in } \mathcal{B}, && (3.36)\\ \dot{s} &\leqslant 0 \quad \text{in } \mathcal{B}, && (3.37)\\ -\Big(2(1-\kappa)s_+\big[\widetilde{\Psi}^+\big] - \frac{G_c}{l}(1-s) - G_c l\delta s\Big)\,\dot{s} &= 0 \quad \text{in } \mathcal{B}, && (3.38)\\ \nabla s\cdot\boldsymbol{n} &= 0 \quad \text{on } \partial\mathcal{B}. && (3.39) \end{aligned}$$

The mentioned inequality minimization problem for the phase-field equation can be resolved through: (a) fixing the fracture with *Dirichlet conditions* [23]; (b) *the penalty method*; see [98, 47]; (c) *an Augmented Lagrangian penalization*; see [124]; (d) *the primal-dual active set method*; see [58, 78]; and (e) *the maximum crack driving state function*; see [92, 95]. In the present study, we consider the maximum crack driving state function to prevent crack healing through having a positive crack dissipation known as irreversibility criteria, which is described in detail in Section 3.1.7.

3.1.6. Global balance principle of the continuum phase-field

This section describes thermodynamical consistency for preserving the principle of energy balance by considering a sequence of variational substitutions. As a point of departure, recall the weak forms derived for the displacement and phase-field given in Formulation (3.1.3). To derive a global balance of energy, we choose $\delta\boldsymbol{u} =: \dot{\boldsymbol{u}}$ and $\delta s =: \dot{s}$ as test functions and restate Formulation (3.1.3) for the mechanical part as follows:

$$\mathcal{E}_{\boldsymbol{u}}(\boldsymbol{u}, s_+; \dot{\boldsymbol{u}}) = \int_{\mathcal{B}} g(s_+)\widetilde{\boldsymbol{\sigma}}^+(\boldsymbol{u}) : \nabla\dot{\boldsymbol{u}}\mathrm{d}\boldsymbol{x} + \int_{\mathcal{B}} \widetilde{\boldsymbol{\sigma}}^-(\boldsymbol{u}) : \nabla\dot{\boldsymbol{u}}\mathrm{d}\boldsymbol{x} - \int_{\partial_N\mathcal{B}} \bar{\boldsymbol{\tau}}\cdot\dot{\boldsymbol{u}}\,\mathrm{d}a = 0 \quad \forall\dot{\boldsymbol{u}} \in V. \tag{3.40}$$

We define the second-order displacement gradient denoted as $\boldsymbol{H} := \nabla\boldsymbol{u}$, and then (3.40) reduces to

$$\mathcal{E}_{\boldsymbol{u}}(\boldsymbol{u}, s_+; \dot{\boldsymbol{u}}) = \int_{\mathcal{B}} g(s_+)\widetilde{\boldsymbol{\sigma}}^+(\boldsymbol{u}) : \dot{\boldsymbol{H}}\mathrm{d}\boldsymbol{x} + \int_{\mathcal{B}} \widetilde{\boldsymbol{\sigma}}^-(\boldsymbol{u}) : \dot{\boldsymbol{H}}\mathrm{d}\boldsymbol{x} - \int_{\partial_N\mathcal{B}} \bar{\boldsymbol{\tau}} \cdot \dot{\boldsymbol{u}}\,\mathrm{d}a = 0 \quad \forall \dot{\boldsymbol{u}} \in V, \tag{3.41}$$

that is

$$\int_{\mathcal{B}} \dot{w}_{bulk}\Big(\boldsymbol{u}, \boldsymbol{\varepsilon}(\boldsymbol{u}), s_+\Big)\,\mathrm{d}\boldsymbol{x} - \int_{\mathcal{B}} \frac{\partial w_{bulk}}{\partial s}\dot{s}\,\mathrm{d}\boldsymbol{x} - P^{ext} = 0, \tag{3.42}$$

$$\Leftrightarrow \qquad P^{int} - \int_{\mathcal{B}} \frac{\partial w_{bulk}}{\partial s}\dot{s}\,\mathrm{d}\boldsymbol{x} - P^{ext} = 0. \tag{3.43}$$

Herein, the rate of internal mechanical power which describes the response of a domain $\mathcal{B}$ done by the stress field is

$$\begin{aligned} P^{int}(\dot{\boldsymbol{u}}, \dot{s}) = \dot{\mathcal{E}}_{bulk}(\boldsymbol{u}, s_+) &= \int_{\mathcal{B}} \dot{w}_{bulk}\Big(\boldsymbol{u}, \boldsymbol{\varepsilon}(\boldsymbol{u}), s_+\Big) \\ &= \int_{\mathcal{B}} \frac{\partial w_{bulk}}{\partial \boldsymbol{u}}.\dot{\boldsymbol{u}}\,\mathrm{d}\boldsymbol{x} + \int_{\mathcal{B}} \frac{\partial w_{bulk}}{\partial \boldsymbol{\varepsilon}} : \dot{\boldsymbol{\varepsilon}}\,\mathrm{d}\boldsymbol{x} + \int_{\mathcal{B}} \frac{\partial w_{bulk}}{\partial s}\dot{s}\,\mathrm{d}\boldsymbol{x}, \end{aligned} \tag{3.44}$$

and the external mechanical power is

$$P^{ext}(\dot{\boldsymbol{u}}) = \dot{\mathcal{E}}_{ext}(\boldsymbol{u}) = \int_{\partial_N\mathcal{B}} \bar{\boldsymbol{\tau}} \cdot \dot{\boldsymbol{u}}\,\mathrm{d}a, \tag{3.45}$$

Accordingly, through Formulation (3.1.3) for the phase-field part, we derive

$$\mathcal{E}_s(\boldsymbol{u}, s_+; \dot{s}) = \int_{\mathcal{B}} \frac{\partial w_{bulk}}{\partial s}\dot{s}\,\mathrm{d}\boldsymbol{x} + G_c \int_{\mathcal{B}} \Big(\frac{1}{l}(s-1).\dot{s} + l(\nabla s)\nabla\dot{s}\Big)\,\mathrm{d}\boldsymbol{x} = 0 \qquad \forall \dot{s} < 0 \in W. \tag{3.46}$$

It is important to note that the inequality $\mathcal{E}_s(\cdot\,;\,\cdot)$ in Formulation (3.1.3) becomes an equality in (3.46), because we consider the situation in which the inequality constraint (3.37) is strictly fulfilled, namely $\dot{s} < 0$. In this case equality must hold in (3.36) (and thus in $\mathcal{E}_s(\cdot\,;\,\cdot)$) because otherwise the compatibility condition (3.38) is not fulfilled. We can restate (3.46) as follows,

$$\dot{\mathcal{E}}_{frac}(s) = \int_{\mathcal{B}} G_c \delta_s \gamma_l(s, \nabla s)\dot{s}\mathrm{d}\boldsymbol{x} = -\int_{\mathcal{B}} \frac{\partial w_{bulk}}{\partial s}\dot{s}\,\mathrm{d}\boldsymbol{x}\ . \tag{3.47}$$

Here, $\delta_s\gamma_l(s, \nabla s)$ is the functional derivative of γ_l with respect to s which is obtained through:

$$\int_{\mathcal{B}} \delta_s\gamma_l(s, \nabla s)\mathrm{d}\boldsymbol{x} := \int_{\mathcal{B}} \Big(\frac{\partial \gamma_l}{\partial s} + \frac{\partial \gamma_l}{\partial \nabla s}\Big)\mathrm{d}\boldsymbol{x} = \int_{\mathcal{B}} \Big(\frac{\partial \gamma_l}{\partial s} - \nabla.[\frac{\partial \gamma_l}{\partial \nabla s}]\Big)\mathrm{d}\boldsymbol{x}\ , \tag{3.48}$$

that is,

$$\int_{\mathcal{B}} \delta_s\gamma_l(s, \nabla s)\mathrm{d}\boldsymbol{x} = \int_{\mathcal{B}} \frac{1}{l}[(s-1) - l^2\delta s]\mathrm{d}\boldsymbol{x}\ , \tag{3.49}$$

due to $\frac{\partial \gamma_l(s,\nabla s)}{\partial \nabla s} \cdot \boldsymbol{n} = l\nabla s \cdot \boldsymbol{n} = 0$.

The left-hand side of (3.47) is considered to be a functional of the rate of the crack phase-field, namely the *global crack dissipation* functional $\dot{\mathcal{E}}_{frac}(s)$, and hence

$$\dot{\mathcal{E}}_{frac}(s) \geqslant 0. \tag{3.50}$$

Through the second term in (3.47) and considering (3.50), the local form of crack dissipation reads as follows:

$$\delta_s \gamma_l(d, \nabla s) \leqslant 0 \qquad \text{and} \qquad \dot{s} \leqslant 0, \tag{3.51}$$

and the third term of (3.47) leads to the additional local condition; that is

$$\beta_s := \frac{\partial w_{bulk}(\boldsymbol{u}, s_+)}{\partial s} \geqslant 0. \tag{3.52}$$

Herein, β_s is introduced as a driving force that is conjugate to the phase-field variable, that is

$$\beta_s = 2(1-\kappa)s_+\Psi(\boldsymbol{\varepsilon}(\boldsymbol{u})). \tag{3.53}$$

In our formulation, compared with Miehe et al. [92], we have $\beta_s = -f$ (because the definition of the crack phase-field is like the damage variable in [92]). Note that β_d becomes zero on the fracture surface (i.e., $\mathcal{C}$) as s becomes zero.

The right-hand side of (3.47), namely $-\int_{\mathcal{B}} \beta_d \dot{s} \, \mathrm{d}\boldsymbol{x}$, can also be obtained using (3.43) and hence (3.47) is restated as

$$\boxed{\mathcal{E}(\dot{\boldsymbol{u}}, \dot{s}) = \dot{\mathcal{E}}_{frac}(s) + P^{int}(\dot{\boldsymbol{u}}, \dot{s}) - P^{ext}(\dot{\boldsymbol{u}}) = 0.} \tag{3.54}$$

This is the global form of the balance of energy for the coupled two-field problem describing the evolution of internal energy and crack dissipation energy (i.e., $\dot{\mathcal{E}}_{frac}(s) + P^{int}$) in a system due to the external loads (i.e., P^{ext}).

Remark 3.1.4. *It is noted in the loading state (i.e.,* $\dot{s} < 0$*), due to the compatibility condition (3.38), one may observe* $\beta_s + G_c\delta_s\gamma_l(s, \nabla s) = 0$ *and in the unloading state, i.e.,* $\dot{s} = 0$*, we have* $\beta_s + G_c\delta_s\gamma_l(d, \nabla s) < 0$*.*

3.1.7. Resolving the crack irreversibility constraint

In this section, we aim to cope with the inequality minimization problem arises from the phase-field equation. As a point of departure, recall the phase-field fracture PDE given in Formulation (3.1.4) to be reformulated in the following abstract form:

$$\underbrace{-g'(s_+)\widetilde{D}}_{crack\ driving\ force} - \underbrace{l\delta_s\gamma_l}_{resistance} \geq 0, \tag{3.55}$$

as outlined in the works of MIEHE and coworkers [95, 94]. Here, $\widetilde{D}$ is a *crack driving state function* which depends on a *state* array of strain- or stress like quantities. To remove the above mentioned inequality evolution problem, we maximize the inequality equation given in (3.55) for the full process history $s \in [0, t_n]$,

$$-g'(s_+) \max_{s\in[0,t_n]} \widetilde{D} = l\delta_s\gamma_l \ . \tag{3.56}$$

We introduce maximum positive crack driving force $\mathcal{H}$ in $t \in [0, t_n]$ denoted as,

$$\mathcal{H}(\boldsymbol{x}, t) := \max_{s\in[0,t_n]} \widetilde{D}\big(state(\boldsymbol{x}, \boldsymbol{\varepsilon}(s))\big), \tag{3.57}$$

and hence (3.55) can be restated as follows,

$$\boxed{\underbrace{-g'(s_+)\mathcal{H}}_{max\ crack\ driving\ force} \quad - \underbrace{l\delta_s.\gamma_l}_{resistance} = 0.} \tag{3.58}$$

Depending on the type of the crack driving state function, which can be either without or with threshold, $\widetilde{D}$ can take different descriptions; see [2].

By defining the maximum positive crack driving force $\mathcal{H}$ in terms of the crack driving state function $\widetilde{D}$ at hand, Formulation (3.1.3) can be stated as an equality minimization. Thus $\mathcal{H}$ substitutes the corresponding $\big[\widetilde{\Psi}^+\big]$ term in the original $\mathcal{E}_s$. To derive the crack driving state function, we recall (3.36) in Formulation (3.1.4), thus we have:

$$-\delta_s w = (\kappa - 1)2s_+\big[\widetilde{\Psi}^+\big] - G_c\delta_s\gamma_l(s, \nabla s) \geq 0 \ . \tag{3.59}$$

The maximization of this inequality in the full process history $s \in [0, t_n]$, yields

$$(\kappa - 1)2s_+ \max_{s\in[0,t_n]} \big[\widetilde{\Psi}^+\big] = G_c\delta_s\gamma_l(s, \nabla s) \ . \tag{3.60}$$

To follow the phase-field fracture equation defined in (3.55), we multiply (3.60) by $\frac{l}{G_c}$. With the definition of the maximum positive crack driving force, (3.60) is restated as follows:

$$(\kappa - 1)2s_+\mathcal{H} = l\delta_s\gamma_l \ \text{ if } \mathcal{H} := \max_{s\in[0,t_n]} \widetilde{D} \ \text{ with } \ \widetilde{D} := \frac{l\big[\widetilde{\Psi}^+\big]}{G_c} \ . \tag{3.61}$$

It is evident that the crack driving state function given by (3.61) is directly affected by the regularization parameter l. Hence, the crack driving state function has the property of length-scale dependency.

Formulation 3.1.5 (Final Euler-Lagrange equations)**.** *Let λ, μ be given with the initial conditions $\boldsymbol{u}_0 = \boldsymbol{u}(\boldsymbol{x}, 0)$ and $s_0 = s(\boldsymbol{x}, 0)$. For the loading increments $n = 1, 2, \ldots, N$, find $\boldsymbol{u} := \boldsymbol{u}^n \in V$ and $s := s^n \in W$:*

$$\begin{aligned}
\mathcal{E}_{\boldsymbol{u}}(\boldsymbol{u}, s_+; \delta\boldsymbol{u}) &= \int_{\mathcal{B}} g(s_+)\widetilde{\boldsymbol{\sigma}}^+_{\boldsymbol{\varepsilon}}(\boldsymbol{u}) : \boldsymbol{\varepsilon}(\delta\boldsymbol{u})\mathrm{d}\boldsymbol{x} + \int_{\mathcal{B}} \widetilde{\boldsymbol{\sigma}}^-(\boldsymbol{u}) : \boldsymbol{\varepsilon}(\delta\boldsymbol{u})\mathrm{d}\boldsymbol{x} \\
&\quad - \int_{\partial_N\mathcal{B}} \bar{\boldsymbol{\tau}} \cdot \delta\boldsymbol{u}\,\mathrm{d}a = 0 \quad \forall\delta\boldsymbol{u} \in V, \\
\mathcal{E}_s(\boldsymbol{u}, s; \delta s) &= (1 - \kappa)\int_{\mathcal{B}} 2s_+\mathcal{H}\delta s\mathrm{d}\boldsymbol{x} \\
&\quad + \int_{\mathcal{B}} \Big((s - 1).\delta s + l^2\nabla s.\nabla\delta s\Big)\mathrm{d}\boldsymbol{x} = 0 \quad \forall\delta s \in W.
\end{aligned} \tag{3.62}$$

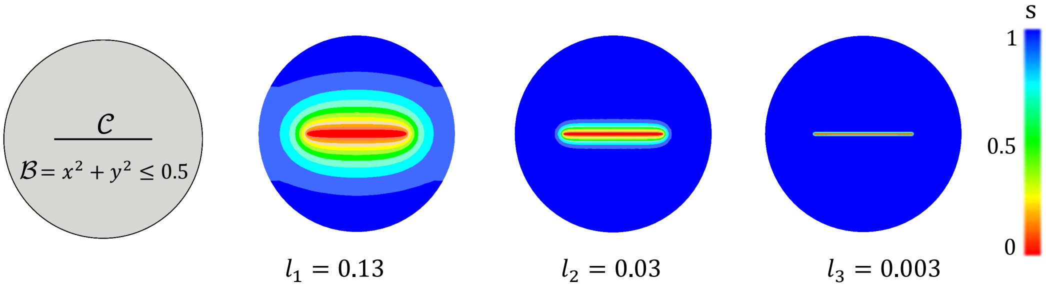

Figure 3.2: Regularization of crack discontinuities. Solutions of the crack phase-field PDE in (3.36) with a pre-given sharp crack $\mathcal{C}$. The crack phase-field response is computed for three different length-scales $l_1 > l_2 > l_3$.

The diffusivity zone through different regularized parameters is shown in Fig. 3.2. This is obtained by solving the phase-field weak from in (3.62)2 while we set $\mathcal{H} = 0$ for different length-scales. It turns out that reducing l results in a narrow diffusivity zone.

3.2. Variational phase-field modeling of brittle fracture at finite strain

3.2.1. Primary fields of brittle solids at finite strain

In the following, let undeformed configuration $\mathcal{B} \subset \mathcal{R}^\delta$, $\delta = \{2, 3\}$ be a smooth open and bounded set with $\partial\mathcal{B}$ denoted as its boundary. We assume Dirichlet boundary conditions $\partial_D\mathcal{B}$ and Neumann boundary conditions on $\partial_N\mathcal{B} := \Gamma_N \cup \mathcal{C}$, where Γ_N denotes the outer domain boundary and the lower-dimensional fracture $\mathcal{C} \in \mathcal{R}^{\delta-1}$ is the crack surface, as illustrated in Fig. 3.3 in the material description. Using a phase-field approach, the fracture surface $\mathcal{C}$ is approximated in $\mathcal{B}_L \subset \mathcal{B} \in \mathbb{R}^\delta$ the so-called *local domain*. The intact region with no fracture is denoted as a *complementary domain* $\mathcal{B}_C := \mathcal{B} \backslash \mathcal{B}_L \subset \mathcal{B} \in \mathbb{R}^\delta$, such that $\mathcal{B}_C \cup \mathcal{B}_L =: \mathcal{B}$ and $\mathcal{B}_C \cap \mathcal{B}_L = \varnothing$. The loading interval $\mathcal{T} := (t_0, T)$ is discretized using the discrete time (loading) points

$$0 = t_0 < t_1 < \ldots < t_n < \ldots < t_N = T,$$

with the end time value $T > 0$.

Employing the phase-field approach to fracture, the multi-field problem depends on the *deformation map* and *crack phase-field* by

$$\boldsymbol{\varphi} : \left\{ \begin{array}{l} \mathcal{B} \times \mathcal{T} \to \mathcal{B}^t \subset \mathcal{R}^\delta \\ (\boldsymbol{X}, t) \mapsto \boldsymbol{x} = \boldsymbol{\varphi}(\boldsymbol{X}, t) \end{array} \right. \quad \text{and} \quad s : \left\{ \begin{array}{l} \mathcal{B} \times \mathcal{T} \to [0, 1] \\ (\boldsymbol{X}, t) \mapsto s(\boldsymbol{X}, t) \end{array} \right. , \tag{3.63}$$

of a material point $\boldsymbol{X} \in \mathcal{B}$ at time $t \in \mathcal{T}$. Specifically, we deal with a diffusive formulation interpolating between the unbroken $s = 1$ and fully broken state of the material $s = 0$ at $\boldsymbol{X} \in \mathcal{B}$, such that the Neumann boundary condition $\nabla s.\boldsymbol{N} = 0$ is imposed on $\partial\mathcal{B}$, where $\boldsymbol{N}$ is the material outward normal to the surface.

3.2.2. Variational formulation for the multi-field problem

In this section, we recapitulate a variational approach to brittle fracture in elastic solids at finite strain. The following three invariants characterize the energy stored in a

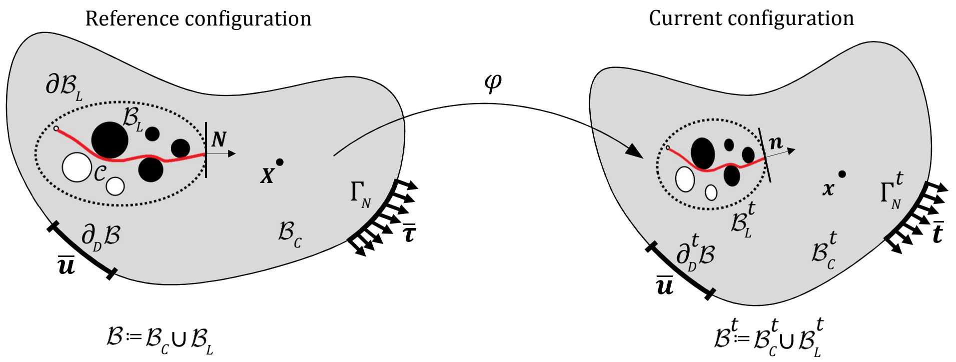

Figure 3.3: Setup of the notation: the unbroken domain is denoted by $\mathcal{B}_C$ in the material configuration. The smeared crack phase-field $\mathcal{C}$ is approximated in the domain $\mathcal{B}_L$. The whole domain is defined as a close subset as $\mathcal{B} := \mathcal{B}_C \cup \mathcal{B}_L$. At the undeformed configuration, the fracture domain boundary is $\partial\mathcal{B}_L$ and the outer boundary of the domain is $\partial\mathcal{B}$. The current configuration is shown by $\mathcal{B}^t$.

bulk strain density for the isotropic material,

$$I_1(\boldsymbol{C}) = tr(\boldsymbol{C}) \quad , \quad I_2(\boldsymbol{C}) = \frac{1}{2}\big(tr(\boldsymbol{C})^2 - tr(\boldsymbol{C}^2)\big) \quad , \quad I_3(\boldsymbol{C}) = det(\boldsymbol{C}) = J^2. \tag{3.64}$$

Let the effective strain density function $\Psi(\boldsymbol{C})$ possess the property of the isotropic setting, which has the coordinate-free representation for the material undergoing a rotation. It reads

$$\Psi(\boldsymbol{C}) =: \Psi(\boldsymbol{Q}\boldsymbol{C}\boldsymbol{Q}^T) \quad \forall \boldsymbol{Q} \in \mathcal{G} \subset \mathcal{O}(3), \tag{3.65}$$

which holds for all orthogonal tensor $\boldsymbol{Q}$ (i.e., $\boldsymbol{Q}^T\boldsymbol{Q} = \boldsymbol{Q}\boldsymbol{Q}^T = \boldsymbol{I}$), that is a subset of the symmetry group $\mathcal{G}$ of the isotropic material. We denote $\Psi(\boldsymbol{C})$ as a scalar-valued isotropic tensor function of symmetric strain tensor $\boldsymbol{C}$. Hence, the scalar-valued effective strain density function is invariant in *space and time* between two pairs of points in the given domain under rotation. Thus $\Psi(\boldsymbol{C})$ can be represented by the principal invariants of $\boldsymbol{C}$, which are the intrinsic physical properties, through

$$\Psi(\boldsymbol{C}) =: \widetilde{\Psi}\big(I_1(\boldsymbol{C}), I_3(\boldsymbol{C})\big) = \frac{\mu}{2}(I_1 - 3) - \mu \ln J + \frac{\lambda}{2}(\ln J)^2. \tag{3.66}$$

Using these definitions, to establish a variational-based phase-field approach to brittle fractures, we define the bulk free energy functional, which represents the stored energy in bulk, as follows:

$$\mathcal{E}_{bulk}(\boldsymbol{\varphi}) = \int_{\mathcal{B}_C} \Psi(\boldsymbol{C})\mathrm{d}\boldsymbol{X} - \int_{\partial_N\mathcal{B}_C} \bar{\boldsymbol{\tau}} \cdot \boldsymbol{\varphi}\,\mathrm{d}A, \tag{3.67}$$

herein, $\bar{\boldsymbol{\tau}}$ denotes traction forces on the complementary boundaries $\partial_N\mathcal{B}_C := \Gamma_N \cup \mathcal{C}$.

The total energy functional based on both the bulk energy and fracture dissipation is rooted in the work of [43], yields

$$\mathcal{E}(\boldsymbol{\varphi}, \mathcal{C}) = \mathcal{E}_{bulk}(\boldsymbol{C}) + G_c\mathcal{H}^{\delta-1}(\mathcal{C})\,. \tag{3.68}$$

For the numerical treatment we regularize (3.68) following [23]. Similar to the small deformation setting, we account for the crack irreversibility constraint through:

$$\dot{s} \leq 0 \ . \tag{3.69}$$

In the incremental version, this condition reads as follows:

$$s \leq s^{old} \ ,$$

where $s := s(t_n)$ and $s^{old} := s(t_{n-1})$. For stating the variational formulations, we now introduce the following spaces:

$$\begin{gathered} \boldsymbol{V} := \{\mathbf{H}^1(\mathcal{B})^\delta : \boldsymbol{\varphi} = \mathbf{0} \text{ on } \Gamma_{D,0},\ \boldsymbol{\varphi} = \bar{\boldsymbol{\varphi}} \text{ on } \Gamma_{D,1}\}, \quad W := \mathrm{H}^1(\mathcal{B}), \\ W_{in} := \{s \in \mathrm{H}^1(\mathcal{B})^{\delta-1} |\ 0 \leq s \leq s^{old}\}. \end{gathered} \tag{3.70}$$

3.2.3. Phase-field approximation of isotropic crack topologies

To formulate a variational setting of the phase-field approach at finite strain, we next define a regularized *isotropic crack surface energy functional* of the solid at the material description using

$$G_c \mathcal{H}^{\delta-1}(\mathcal{C}) := G_c \int_{\mathcal{B}} \gamma_l(s, \nabla s) \mathrm{d}\boldsymbol{X} \quad \text{with} \quad \gamma_l(s, \nabla s) := \frac{1}{2l}(1-s)^2 + \frac{l}{2} \nabla s . \nabla s, \tag{3.71}$$

in terms of the isotropic crack surface density function per unit volume of the solid γ_l.

Formulation 3.2.1 (Energy functional for the crack phase-field)**.** *Let* λ, μ *be given with the initial conditions* $\boldsymbol{\varphi} = \boldsymbol{\varphi}(\boldsymbol{X}, 0)$ *and* $s_0 = s(\boldsymbol{X}, 0)$*. For the loading increments* $n = 1, 2, \ldots, N$*, find* $\boldsymbol{\varphi} := \boldsymbol{\varphi}^n \in V$ *and* $s := s^n \in W_{in}$ *such that the functional*

$$\begin{aligned} \mathcal{E}(\boldsymbol{\varphi}, s) &:= \mathcal{E}_{bulk}(\boldsymbol{C}, s_+) + \ \mathcal{E}_{frac}(s) + \ \mathcal{E}_{ext}(\boldsymbol{\varphi}) \\ &= \int_{\mathcal{B}} w_{bulk}(\boldsymbol{C}, s) \mathrm{d}\boldsymbol{X} + \int_{\mathcal{B}} w_{frac}(s, \nabla s)\, \mathrm{d}\boldsymbol{X} - \int_{\partial_N \mathcal{B}} \bar{\boldsymbol{\tau}} \cdot \boldsymbol{\varphi}\, \mathrm{d}A, \end{aligned}$$

is minimized. The elastic bulk density w_{bulk} *along with the fracture contribution* w_{frac} *define the so-called total pseudo-energy density function as*

$$w(\boldsymbol{C}, d, \nabla s) = w_{bulk}(\boldsymbol{C}, s) + w_{frac}(s, \nabla s), \tag{3.72}$$

$$w_{bulk}(\boldsymbol{C}, s) = g(s_+)\Psi(\boldsymbol{C}), \tag{3.73}$$

$$w_{frac}(s, \nabla s) = G_c \gamma_l(s, \nabla s). \tag{3.74}$$

In particular, the symmetric second Piola-Kirchhoff stress $\mathbf{S}(\boldsymbol{C})$, reads

$$\mathbf{S}(\boldsymbol{C}) := \frac{\partial w_{bulk}(\boldsymbol{C}, s)}{\partial \boldsymbol{C}} = g(s_+) \frac{\partial \Psi(\boldsymbol{C})}{\partial \boldsymbol{C}} = g(s_+)\big(\mu(\mathbf{I} - \mathbf{C}^{-1}) + \lambda \ln J \mathbf{C}^{-1}\big). \tag{3.75}$$

Here, $\Psi(\boldsymbol{C})$ is defined in (3.66). The related counterparts of the standard fourth-order elasticity tensor $\mathbb{C}$ implies

$$\mathbb{C}(\boldsymbol{C}) := 2 \frac{\partial \mathbf{S}(\boldsymbol{C})}{\partial \boldsymbol{C}} = g(s_+)\big(\lambda \mathbf{C}^{-1} \otimes \mathbf{C}^{-1} + 2(\mu - \lambda \ln J)\mathbb{I}\big). \tag{3.76}$$

3.2.4. Decoupled strain-energy function through volumetric- and isochoric-based decomposition

Here, we employ the consistent additive split for the strain energy density function, i.e., $\Psi\big(I_1(\boldsymbol{C}), I_2(\boldsymbol{C})\big)$, to describe different fracture response in tension and compression modes. Hence, instead of dealing directly with $\boldsymbol{F}$, we perform multiplicative decomposition of the deformation gradient into *volume-changing* (volumetric part) and *volume-preserving* (deviatoric part) counterparts; that is,

$$\boldsymbol{F} := \boldsymbol{F}^{vol}\boldsymbol{F}^{dev} \quad \text{with} \quad \boldsymbol{F}^{vol} = J^{1/3}\boldsymbol{I} \quad \text{and} \quad \boldsymbol{F}^{dev} = \bar{\boldsymbol{F}}, \tag{3.77}$$

with the volumetric deformation gradient $\boldsymbol{F}^{vol}$ and deviatoric deformation gradient $\boldsymbol{F}^{dev}$ such that $det(\boldsymbol{F}^{vol}) = J$ and $det(\boldsymbol{F}^{dev}) = 1$ holds. Here, $\bar{\boldsymbol{F}}$ called the modified deformation gradient. Accordingly, the right Cauchy-Green tensor reads as follows:

$$\boldsymbol{C} := \boldsymbol{C}^{vol}\boldsymbol{C}^{dev} \quad \text{with} \quad \boldsymbol{C}^{vol} = J^{2/3}\boldsymbol{I} \quad \text{and} \quad \boldsymbol{C}^{dev} = \bar{\boldsymbol{C}}, \tag{3.78}$$

with the volumetric and deviatoric right Cauchy-Green tensor $\boldsymbol{C}^{vol}$ and $\boldsymbol{C}^{dev}$, respectively, such that $det(\boldsymbol{C}^{vol}) = J^2$ and $det(\boldsymbol{C}^{dev}) = 1$ holds. Here, $\bar{\boldsymbol{C}}$ is called the modified right Cauchy-Green tensor. Accordingly, a decoupled representation of the strain-energy function into the so-called tension and compression contribution is given as follows:

$$\Psi\big(I_1(\boldsymbol{C}), I_3(\boldsymbol{C})\big) := \underbrace{\widetilde{\Psi}^{vol}(J)}_{\text{volumetric term}} + \underbrace{\widetilde{\Psi}^{dev}\big(I_1(\bar{\boldsymbol{C}})\big)}_{\text{deviatoric term}}. \tag{3.79}$$

Therein, the volumetric contribution of the strain energy density function reads,

$$\widetilde{\Psi}^{vol}(J) := \frac{K_\delta}{4}(J^2 - 1 - 2lnJ), \tag{3.80}$$

where $K_\delta := \frac{2}{\delta}\mu + \lambda$ is the bulk modulus and $\delta \in \{2, 3\}$. The deviatoric contribution of the strain energy density function is

$$\widetilde{\Psi}^{dev}\big(I_1(\bar{\boldsymbol{C}})\big) := \frac{\mu}{2}(I_1(\bar{\boldsymbol{C}}) - 3). \tag{3.81}$$

The modified bulk strain energy density function for the fracturing material becomes,

$$w_{bulk}(\boldsymbol{C}, s; H_J) := g(s)\widetilde{\Psi}^{+}(\boldsymbol{C}; H_J) + \widetilde{\Psi}^{-}(J), \tag{3.82}$$

which is assumed there is no degradation in compression mode. The positive part of the strain energy density function reads

$$\widetilde{\Psi}^{+}(\boldsymbol{C}; H_J) = H_J\widetilde{\Psi}^{vol}(J) + \widetilde{\Psi}^{dev}\big(I_1(\bar{\boldsymbol{C}})\big), \tag{3.83}$$

where, $H_J := H^{+}(J-1)$ is a *positive Heaviside function*, such that if $(J-1)$ is positive, it returns one and otherwise gives a zero value. Notably, due to identity $J = \frac{dv}{dV}$, the positive Heaviside function indicates the points in a domain which are in the tensile part, i.e., $H_J = 1$ and compression part, i.e., $H_J = 0$. The negative strain energy density function, which describes the compression part of the full strain energy density function, is

$$\widetilde{\Psi}^{-}(J; H_J) = \big(1 - H_J\big)\widetilde{\Psi}^{vol}(J). \tag{3.84}$$

The constitutive equation corresponding to w_{bulk}, as denoted by $\mathbf{S}(\boldsymbol{C}, s; H_J)$, is additively decomposed to a purely tensile contribution, i.e., $\mathbf{S}^+(\boldsymbol{C}; H_J)$ and a purely compression contribution, i.e., $\mathbf{S}^-(\boldsymbol{C}; H_J)$, reads

$$\begin{aligned}\mathbf{S}(\boldsymbol{C}, s; H_J) : &= 2\frac{\partial w_{bulk}(\boldsymbol{C}, s_+; H_J)}{\partial \boldsymbol{C}} = 2g(s_+)\frac{\partial \widetilde{\Psi}^+(\boldsymbol{C}; H_J)}{\partial \boldsymbol{C}} + 2\frac{\partial \widetilde{\Psi}^-(J; H_J)}{\partial \boldsymbol{C}} \\ &= g(s_+)\widetilde{\mathbf{S}}^+(\boldsymbol{C}; H_J) + \widetilde{\mathbf{S}}^-(\boldsymbol{C}; H_J).\end{aligned} \tag{3.85}$$

Therein,

$$\widetilde{\mathbf{S}}^+(\boldsymbol{C}; H_J) = H^+(J-1)\mathbf{S}^{vol} + \mathbf{S}^{dev}, \quad \text{and} \quad \widetilde{\mathbf{S}}^-(\boldsymbol{C}; H_J) = \big(1 - H^+(J-1)\big)\mathbf{S}^{vol}.$$

such that the volumetric and deviatoric second Piola-Kirchhoff stress tensors are

$$\mathbf{S}^{vol}(\boldsymbol{C}) = \big(\frac{\kappa_\delta}{2}(J^2-1)\boldsymbol{C}^{-1}\big), \quad \text{and} \quad \mathbf{S}^{dev}(\boldsymbol{C}) = \mu J^{-\frac{2}{3}}(\mathbf{I} - \frac{1}{3}\mathbf{I}_1(\boldsymbol{C})\boldsymbol{C}^{-1}).$$

The decoupled representation of the fourth-order elasticity tensor through the additive decomposition of the stress tensor reads as follows:

$$\begin{aligned}\mathbb{C}(\boldsymbol{C}, s; H_J) : &= 2\frac{\partial \mathbf{S}(\boldsymbol{C}, s; H_J)}{\partial \boldsymbol{C}} = 2g(s_+)\frac{\partial \widetilde{\mathbf{S}}^+(\boldsymbol{C}; H_J)}{\partial \boldsymbol{C}} + 2\frac{\partial \widetilde{\mathbf{S}}^-(\boldsymbol{C}; H_J)}{\partial \boldsymbol{C}} \\ &= g(s_+)\widetilde{\mathbb{C}}^+(\boldsymbol{C}; H_J) + \widetilde{\mathbb{C}}^-(\boldsymbol{C}; H_J),\end{aligned} \tag{3.86}$$

with

$$\widetilde{\mathbb{C}}^+(\boldsymbol{C}; H_J) = H^+(J-1)\mathbb{C}^{vol} + \mathbb{C}^{dev}, \quad \text{and} \quad \widetilde{\mathbb{C}}^-(\boldsymbol{C}; H_J) = \big(1 - H^+(J-1)\big)\mathbb{C}^{vol},$$

such that, the volumetric and deviatoric fourth-order elasticity tensors are given by

$$\begin{aligned}&\mathbb{C}^{vol}(\boldsymbol{C}) = \kappa_\delta J^2 \boldsymbol{C}^{-1} \otimes \boldsymbol{C}^{-1} - \kappa_0(J^2-1)\mathbb{I}, \\ &\mathbb{C}^{dev}(\boldsymbol{C}) = -\frac{2}{3}\mu J^{-\frac{2}{3}}\left[\mathbf{C}^{-1} \otimes \mathbf{I} + \mathbf{I} \otimes \boldsymbol{C}^{-1} - I_1(\boldsymbol{C})(\mathbb{I} + \frac{1}{3}\mathbf{C}^{-1} \otimes \mathbf{C}^{-1})\right].\end{aligned} \tag{3.87}$$

Here, the identity $I_1(\bar{\boldsymbol{C}}) = J^{-\frac{2}{3}} I_1(\boldsymbol{C})$ and the fourth-order tensor $\frac{\partial \boldsymbol{C}_{ij}^{-1}}{\partial \boldsymbol{C}_{kl}} := -\mathbb{I}_{ijkl} = -\frac{1}{2}[\boldsymbol{C}_{ik}^{-1}\boldsymbol{C}_{jl}^{-1} + \boldsymbol{C}_{il}^{-1}\boldsymbol{C}_{jk}^{-1}]$ are used.

3.2.5. Extension toward Mooney-Rivlin hyperelastic solid material

The deviatoric contribution of the strain energy density function within the hyperelastic Neo-Hookean model contains only one material parameter that is μ. Using the Mooney-Rivlin hyperelastic model, we can use two material parameters for the deviatoric contribution of the strain energy density function denoted by μ_1 and μ_2. Hence, we have

$$\widetilde{\Psi}^{dev}\Big(I_1(\bar{\boldsymbol{C}}), I_2(\bar{\boldsymbol{C}})\Big) := \frac{\mu_1}{2}(I_1(\bar{\boldsymbol{C}}) - 3) + \frac{\mu_2}{2}(I_2(\bar{\boldsymbol{C}}) - 3), \tag{3.88}$$

while the identity for the shear modulus $\mu = \mu_1 - \mu_2$ holds. We define $f_{MN} \in [0,1]$ as a *given interpolant parameter* between μ_1 and μ_2, such that

$$\mu_1 = f_{MN}\mu \quad \text{and} \quad \mu_2 = (f_{MN}-1)\mu \quad \text{with} \quad \mu = \mu_1 - \mu_2 \quad \text{for } f_{MN} \in [0,1]. \tag{3.89}$$

Note that for $f_{MN} = 1$, the hyperelastic Neo-Hookean model is recovered. Together with the volumetric contribution of the strain energy density function given in (3.80), the modified strain energy density function for the fracturing material in (3.82) can be determined. Thus, a deviatoric second Piola-Kirchhoff stress tensor for the Mooney-Rivlin hyperelastic solid material reads as follows:

$$\mathbf{S}^{dev}(\boldsymbol{C}) = J^{-\frac{2}{3}}\Big(\bar{\boldsymbol{S}} - \frac{1}{3}(\bar{\boldsymbol{S}} : \boldsymbol{C})\boldsymbol{C}^{-1}\Big),$$

with fictitious second Piola-Kirchhoff stress tensor denoted by $\bar{\boldsymbol{S}}$ which is given by

$$\bar{\boldsymbol{S}} := 2\frac{\partial \widetilde{\Psi}^{dev}}{\partial \bar{\boldsymbol{C}}} = \Big(\mu_1 - \mu_2 I_1(\bar{\boldsymbol{C}})\Big)\boldsymbol{I} + \mu_2 J^{-2/3}\boldsymbol{C}.$$

Accordingly, the deviatoric fourth-order elasticity tensor reads

$$\mathbb{C}^{dev}(\boldsymbol{C}) = \mathbb{P} : \bar{\mathbb{C}} : \mathbb{P}^T + \frac{2}{3}Tr(J^{-2/3}\bar{\boldsymbol{S}})\widetilde{\mathbb{P}} - \frac{2}{3}(\boldsymbol{C}^{-1} \otimes \boldsymbol{S}^{dev} + \boldsymbol{S}^{dev} \otimes \boldsymbol{C}^{-1}), \tag{3.90}$$

such that, a Trace operator is defined through $Tr(\bullet) = (\bullet) : \boldsymbol{C}$. Additionally, the fictitious fourth-order elasticity tensor denoted by $\mathbb{C}^{dev}(\boldsymbol{C})$ is given by

$$\bar{\mathbb{C}} = 2\mu_2 J^{-4/3}(\mathbb{I} - \boldsymbol{I} \otimes \boldsymbol{I}) \ . \tag{3.91}$$

Here, the identity $I_2(\bar{\boldsymbol{C}}) = J^{-\frac{4}{3}} I_2(\boldsymbol{C})$ is used. Two fourth-order projection tensors, namely $\mathbb{P}$ and $\widetilde{\mathbb{P}}$ in (3.90), are further defined by

$$\mathbb{P} = \mathbb{I} - \frac{1}{3}\boldsymbol{C}^{-1} \otimes \boldsymbol{C} \quad \text{and} \quad \widetilde{\mathbb{P}} = \boldsymbol{C}^{-1} \odot \boldsymbol{C}^{-1} - \frac{1}{3}\boldsymbol{C}^{-1} \otimes \boldsymbol{C}^{-1}. \tag{3.92}$$

Formulation 3.2.2 (Energy functional for the crack phase-field)**.** *Let* λ*,* μ*,* f_{MN} *be given with the initial conditions* $\boldsymbol{\varphi}_0 = \boldsymbol{\varphi}(\boldsymbol{X}, 0)$ *and* $s_0 = s(\boldsymbol{X}, 0)$*. For the loading increments* $n = 1, 2, \ldots, N$*, find* $\boldsymbol{\varphi} := \boldsymbol{\varphi}^n \in V$ *and* $s := s^n \in W_{in}$ *such that the functional*

$$\mathcal{E}(\boldsymbol{\varphi}, s; H_J) = \underbrace{\int_{\mathcal{B}} \big[g(s_+)\widetilde{\Psi}^+(\boldsymbol{C}; H_J) + \widetilde{\Psi}^-(J; H_J)\big]\mathrm{d}\boldsymbol{X}}_{\textit{deformation term}} + G_c \underbrace{\int_{\mathcal{B}} \gamma_l(s, \nabla s)\mathrm{d}\boldsymbol{X}}_{\textit{fracture term}} - \underbrace{\int_{\partial_N \mathcal{B}} \bar{\boldsymbol{\tau}} \cdot \boldsymbol{\varphi}\, \mathrm{d}A}_{\textit{external load}},$$

is minimized. Both the modified elastic bulk density w_{bulk} *and the fracture contribution* w_{frac} *define the so-called alternative total pseudo-energy density function as*

$$w(\boldsymbol{C}, s, \nabla s; H_J) = w_{bulk}(\boldsymbol{C}, s; H_J) + w_{frac}(s, \nabla s).$$

The minimization problem for the given energy functional of the isotropic crack topology in Formulation 3.2.2 takes the following compact form:

$$\boxed{\{\boldsymbol{\varphi}, s\} = \arg\{ \min_{\boldsymbol{\varphi} \in V} \min_{s \in W_{in}} [\ \mathcal{E}(\boldsymbol{\varphi}, s; H_J)\ ]\ \}.} \tag{3.93}$$

The stationary points of the energy functional in Formulation 3.2.2 are characterized by the first-order necessary conditions, namely the so-called Euler-Lagrange equations, are obtained through differentiation with respect to $\boldsymbol{\varphi}$ and d.

Formulation 3.2.3 (Euler-Lagrange equations)**.** *Let* λ*,* μ*,* f_{MN} *be given with the initial conditions* $\boldsymbol{\varphi}_0 = \boldsymbol{\varphi}(\boldsymbol{X}, 0)$ *and* $s_0 = s(\boldsymbol{X}, 0)$ *in the undeformed configuration. For the loading increments* $n = 1, 2, \dots, N$*, find* $\boldsymbol{\varphi} := \boldsymbol{\varphi}^n \in V$ *and* $s := s^n \in W_{in}$ *:*

$$\begin{aligned}
\mathcal{E}_{\boldsymbol{\varphi}}(\boldsymbol{\varphi}, s; \delta\boldsymbol{\varphi}) &= \int_{\mathcal{B}} \frac{1}{2} g(s_+) \widetilde{\mathbf{S}}^+(\boldsymbol{\varphi}) : \delta\boldsymbol{C} \mathrm{d}\boldsymbol{X} + \int_{\mathcal{B}} \frac{1}{2} \widetilde{\mathbf{S}}^-(\boldsymbol{\varphi}) : \delta\boldsymbol{C} \mathrm{d}\boldsymbol{X} \\
&\quad - \int_{\partial_N \mathcal{B}} \bar{\boldsymbol{\tau}} \cdot \delta\boldsymbol{\varphi} \, \mathrm{d}A = 0 \quad \forall \delta\boldsymbol{\varphi} \in \boldsymbol{V}, \\
\mathcal{E}_s(\boldsymbol{\varphi}, s; \delta s - s) &= (1-\kappa) \int_{\mathcal{B}} 2 s_+ \widetilde{\Psi}^+(\boldsymbol{C}; H_J).(\delta s - s) \mathrm{d}\boldsymbol{X} \\
&\quad + G_c \int_{\mathcal{B}} \left(\frac{1}{l}(s-1).(\delta s - s) + l \nabla s . \nabla(\delta s - s) \right) \mathrm{d}\boldsymbol{X} \\
&\quad \geq 0 \quad \forall \delta s \in W \cap L^\infty.
\end{aligned} \tag{3.94}$$

Herein, $\mathcal{E}_{\boldsymbol{\varphi}}$ and $\mathcal{E}_s$ are the directional derivatives of the energy functional with respect to $\boldsymbol{\varphi}$ and d, respectively. Furthermore, $\delta\boldsymbol{\varphi} \in \{\mathbf{H}^1(\mathcal{B})^\delta : \delta\boldsymbol{\varphi} = \mathbf{0} \text{ on } \Gamma_{D,0} \cup \Gamma_{D,1}\}$ is the deformation test function and $\delta s \in H^1(\mathcal{B})$ is the phase-field test function.

3.2.6. Euler-Lagrange equations in a strong form

To complete our derivations, the strong form of Formulation 3.2.3 is derived in this section. Using integration by parts, we obtain a quasi-stationary elliptic system for the displacements and phase-field variable, where the latter is subjected to an inequality constraint in time and therefore needs to be complemented with a complementary condition:

Formulation 3.2.4 (Strong form of the Euler-Lagrange equations)**.** *Let* λ*,* μ*,* f_{MN} *be given with the initial conditions* $\boldsymbol{\varphi}_0 = \boldsymbol{\varphi}(\boldsymbol{X}, 0)$ *and* $s_0 = s(\boldsymbol{X}, 0)$*. For the loading increments* $n = 1, 2, \dots, N$*, we solve a displacement equation where we seek* $\boldsymbol{\varphi} := \boldsymbol{\varphi}^n : \mathcal{B} \to \mathbb{R}^\delta$ *such that*

$$\begin{aligned}
-Div(\mathbf{FS}) &= \boldsymbol{0} \quad && \text{in } \mathcal{B}, \\
\boldsymbol{\varphi} &= \bar{\boldsymbol{\varphi}} && \text{on } \partial_D \mathcal{B}, \\
\boldsymbol{PN} &= \bar{\boldsymbol{\tau}} && \text{on } \Gamma_{N0},
\end{aligned}$$

in terms of the symmetric second Piola-Kirchhof stress tensor $\mathbf{S}$ *defined in (3.85) and the given deformation field* $\bar{\boldsymbol{\varphi}}$*. Here and in the following, we define first Piola-Kirchhof stress tensor using* $\boldsymbol{P} := \boldsymbol{FS}$*. The phase-field system consists of four parts: the PDE, the inequality constraint and a compatibility condition along with the Neumann-type boundary conditions. Find* $s := s^n : \mathcal{B} \to [0, 1]$ *such that*

$$\begin{aligned}
-\Big(2(1-\kappa)s_+\widetilde{\Psi}^+(\boldsymbol{C}; H_J) - \frac{G_c}{l}(1-s) - G_c l \Delta s\Big) \geq 0 \quad && \text{in } \mathcal{B}, \\
\dot{s} \leqslant 0 \quad && \text{in } \mathcal{B}, \\
-\Big(2(1-\kappa)s_+\widetilde{\Psi}^+(\boldsymbol{C}; H_J) - \frac{G_c}{l}(1-s)\Big) \, \dot{s} = 0 \quad && \text{in } \mathcal{B}, \\
\nabla s \cdot \boldsymbol{n} = 0 \quad && \text{on } \partial\mathcal{B}.
\end{aligned}$$

Identical to a small deformation setting, the aforementioned inequality minimization problem is resolved through the maximum crack driving state function to prevent crack healing. This is achieved by having a positive crack dissipation known as the irreversibility criteria, which is described in detail in Section 3.2.8.

3.2.7. Global balance principle of continuum phase-field at finite strain

In this section, thermodynamical consistency for the preservation of the principle of energy balance at finite strain is formulated. Recall, the weak forms for the deformation $\boldsymbol{\varphi}$ and phase-field d given in Formulation (3.2.3). To derive a global balance of energy, we choose $\delta\boldsymbol{\varphi} =: \dot{\boldsymbol{\varphi}}$ and $\delta s =: \dot{s}$ as test functions and restate Formulation (3.2.3) for the mechanical part as follows:

$$\begin{aligned}\mathcal{E}_{\varphi}(\boldsymbol{\varphi}, s; \dot{\boldsymbol{\varphi}}) = &\int_{\mathcal{B}} \frac{1}{2} g(s_+) \widetilde{\mathbf{S}}^+(\boldsymbol{\varphi}) : \dot{\boldsymbol{C}} \mathrm{d}\boldsymbol{X} + \int_{\mathcal{B}} \frac{1}{2} \widetilde{\mathbf{S}}^-(\boldsymbol{\varphi}) : \dot{\boldsymbol{C}} \mathrm{d}\boldsymbol{X} \\ &- \int_{\partial_N \mathcal{B}} \bar{\boldsymbol{\tau}} \cdot \dot{\boldsymbol{\varphi}} \, \mathrm{d}A = 0 \quad \forall \dot{\boldsymbol{\varphi}} \in V,\end{aligned} \tag{3.95}$$

that is

$$\int_{\mathcal{B}} \dot{w}_{bulk}(\boldsymbol{\varphi}, s_+) \, \mathrm{d}\boldsymbol{X} - \int_{\mathcal{B}} \frac{\partial w_{bulk}}{\partial s} \dot{s} \, \mathrm{d}\boldsymbol{X} - P^{ext} = 0, \tag{3.96}$$

$$\Leftrightarrow \qquad P^{int} - \int_{\mathcal{B}} \frac{\partial w_{bulk}}{\partial s} \dot{s} \, \mathrm{d}\boldsymbol{X} - P^{ext} = 0. \tag{3.97}$$

Herein, the rate of internal mechanical power which describes the response of the undeformed domain $\mathcal{B}$ done by the stress field is given as

$$\begin{aligned}P^{int}(\dot{\boldsymbol{\varphi}}, \dot{s}) = \dot{\mathcal{E}}_{bulk}(\boldsymbol{\varphi}, s_+) &= \int_{\mathcal{B}} \dot{w}_{bulk}(\boldsymbol{\varphi}, s_+) \\ &= \int_{\mathcal{B}} \frac{\partial w_{bulk}}{\partial \boldsymbol{C}} : \dot{\boldsymbol{C}} \, \mathrm{d}\boldsymbol{X} + \int_{\mathcal{B}} \frac{\partial w_{bulk}}{\partial s} \dot{s} \, \mathrm{d}\boldsymbol{X},\end{aligned} \tag{3.98}$$

and

$$P^{ext}(\dot{\boldsymbol{u}}) = \dot{\mathcal{E}}_{ext}(\boldsymbol{u}) = \int_{\partial_N \mathcal{B}} \bar{\boldsymbol{\tau}} \cdot \dot{\boldsymbol{\varphi}} \, \mathrm{d}A \ . \tag{3.99}$$

Accordingly, through Formulation (3.2.3) for the phase-field part, we derive

$$\mathcal{E}_s(\boldsymbol{\varphi}, s; \dot{s}) = \int_{\mathcal{B}} \frac{\partial w_{bulk}}{\partial s} \dot{s} \, \mathrm{d}\boldsymbol{X} + \int_{\mathcal{B}} G_c \left(\frac{1}{l}(s-1).\dot{s} + l(\nabla s)\nabla\dot{s} \right) \mathrm{d}\boldsymbol{X} = 0 \qquad \forall \dot{s} < 0 \in W. \tag{3.100}$$

We restate (3.100) using,

$$\dot{\mathcal{E}}_{frac}(s) = \int_{\mathcal{B}} G_c \delta_s \gamma_l(s, \nabla s) \dot{s} \mathrm{d}\boldsymbol{X} = -\int_{\mathcal{B}} \frac{\partial w_{bulk}}{\partial s} \dot{s} \, \mathrm{d}\boldsymbol{X} \ . \tag{3.101}$$

Following the same procedure described in Section 2.6.4, the global form of the energy balance for the coupled two-field variational phase-field problem at finite strain reads,

$$\boxed{\mathcal{E}(\dot{\boldsymbol{\varphi}}, \dot{s}) = \dot{\mathcal{E}}_{frac}(s) + P^{int}(\dot{\boldsymbol{\varphi}}, \dot{s}) - P^{ext}(\dot{\boldsymbol{\varphi}}) = 0.} \tag{3.102}$$

3.2.8. Resolving the crack irreversibility constraint

As a point of departure, in line with Section 3.1.7, the phase-field fracture PDE given in Formulation (3.2.4) is reformulated in the following abstract form:

$$\underbrace{-g'(s_+)\mathcal{H}}_{max\ crack\ driving\ force} \quad - \underbrace{l\delta_s.\gamma_l}_{resistance} = 0, \tag{3.103}$$

with the maximum positive crack driving force $\mathcal{H}$ under large strain setting in $t \in [0, t_n]$ by

$$\mathcal{H}(\boldsymbol{X}, t) := \max_{s\ \forall\ t\in[0,t_n]} \widetilde{D}\big(state(\boldsymbol{X}, \boldsymbol{C}(s))\big)\ . \tag{3.104}$$

With the definition of $\mathcal{H}$ in terms of the crack driving state function $\widetilde{D}$ at hand, Formulation 3.2.3 can be stated in the equality minimization; thus, $\mathcal{H}$ substitutes the corresponding $\widetilde{\Psi}^+(\boldsymbol{C}; H_J)$ term in the original $\mathcal{E}_s$. To derive the crack driving state function, we recall phase-field PDE in Formulation (3.2.4); thus we have:

$$-\delta_s w = (\kappa - 1)2s_+\widetilde{\Psi}^+(\boldsymbol{C}; H_J) - G_c\delta_s\gamma_l(s, \nabla s) \leqslant 0. \tag{3.105}$$

By maximizing the inequality equation in (3.105) with respect to s up to the current time (i.e., $t \in [0, t_n]$), it becomes

$$(\kappa - 1)2s_+ \max_{s\ \forall\ t\in[0,t_n]} \widetilde{\Psi}^+(\boldsymbol{C}; H_J) = G_c\delta_s\gamma_l(s, \nabla s)\ . \tag{3.106}$$

To follow the phase-field fracture equation defined in (3.103), we multiply (3.106) by $\frac{l}{G_c}$, which results in the definition of a positive crack driving force; hence, (3.106) is restated as

$$(\kappa - 1)2s_+\mathcal{H} = l\delta_s\gamma_l \ \texttt{if}\ \mathcal{H} := \max_{s\ \forall\ t\in[0,t_n]} \widetilde{D} \ \texttt{with}\ \widetilde{D} := \frac{l\widetilde{\Psi}^+(\boldsymbol{C}; H_J)}{G_c}\ . \tag{3.107}$$

Formulation 3.2.5 (Final Euler-Lagrange equations). *Let* λ, μ, f_{MN} *be given with the initial conditions* $\boldsymbol{\varphi}_0 = \boldsymbol{\varphi}(\boldsymbol{X}, 0)$ *and* $s_0 = s(\boldsymbol{X}, 0)$. *For the loading increments* $n = 1, 2, \dots, N$, *find* $\boldsymbol{\varphi} := \boldsymbol{\varphi}^n \in V$ *and* $s := s^n \in W_{in}$:

$$\begin{aligned}
\mathcal{E}_{\boldsymbol{\varphi}}(\boldsymbol{\varphi}, s; \delta\boldsymbol{\varphi}) &= \int_{\mathcal{B}} \frac{1}{2} g(s_+)\widetilde{\mathbf{S}}^+(\boldsymbol{\varphi}) : \delta\boldsymbol{C}\mathrm{d}\boldsymbol{X} + \int_{\mathcal{B}} \frac{1}{2}\widetilde{\mathbf{S}}^-(\boldsymbol{\varphi}) : \delta\boldsymbol{C}\mathrm{d}\boldsymbol{X} \\
&\quad - \int_{\partial_N\mathcal{B}} \bar{\boldsymbol{\tau}} \cdot \delta\boldsymbol{\varphi}\,\mathrm{d}A = 0 \quad \forall\delta\boldsymbol{\varphi} \in V, \\
\mathcal{E}_s(\boldsymbol{\varphi}, s; \delta s) &= (1 - \kappa)\int_{\mathcal{B}} 2s_+\mathcal{H}.\delta s\mathrm{d}\boldsymbol{X} \\
&\quad + \int_{\mathcal{B}} \Big((s - 1).\delta s + l^2\nabla s.\nabla\delta s\Big)\mathrm{d}\boldsymbol{X} = 0 \quad \forall\delta s \in W.
\end{aligned} \tag{3.108}$$

Here, $\delta\boldsymbol{C}$ depends on $\delta\boldsymbol{\varphi}$ and that is $\delta\boldsymbol{C} = 2sym\big(\boldsymbol{\varphi}^T\nabla(\delta\boldsymbol{\varphi})\big)$.

3.3. Numerical framework for solving multi-field boundary value problems

In this section, we briefly describe the solution algorithm used for the variational phase-field formulation. The computational domain is subdivided into quadrilateral or tetrahedral element domains in two- and three-dimensional settings, respectively. Both subproblems are discretized with a Galerkin FEM using H^1-conforming bilinear (2D) or trilinear (3D) elements; for details, we refer readers to [31]. Consequently, the discrete spaces have the properties $\boldsymbol{V}_h \subset \boldsymbol{V}$ and $W_h \subset W$.

The minimization of (3.31) at small deformation and (3.93) at finite strain is numerically challenging for the following reasons:

1. The energy functional $\mathcal{E}(\boldsymbol{u}, s)$ or $\mathcal{E}(\boldsymbol{\varphi}, s; H_J)$ may admit several local minimizers. Thus finding the global minimum is generally infeasible; see for example [24] for discussions on the pure elasticity case.

2. The irreversibility of the crack phase-field (i.e., $|\mathcal{C}_{t-1}| \leq |\mathcal{C}_t|$) is required to provide a thermodynamically consistent minimization problem through positive crack dissipation inequality and enforcing on the temporal derivative of the phase-field function; see for example [93].

3. The minimization problem is characterized by localization of the crack phase-field in bands of a width of order l. From a practical and numerical analysis point of view, $l > h$ must hold (at least one element has to be existed to cover a regularized phased-field). Thus, $h = \mathcal{O}(l)$ holds. The regularization parameter is typically a very small dimensionless value and the accurate fracture response (i.e., converging toward the sharp crack profile) should tend to 0 in the limit of $h \to 0$ to resolve the bands; see for example [48].

4. The linear system of equations arises from the Hessian matrix of the $\mathcal{E}(\boldsymbol{u}, s)$ or $\mathcal{E}(\boldsymbol{\varphi}, s; H_J)$ are typically badly conditioned because of the presence of a crack phase-field localizations band where the elastic stiffness varies rapidly from the intact value to zero; see for example [40].

Stemming from the irreversibility constraint $s_{t-1} \geq s$ the staggered solution algorithm for the system of the multi-field variational phase-field problem (i.e., Formulation 3.1.5 at small deformation and Formulation 3.2.5 at finite strain) implies alternately fixing deformation and the phase-field, and also solving the corresponding equations until convergence. The algorithm is sketched in Table 1 for the coupled variational phase-field Formulation 3.2.5 at finite strain. The same solutions procedure holds for Formulation 3.1.5 at small strain at a fixed loading step; see [48].

3.4. Numerical examples

This section presents the variational phase-field modeling performance for quasi-brittle fracture at small and large deformations. We consider two numerical model problems for the tension and shear tests. Specifically, we aim to investigate different crack phase-field formulations in our given BVP. As a setup for the numerical investigations, we use the following:

Algorithm 1 *Staggered iterative solution process for Formulation 3.2.5 at finite strain at a fixed loading step.*

```
Input: loading data $(\bar{\boldsymbol{\varphi}}_n, \bar{\boldsymbol{t}}_n)$ on $\partial_D\mathcal{B}, \Gamma_N \subset \partial\mathcal{B}$;
       solution $(\boldsymbol{\varphi}_{n-1}, s_{n-1})$ from step $n-1$.
    Initialization, $k = 0$:
      • set $(\boldsymbol{\varphi}^0, s^0) := (\boldsymbol{\varphi}_{n-1}, s_{n-1})$.
    Staggered iteration $k \geq 1$:
      • given $s^{k-1}$, solve $\mathcal{E}_{\boldsymbol{\varphi}}(\boldsymbol{\varphi}, s_+^{k-1}; \boldsymbol{\delta\varphi}) = 0$ for $\boldsymbol{\varphi}$, set $\boldsymbol{\varphi} =: \boldsymbol{\varphi}^k$,
      • given $\boldsymbol{\varphi}^k$, solve $\mathcal{E}_s(\boldsymbol{\varphi}^k, s; \delta s) = 0$ for $s$, set $s =: s^k$,
      • for the obtained pair $(\boldsymbol{\varphi}^k, s^k)$, check $\mathrm{Res}^k_{\mathrm{Stag}} := |\mathcal{E}_{\boldsymbol{\varphi}}(\boldsymbol{\varphi}^k, s^k; \boldsymbol{\delta\varphi})| \leq \mathtt{TOL}_{\mathrm{Stag}},\ \forall\, \boldsymbol{\delta\varphi} \in V$,
      • if fulfilled, set $(\boldsymbol{\varphi}^k, s^k) =: (\boldsymbol{\varphi}_n, s_n)$ and stop;
        otherwise $k + 1 \to k$.
Output: solution $(\boldsymbol{\varphi}_n, s_n)$.
```

- **Material parameters:** In this section, the constitutive parameters for the isotropic material are the same as in [93] and given as $\lambda = 121.15$ kN/mm^2, $\mu = 80.77$ kN/mm^2. Griffith's critical elastic energy release rate is set as $G_c = 2.7 \times 10^{-3}$ kN/mm. For the variational phase-field modeling at finite strain, if the hyperelastic Mooney-Rivlin model is used, we set $f_{MN} = 0.48$; hence, $\mu_1 = 0.48\mu$ and $\mu_2 = -0.52\mu$; see (3.89).

- **Model parameters:** The phase-field parameters are chosen as $\kappa = 10^{-10}$ and $l = 2h$.

- **The solution of the nonlinear problems:** An alternate minimization scheme is used for solving the BVP based on Algorithm 1. Notably, owing to the 'nested in' nature of the Newton-Raphson process, it has to be $\mathtt{TOL}_{\mathrm{NR}} < \mathtt{TOL}_{\mathrm{Stag}}$. In the presented numerical examples, we adopt $\mathtt{TOL}_{\mathrm{NR}} := 10^{-8} < \mathtt{TOL}_{\mathrm{Stag}} := 10^{-5}$. Specifically, the relative residual norm is given by `Residual` : $\|\boldsymbol{F}(\boldsymbol{x}_{k+1})\| \leq \mathtt{Tol}_{\mathtt{N-R}}\|\boldsymbol{F}(\boldsymbol{x}_k)\|$. Here, $\boldsymbol{F}$ refers to the residual of the equilibrium equation of the nonlinear reference BVP.

- **Software:** The implementation is based on MATLAB R2015b [89] and FORTRAN 90 [29]. The user elements including the constitutive modeling at each Gaussian quadrature points are written in FORTRAN 90 as a MEX-FILE.

3.4.1. Example 1: Single-edge-notched test at small deformation

In this numerical example, we investigate the variational phase-field model for the quasi-brittle material at small deformation. The necessity of using different formulations of the variational phase-field model is investigated. This is the benchmark example and is reported in [5, 93] for small deformation. We mainly concentrate on the three different models formulated earlier. These models include elasticity without splitting given in (3.11), elasticity with the volumetric-isochoric split given in (3.17), and elasticity with spectral decomposition given in (3.26).

Case a: Three-dimensional tension test. In the first numerical example, a BVP applied to the three-dimensional square plate is shown in Fig. 3.4. We set $A = 0.5$ *mm* and $B = 0.15\ mm$; hence, $\mathcal{B} = (0,1,0)^2 \times (0,0,0.15)\ mm^3$, which includes a predefined single notch $\mathcal{C}$ of surface $0.5 \times 0.15\ m^2$, that is a predefined single notch in the $y = A$ plane from the left edge to the body center, as depicted in Fig. 3.4. Here, finite element discretization is modeled with a minimum element size of $h = 0.004$ such that the spatial discretization of the model includes 204,430 four-node tetrahedral elements.

In the crack phase-field simulation, two important aspects have to be verified: the crack phase-field pattern and the load-displacement curve. Here, the displacement control is used with increments of $\Delta\bar{u} = 2 \times 10^{-5}$.

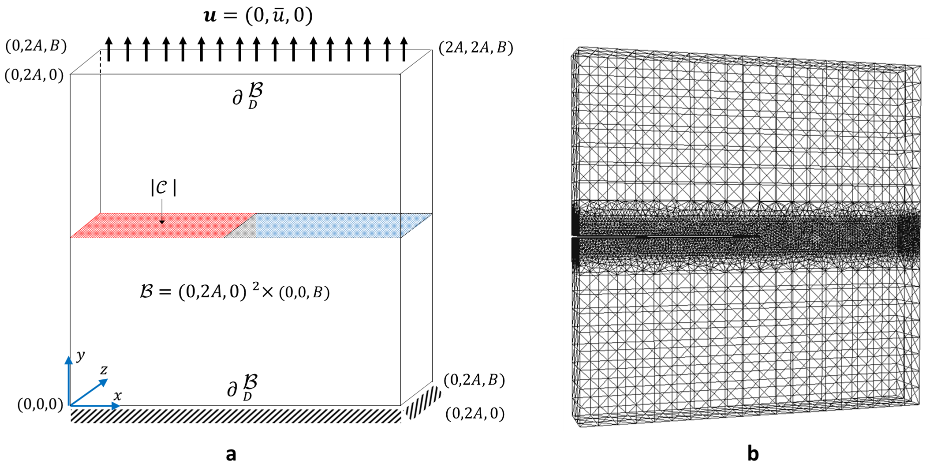

Figure 3.4: Example 1 (Case a). Geometry and loading setup for the single-edge-notched tension test. (a) Boundary value problem, and (b) finite element discretization.

The smeared crack phase-field for different stages up to complete failure is shown in Fig. 3.5. All the crack fractured patterns almost exhibit identical responses for all the methods. Accordingly, the resulting load-displacement curves are given in Fig. 3.6a for different models. Here, three different crack phase-field models are provided, including elasticity without split which is shown by the continuous black color, elasticity with volumetric-isochoric split which is shown by the red dashed line, and elasticity with spectral decomposition which is shown by continuous blue color. For this numerical example, which explains mode I of fracture (i.e., tension test), all methods are shown to be in a very good agreement with each other.

Case b: Three-dimensional shear test. Here, finite element discretization is modeled with a minimum element size of $h = 0.002$ such that the spatial discretization of the model includes 262,545 four-node tetrahedral elements. Identical geometry is used as in Case a, but a horizontal displacement field is imposed on the top surface. This test is known as the single-edge-notched shear test, and it is used to evaluate the shear mode of fracture. Here, we aim to investigate the necessity of using different decomposition split on the fracture response for the shear mode.

For the shear test problem, the smeared crack phase-field for different stages up to complete failure is shown in Fig. 3.8. Since the fracturing material behaves quite differently under tension and compression within a solid body, the smeared crack fractured pattern shows different responses for different methods.

The resulting load-displacement curves are depicted in Fig. 3.6b for different models.

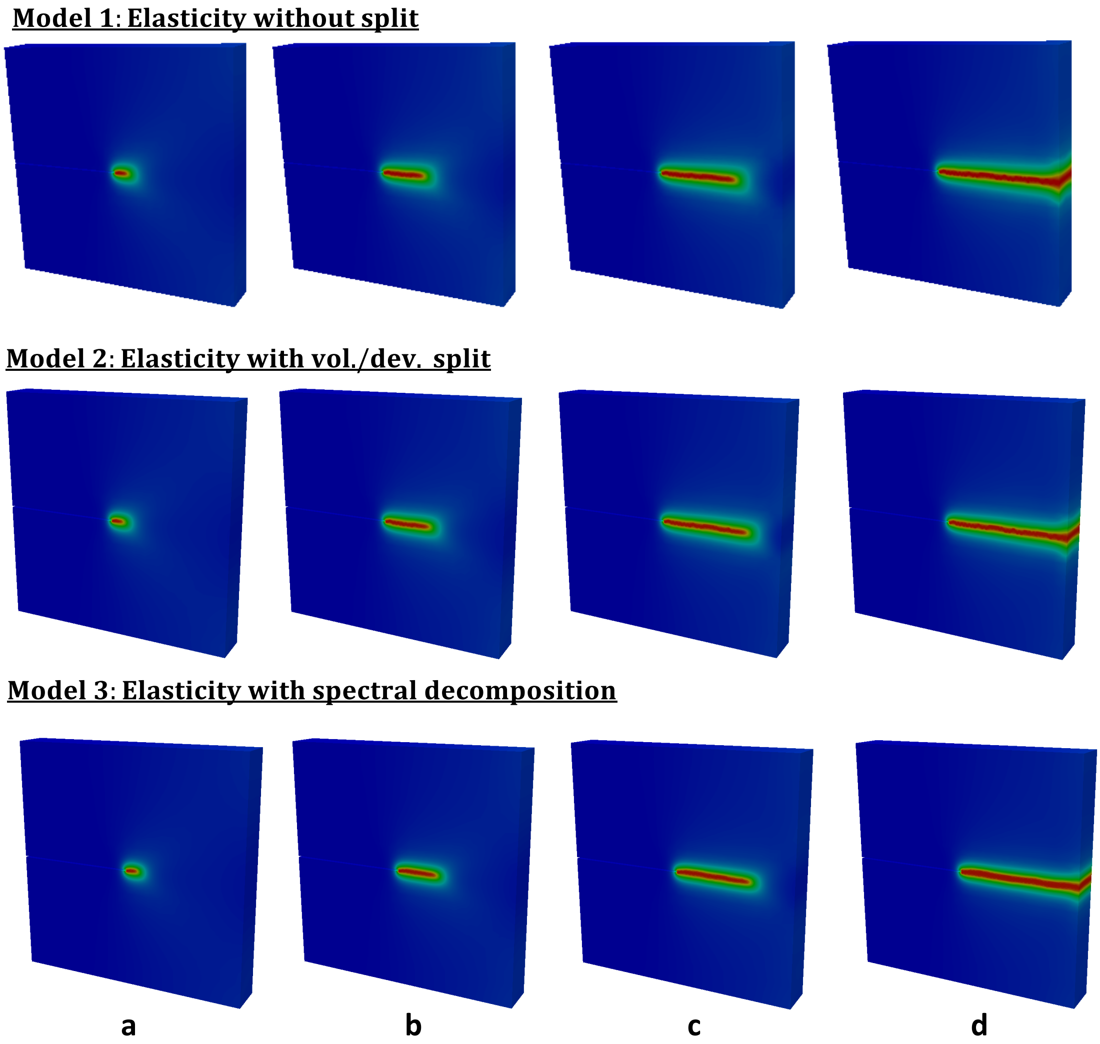

Figure 3.5: Example 1 (Case a). Smeared crack phase-field profiles for different deformation stages up to complete failure at (a) $u_y = 0.0066\ mm$ (b) $u_y = 0.0067\ mm$ (c) $u_y = 0.0068\ mm$ (d) $u_y = 0.007\ mm$.

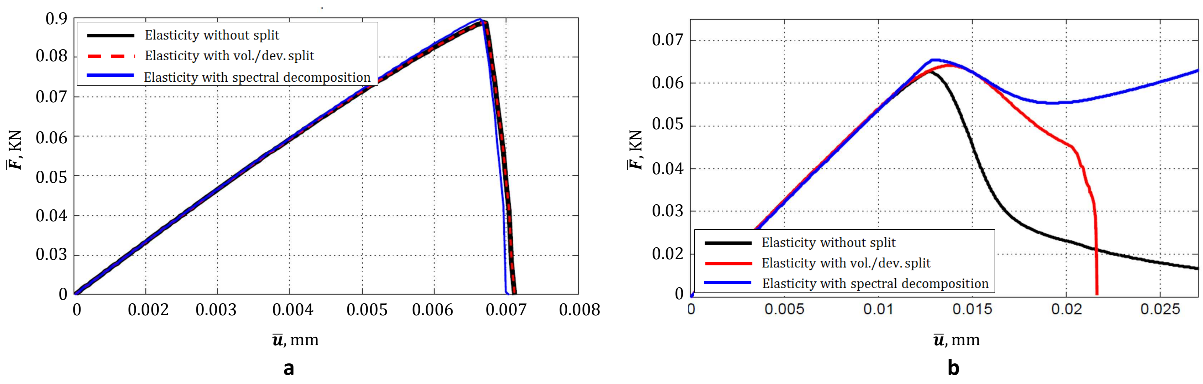

Figure 3.6: Example1. Load-displacement curves for the three-dimensional single-edge-notched test at small deformation. (a) Case a: tension test, and (b) Case b: shear test.

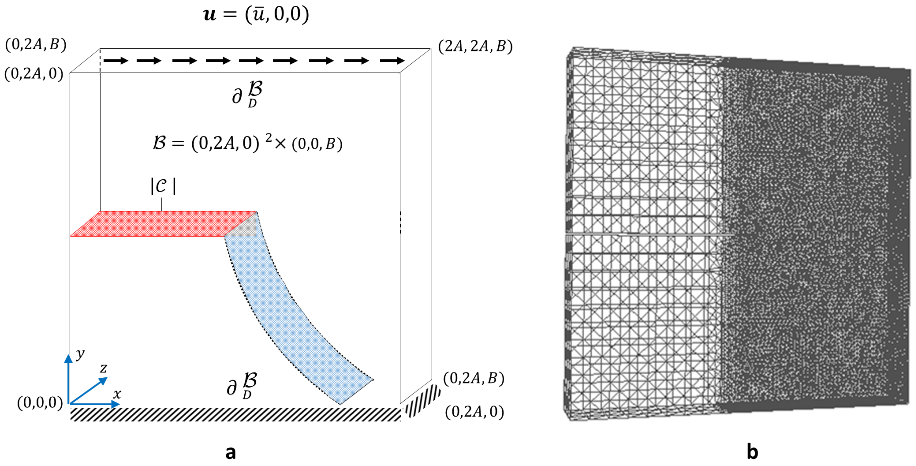

Figure 3.7: Example 1 (Case b). Geometry and loading setup for the single-edge-notched shear test. (a) Boundary value problem, and (b) finite element discretization.

Indeed, the result shows the necessity of splitting the elastic energy function, where only tension/isochoric parts of the material have to be degraded. Notably, the results reveal an identical response to the two-dimensional test reported in [5]. For a detail discussion, see [5, 93].

3.4.2. Example 2: Single-edge-notched test at finite strain

In this numerical example, we investigate the variational phase-model for the material undergoing finite strain. This example provides a benchmark example and is reported in [60]. We mainly concentrate on the three different models formulated earlier. These are the hyperelastic Neo-Hookean model without split given in (3.73), the hyperelastic Neo-Hookean model with volumetric-isochoric split given in (3.82), and the hyperelastic Mooney-Rivlin model with volumetric-isochoric split given in Section (3.1.5).

Case a: Two-dimensional tension test. In the second numerical example, a two-dimensional BVP applied to the square plate is shown in Fig. 3.9. We set $A = 0.5\ mm$ and hence $\mathcal{B} = (0,1)^2\ mm^2$, which includes a predefined single notch $\mathcal{C}$ of length $0.5\ m$ in the $y = A$ plane from the left edge to the body center, as depicted in Fig. 3.9. Here, finite element discretization is modeled with a minimum element size of $h = 0.005$ such that the spatial discretization of the model includes 122,77 four-node quadrilateral elements.

The displacement control is used with increments of $\Delta\bar{u} = 2\times10^{-5}$ with 320 time steps. The crack phase-field solution for different stages, as well as the complete failure state, are shown in Fig. 3.10. All the crack patterns show almost identical responses for all the methods. Accordingly, the resulting load-displacement curves are presented in Fig. 3.12a for different models. Here, the three different crack phase-field models are investigated, including the hyperelastic Neo-Hookean model without split which is shown by the blue line, the hyperelastic Neo-Hookean model with volumetric-isochoric which is shown by black line, and the hyperelastic Mooney-Rivlin model with a volumetric-isochoric split which is depicted by the red dashed line. For this numerical example, which explains mode I of fracture at finite strain, all methods provide an identical response.

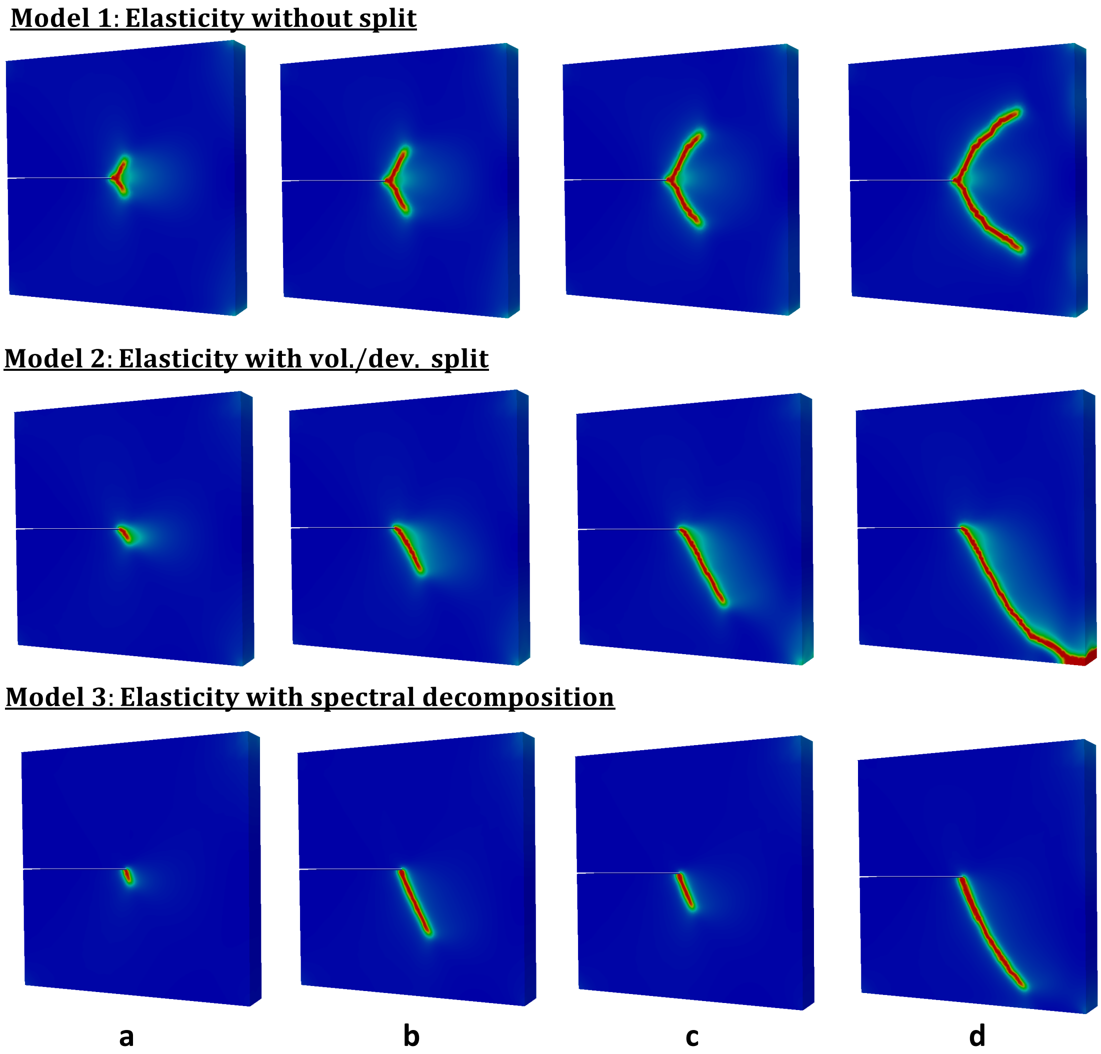

Figure 3.8: Example 1 (Case b). Smeared crack phase-field profiles for different deformation stages up to final failure at (a) $u_y = 0.014\ mm$, (b) $u_y = 0.015\ mm$, (c) $u_y = 0.017\ mm$, and (d) $u_y = 0.028\ mm$

Case b: Two-dimensional shear test. Here, finite element discretization is modeled with a minimum element size of $h = 0.005$ such that the spatial discretization of the model includes 278,17 four-node quadrilateral elements. Identical geometry is used as in Case a, but a horizontal displacement field is imposed at the top edge. The displacement control is used with increments of $\Delta\bar{u} = 2 \times 10^{-5}$ with 800 time steps.

Because the crack is free from the compression mode, the additive split is considered for the strain energy. The smeared crack phase-field for different stages, as well as the complete failure state, are shown in Fig. 3.11. Here, the hyperelastic Neo-Hookean model with volumetric-isochoric split, and hyperelastic Mooney-Rivlin model with volumetric-isochoric show nearly identical results. Notably, depending on the choice of f_{MN}, which relates μ_1 and μ_2 for the hyperelastic Mooney-Rivlin density function in (3.89), different responses may be obtained. Additionally, the load-displacement curves are depicted in Fig. 3.12b for the hyperelastic Neo-Hookean and Mooney-Rivlin models. It turns out that the resulting load-displacement curves from two models have nearly an identical response.

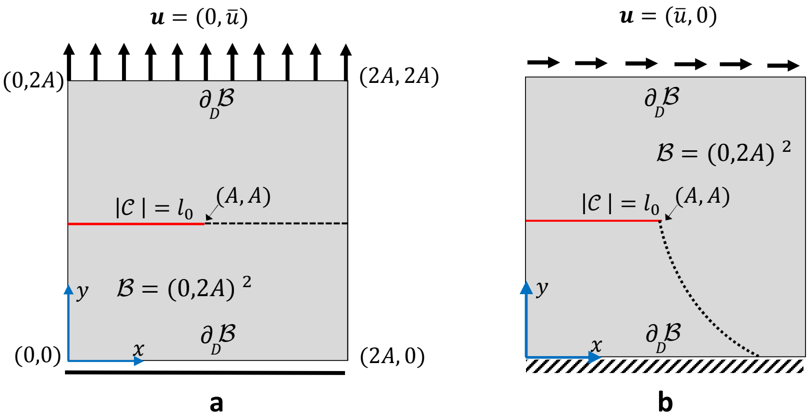

Figure 3.9: Example 2. Geometry and loading setup for the two-dimensional single-edge-notched test. (a) Case a: tension test, and (b) Case b: shear test.

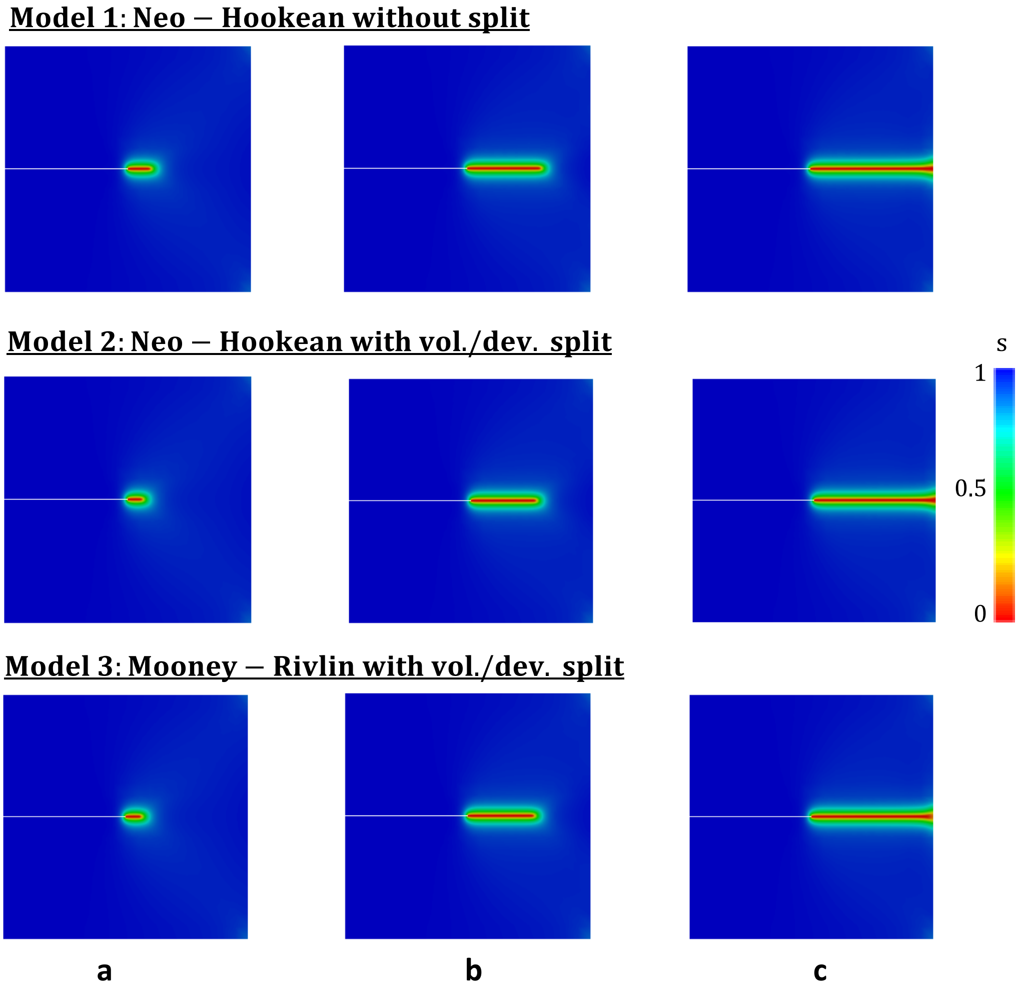

Figure 3.10: Example 2 (Case a). Crack phase-field profiles for different deformation stages up to complete failure at (a) $u_y = 0.00554$ mm (b) $u_y = 0.00589$ mm (c) $u_y = 0.0069$ mm.

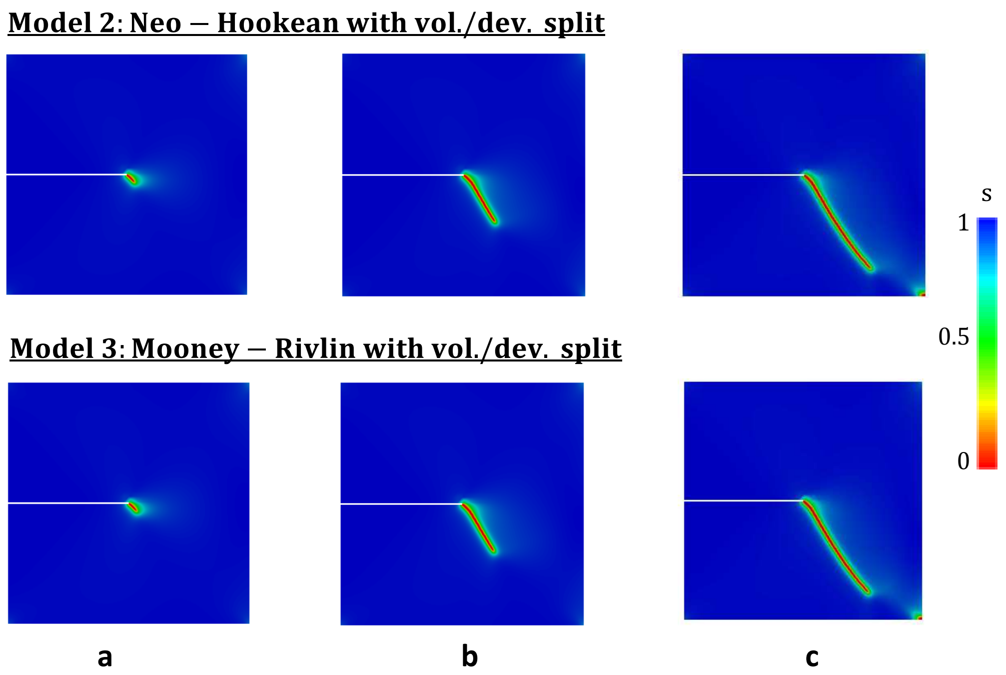

Figure 3.11: Example 2 (Case b). Smeared crack phase-field profiles for different deformation stages up to complete failure at (a) $u_y = 0.011\ mm$, (b) $u_y = 0.012\ mm$, and (c) $u_y = 0.015\ mm$.

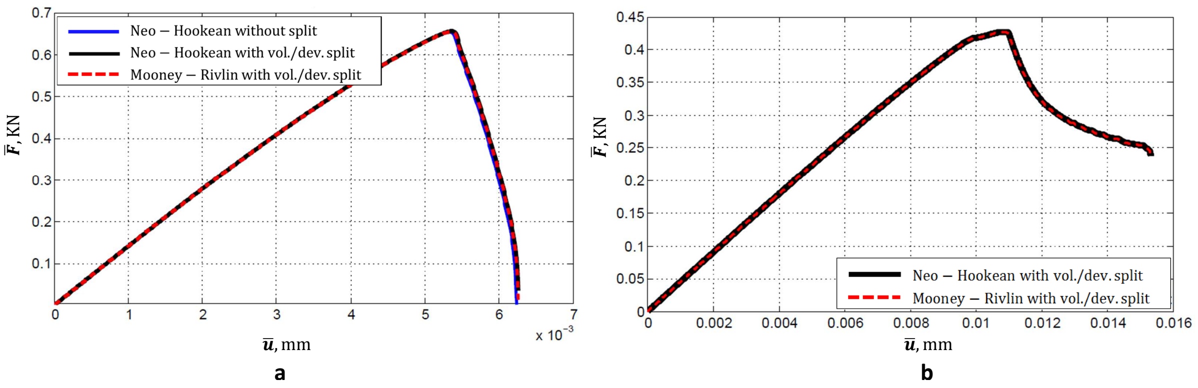

Figure 3.12: Example 2. Load-displacement curves for the two-dimensional single-edge-notched test at finite strain. (a) Case a: tension test, and (b) Case b: shear test.

Chapter 4

Global-Local Approach Applied to the Phase-Field Fracture at Small Deformation

For the fracturing material, the finite element treatment of the phase-field formulation is computationally demanding. Mainly, because it is required to use a sufficiently small length-scale to be resolved as well as the non-convexity of the energy functional to be minimized with respect to the displacement and phase-field; see [58, 46, 128]. In fact, the failure behavior is solely analyzed in a (small) local region whereas in the surrounding medium a simplified and linearized system of equations could be solved [99, 129]; see Fig. 4.1 . Thus, an idea of a Global-Local formulation, in which the full displacement/phase-field problem is solved on a *lower* (local) scale, while dealing with a purely linear elastic problem on an *upper* (global) scale, particularly appealing.

In this study, the Global-Local approach is employed as a computational framework for solving fracture mechanics problems as it was first formulated in [48]. Therein, the following assumptions were made [42, 57]:

i. The nonlinear behavior (e.g., fracture) is embedded at the local scale, and linear behavior is assumed at a global scale.

ii. The global level is free from geometrical imperfections and hence heterogeneities exist *only* at the local level.

iii. At the local level, we consider a divergence-free assumption for the stress state to ensure it is free from any external imposed forces.

Accordingly, we developed an interface energy functional based on the localized Lagrange multiplier method [109, 110] for the coupling of different domains and scales.

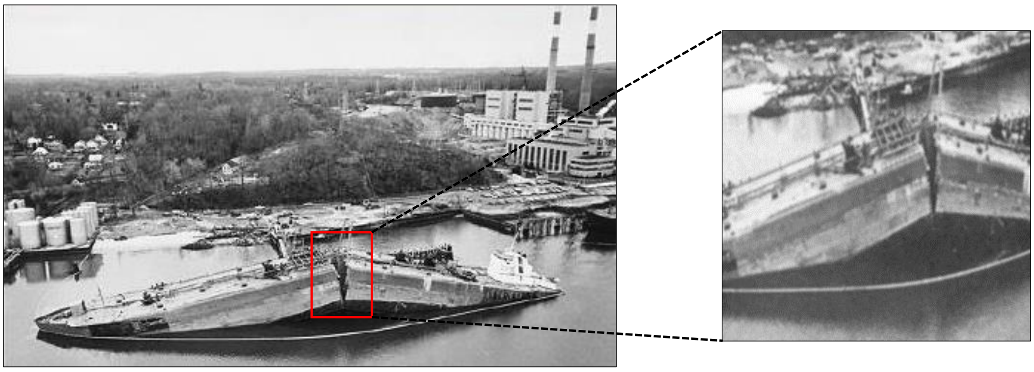

Figure 4.1: Application of the failure process of a large structure. Liberty ship damaged due to the brittle fracture [50]. The ship was built during World Wide II.

In this chapter, an efficient Global-Local formulation is derived for the fracturing material undergoing small deformation. Specifically, this chapter investigates the adoption of Global-Local approaches while modeling fracture using the variational phase-field framework provided in the previous chapter.

Because of the extreme difference in stiffness between the global counterpart of the zone to be analyzed locally and its actual response when undergoing extensive cracking, the main issues are robustness, accuracy, and efficiency of the fixed point iterative algorithm, which is at the core of this method [48]. These issues are tackled in this chapter. The convergence performance is investigated using the Global-Local algorithm, and the obtained results are shown to be identical to the reference phase-field solution. We also equip the Global-Local solution update procedure with relaxation/acceleration techniques. Furthermore, we introduce Robin-type boundary conditions to relax the stiff local response at the global scale and enhance its stabilization. The important ingredient of Robin-type boundary conditions is an optimal augmented interfaced operator, the construction of which is generally challenging and accomplished in our case using sensitivity analysis. This chapter is substantiated with some numerical tests.

4.1. Non-overlapping domain decomposition formulation

Recall, the complementary domain $\mathcal{B}_C := \mathcal{B}\backslash\mathcal{B}_L \subset \mathcal{B} \in \mathbb{R}^\delta$, $\delta = \{2,3\}$ corresponds to the intact region and let $\mathcal{B}_L$ be a bounded open domain, where the fracture surface is approximated in this region; see Fig. 4.2(a). It is assumed the fracture surface in $\mathcal{B}_L$ represents a reasonably small 'fraction' of $\mathcal{B}$ such that $|\mathcal{B}_L| \ll |\mathcal{B}_C|$. We further define an interface between an unfractured domain $\mathcal{B}_C$ and fractured domain $\mathcal{B}_L$ by $\Gamma \in \mathcal{R}^{\delta-1} \subset \mathcal{B}$ in the continuum setting to be the interface between $\mathcal{B}_L$ and $\mathcal{B}_C$, such that $\mathcal{B} \equiv \mathcal{B}_L \cup \Gamma \cup \mathcal{B}_C$. We further assume that $\mathcal{B}_L$ is free from any externally imposed load and hence we have prescribed loads *only* in $\mathcal{B}_C$. Such an assumption is standard for the multi-scale setting, see [42].

Consider a domain decomposition with a geometric sketch in Fig. 4.2(b) applied to the reference domain plotted in Fig. 4.2(a). Three functions on $\mathcal{B}_L$ and $\mathcal{B}_C$ are considered, namely $\boldsymbol{u}_L \in \mathbf{V_L}$, $s_L \in W_L$ and $\boldsymbol{u}_C \in \mathbf{V_C}$, where we introduce additional three sets:

$$\boldsymbol{V}_L := \mathbf{H}^1_0(\mathcal{B}_L)^\delta, \quad \boldsymbol{V}_C := \mathbf{V}(\mathcal{B}_C), \quad \text{and } \; W_L := W_{in}(\mathcal{B}_L) \; ,$$

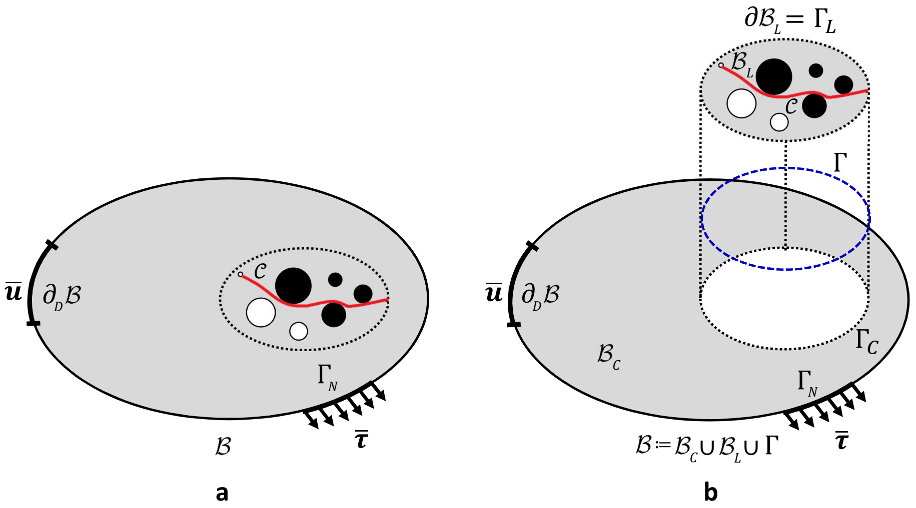

Figure 4.2: Domain decomposition scheme. (*a*) Geometry and loading setup of the reference BVP, and (*b*) non-overlapping domain decomposition setting whereas $\mathcal{B}$ is decomposed into the intact and fracture region denoted as complementary and local domains $\mathcal{B}_L$ and $\mathcal{B}_C$, respectively.

referring to the spaces defined in (3.8).

A descriptive motivation of the domain decomposition approach applied to the variational phase-field modeling is related to two restrictions in the model: (*i*) the strong coupling scheme that is the strong displacement continuity condition that holds along with (*ii*) the predefined interface. To this end, one needs to assume that the discrete interfaces for both complementary and local domain do exactly coincide in the strong sense, yielding

$$\boldsymbol{u}_L \overset{!}{=} \boldsymbol{u}_C \quad \text{at} \quad \boldsymbol{x} \in \Gamma = \Gamma_C = \Gamma_L. \tag{4.1}$$

This displacement continuity is often called *primal* approach in the literature; see e.g. [84].

Let the *reference displacement field* $\boldsymbol{u} \in \mathbf{V}$ be the solution of the multi-field variational problem in (3.31). It is decomposed as

$$\boldsymbol{u}(\boldsymbol{x}, t) := \begin{cases} \boldsymbol{u}_L & \text{for } \boldsymbol{x} \in \mathcal{B}_L, \\ \boldsymbol{u}_C & \text{for } \boldsymbol{x} \in \mathcal{B}_C. \end{cases} \tag{4.2}$$

Since the fracture surface lives only in $\mathcal{B}_L$ we introduce scalar-valued function $s_L : \mathcal{B}_L \to [0, 1] \in W_L$. The *reference phase-field* s is then decomposed in the following form

$$s(\boldsymbol{x}, t) := \begin{cases} s_L & \text{for } \boldsymbol{x} \in \mathcal{B}_L, \\ 1 & \text{for } \boldsymbol{x} \in \mathcal{B}_C. \end{cases} \tag{4.3}$$

By imposing (4.2) and (4.3) to the energy functional, indicated in Formulation 3.1.2, thus the energy functionals corresponding to $\mathcal{B}_C$ and $\mathcal{B}_L$ read

$$\widehat{\mathcal{E}}_C(\boldsymbol{u}_C) := \int_{\mathcal{B}_C} w(\boldsymbol{\varepsilon}_C, 1, 0)\,\mathrm{d}\boldsymbol{x} - \int_{\partial_N\mathcal{B}_C} \bar{\boldsymbol{\tau}} \cdot \boldsymbol{u}_C\,\mathrm{d}a\ , \tag{4.4}$$

and

$$\widehat{\mathcal{E}}_L(\boldsymbol{u}_L, s_L) := \int_{\mathcal{B}_L} w(\boldsymbol{\varepsilon}_L, s_L, \nabla s_L)\,\mathrm{d}\boldsymbol{x} \ , \tag{4.5}$$

for the total energy density defined in Formulation 3.1.1. With the strong displacement continuity in (4.1) we obtain

$$\mathcal{E}(\boldsymbol{u}, s) \equiv \widehat{\mathcal{E}}(\boldsymbol{u}_C, \boldsymbol{u}_L, s_L) := \widehat{\mathcal{E}}_C(\boldsymbol{u}_C) + \widehat{\mathcal{E}}_L(\boldsymbol{u}_L, s_L) \ , \tag{4.6}$$

where $\mathcal{E}$ is the original reference functional in Formulation 3.1.2. As a result, the domain decomposition variational formulation is *equivalent* to the reference formulation (3.31)

$$\{\boldsymbol{u}_C, \boldsymbol{u}_L, s_L\} = \arg\{ \min_{\boldsymbol{u}_C \in \mathbf{V_C}, \boldsymbol{u}_L \in \mathbf{V_L}} \min_{s_L \in W_L} [\ \widehat{\mathcal{E}}(\boldsymbol{u}_C, \boldsymbol{u}_L, s_L)\ ]\ \} \ . \tag{4.7}$$

Note, the major advantage of using this minimization problem instead of the one in (3.31) is the reduction of the nonlinearity order of the complementary domain (which is free from the fracture state), and more specifically in small deformation setting that is a linear minimization problem.

Remark 4.1.1. *The strong displacement continuity requirement given in (4.1) is too restrictive from the computational standpoint [38]. Additionally, to resolve the phase-field problem, one requires $h_L \ll h_G$. But, if we assume $\boldsymbol{u}_L \overset{!}{=} \boldsymbol{u}_C$ on Γ, this yields $\Gamma_L = \Gamma_C$ in a discretized setting hence $h_L = h_G$ on Γ which has the contradiction with $h_L \ll h_G$.*

Following Remark 4.1.1, we relax (4.1) in a weak sense by introducing traction-like terms in the corresponding energy functionals (4.4) and (4.5). This results in

$$\widehat{\mathcal{E}}_C(\boldsymbol{u}_C, \boldsymbol{\lambda}_C) := \int_{\mathcal{B}_C} w(\boldsymbol{\varepsilon}_C, 1, 0)\,\mathrm{d}\boldsymbol{x} - \int_{\Gamma_C} \boldsymbol{\lambda}_C \cdot \boldsymbol{u}_C\,\mathrm{d}a - \int_{\Gamma_{N,C}} \bar{\boldsymbol{\tau}} \cdot \boldsymbol{u}_C\,\mathrm{d}a \ , \tag{4.8}$$

and

$$\widehat{\mathcal{E}}_L(\boldsymbol{u}_L, s_L, \boldsymbol{\lambda}_L) := \int_{\mathcal{B}_L} w(\boldsymbol{\varepsilon}_L, s_L, \nabla s_L)\,\mathrm{d}\boldsymbol{x} - \int_{\Gamma_L} \boldsymbol{\lambda}_L \cdot \boldsymbol{u}_L\,\mathrm{d}a \ , \tag{4.9}$$

with $\boldsymbol{\lambda}_C, \boldsymbol{\lambda}_L \in \mathbf{L}^2(\Gamma)$ being the unknown Lagrange multipliers, which represent traction forces on the interface. The saddle point problem including complementary and local domains assumes the form

$$\widehat{\mathcal{E}}(\boldsymbol{u}_C, \boldsymbol{u}_L, s_L, \boldsymbol{\lambda}_L, \boldsymbol{\lambda}_C) := \widehat{\mathcal{E}}_C(\boldsymbol{u}_C, \boldsymbol{\lambda}_C) + \widehat{\mathcal{E}}_L(\boldsymbol{u}_L, s_L, \boldsymbol{\lambda}_L) \ ,$$

which is under-determined, since no relation is yet specified between $\boldsymbol{u}_L$ and $\boldsymbol{u}_C$, nor between $\boldsymbol{\lambda}_L$ and $\boldsymbol{\lambda}_C$. The latter is achieved by introducing the functional

$$\widehat{\mathcal{E}}_\Gamma(\boldsymbol{u}_\Gamma, \boldsymbol{\lambda}_C, \boldsymbol{\lambda}_L) := \int_\Gamma \boldsymbol{u}_\Gamma \cdot (\boldsymbol{\lambda}_L + \boldsymbol{\lambda}_C)\,\mathrm{d}a \ , \tag{4.10}$$

with $\boldsymbol{u}_\Gamma \in \mathbf{H}^1(\Gamma)$ representing the (unknown) Lagrange multiplier, which has the dimension of a displacement, also called displacement interface. Summing $\mathcal{E}_C$ and $\mathcal{E}_L$ with $\mathcal{E}_\Gamma$, we get

$$\begin{aligned} \widehat{\mathcal{E}}(\boldsymbol{u}_C, \boldsymbol{u}_L, s_L, \boldsymbol{u}_\Gamma, \boldsymbol{\lambda}_C, \boldsymbol{\lambda}_L) := &\int_{\mathcal{B}_C} w(\boldsymbol{\varepsilon}_C, 1, 0)\,\mathrm{d}\boldsymbol{x} + \int_{\mathcal{B}_L} w(\boldsymbol{\varepsilon}_L, s_L, \nabla s_L)\,\mathrm{d}\boldsymbol{x} \\ &+ \int_\Gamma \{\boldsymbol{\lambda}_C \cdot (\boldsymbol{u}_\Gamma - \boldsymbol{u}_C) + \boldsymbol{\lambda}_L \cdot (\boldsymbol{u}_\Gamma - \boldsymbol{u}_L)\}\,\mathrm{d}a - \int_{\Gamma_{N,C}} \bar{\boldsymbol{\tau}} \cdot \boldsymbol{u}_C\,\mathrm{d}a. \end{aligned} \tag{4.11}$$

Here, the introduction of the intermediate displacement $\boldsymbol{u}_\Gamma$ satisfies the weak traction continuity between $\boldsymbol{\lambda}_L$ and $\boldsymbol{\lambda}_C$ along Γ. This is in addition to the weak displacement continuity between $\boldsymbol{u}_L$ and $\boldsymbol{u}_C$ across Γ. Hence, both displacement and traction continuity are imposed implicitly in the weak sense to the energy functional [109]. The coupling interface energy functional used in (4.11) (i.e., third term) is called *Localized Lagrange Multipliers*; see e.g. [110, 120].

The variational formulation of (4.11) is equivalent to the reference minimization problem in (3.31), such that $\mathcal{E} \approx \widehat{\mathcal{E}}$, yields

$$\boldsymbol{s} = \arg\{ \min_{\boldsymbol{u}_C \in \boldsymbol{V}_C, \boldsymbol{u}_L \in \boldsymbol{V}_L, \boldsymbol{u}_\Gamma \in \boldsymbol{H}^1(\Gamma), s_L \in W_L} \; \max_{\boldsymbol{\lambda}_C, \boldsymbol{\lambda}_L \in \mathbf{L}^2(\Gamma)} [\, \widehat{\mathcal{E}}(\boldsymbol{u}_C, \boldsymbol{u}_L, s_L, \boldsymbol{u}_\Gamma, \boldsymbol{\lambda}_C, \boldsymbol{\lambda}_L) \,]\}, \tag{4.12}$$

where $\boldsymbol{s} := (\boldsymbol{u}_C, \boldsymbol{u}_L, s_L, \boldsymbol{u}_\Gamma, \boldsymbol{\lambda}_C, \boldsymbol{\lambda}_L)$. Accordingly, the reference displacement field $\boldsymbol{u}$, is decomposed as

$$\boldsymbol{u} = \begin{cases} \boldsymbol{u}_L & \text{for } \boldsymbol{x} \in \mathcal{B}_L, \\ \boldsymbol{u}_C & \text{for } \boldsymbol{x} \in \mathcal{B}_C, \\ \boldsymbol{u}_\Gamma & \text{for } \boldsymbol{x} \in \Gamma, \end{cases} \tag{4.13}$$

which is based on the solution triple $(\boldsymbol{u}_C, \boldsymbol{u}_L, \boldsymbol{u}_\Gamma)$ as a minimizer of the (4.11). Note, the representation for s in terms of s_L defined by (4.3) remains same.

Note, the term "localized" in localized Lagrange multipliers (LLM) is used to associate the multipliers $\boldsymbol{\lambda}_C$, $\boldsymbol{\lambda}_L$ and $\boldsymbol{u}_\Gamma$ with the corresponding sub-domains; see e.g. [109, 110, 120]. In contrast to the LLM, basically different types of coupling approaches through domain decomposition techniques can be described. For the sake of completeness, Table 4.1 briefly summarizes the considered formulations.

Table 4.1: *Domain decomposition formulations of the reference problem in Formulation 3.1.2.*

Formulation	Imposed continuity between		Unknowns
	$\boldsymbol{u}_C$ & $\boldsymbol{u}_L$	$\boldsymbol{\lambda}_C$ & $\boldsymbol{\lambda}_L$	
Primal, [77]	strong	—	$(\boldsymbol{u}_C, \boldsymbol{u}_L, s_L)$
Dual, [38]	weak	strong	$(\boldsymbol{u}_C, \boldsymbol{u}_L, s_L, \boldsymbol{\lambda})$
LLM, [110]	weak	weak	$(\boldsymbol{u}_C, \boldsymbol{u}_L, s_L, \boldsymbol{u}_\Gamma, \boldsymbol{\lambda}_C, \boldsymbol{\lambda}_L)$

It is noted that Formulation (4.7) is seemingly less computationally demanding than (4.12), since there is only one extra field $\boldsymbol{\lambda}$ to be solved for in the former case, versus the triple $(\boldsymbol{u}_\Gamma, \boldsymbol{\lambda}_C, \boldsymbol{\lambda}_L)$ of unknown fields in the latter one. The potential advantage of (4.12) over (4.7) is greater flexibility, at the finite element discretization stage, of handling the interface between complementary and local domains. See Chapter 6 for a detailed discussion.

As follows, we move on with the LLM formulation (4.12) and extend it to the *Global-Local* setting, for which, in turn, a non-intrusive solution procedure is devised. This will lead to a *non-intrusive Global-Local approach* to the phase-field formulation described in Chapter 3.

4.2. Global-Local formulation

In this section, the formulation is further extended toward the Global-Local approach in line with [48]. Specifically, we extend the Global-Local approach to the crack phase-field formulation at small deformation.

Let us define open and bounded *fictitious domain* $\mathcal{B}_F$ to *recover the space* of $\mathcal{B}$ that is obtained by removing $\mathcal{B}_L$ from its continuum domain; see Fig. 4.3. Indeed, the fictitious domain is a prolongation of the $\mathcal{B}_C$ towards $\mathcal{B}$. This gives the same constitutive modeling used in $\mathcal{B}_C$ for $\mathcal{B}_F$. Thus, the energy functional of the complementary and fictitious domain is the same. We also use the identical discretization space for both $\mathcal{B}_F$ and $\mathcal{B}_C$, which results in $h_F := h_C$. We further define, an open and bounded *global domain* $\mathcal{B}_G$ such that $\mathcal{B}_G = \mathcal{B}_F \cup \Gamma \cup \mathcal{B}_C$. It yields the same energy functional for $\mathcal{B}_C$, $\mathcal{B}_F$ and $\mathcal{B}_G$. Hence, the material parameters are identical for $\mathcal{B}_C$, $\mathcal{B}_F$ and $\mathcal{B}_G$. Additionally, this unification yields on identical discretization space for the $\mathcal{B}_F$, $\mathcal{B}_C$, and $\mathcal{B}_G$ hence results in $h_G \approx h_F \approx h_C$ referring to the element size. Note that the fictitious domain $\mathcal{B}_F$ is assumed to be free from geometrical *imperfections*, which may be present in $\mathcal{B}_L$; see Fig. 4.3(b). Thus, the global domain is assumed to be free from any given imperfection. Let us also define, global and local interfaces denoted as $\Gamma_G \subset \mathcal{B}_G$ and $\Gamma_L \subset \mathcal{B}_L$, such that in the continuum setting we have $\Gamma = \Gamma_G = \Gamma_L$.

It is assumed that there exists a continuous prolongation of $\boldsymbol{u}_C$ into $\mathcal{B}_F$. Hence, we introduce a function $\boldsymbol{u}_G \in \mathbf{V}(\mathcal{B}_G)$ such that $\boldsymbol{u}_G|_{\mathcal{B}_C} \equiv \boldsymbol{u}_C$ and $\boldsymbol{u}_G = \boldsymbol{u}_C$ on Γ in the sense of a trace. Thus, the boundary conditions for $\mathcal{B}_G$ is same as the $\mathcal{B}_C$, therefore it holds $\boldsymbol{u}_G = \bar{\boldsymbol{u}}$ on $\partial_D \mathcal{B}$ and $\boldsymbol{\tau} = \bar{\boldsymbol{\tau}}$ on $\Gamma_{N,G}$.

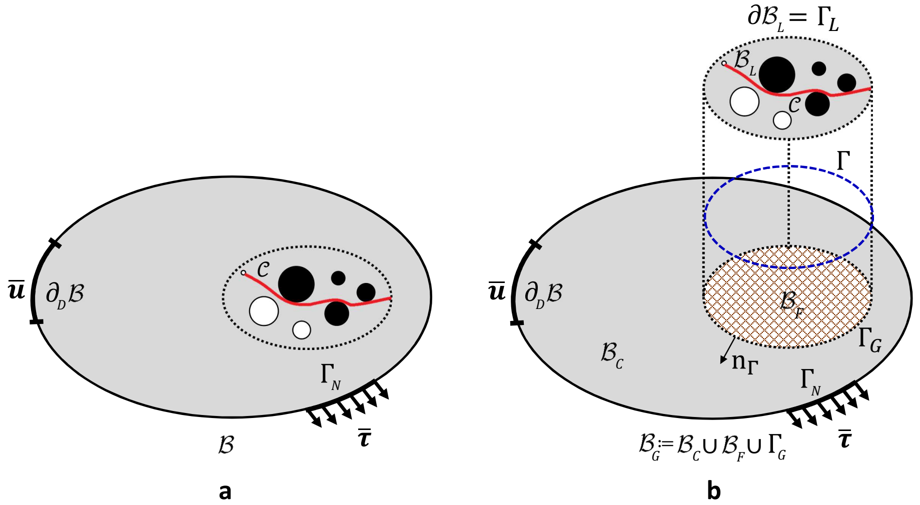

Figure 4.3: Illustration of the (a) geometry and loading setup of the reference BVP, and (b) Global-Local setting, by introduction of the fictitious domain $\mathcal{B}_F$ through prolongation of $\mathcal{B}_C$ to the entire domain whereas its unification is the so-called global domain $\mathcal{B}_G := \mathcal{B}_C \cup \mathcal{B}_F \cup \Gamma_G$.

Using the fictitious domain, the first term in (4.11) is recast as follows

$$\begin{aligned}\int_{\mathcal{B}_C} w(\boldsymbol{\varepsilon}(\boldsymbol{u}_C),1,0)\,\mathrm{d}\boldsymbol{x} &= \int_{\mathcal{B}_C} w(\boldsymbol{\varepsilon}(\boldsymbol{u}_G),1,0)\,\mathrm{d}\boldsymbol{x} \\ &= \int_{\mathcal{B}_G} w(\boldsymbol{\varepsilon}(\boldsymbol{u}_G),1,0)\,\mathrm{d}\boldsymbol{x} - \int_{\mathcal{B}_F} w(\boldsymbol{\varepsilon}(\boldsymbol{u}_G),1,0)\,\mathrm{d}\boldsymbol{x}\,.\end{aligned} \tag{4.14}$$

Note, we substitute $\boldsymbol{u}_G$ for $\boldsymbol{u}_C$ in the second and fourth integrals in (4.14). That is trivial by means of the prolongation concept such that $\boldsymbol{u}_G|_{\mathcal{B}_F} \equiv \boldsymbol{u}_F$ and $\boldsymbol{u}_G = \boldsymbol{u}_F$ on Γ. This provides the *Global-Local* approximation of the reference energy functional $\mathcal{E}$ indicated in Formulation 3.1.2 by

$$\begin{aligned}\widetilde{\mathcal{E}}(\boldsymbol{u}_G,\boldsymbol{u}_L,s_L,\boldsymbol{u}_\Gamma,\boldsymbol{\lambda}_C,\boldsymbol{\lambda}_L) :=\ & \underbrace{\int_{\mathcal{B}_G} w(\boldsymbol{\varepsilon}_G,1,0)\,\mathrm{d}\boldsymbol{x} - \int_{\mathcal{B}_F} w(\boldsymbol{\varepsilon}_F,1,0)\,\mathrm{d}\boldsymbol{x} - \int_{\Gamma_{N,G}} \bar{\boldsymbol{\tau}}\cdot\boldsymbol{u}_G\,\mathrm{d}a}_{\text{global terms}} \\ & + \underbrace{\int_{\mathcal{B}_L} w(\boldsymbol{\varepsilon}_L,s_L,\nabla s_L)\,\mathrm{d}\boldsymbol{x}}_{\text{local term}} \\ & + \underbrace{\int_{\Gamma} \{\boldsymbol{\lambda}_C\cdot(\boldsymbol{u}_\Gamma-\boldsymbol{u}_G)+\boldsymbol{\lambda}_L\cdot(\boldsymbol{u}_\Gamma-\boldsymbol{u}_L)\}\,\mathrm{d}a}_{\text{coupling terms}}\,.\end{aligned} \tag{4.15}$$

where the approximation $\mathcal{E} \equiv \widetilde{\mathcal{E}}$ holds.

Formulation 4.2.1 (Global-Local energy functional applied to the isotropic crack topology)**.** *Let* λ*,* μ *be given with initial conditions* $\boldsymbol{u}_0 = \boldsymbol{u}(\boldsymbol{x},0)$ *and* $s_0 = s(\boldsymbol{x},0)$*. For the loading increments* $n = 1,2,\dots,N$*, find* $\boldsymbol{u}_G := \boldsymbol{u}_G^n \in \mathbf{V_G}$*,* $\boldsymbol{u}_L := \boldsymbol{u}_L^n \in \mathbf{V_L}$*,* $\boldsymbol{u}_\Gamma := \boldsymbol{u}_\Gamma^n \in \mathbf{H}^1(\Gamma)$*,* $s_L := s_L^n \in W_L$*,* $\boldsymbol{\lambda}_C := \boldsymbol{\lambda}_C^n \in \mathbf{L}^2(\Gamma)$ *and* $\boldsymbol{\lambda}_L := \boldsymbol{\lambda}_L^n \in \mathbf{L}^2(\Gamma)$*, such that the functional*

$$\begin{aligned}&\widetilde{\mathcal{E}}(\boldsymbol{u}_G,\boldsymbol{u}_L,s_L,\boldsymbol{u}_\Gamma,\boldsymbol{\lambda}_C,\boldsymbol{\lambda}_L) = \\ &\quad \underbrace{\int_{\mathcal{B}_G}(\frac{\lambda}{2}I_1^2+\mu I_2)\mathrm{d}\boldsymbol{x}}_{\textit{global deformation term}} - \underbrace{\int_{\mathcal{B}_F}(\frac{\lambda}{2}I_1^2+\mu I_2)\mathrm{d}\boldsymbol{x}}_{\textit{fictitious deformation term}} - \underbrace{\int_{\Gamma_{N,G}}\bar{\boldsymbol{\tau}}\cdot\boldsymbol{u}_G\,\mathrm{d}a}_{\textit{global external load}} \\ &\quad + \underbrace{\int_{\mathcal{B}_L} g(s_{L+})\big(\frac{\lambda}{2}I_1^{+2}+\mu I_2^{+}\big)\mathrm{d}\boldsymbol{x} + \int_{\mathcal{B}_L}(\frac{\lambda}{2}I_1^{-2}+\mu I_2^{-})\mathrm{d}\boldsymbol{x}}_{\textit{local deformation term}} \\ &\quad + G_c\underbrace{\int_{\mathcal{B}_L}\{\frac{1}{2l}(1-s_L)^2+\frac{l}{2}\nabla s_L.\nabla s_L\}\mathrm{d}\boldsymbol{x}}_{\textit{local fracture term}} \\ &\quad + \underbrace{\int_{\Gamma}\{\boldsymbol{\lambda}_C\cdot(\boldsymbol{u}_\Gamma-\boldsymbol{u}_G)+\boldsymbol{\lambda}_L\cdot(\boldsymbol{u}_\Gamma-\boldsymbol{u}_L)\}\,\mathrm{d}a}_{\textit{interface coupling term}},\end{aligned}$$

is minimized.

Note, we are not anymore using $\partial_N \mathcal{B}$ for the applied surface load, and hence $\Gamma_{N,G}$ is considered. This is because the global domain is free from any fracture state. The minimization problem for the Global-Local energy functional given in Formulation 4.2.1 that is applied to the isotropic crack topology takes the following compact form,

$$\boxed{\boldsymbol{s} = \arg\{ \min_{\boldsymbol{u}_G \in \boldsymbol{V}_G, \boldsymbol{u}_L \in \boldsymbol{V}_L, \boldsymbol{u}_\Gamma \in \, \mathbf{H}^1(\Gamma), s_L \in W_L} \; \max_{\boldsymbol{\lambda}_C, \boldsymbol{\lambda}_L \in \mathbf{L}^2(\Gamma)} [\, \widetilde{\mathcal{E}}(\boldsymbol{u}_G, \boldsymbol{u}_L, s_L, \boldsymbol{u}_\Gamma, \boldsymbol{\lambda}_C, \boldsymbol{\lambda}_L)]\},} \tag{4.16}$$

where $\boldsymbol{s} := (\boldsymbol{u}_G, \boldsymbol{u}_L, s_L, \boldsymbol{u}_\Gamma, \boldsymbol{\lambda}_C, \boldsymbol{\lambda}_L)$. The relation between the solution $\boldsymbol{u}$ of the minimization problem in (3.31) and the solution triple $(\boldsymbol{u}_G, \boldsymbol{u}_L, \boldsymbol{u}_\Gamma)$ of (4.16) reads

$$\boldsymbol{u} = \begin{cases} \boldsymbol{u}_L, & \text{for } \boldsymbol{x} \in \mathcal{B}_L, \\ \boldsymbol{u}_G, & \text{for } \boldsymbol{x} \in \mathcal{B}_C, \\ \boldsymbol{u}_\Gamma, & \text{for } \boldsymbol{x} \in \Gamma. \end{cases}$$

Remark 4.2.1. *When using standard reference phase-field modeling, we are most of the time not dealing with a uniform mesh, and hence the domain is divided into coarser and finer mesh elements. To resolve the crack phase-field, we need to have $l \geq h$ must hold at every point of the domain [24, 87]; thus results in $l \geq h_c \geq h_f$ (c and f refer to the coarse and fine region in the domain, respectively). This typically leads to a finer mesh even for the area sufficiently far from the fracture zone; thus increasing the computational time considerably. However, this is not the case for the Global-Local approach, where the phase-field formulation is only embedded within the local domain and not the entire domain. Hence, the computational time is reduced drastically.*

4.3. Variational formulation for the Global-Local coupling system

Now, we consider the weak formulation of (4.16). The directional derivatives of the functional $\widetilde{\mathcal{E}}$ yield for the global weak form

$$\begin{aligned} \widetilde{\mathcal{E}}_{\boldsymbol{u}_G}(\boldsymbol{s}; \delta \boldsymbol{u}_G) := & \int_{\mathcal{B}_G} \boldsymbol{\sigma}(\boldsymbol{u}_G) : \boldsymbol{\varepsilon}(\delta \boldsymbol{u}_G)\, \mathrm{d}\boldsymbol{x} - \int_{\mathcal{B}_F} \boldsymbol{\sigma}(\boldsymbol{u}_G) : \boldsymbol{\varepsilon}(\delta \boldsymbol{u}_G)\, \mathrm{d}\boldsymbol{x} \\ & - \int_{\Gamma_G} \boldsymbol{\lambda}_C \cdot \delta \boldsymbol{u}_G \, \mathrm{da} - \int_{\Gamma_{N,G}} \bar{\boldsymbol{\tau}} \cdot \delta \boldsymbol{u}_G \, \mathrm{da} = 0, \end{aligned} \tag{G}$$

where $\boldsymbol{\sigma}(\boldsymbol{u}_G) := \partial_{\boldsymbol{\varepsilon}} w(\boldsymbol{\varepsilon}(\boldsymbol{u}_G), 1, 1)$ and $\delta \boldsymbol{u}_G \in \{\mathbf{H}^1(\mathcal{B}_G) : \delta \boldsymbol{u}_G = \mathbf{0} \text{ on } \partial_D \mathcal{B}\}$ is the test function. The local weak formulations assume the form

$$\begin{cases} \widetilde{\mathcal{E}}_{\boldsymbol{u}_L}(\boldsymbol{s}; \delta \boldsymbol{u}_L) := \displaystyle\int_{\mathcal{B}_L} \boldsymbol{\sigma}(\boldsymbol{u}_L, s_L) : \boldsymbol{\varepsilon}(\delta \boldsymbol{u}_L)\, \mathrm{d}\boldsymbol{x} - \int_{\Gamma_L} \boldsymbol{\lambda}_L \cdot \delta \boldsymbol{u}_L \, \mathrm{da} = 0, \\ \widetilde{\mathcal{E}}_{s_L}(\boldsymbol{s}; \delta s_L) := (1-\kappa) \displaystyle\int_{\mathcal{B}_L} 2 s_{L+} \mathcal{H}(\boldsymbol{\varepsilon}(\boldsymbol{u}_L)) . \delta s_L \mathrm{d}\boldsymbol{x} + \int_{\mathcal{B}_L} (s_L - 1) . \delta s_L \mathrm{d}\boldsymbol{x} \\ \qquad + \displaystyle\int_{\mathcal{B}_L} l^2 \nabla s_L . \nabla(\delta s_L)\, \mathrm{d}\boldsymbol{x} = 0, \end{cases} \tag{L}$$

where $\boldsymbol{\sigma}(\boldsymbol{u}_L, s_L) = \partial_{\boldsymbol{\varepsilon}} w(\boldsymbol{\varepsilon}_L, s_L, \nabla s_L) = \boldsymbol{\sigma}_{\boldsymbol{\varepsilon}}(\boldsymbol{\varepsilon}_L, s_L)$ is defined in (3.27), $\delta \boldsymbol{u}_L \in \mathbf{H}^1(\mathcal{B}_L)$ is the local test function and $\delta s_L \in \mathrm{H}^1(\mathcal{B}_L)$ is the local phase-field test function. The variational derivatives of $\widetilde{\mathcal{E}}$ with respect to $(\boldsymbol{u}_\Gamma, \boldsymbol{\lambda}_C, \boldsymbol{\lambda}_L)$ provide kinematic equations due to weak coupling between global and local forms, through

$$\widetilde{\mathcal{E}}_{\boldsymbol{u}_\Gamma}(\boldsymbol{s}; \delta \boldsymbol{u}_\Gamma) := \int_\Gamma (\boldsymbol{\lambda}_C + \boldsymbol{\lambda}_L) \cdot \delta \boldsymbol{u}_\Gamma \,\mathrm{d}a = 0, \tag{C$_1$}$$

$$\widetilde{\mathcal{E}}_{\boldsymbol{\lambda}_C}(\boldsymbol{s}; \delta \boldsymbol{\lambda}_C) := \int_\Gamma (\boldsymbol{u}_\Gamma - \boldsymbol{u}_G) \cdot \delta \boldsymbol{\lambda}_C \,\mathrm{d}a = 0, \tag{C$_2$}$$

$$\widetilde{\mathcal{E}}_{\boldsymbol{\lambda}_L}(\boldsymbol{s}; \delta \boldsymbol{\lambda}_L) := \int_\Gamma (\boldsymbol{u}_\Gamma - \boldsymbol{u}_L) \cdot \delta \boldsymbol{\lambda}_L \,\mathrm{d}a = 0. \tag{C$_3$}$$

Herein $\delta \boldsymbol{u}_\Gamma \in \mathbf{H}^1(\Gamma)$ and $\delta \boldsymbol{\lambda}_C, \delta \boldsymbol{\lambda}_L \in \mathbf{L}^2(\Gamma)$ are the corresponding test functions.

Let us now focus on the global variational in (G). The presence of the two domain integrals over $\mathcal{B}_G$ and $\mathcal{B}_F$ would imply, in this case, the need to simultaneously access the corresponding stiffness matrices. Avoiding this can be done as follows: We focus on the domain integral over $\mathcal{B}_F$ in (G). The idea is to transform the domain integral in $\mathcal{B}_F$ to the global interface Γ_G. The divergence theorem leads to

$$\int_{\mathcal{B}_F} \boldsymbol{\sigma}(\boldsymbol{u}_G) : \boldsymbol{\varepsilon}(\delta \boldsymbol{u}_G) \,\mathrm{d}\boldsymbol{x} = - \int_{\mathcal{B}_F} \mathrm{div}(\boldsymbol{\sigma}(\boldsymbol{u}_G)) \cdot \delta \boldsymbol{u}_G \,\mathrm{d}\boldsymbol{x} + \int_{\partial \mathcal{B}_F} \boldsymbol{\sigma}(\boldsymbol{u}_G) \cdot \boldsymbol{n}_{\partial \mathcal{B}_F} \cdot \delta \boldsymbol{u}_G \,\mathrm{d}a, \tag{4.17}$$

where $\boldsymbol{n}_{\partial \mathcal{B}_F}$ is the unit outward normal vector to $\partial \mathcal{B}_F$. The first term in the right-hand side of in (4.17) can be canceled by using the divergence-free assumption for the stress (no body forces in $\mathcal{B}_F$). Following a detailed argument in GERASIMOV ET AL. [48], the second term can be further simplified

$$\int_{\partial \mathcal{B}_F} \boldsymbol{\sigma}(\boldsymbol{u}_G) \cdot \boldsymbol{n}_{\partial \mathcal{B}_F} \cdot \delta \boldsymbol{u}_G \,\mathrm{d}a = \int_{\Gamma_G} \boldsymbol{\sigma}(\boldsymbol{u}_G) \cdot \boldsymbol{n}_\Gamma \cdot \delta \boldsymbol{u}_G \,\mathrm{d}a + \int_{\partial \mathcal{B}_F \cap \Gamma_{N,G}} \bar{\boldsymbol{\tau}} \cdot \delta \boldsymbol{u}_G \,\mathrm{d}a.$$

Here, $\boldsymbol{n}_\Gamma := \boldsymbol{n}_{\partial \mathcal{B}_F}$ denotes the normal vector on Γ_G, outward of $\mathcal{B}_F$, as illustrated in Fig. 4.3. Furthermore, it is possible to choose $\mathcal{B}_L$ and its coarse representation into the global level as $\mathcal{B}_F$ such that $\partial \mathcal{B}_F \cap \Gamma_{N,G} = \emptyset$. This is in line with the assumption introduced in Section 4.1 that the local domain $\mathcal{B}_L$ and additionally $\mathcal{B}_F$ is free from any applied external load. Thus, the last surface integral cancels and (4.17) can be restated as,

$$\int_{\mathcal{B}_F} \boldsymbol{\sigma}(\boldsymbol{u}_G) : \boldsymbol{\varepsilon}(\delta \boldsymbol{u}_G) \,\mathrm{d}\boldsymbol{x} = \int_{\Gamma_G} \boldsymbol{\sigma}(\boldsymbol{u}_G) \cdot \boldsymbol{n}_\Gamma \cdot \delta \boldsymbol{u}_G \,\mathrm{d}a, \tag{4.18}$$

such that there exists a fictitious Lagrange multiplier $\boldsymbol{\lambda}_F \in \mathbf{L}^2(\Gamma)$ with

$$\int_{\Gamma_G} \boldsymbol{\sigma}(\boldsymbol{u}_G) \cdot \boldsymbol{n}_\Gamma \cdot \delta \boldsymbol{u}_G \,\mathrm{d}a =: \int_{\Gamma_G} \boldsymbol{\lambda}_F \cdot \delta \boldsymbol{u}_G \,\mathrm{d}a. \tag{4.19}$$

Here, $\boldsymbol{\lambda}_F$ is a traction-like quantity on Γ_G. Due to (4.18)–(4.19), the *partitioned* representation of equation (G) takes the following form

$$\int_{\mathcal{B}_G} \boldsymbol{\sigma}(\boldsymbol{u}_G) : \boldsymbol{\varepsilon}(\delta \boldsymbol{u}_G) \,\mathrm{d}\boldsymbol{x} - \int_{\Gamma_G} \boldsymbol{\lambda}_F \cdot \delta \boldsymbol{u}_G \,\mathrm{d}a - \int_{\Gamma_G} \boldsymbol{\lambda}_C \cdot \delta \boldsymbol{u}_G \,\mathrm{d}a - \int_{\Gamma_{N,G}} \bar{\boldsymbol{\tau}} \cdot \delta \boldsymbol{u}_G \,\mathrm{d}a = 0, \tag{G$_1$}$$

with $\boldsymbol{\lambda}_F$ satisfying

$$\int_{\Gamma_G} \boldsymbol{\lambda}_F \cdot \delta \boldsymbol{u}_G \,\mathrm{d}a = \int_{\mathcal{B}_F} \boldsymbol{\sigma}(\boldsymbol{u}_G) : \boldsymbol{\varepsilon}(\delta \boldsymbol{u}_G) \,\mathrm{d}\boldsymbol{x}. \tag{G$_2$}$$

Equations (G$_1$), (G$_2$) refer to the global system of equations. The system of equations (L) is called a local variational equation and additionally (C$_1$), (C$_2$), (C$_3$) refer to the coupling terms. The entire system is the basis for the *Global-Local approach.*

4.4. $g/l-1$: Dirichlet-Neumann-type boundary conditions

To accommodate a Global-Local computational scheme, instead of finding the stationary solution of the (G_1), (G_2), (L) along with (C_1), (C_2), (C_3) in the monolithic sense, an alternate minimization scheme is used. This is in line with [48], which leads to the Global-Local formulation through the concept of non-intrusive coupling. Here, the global and local levels are solved in a multiplicative manner according to the idea of Schwarz alternating method [103]. We refer to this type of Global-Local formulation by $g/l-1$ method.

4.4.1. Non-intrusive computational scheme

Let $k \geq 0$ be the iteration index. For designing at a fixed loading step n the iterative solution procedure for the Global-Local system defined by (G_1), (G_2), (L), and (C_1), (C_2), (C_3), the following prerequisites are taken into account:

(a) Since the data $(\bar{\boldsymbol{u}}_n, \bar{\boldsymbol{\tau}}_n)$ are posed on $\partial_D\mathcal{B}, \Gamma_N \subset \partial\mathcal{B}_G$, the process initialization (i.e., iteration $k=0$) is started with the solution of global problem (G_1), (G_2).

(b) In order to fit equation (G_1) with $\boldsymbol{\lambda}_F = \boldsymbol{\lambda}_F(\boldsymbol{u}_G)$ in the concept of non-intrusiveness, $\boldsymbol{\lambda}_F$ must be treated as a known quantity. This defines the order in which equations (G_1) and (G_2) are solved at any iteration $k \geq 0$: the solution of (G_2) precedes the solution of (G_1). In this case, as desired, the stiffness matrix $\mathbf{K}_G$ remains unaltered; the access to $\mathbf{K}_F$ is still required, but only at the stage of solving (G_2), not (G_1).

(c) For solving (G_1), $\boldsymbol{\lambda}_C$ must be also known. At $k=0$, $\boldsymbol{\lambda}_C$ can simply be taken from the previous loading step. At $k \geq 1$, we use the coupling equation (C_1) for the extraction of $\boldsymbol{\lambda}_C$, assuming $\boldsymbol{\lambda}_L$ is already known. This defines the order in which the global and local problems are solved: at any iteration starting from $k=1$, the solution of (L) precedes the solution of (G_1).

We also notice that:

(d) Coupling equation (C_3) provides the boundary condition for $\boldsymbol{u}_L$ of the local problem (L).

(e) Coupling equation (C_2) is used for the recovery of $\boldsymbol{u}_\Gamma$.

Following (c) and (e), elimination of $\boldsymbol{\lambda}_C$ and $\boldsymbol{u}_\Gamma$ from the set of unknowns to be originally solved for is achieved. These two quantities, as well as $\boldsymbol{\lambda}_F$, are the recovered ones.

The summary of the solution operations to be performed at any iteration k of the Global-Local formulation is as follows:

- Dirichlet local problem: solution of local problem (L) coupled with (C_3),
- Pre-processing global level: recovery phase using (C_1) and (G_2),
- Neumann global problem: solution of global problem (G_1),
- Post-processing global level: recovery phase using (C_2).

The detailed Global-Local formulation using Dirichlet-Neumann-type boundary conditions $g/l-1$ is depicted in Algorithm 2, including the iteration $k=0$. Accordingly, Fig. 4.4a depicts one iteration of the Global-Local approach using the Dirichlet-Neumann-type boundary conditions.

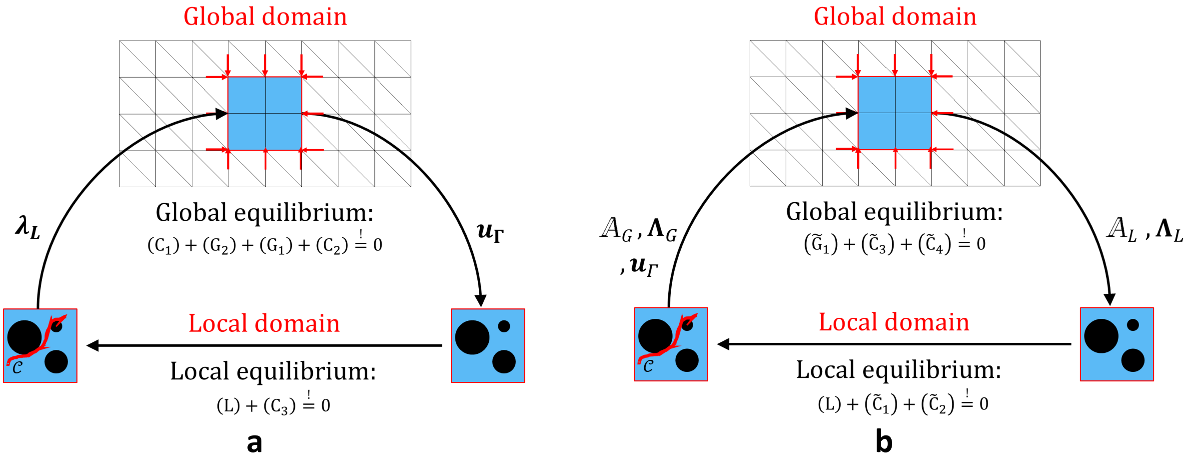

Figure 4.4: Global-Local scheme at small deformation. (a) Dirichlet-Neumann-type boundary conditions $g/l-1$, and (b) Robin-type boundary conditions $g/l-2$.

Algorithm 2 *Global-Local iterative scheme combined with Dirichlet-Neumann-type boundary conditions, namely* $g/l-1$.

```
Input: loading data $(\bar{\boldsymbol{u}}_n, \bar{\boldsymbol{\tau}}_n)$ on $\partial_D\mathcal{B}$ and $\Gamma_N$, respectively;
       solution $(\bar{\boldsymbol{u}}_{G,n-1}, \bar{\boldsymbol{u}}_{L,n-1}, s_{L,n-1}, \bar{\boldsymbol{u}}_{\Gamma,n-1}, \boldsymbol{\lambda}_{C,n-1}, \boldsymbol{\lambda}_{L,n-1})$ and $\mathcal{H}_{L,n-1}$ from step $n-1$.

    Initialization, $k=0$:
      • given $\boldsymbol{\lambda}_{C,n-1}$, set $\boldsymbol{\lambda}_{C,n-1} =: \boldsymbol{\lambda}_C^0$,
      • given $\boldsymbol{u}_{G,n-1}$, solve
            $\int_{\Gamma_{G0}} \boldsymbol{\lambda}_F \cdot \delta\boldsymbol{u}_G \,\mathrm{da} = \int_{\mathcal{B}_{F0}} \boldsymbol{\sigma}(\boldsymbol{u}_{G,n-1}) : \boldsymbol{\varepsilon}(\delta\boldsymbol{u}_G)\,\mathrm{d}\boldsymbol{x}$,
        for $\boldsymbol{\lambda}_F$, set $\boldsymbol{\lambda}_F =: \boldsymbol{\lambda}_F^0$,
      • given $\boldsymbol{\lambda}_F^0$ and $\boldsymbol{\lambda}_C^0$, solve
            $\int_{\mathcal{B}_{G0}} \boldsymbol{\sigma}(\boldsymbol{u}_G) : \boldsymbol{\varepsilon}(\delta\boldsymbol{u}_G)\,\mathrm{d}\boldsymbol{x} - \int_{\Gamma_{G0}} \boldsymbol{\lambda}_F^0 \cdot \delta\boldsymbol{u}_G \,\mathrm{da} - \int_{\Gamma_{G0}} \boldsymbol{\lambda}_C^0 \cdot \delta\boldsymbol{u}_G \,\mathrm{da} - \int_{\Gamma_{N,G0}} \bar{\boldsymbol{\tau}} \cdot \delta\boldsymbol{u}_G \,\mathrm{da} = 0$,
        for $\boldsymbol{u}_G$, set $\boldsymbol{u}_G =: \boldsymbol{u}_G^0$,
      • given $\boldsymbol{u}_G^0$, solve
            $\int_{\Gamma} (\boldsymbol{u}_\Gamma - \boldsymbol{u}_G^0) \cdot \delta\boldsymbol{\lambda}_C \,\mathrm{da} = 0$
        for $\boldsymbol{u}_\Gamma$, set $\boldsymbol{u}_\Gamma =: \boldsymbol{u}_\Gamma^0$.

Global-Local iteration $k \geq 1$:
    Local boundary value problem:
        • given $\boldsymbol{u}_\Gamma^{k-1}, \mathcal{H}_{L,n-1}$, solve
              phase-field part:
              $(1-\kappa)\int_{\mathcal{B}_L} 2s_{L+}\mathcal{H}(\boldsymbol{\varepsilon}(\boldsymbol{u}_L)).\delta s_L \mathrm{d}\boldsymbol{x} + \int_{\mathcal{B}_L} (s_L - 1).\delta s_L \mathrm{d}\boldsymbol{x}$
                $+ \int_{\mathcal{B}_L} l^2 \nabla s_L.\nabla(\delta s_L)\mathrm{d}\boldsymbol{x} = 0$,
              mechanical part:
              $\begin{cases} \int_{\mathcal{B}_{L0}} \boldsymbol{\sigma}(\boldsymbol{u}_L, s_L) : \boldsymbol{\varepsilon}(\delta\boldsymbol{u}_L)\,\mathrm{d}\boldsymbol{x} - \int_{\Gamma_L} \boldsymbol{\lambda}_L \cdot \delta\boldsymbol{u}_L \,\mathrm{da} = 0, \\ \int_{\Gamma} (\boldsymbol{u}_\Gamma^{k-1} - \boldsymbol{u}_L) \cdot \delta\boldsymbol{\lambda}_L \,\mathrm{da} = 0, \end{cases}$
          set $(\boldsymbol{u}_L, s_L, \boldsymbol{\lambda}_L) =: (\boldsymbol{u}_L^k, s_L^k, \boldsymbol{\lambda}_L^k)$,
    Global boundary value problem:
      • given $\boldsymbol{\lambda}_L^k$, solve
            $\int_{\Gamma} (\boldsymbol{\lambda}_C + \boldsymbol{\lambda}_L^k) \cdot \delta\boldsymbol{u}_\Gamma \,\mathrm{da} = 0$
        for $\boldsymbol{\lambda}_C$, set $\boldsymbol{\lambda}_C =: \boldsymbol{\lambda}_C^k$,
      • given $\boldsymbol{u}_G^{k-1}$, solve
            $\int_{\Gamma_{G0}} \boldsymbol{\lambda}_F \cdot \delta\boldsymbol{u}_G \,\mathrm{da} = \int_{\mathcal{B}_{F0}} \boldsymbol{\sigma}\big(\boldsymbol{u}_G^{k-1}\big) : \boldsymbol{\varepsilon}(\delta\boldsymbol{u}_G)\,\mathrm{d}\boldsymbol{x}$,
        for $\boldsymbol{\lambda}_F$, set $\boldsymbol{\lambda}_F =: \boldsymbol{\lambda}_F^k$,
      • given $\boldsymbol{\lambda}_F^k$ and $\boldsymbol{\lambda}_C^k$, solve
            $\int_{\mathcal{B}_{G0}} \boldsymbol{\sigma}(\boldsymbol{u}_G) : \boldsymbol{\varepsilon}(\delta\boldsymbol{u}_G)\,\mathrm{d}\boldsymbol{x} - \int_{\Gamma_{G0}} \boldsymbol{\lambda}_F^k \cdot \delta\boldsymbol{u}_G \,\mathrm{da} - \int_{\Gamma_{G0}} \boldsymbol{\lambda}_C^k \cdot \delta\boldsymbol{u}_G \,\mathrm{da} - \int_{\Gamma_{N,G0}} \bar{\boldsymbol{\tau}} \cdot \delta\boldsymbol{u}_G \,\mathrm{da} = 0$,
        for $\boldsymbol{u}_G$, set $\boldsymbol{u}_G =: \boldsymbol{u}_G^k$,
      • given $\boldsymbol{u}_G^k$, solve
            $\int_{\Gamma} (\boldsymbol{u}_\Gamma - \boldsymbol{u}_G^k) \cdot \delta\boldsymbol{\lambda}_C \,\mathrm{da} = 0$
        for $\boldsymbol{u}_\Gamma$, set $\boldsymbol{u}_\Gamma =: \boldsymbol{u}_\Gamma^k$.

      • Accuracy/convergence check: $\eta^k \leq \widetilde{\mathtt{TOL}}_{\mathrm{GL}}$,
      • if fulfilled, set $(\boldsymbol{u}_G^k, \boldsymbol{u}_L^k, s_L^k, \boldsymbol{u}_\Gamma^k, \boldsymbol{\lambda}_C^k, \boldsymbol{\lambda}_L^k) =: (\boldsymbol{u}_{G,n}, \boldsymbol{u}_{L,n}, s_{L,n}, \boldsymbol{u}_{\Gamma,n}, \boldsymbol{\lambda}_{C,n}, \boldsymbol{\lambda}_{L,n})$ and stop;
        else $k+1 \to k$.

Output: solution $(\boldsymbol{u}_{G,n}, \boldsymbol{u}_{L,n}, s_{L,n}, \boldsymbol{u}_{\Gamma,n}, \boldsymbol{\lambda}_{C,n}, \boldsymbol{\lambda}_{L,n})$.
```

4.5. Accuracy/convergence performance of the $g/l-1$

Derivation of the convergence and stopping criteria for the Global-Local iterative solution process in Table 2 is rather straightforward. Despite of its strong non-intrusive implementation point of view [45], there are two shortcomings embedded in the system which have to be resolved. (a) Due to the extreme difference in stiffness between the local domain and its projection to the global level, i.e., fictitious domain, the relaxation/acceleration techniques has to be used, see [48]. (b) Additionally, it turns out that if the solution vector $(\boldsymbol{u}_G^k, \boldsymbol{u}_L^k, s_L^k, \boldsymbol{u}_\Gamma^k, \boldsymbol{\lambda}_C^k, \boldsymbol{\lambda}_L^k)$ is plugged into equations (G$_1$), (G$_2$), (L), (C$_1$), (C$_2$), (C$_3$), the imbalanced quantities follow

$$\int_\Gamma (\boldsymbol{u}_\Gamma^k - \boldsymbol{u}_L^k) \cdot \delta\boldsymbol{\lambda}_L \,\mathrm{d}a \neq 0 \quad \texttt{and} \quad \int_\Gamma \boldsymbol{\lambda}_F^k \cdot \delta\boldsymbol{u}_G \,\mathrm{d}a \neq \int_{\mathcal{B}_F} \boldsymbol{\sigma}(\boldsymbol{u}_G^k) : \boldsymbol{\varepsilon}(\delta\boldsymbol{u}_G)\,\mathrm{d}\boldsymbol{x}, \tag{4.20}$$

resulting in the *iterative* Global-Local computation scheme. Figure 4.4a depicts one iteration of the Global-Local approach using the Dirichlet-Neumann-type boundary conditions. The aforementioned difficulties motivate us to provide an alternative coupling conditions that overcome these challenges, which are explained in the following section. Therefore, the solution accuracy at k is measured by the quantity

$$\mathrm{Res}_{\mathrm{GL}}^k := \mathrm{Res}_{\mathrm{Stag}}^{'\mathrm{last}\ k'} + \left| \int_\Gamma (\boldsymbol{u}_\Gamma^k - \boldsymbol{u}_L^k) \cdot \delta\boldsymbol{\lambda}_L \,\mathrm{d}a \right| + \left| \int_\Gamma (\boldsymbol{\lambda}_F^k - \boldsymbol{\lambda}_F^{k+1}) \cdot \delta\boldsymbol{u}_G \,\mathrm{d}a \right|, \quad \forall\, (\delta\boldsymbol{\lambda}_L, \delta\boldsymbol{u}_G), \tag{4.21}$$

where $\mathrm{Res}_{\mathrm{Stag}}$ is the staggered residual of the local problem with 'last k' denoting the index of the converged staggered solution (see Table 1 for a detail), and $\boldsymbol{\lambda}_F^{k+1}$ is recovered (post-processed) from the right-hand side of (4.20)2. The stopping criterion for the Global-Local loop can then be defined as

$$\mathrm{Res}_{\mathrm{GL}}^k \leq \texttt{TOL}_{\mathrm{GL}}, \tag{4.22}$$

with $\texttt{TOL}_{\mathrm{GL}}$ to be prescribed. Owing to the 'nested in' nature of the staggered process, it has to be $\texttt{TOL}_{\mathrm{Stag}} < \texttt{TOL}_{\mathrm{GL}}$.

In our computations (see Table 2), we use a more convenient form of the stopping criterion. Setting

$$\eta_{\boldsymbol{u}}^k := \left\| \boldsymbol{u}_\Gamma^k - \boldsymbol{u}_L^k \right\|_{\mathbf{L}^2(\Gamma)}, \quad \eta_{\boldsymbol{\lambda}}^k := \left\| \boldsymbol{\lambda}_F^k - \boldsymbol{\lambda}_F^{k+1} \right\|_{\mathbf{L}^2(\Gamma)}, \tag{4.23}$$

we define $\eta^k := \sqrt{(\eta_{\boldsymbol{u}}^k)^2 + (\eta_{\boldsymbol{\lambda}}^k)^2}$, and use this quantity to now check

$$\eta^k \leq \widetilde{\texttt{TOL}}_{\mathrm{GL}} := 10^{-6}. \tag{4.24}$$

This choice of $\widetilde{\texttt{TOL}}_{\mathrm{GL}}$ fulfills the requirement $\eta^k \overset{!}{<} \texttt{TOL}_{\mathrm{GL}} - \texttt{TOL}_{\mathrm{Stag}}$, which is stipulated by (4.21), (4.22), and the already prescribed above magnitudes of $\texttt{TOL}_{\mathrm{GL}}$ and $\texttt{TOL}_{\mathrm{Stag}}$.

Since the quantity η naturally stem from the Global-Local solution accuracy check $\widetilde{\mathcal{E}}_{\boldsymbol{s}}(\boldsymbol{s}^k; \delta\boldsymbol{y}) = 0$, it represents not only the *iterative convergence* indicator, but also the *solution accuracy* indicator – a very desired property, since the former is only suitable for tracing the convergence of the corresponding iterative solution process, but, clearly, is not adequate for stopping criterion. The corresponding ingredients $\eta_{\boldsymbol{u}}$ and $\eta_{\boldsymbol{\lambda}}$ are only iterative convergence indicators, but none of them provides an adequate check of the solution accuracy. In particular, since $\eta_{\boldsymbol{u}}$ measures, though implicitly, the *displacement continuity* – a match between $\boldsymbol{u}_G$ and $\boldsymbol{u}_L$ across Γ (recall that the *traction continuity* – a match between $\boldsymbol{\lambda}_C$ and $\boldsymbol{\lambda}_L$ on Γ – is, in our case, fulfilled automatically), it is also the indicator of a good "gluing" between the two models.

4.6. $g/l - 1$ via incremental setting augmented with relaxation/ acceleration techniques

For later developments, it proves convenient to reformulate the global equation in incremental form. It is straightforward to see that for a given Global-Local iteration $k \geq 1$, this reads: given the triple $(\boldsymbol{u}_G^{k-1}, \boldsymbol{\lambda}_F^{k-1}, \boldsymbol{\lambda}_C^{k-1})$ known from the iteration $k-1$, as well as $(\boldsymbol{\lambda}_F^k, \boldsymbol{\lambda}_C^k)$ 'recovered' at the iteration k, we solve

$$\int_{\mathcal{B}_G} \boldsymbol{\sigma}(\Delta \boldsymbol{u}_G) : \boldsymbol{\varepsilon}(\delta \boldsymbol{u}_G)\, \mathrm{d}\boldsymbol{x} - \int_\Gamma (\boldsymbol{\lambda}_F^k - \boldsymbol{\lambda}_F^{k-1}) \cdot \delta \boldsymbol{u}_G\, \mathrm{d}a - \int_\Gamma (\boldsymbol{\lambda}_C^k - \boldsymbol{\lambda}_C^{k-1}) \cdot \delta \boldsymbol{u}_G\, \mathrm{d}a = 0, \quad (\mathrm{G}_{\mathrm{incr}})$$

for $\Delta \boldsymbol{u}_G =: (\Delta \boldsymbol{u}_G)^k$ and set

$$\boldsymbol{u}_G^k := \boldsymbol{u}_G^{k-1} + (\Delta \boldsymbol{u}_G)^k. \tag{4.25}$$

We term equation (4.25) a 'direct update' within the Global-Local iterative procedure. This is in contrast to the notion of a 'relaxed/accelerated update' to be considered in the following sections.

Following [36] and [79], we will consider and incorporate two types of relaxation/ acceleration techniques into our approach: Aitken's Δ^2-method (also known as dynamic relaxation, whose efficient implementation in fluid-structure interaction computations has already been reported [75, 37]) and Quasi-Newton correction. Within the family of Quasi-Newton correction formula, we restrict ourselves to the Symmetric Rank One (SR1) and the Broyden update versions. Technically, both types deal with the global solution update equation (4.25) and modify it specifically. Let us consider (4.25) written in terms of the nodal displacements

$$\hat{\boldsymbol{u}}_G^k := \hat{\boldsymbol{u}}_G^{k-1} + (\Delta \hat{\boldsymbol{u}}_G)^k \quad \text{s.t.} \quad (\Delta \hat{\boldsymbol{u}}_G)^k = \mathbf{K}_G^{-1} \mathbf{r}_{\boldsymbol{\Gamma}}^{\mathbf{k}}, \tag{4.26}$$

where, owing to $(\mathrm{G}_{\mathrm{incr}})$, one has

$$\mathbf{K}_G := \int_{\mathcal{B}} (\boldsymbol{B}_u^G)^{\mathsf{T}}\, \widetilde{\mathbb{C}}\, \boldsymbol{B}_u^G\, \mathrm{d}\boldsymbol{x},$$

with $\widetilde{\mathbb{C}}$ as a 3×3-matrix representation of $\mathbb{C}$, and

$$\mathbf{r}_\Gamma^k := \int_\Gamma (\boldsymbol{N}_u^G)^{\mathsf{T}}\, (\boldsymbol{\lambda}_F^k - \boldsymbol{\lambda}_F^{n-1})\, \mathrm{d}a + \int_\Gamma (\boldsymbol{N}_u^G)^{\mathsf{T}}\, (\boldsymbol{\lambda}_C^k - \boldsymbol{\lambda}_C^{n-1})\, \mathrm{d}a.$$

4.6.1. Necessity of using relaxation/acceleration techniques

This section evaluates the convergence performance of the Global-Local iterative formulation. Let us now investigate the numerical example depicted in Fig. 4.5, to evaluate the convergence performance of the Global-Local iterative scheme. The left edge of a reference problem as well as the global domain, is fixed along the $x-$ and $y-$directions, and uniform displacement ($u_x = 2\ mm$) is applied monotonically in one increment over the right edge. A quarter of the global scale is considered to be the fictitious domain, $\mathcal{B}_F$, for which re-localization needs to be performed. The local scale, $\mathcal{B}_L$, by refining and keeping the outer boundary of the $\mathcal{B}_F$, is designed by additionally including two soft inclusions. The elastic properties are set as $\lambda = 121.15$ kN/mm^2, and the shear modulus is $\mu = 80.77$ kN/mm^2 for both global and local levels.

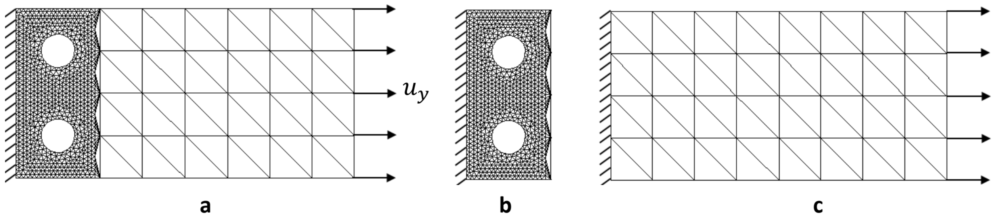

Figure 4.5: Geometric setup, and boundary conditions. (*a*) Reference problem, (*b*) local domain, and (*c*) global domain.

By $\chi = \frac{E_L}{E_G}$ we mean the mismatch ratio between the local and global Young's modulus. The efficiency of the Global-Local coupling scheme for three different values of χ is investigated. As soon as χ becomes greater than one, the local response will be stiffer than the global level. Figure 4.6a presents the Global-Local iteration procedure based on different values of χ (represented in a logarithmic base).

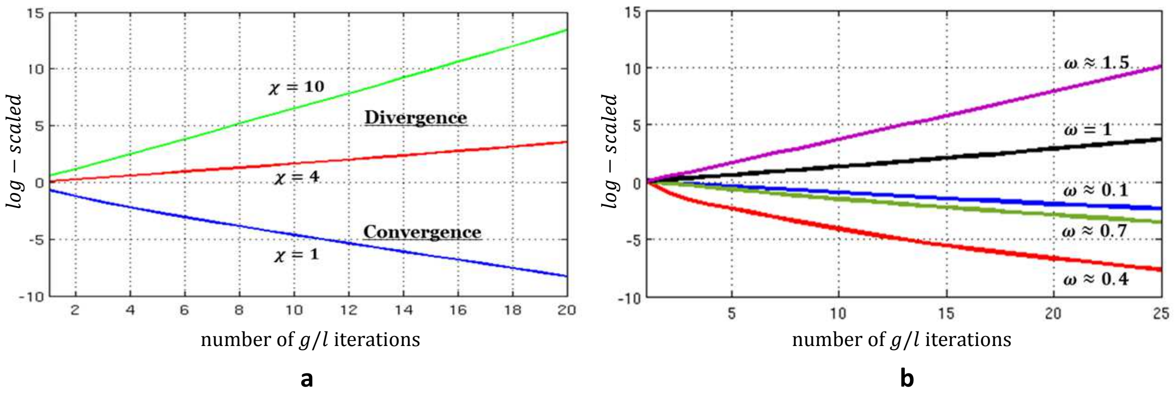

Figure 4.6: Iterative convergence performance of the Global-Local coupling approach. (*a*) Different $\chi = (1, 4, 10)$, and (*b*) at fixed $\chi = 4$ by imposing different ω.

Here, we only plot the error indicator η and not its ingredients for the iterative Global-Local formulation; see Section 4.5. We observe that the convergence performance of the Global-Local approach is affected by the stiffer response transferred from the local level. Hence, if the local response is stiffer than the global one (e.g., $\chi = 4$ or 10), then divergence behavior is observed.

To overcome this issue, one could use an explicit damping factor (i.e., a constant parameter ω) to modify the incremental solution used in (4.26) (i.e., $\omega\Delta\hat{\boldsymbol{u}}_G$). Now, let $\chi = 4$ to investigate the effect of the different damping factors (and possibly improve the convergence behavior). Figure 4.6b compares the impact of the explicit damping factor on the convergence performance during the Global-Local iterations.

It is clear that by imposing "an appropriate" damping factor, the stiff local response is relaxed, which for some values convergence is achieved (e.g., $\omega = 0.4$) while for some others divergence is obtained (e.g., $\omega = 1.5$). Thus, an appropriate damping factor cannot be a priori known; therefore, specific treatment needs to be considered to identify a suitable damping factor for relaxing the Global-Local iterations; see Section 4.6.4. To this end, we discuss in detail relaxation/acceleration techniques in the following sections.

4.6.2. Symmetric Rank One method

The quasi-Newton method is used at the global level to obtain a new approximation of the global tangent stiffness matrix in the recursive manner. The main ingredient of this method is to replace the tangential stiffness matrix with its secant approximation. More precisely, the quasi-Newton method modifies (4.26) at any iteration $k \geq 2$ by replacing the matrix $\mathbf{K}_G$ with $\widetilde{\mathbf{K}}^k = f(\widetilde{\mathbf{K}}^{k-1}, \mathbf{r}_\Gamma^k, (\Delta\hat{\boldsymbol{u}}_G)^{k-1})$ s.t. $\widetilde{\mathbf{K}}^1 = \mathbf{K}_G$, thus resulting in

$$\hat{\boldsymbol{u}}_G^k := \hat{\boldsymbol{u}}_G^{k-1} + (\widetilde{\mathbf{K}}^k)^{-1}\mathbf{r}_\Gamma^k \ . \tag{4.27}$$

Let us now consider symmetric rank one (SR1) update. The classical recursive update formulation for the SR1 method renders the following form:

$$\widetilde{\mathbf{K}}_{i+1}=\widetilde{\mathbf{K}}_i+\frac{\mathbf{r}_\Gamma^{i+1}(\mathbf{r}_\Gamma^{i+1})^T}{\Delta\hat{\boldsymbol{u}}_G^i(\mathbf{r}_\Gamma^{i+1})^T} \ . \tag{4.28}$$

Herein, the subscripted $0 \leq i < k$ designates the iteration number of the SR1 formulation that is recursively computed up to the current Global-Local iteration, k. Through SR1 formulation in (4.28) symmetric property of the tangent stiffness matrix still holds, which means that if $\widetilde{\mathbf{K}}_i$ is symmetric then $\widetilde{\mathbf{K}}_{i+1}$ is also symmetric [32].

We apply the Sherman-Morrison formula [119]; that is, $(\mathbf{A}+\Delta\mathbf{A})^{-1} = \mathbf{A}^{-1}+\mathbf{A}^{-1}\mathbf{B}(\mathbf{A}, \Delta\mathbf{A})\mathbf{A}^{-1}$ for any given square and invertible matrix $\mathbf{A}$ on (4.28). This results in the update formulation for the inverse of tangent stiffness matrix, which yields

$$\widetilde{\mathbf{K}}_{i+1}^{-1}=\widetilde{\mathbf{K}}_i^{-1} + \widetilde{\mathbf{K}}_i^{-1}\mathbf{B}(\widetilde{\mathbf{K}}_i, \Delta\widetilde{\mathbf{K}}_i)\widetilde{\mathbf{K}}_i^{-1} \ , \tag{4.29}$$

such that,

$$\mathbf{B}(\widetilde{\mathbf{K}}_i, \Delta\widetilde{\mathbf{K}}_i) = -\mathbf{r}_\Gamma^{i+1}\frac{(\mathbf{r}_\Gamma^{i+1})^T}{(\mathbf{r}_\Gamma^{i+1})^T(\Delta\hat{\mathbf{u}}_G^i+\widetilde{\mathbf{K}}_i^{-1}\mathbf{r}_\Gamma^{i+1})} \ . \tag{4.30}$$

Multiplying the left- and right- hand sides of (4.29) by the current residual vector (i.e., $\mathbf{r}_\Gamma^k$) results in

$$\widetilde{\mathbf{K}}_{i+1}^{-1}\mathbf{r}_\Gamma^k=\widetilde{\mathbf{K}}_i^{-1}\mathbf{r}_\Gamma^k-\widetilde{\mathbf{K}}_i^{-1}\mathbf{r}_\Gamma^{i+1}\frac{(\mathbf{r}_\Gamma^{i+1})^T(\widetilde{\mathbf{K}}_i^{-1}\mathbf{r}_\Gamma^k)}{(\mathbf{r}_\Gamma^{i+1})^T(\Delta\hat{\mathbf{u}}_G^i+\widetilde{\mathbf{K}}_i^{-1}\mathbf{r}_\Gamma^{i+1})} \ . \tag{4.31}$$

In the last iteration (i.e., $i = k - 1$), the modified SR1 recursive formulation (4.29) resembles $\Delta\hat{\mathbf{u}}_G^k = \widetilde{\mathbf{K}}_k^{-1}\mathbf{r}_\Gamma^k$, which turns out to be the current global incremental solution.

For the implementation standpoint, we reformulate (4.31) in a compact form. Let us define $\mathbf{w}_{i+1} = \widetilde{\mathbf{K}}_{i+1}^{-1}\mathbf{r}_\Gamma^k$, and $\mathbf{v}_{i+1} = \widetilde{\mathbf{K}}_i^{-1}\mathbf{r}_\Gamma^{i+1}$, for which the following re-formulation of

(4.31) is achieved:

$$\mathbf{w}_{i+1} = \mathbf{w}_i + \Delta\mathbf{w}_i \ \text{ s.t. } \ \Delta\mathbf{w}_i = -\mathbf{v}_{i+1}\frac{(\mathbf{r}_\Gamma^{i+1})^T\mathbf{w}_i}{(\mathbf{r}_\Gamma^{i+1})^T\big(\Delta\hat{\mathbf{u}}_G^i + \mathbf{v}_{i+1}\big)} \ . \tag{4.32}$$

Here, the recursive formulation is initialized through a given initial global solution, namely $\mathbf{w}_0 = \mathbf{u}_G^0$. Furthermore, for the next Global-Local iteration, three vectors $\mathbf{v}_k = \mathbf{w}_{k-1}$, $\mathbf{r}_\Gamma^k$ and $\Delta\hat{\mathbf{u}}_G^k$ have to be retained. The corrected incremental global solution is obtained by the last recursive step (i.e., $\mathbf{w}_k =: \Delta\hat{\mathbf{u}}_G^k$).

Remark 4.6.1. *The SR1 algorithm is in convergence state if the updated term of* $\widetilde{\mathbf{K}}_{i+1}$ *(second term of the right-hand side) in (4.28) is well-defined [32]. Moreover, the denominator of the update term within (4.28) should not to be so small. Therefore, the update SR1 formulation given in (4.29) is used only if the following criterion is satisfied:*

$$\left\|\Delta\hat{\mathbf{u}}_G^i(\mathbf{r}_\Gamma^{i+1})^T\right\|_2 > c_1 \left\|\Delta\hat{\mathbf{u}}_G^i\right\|_2 \left\|\mathbf{r}_\Gamma^{i+1}\right\|_2 .$$

Herein, $c_1 \epsilon (0,1)$ *is a constant variable that is usually taken to be square root of our floating-point computational environment,* $\sqrt{10^{-16}}$ *[32]. If this criterion does not hold, then the SR1 update formulation is not applied (i.e.,* $\mathbf{w}_{i+1} = \mathbf{w}_i$*).*

4.6.3. Broyden's method

One of the drawbacks of the SR1 method in the context of the Global-Local coupling approach is storing three vectors at each Global-Local iteration. Additionally, the denominator of the SR1 update formulation can be very small quantity. Therefore, an alternative quasi-Newton method is also considered. Broyden's method, as one of the standard quasi-Newton methods, can be used to accelerate the convergence rate of the Global-Local iterations. Analogous to the SR1 method, Broyden's method is used at the global level for determining stable and efficient updates of the tangent stiffness matrix, but with less computational cost compared to SR1. The recursive update formulation for Broyden's method through basic algebraic manipulation yields the following form:

$$\widetilde{\mathbf{K}}_{i+1} = \widetilde{\mathbf{K}}_i + \frac{\mathbf{r}_\Gamma^{i+1}(\Delta\hat{\mathbf{u}}_G^i)^T}{(\Delta\hat{\mathbf{u}}_G^i)^T\Delta\hat{\mathbf{u}}_G^i} \ . \tag{4.33}$$

It can be observed that the update term of $\widetilde{\mathbf{K}}_{i+1}$ in the SR1 method, namely the second term of the right side of (4.28), is more influenced by the global residual vector, namely $\mathbf{r}_\Gamma^i$, whereas the update term of $\widetilde{\mathbf{K}}_{i+1}$ in Broyden's method in (4.33) is more sensitive to the global incremental displacement solution, namely $\Delta\hat{\mathbf{u}}_G^i$. Applying Sherman-Morrison [119] to (4.33) (in a similar manner to the SR1 method) and then multiplying left- and right-hand sides of equality by the current residual vector (i.e., $\mathbf{r}_\Gamma^k$) results in the following equation:

$$\widetilde{\mathbf{K}}_{i+1}^{-1}\mathbf{r}_\Gamma^k = \widetilde{\mathbf{K}}_i^{-1}\mathbf{r}_\Gamma^k - \widetilde{\mathbf{K}}_i^{-1}\mathbf{r}_\Gamma^{i+1}\frac{(\Delta\hat{\mathbf{u}}_G^i)^T(\widetilde{\mathbf{K}}_i^{-1}\mathbf{r}_\Gamma^k)}{(\Delta\hat{\mathbf{u}}_G^i)^T(\Delta\hat{\mathbf{u}}_G^i + \widetilde{\mathbf{K}}_i^{-1}\mathbf{r}_\Gamma^{i+1})} \ . \tag{4.34}$$

In contrast to the SR1 method, a significant feature of Broyden's update formulation in (4.34), is its capability to approximate $\widetilde{\mathbf{K}}_{i+1}^{-1}\mathbf{r}_\Gamma^k$ with the knowledge of two quantities, namely $\Delta\hat{\mathbf{u}}_G^i$ and $\widetilde{\mathbf{K}}_i^{-1}\mathbf{r}_\Gamma^{i+1}$, through previous Global-Local iterations and not necessarily $\mathbf{r}_\Gamma^{i+1}$.

For the implementation standpoint, we need to reformulate (4.34) in a compact form. Let us define $\mathbf{w}_{i+1} = \widetilde{\mathbf{K}}_{i+1}^{-1}\mathbf{r}_\Gamma^k$, $\mathbf{v}_{i+1} = \widetilde{\mathbf{K}}_i^{-1}\mathbf{r}_\Gamma^{i+1}$, for which, in turn, the following reformulation of (4.29) is achieved:

$$\mathbf{w}_{i+1} = \mathbf{w}_i + \Delta\mathbf{w}_i \quad \text{s.t.} \quad \Delta\mathbf{w}_i = -\mathbf{v}_{i+1}\frac{(\Delta\hat{\mathbf{u}}_G^i)^T\mathbf{w}_i}{(\Delta\hat{\mathbf{u}}_G^i)^T(\Delta\hat{\mathbf{u}}_G^i+\mathbf{v}_{i+1})}\ . \tag{4.35}$$

Similar to the SR1 method, the recursive formulation is initialized through the given initial global solution, namely $\mathbf{w}_0 = \mathbf{u}_G^0$. Moreover, for the next Global-Local iteration, the two vectors $\mathbf{v}_k = \mathbf{w}_{k-1}$ and $\Delta\hat{\mathbf{u}}_G^k$ have to be retained. The corrected incremental global solution is obtained by the last recursive step; that is $\mathbf{w}_k =: \Delta\hat{\mathbf{u}}_G^k$.

4.6.4. Aitken's Δ^2 method

Aitken's Δ^2 method [75, 100] is used to relax the interface displacement quantity by imposing a damping factor on the global incremental solution. This method modifies (4.26) at any iteration of $k \geq 2$ introducing the damping factor $\omega_{k-1} = f\big(\omega_{k-2}, (\Delta\hat{\boldsymbol{u}}_G)^{k-1}, (\Delta\hat{\boldsymbol{u}}_G)^k\big)$ s.t. $\omega_0 = 1$ as follows:

$$\hat{\boldsymbol{u}}_G^k := \hat{\boldsymbol{u}}_G^{k-1} + \omega_{k-1}(\Delta\hat{\boldsymbol{u}}_G)^k, \tag{4.36}$$

Considering a well-chosen damping factor, stability is enforced on the computational scheme which enhances the convergence speed of the Global-Local approach [48]. Within Aitken's Δ^2 method, a damping factor has the following explicit form:

$$\omega_{k-1} := \omega_{k-2}\frac{((\Delta\hat{\boldsymbol{u}}_G)^{k-1})^{\mathsf{T}}\left((\Delta\hat{\boldsymbol{u}}_G)^{k-1} - (\Delta\hat{\boldsymbol{u}}_G)^k\right)}{|(\Delta\hat{\boldsymbol{u}}_G)^{k-1} - (\Delta\hat{\boldsymbol{u}}_G)^k|^2}, \quad k \geq 2, \tag{4.37}$$

with $\omega_0 = 1$. It is clear that in (4.37), two previous global information, namely $\hat{\mathbf{u}}_G^k$ and $\hat{\mathbf{u}}_G^{k-1}$, are retained to establish ω and hence modify the current global solution.

Remark 4.6.2. *It is known that by means of Aitken's Δ^2 method for scalar sequence, the converged solution is achieved if $\omega \in (0,2)$ [37]. In particular, the stabilization of the iterative solution method is achieved while $\omega < 1$, and $\omega > 1$ implies that the acceleration of the iterative process is achieved. But, for the vector sequence this kind of argument is not guaranteed.*

4.7. $g/l-2$: Robin-type boundary conditions

In this section, the Global-Local formulation is enhanced using Robin-type boundary conditions to relax the stiff local response observed at the global level (due to the local non-linearities). Furthermore, the computational time is reduced. This improves the resolution of the imbalanced quantities in (4.20) and accelerates the Global-Local computational scheme. We refer to this type of Global-Local formulation as the $g/l-2$ method.

Recall the coupling equations given in (C_1), (C_2), and (C_3) which arise from the stationary of the interface energy functional. In fact, these couping equations provide the boundary conditions which have to be imposed at the global and local levels. We now introduce the Robin-type boundary conditions (as a linear combination of the coupling equations) for both local and global levels.

- ***Robin-type boundary conditions at the local level***

At the local level, the new coupling term is introduced as a linear combination of (C_1) and (C_2), through

$$\widetilde{\mathcal{E}}_{\boldsymbol{u}_\Gamma}(\boldsymbol{s};\delta\boldsymbol{u}_\Gamma)+\mathbb{A}_L\widetilde{\mathcal{E}}_{\boldsymbol{\lambda}_C}(\boldsymbol{s};\delta\boldsymbol{\lambda}_C)=\int_\Gamma(\boldsymbol{\lambda}_C+\boldsymbol{\lambda}_L)\cdot\delta\boldsymbol{u}_\Gamma\,\mathrm{d}a+\mathbb{A}_L\int_\Gamma(\boldsymbol{u}_\Gamma-\boldsymbol{u}_G)\cdot\delta\boldsymbol{\lambda}_C\,\mathrm{d}a=0. \tag{4.38}$$

We write this for the iteration k, as follows:

$$\int_\Gamma(\boldsymbol{\lambda}_C^{k-1}+\boldsymbol{\lambda}_L^{k})\cdot\delta\boldsymbol{u}_\Gamma\,\mathrm{d}a+\mathbb{A}_L\int_\Gamma(\boldsymbol{u}_\Gamma^{k,\frac{1}{2}}-\boldsymbol{u}_G^{k-1})\cdot\delta\boldsymbol{\lambda}_C\,\mathrm{d}a=0. \tag{4.39}$$

Herein, $\mathbb{A}_L$ is a local augmented stiffness matrix applied at the interface, which serves to regularize the local Jacobian matrix. By means of (4.39) at iteration k, the local system of equations results in the following boundary conditions

$$\int_\Gamma\boldsymbol{\lambda}_L^{k}\cdot\delta\boldsymbol{u}_\Gamma\,\mathrm{d}a+\mathbb{A}_L\int_\Gamma\boldsymbol{u}_\Gamma^{k,\frac{1}{2}}\cdot\delta\boldsymbol{\lambda}_C\,\mathrm{d}a=\boldsymbol{\Lambda}_L^{k-1}, \tag{$\widetilde{\mathrm{C}}_1$}$$

$$\int_\Gamma(\boldsymbol{u}_\Gamma^{k,\frac{1}{2}}-\boldsymbol{u}_L^{k})\cdot\delta\boldsymbol{\lambda}_L\,\mathrm{d}a=0, \tag{$\widetilde{\mathrm{C}}_2$}$$

with a known right-hand side, through

$$\boldsymbol{\Lambda}_L^{k-1}:=\boldsymbol{\Lambda}_L(\boldsymbol{\lambda}_C^{k-1},\boldsymbol{u}_G^{k-1};\mathbb{A}_L)=\mathbb{A}_L\int_\Gamma\boldsymbol{u}_G^{k-1}\cdot\delta\boldsymbol{\lambda}_C\,\mathrm{d}a-\int_\Gamma\boldsymbol{\lambda}_C^{k-1}\cdot\delta\boldsymbol{u}_\Gamma\,\mathrm{d}a. \tag{4.40}$$

Along with (L), the local system of equations has to be solved for $(\boldsymbol{u}_L^k,\boldsymbol{\lambda}_L^k,\boldsymbol{u}_\Gamma^{k,\frac{1}{2}})$ for the given local Robin-type parameters $(\boldsymbol{\Lambda}_L^{k-1},\mathbb{A}_L)$.

- ***Robin-type boundary conditions at the global level***

Accordingly, at the global level, the new coupling term is stated as a linear combination of (C_1) and (C_3), which reads:

$$\widetilde{\mathcal{E}}_{\boldsymbol{u}_\Gamma}(\boldsymbol{s};\delta\boldsymbol{u}_\Gamma)+\mathbb{A}_G\widetilde{\mathcal{E}}_{\boldsymbol{\lambda}_L}(\boldsymbol{s};\delta\boldsymbol{\lambda}_L)=\int_\Gamma(\boldsymbol{\lambda}_C+\boldsymbol{\lambda}_L)\cdot\delta\boldsymbol{u}_\Gamma\,\mathrm{d}a+\mathbb{A}_G\int_\Gamma(\boldsymbol{u}_\Gamma-\boldsymbol{u}_L)\cdot\delta\boldsymbol{\lambda}_L\,\mathrm{d}a=0. \tag{4.41}$$

We write this for the iteration k through

$$\int_\Gamma(\boldsymbol{\lambda}_C^{k}+\boldsymbol{\lambda}_L^{k})\cdot\delta\boldsymbol{u}_\Gamma\,\mathrm{d}a+\mathbb{A}_G\int_\Gamma(\boldsymbol{u}_\Gamma^{k}-\boldsymbol{u}_L^{k})\cdot\delta\boldsymbol{\lambda}_L\,\mathrm{d}a=0,$$

where $\mathbb{A}_G$ is a global augmented stiffness matrix applied to the interface.

Through (4.41) at iteration k, the Robin-type boundary condition at the global level follows

$$\int_\Gamma\boldsymbol{\lambda}_C^{k}\cdot\delta\boldsymbol{u}_\Gamma\,\mathrm{d}a+\mathbb{A}_G\int_\Gamma\boldsymbol{u}_\Gamma^{k}\cdot\delta\boldsymbol{\lambda}_L\,\mathrm{d}a=\boldsymbol{\Lambda}_G^{k}, \tag{$\widetilde{\mathrm{C}}_3$}$$

$$\int_\Gamma (\boldsymbol{u}_\Gamma^{k,\frac{1}{2}} - \boldsymbol{u}_G^k) \cdot \delta\boldsymbol{\lambda}_C \,\mathrm{d}a = 0, \tag{$\widetilde{\mathrm{C}}_4$}$$

with a known right-hand side,

$$\boldsymbol{\Lambda}_G^k := \boldsymbol{\Lambda}_G(\boldsymbol{\lambda}_L^k, \boldsymbol{u}_L^k; \mathbb{A}_G) = \mathbb{A}_G \int_\Gamma \boldsymbol{u}_L^k \cdot \delta\boldsymbol{\lambda}_L \,\mathrm{d}a - \int_\Gamma \boldsymbol{\lambda}_L^k \cdot \delta\boldsymbol{u}_\Gamma \,\mathrm{d}a. \tag{4.42}$$

Together with (G$_1$) and (G$_2$), the global system of equations has to be solved for $(\boldsymbol{u}_G^k, \boldsymbol{\lambda}_C^k, \boldsymbol{u}_\Gamma^k)$ for a given $(\boldsymbol{\Lambda}_G^k, \mathbb{A}_G, \boldsymbol{u}_\Gamma^{k,\frac{1}{2}})$. Here, $\mathbb{A}_G$ and $\boldsymbol{\Lambda}_G^k$ stand for the global Robin-type parameters.

Based on the new boundary conditions provided in ($\widetilde{\mathrm{C}}_1$), ($\widetilde{\mathrm{C}}_2$), ($\widetilde{\mathrm{C}}_3$) and ($\widetilde{\mathrm{C}}_4$) the imbalanced quantities in the Global-Local iterations read as follows:

$$\int_\Gamma (\boldsymbol{u}_\Gamma^k - \boldsymbol{u}_\Gamma^{k,\frac{1}{2}}) \cdot \delta\boldsymbol{\lambda}_L \,\mathrm{d}a \neq 0 \quad \texttt{and} \quad \int_\Gamma \boldsymbol{\lambda}_F^k \cdot \delta\boldsymbol{u}_G \,\mathrm{d}a \neq \int_{\mathcal{B}_F} \boldsymbol{\sigma}(\boldsymbol{u}_G^k) : \boldsymbol{\varepsilon}(\delta\boldsymbol{u}_G) \,\mathrm{d}\boldsymbol{x}, \tag{4.43}$$

For the specific Robin-type boundary conditions, we can resolve $(4.43)_1$ such that this term does not produce any error in the iterative procedure. To do so, following Appendix A, the global and local augmented stiffness matrices within the Robin-type boundary conditions are given by

$$\boxed{\mathbb{A}_G = \boldsymbol{L}_L^T \boldsymbol{T}_L^{-T} \boldsymbol{\mathcal{S}}_L \quad \text{and} \quad \mathbb{A}_L := \boldsymbol{\mathcal{S}}_C.} \tag{4.44}$$

Here, $\mathbb{A}_G$ and $\mathbb{A}_L$ can be seen as augmented stiffness matrices that regularize the Jacobian stiffness matrix at the global and local levels, respectively.

Remark 4.7.1. *In the Robin-type boundary condition given in ($\widetilde{C}_1$) and ($\widetilde{C}_3$), we can extract different criteria, such as*

- $\mathbb{A}_L \to \infty$*: Dirichlet boundary conditions and* $\mathbb{A}_G \to 0$*: Neumann boundary conditions;*
- $\mathbb{A}_L \to 0$*: Neumann boundary conditions and* $\mathbb{A}_G \to \infty$*: Dirichlet boundary conditions;*
- $\mathbb{A}_L = \boldsymbol{\mathcal{S}}_C$*: Robin-type boundary conditions and* $\mathbb{A}_G \to \infty$*: Dirichlet boundary conditions;*

Hence, depending on the Robin-type parameters, a family of boundary conditions can be formulated.

Additionally, to achieve a balanced state of $(4.43)_2$, we recall the global weak formulation in (G$_1$) which we aim to solve for $\boldsymbol{u}_G$, with

$$\int_{\mathcal{B}_G} \boldsymbol{\sigma}(\boldsymbol{u}_G) : \boldsymbol{\varepsilon}(\delta\boldsymbol{u}_G) \,\mathrm{d}\boldsymbol{x} - \int_{\Gamma_G} \boldsymbol{\lambda}_F \cdot \delta\boldsymbol{u}_G \,\mathrm{d}a - \int_{\Gamma_G} \boldsymbol{\lambda}_C \cdot \delta\boldsymbol{u}_G \,\mathrm{d}a - \int_{\Gamma_{N,G}} \bar{\boldsymbol{\tau}} \cdot \delta\boldsymbol{u}_G \,\mathrm{d}a = 0, \tag{$\widetilde{\mathrm{G}}_1$}$$

(to distinguish our solver with $g/l - 1$, we named it as $\widetilde{\mathrm{G}}_1$ for $g/l - 2$ setting) is now equipped with a linearized $\Delta\boldsymbol{\lambda}_F$ satisfying

$$\int_{\Gamma_G} \Delta\boldsymbol{\lambda}_F \cdot \delta\boldsymbol{u}_G \,\mathrm{d}a = \int_{\Gamma_G} \boldsymbol{\mathcal{S}}_F \Delta\boldsymbol{u}_G \cdot \delta\boldsymbol{u}_G \,\mathrm{d}a, \tag{$\widetilde{\mathrm{G}}_2$}$$

where (A.7) in Appendix A is used; such that we set $\boldsymbol{u}_F = \boldsymbol{u}_G$ in Γ_G. Notably, we are not solving for $\boldsymbol{\lambda}_F$ and in the linearized setting of $(\widetilde{\mathrm{G}}_1)$, the corresponding term (i.e., the second term) is replaced by $(\widetilde{\mathrm{G}}_2)$. Here, the linearized equation of $(\widetilde{\mathrm{G}}_1)$ is solved through the Newton-Raphson method with a single iteration; because we are dealing with a linear elastic constitutive equation at the global level.

The detailed Global-Local formulation using Robin-type boundary conditions is depicted in Algorithm 3. This method provides a generic two-scale finite element algorithms that enables for capturing the local non-linearities. Accordingly, Fig. 4.4b depicts one iteration of the Global-Local coupling scheme by means of the Robin-type boundary conditions.

Algorithm 3 *Global-Local iterative scheme combined with Robin-type boundary conditions namely $g/l-2$.*

```
Input: loading data $(\bar{\boldsymbol{u}}_n, \bar{\boldsymbol{\tau}}_n)$ on $\partial_D\mathcal{B}$ and $\Gamma_N$, respectively;
       solution $(\boldsymbol{u}_{G,n-1}, \boldsymbol{u}_{L,n-1}, s_{L,n-1}, \boldsymbol{u}_{\Gamma,n-1}, \boldsymbol{\lambda}_{C,n-1}, \boldsymbol{\lambda}_{L,n-1})$ and $\mathcal{H}_{L,n-1}$ from step $n-1$.

Global-Local iteration $k \geq 1$:
    Local boundary value problem:
        • given $\mathbb{A}_L, \boldsymbol{\Lambda}_L^{k-1}, \mathcal{H}_{L,n-1}$; solve
            phase-field part:
                $(1-\kappa)\int_{\mathcal{B}_L} 2s_{L+}\mathcal{H}(\boldsymbol{\varepsilon}(\boldsymbol{u}_L)).\delta s_L \mathrm{d}\boldsymbol{x} + \int_{\mathcal{B}_L} (s_L-1).\delta s_L \mathrm{d}\boldsymbol{x}$
                $\quad + \int_{\mathcal{B}_L} l^2 \nabla s_L.\nabla(\delta s_L)\mathrm{d}\boldsymbol{x} = 0,$
            mechanical part:
                $\begin{cases} \int_{\mathcal{B}_L} \boldsymbol{\sigma}(\boldsymbol{u}_L, s_L) : \boldsymbol{\varepsilon}(\delta\boldsymbol{u}_L)\,\mathrm{d}\boldsymbol{x} - \int_\Gamma \boldsymbol{\lambda}_L \cdot \delta\boldsymbol{u}_L\,\mathrm{d}a = 0, \\ \int_\Gamma \boldsymbol{\lambda}_L \cdot \delta\boldsymbol{u}_\Gamma\,\mathrm{d}a + \mathbb{A}_L \int_\Gamma \boldsymbol{u}_\Gamma \cdot \delta\boldsymbol{\lambda}_C\,\mathrm{d}a = \boldsymbol{\Lambda}_L^{k-1}, \\ \int_\Gamma (\boldsymbol{u}_\Gamma - \boldsymbol{u}_L) \cdot \delta\boldsymbol{\lambda}_L\,\mathrm{d}a = 0, \end{cases}$
            set $(\boldsymbol{u}_L, s_L, \boldsymbol{u}_\Gamma, \boldsymbol{\lambda}_L) =: (\boldsymbol{u}_L^k, s_L^k, \boldsymbol{u}_\Gamma^{k,\frac{1}{2}}, \boldsymbol{\lambda}_L^k)$,
        • given $(\boldsymbol{u}_L^k, \boldsymbol{\lambda}_L^k; \mathbb{A}_G)$, set
                $\boldsymbol{\Lambda}_G^k = \mathbb{A}_G \int_\Gamma \boldsymbol{u}_L^k \cdot \delta\boldsymbol{\lambda}_C\,\mathrm{d}a - \int_\Gamma \boldsymbol{\lambda}_L^k \cdot \delta\boldsymbol{u}_\Gamma\,\mathrm{d}a.$

    Global boundary value problem:
        • given $\mathbb{A}_G, \boldsymbol{\Lambda}_G^k, \boldsymbol{u}_\Gamma^{k,\frac{1}{2}}$, solve
                $\begin{cases} \int_{\mathcal{B}_G} \boldsymbol{\sigma}(\boldsymbol{u}_G) : \boldsymbol{\varepsilon}(\delta\boldsymbol{u}_G)\,\mathrm{d}\boldsymbol{x} - \int_\Gamma \boldsymbol{\lambda}_F \cdot \delta\boldsymbol{u}_G\,\mathrm{d}a - \int_\Gamma \boldsymbol{\lambda}_C \cdot \delta\boldsymbol{u}_G\,\mathrm{d}a - \int_{\Gamma_N} \bar{\boldsymbol{\tau}} \cdot \delta\boldsymbol{u}_G\,\mathrm{d}a = 0, \\ \int_\Gamma \boldsymbol{\lambda}_C \cdot \delta\boldsymbol{u}_\Gamma\,\mathrm{d}a + \mathbb{A}_G \int_\Gamma \boldsymbol{u}_\Gamma \cdot \delta\boldsymbol{\lambda}_C\,\mathrm{d}a = \boldsymbol{\Lambda}_G^k, \\ \int_\Gamma (\boldsymbol{u}_\Gamma^{k,\frac{1}{2}} - \boldsymbol{u}_G) \cdot \delta\boldsymbol{\lambda}_C\,\mathrm{d}a = 0, \end{cases}$
            set $(\boldsymbol{u}_G, \boldsymbol{u}_\Gamma, \boldsymbol{\lambda}_C) =: (\boldsymbol{u}_G^k, \boldsymbol{u}_\Gamma^k, \boldsymbol{\lambda}_C^k)$,
        • given $(\boldsymbol{u}_G^k, \boldsymbol{\lambda}_C^k; \mathbb{A}_L)$, set
                $\boldsymbol{\Lambda}_L^k = \mathbb{A}_L \int_\Gamma \boldsymbol{u}_G^k \cdot \delta\boldsymbol{\lambda}_C\,\mathrm{d}a - \int_\Gamma \boldsymbol{\lambda}_C^k \cdot \delta\boldsymbol{u}_\Gamma\,\mathrm{d}a.$
        • if fulfilled, set $(\boldsymbol{u}_G^k, \boldsymbol{u}_L^k, s_L^k, \boldsymbol{u}_\Gamma^k, \boldsymbol{\lambda}_C^k, \boldsymbol{\lambda}_L^k) =: (\boldsymbol{u}_{G,n}, \boldsymbol{u}_{L,n}, s_{L,n}, \boldsymbol{u}_{\Gamma,n}, \boldsymbol{\lambda}_{C,n}, \boldsymbol{\lambda}_{L,n})$ and stop;
          else $k+1 \to k$.

Output: solution $(\boldsymbol{u}_{G,n}, \boldsymbol{u}_{L,n}, s_{L,n}, \boldsymbol{u}_{\Gamma,n}, \boldsymbol{\lambda}_{C,n}, \boldsymbol{\lambda}_{L,n})$ and $\mathcal{H}_{L,n}$.
```

4.8. Finite Element Discretization

The mathematical models for physical science are described based on differential or integral equations. Numerical techniques are frequently used to determine an approximate solution (i.e., unknown quantities) for the physical field. The finite element method is one of the numerical techniques to *discretize* the given BVP in a *continuous setting* with finite (i.e., limited numbers) degrees of freedom. Thus, the reformulation of the continuous differential equation to the *equivalent variational setting* leads to the minimization problem through

$$\textit{Find}\ \ (\boldsymbol{u}, s) \in \boldsymbol{V}\ \ \text{such that}\ \ F(\boldsymbol{u}, s) \leq F(\boldsymbol{v}, g)\ \ \forall(\boldsymbol{v}, g) \in \boldsymbol{V}. \tag{4.45}$$

Here, $(\boldsymbol{u}, s)$ are primary fields that correspond to the deformation and crack phase-field, respectively; $\boldsymbol{V}$ is a given set of admissible continuous functions such that a functional $F : \boldsymbol{V} \rightarrow \mathbb{R}^\delta$ is subjected to minimization. Through finite element discretization techniques, (4.45) is rewritten to the finite-dimensional minimization problem in a discrete space through

$$\textit{Find}\ \ (\boldsymbol{u}_h, s_h) \in \boldsymbol{V}_h\ \ \text{such that}\ \ F(\boldsymbol{u}_h, s_h) \leq F(\boldsymbol{v}_h, g_h)\ \ \forall(\boldsymbol{v}_h, g_h) \in \boldsymbol{V}_h\ , \tag{4.46}$$

for the unknown quantity fields $(\boldsymbol{u}_h, s_h)$. Additionally, $\boldsymbol{V}_h \subset \boldsymbol{V}$ is a given set of admissible discrete functions such that a functional $F : \boldsymbol{V}_h \rightarrow \mathbb{R}^\delta$ is subjected to minimization. This formulation is crossroads of the RITZ-GALERKIN METHOD, such that the space functions $\boldsymbol{V}_h$ are chosen as a piecewise polynomial formulation; see [68]. For the comprehensive theoretical background, readers should refer to HUGHES [64], ZIENKIEWICZ ET AL. [137], and WRIGGERS [135].

To numerically use a finite element discretization technique, a continuous domain $\mathcal{B}$ is approximated to $\mathcal{B}_h$ such that $\mathcal{B} \approx \mathcal{B}_h$; see Fig. 4.7. Approximated domain $\mathcal{B}_h$ is decomposed with non-overlapping finite numbers of bilinear quadrilateral element $\mathcal{B}_e \subset \mathcal{B}_h$ such that

$$\mathcal{B} \approx \mathcal{B}_h = \bigcup_{e}^{n_e} \mathcal{B}_e\ , \tag{4.47}$$

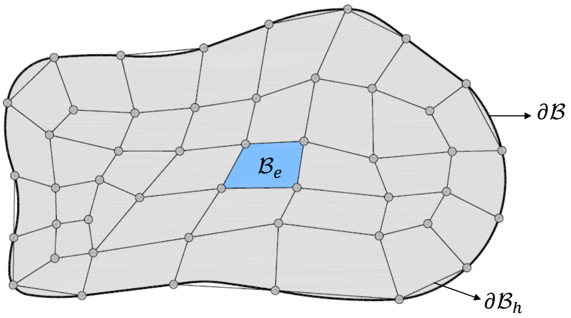

Figure 4.7: Finite element discretization of the material body $\mathcal{B}$ is approximated by $\mathcal{B}_h$ such that $\mathcal{B} \approx \mathcal{B}_h$. The approximated domain $\mathcal{B}_h$ is decomposed with finite numbers of quadrilateral elements $\mathcal{B}_e \subset \mathcal{B}_h$.

Here, $\mathcal{B}_e$ is the so-called element, and h refers to the element size. Additionally, n_e indicates the total number of non-overlapping elements in a discrete domain. Both global and local subproblems are discretized with a Galerkin finite element method using H^1-conforming bilinear (2D) elements; for details, we refer readers to [31]. Consequently, the discrete spaces have the properties of $\boldsymbol{V}_h \subset \boldsymbol{V}$ and $W_h \subset W$. Recall, the continuous primal fields used in Global-Local formulations, namely $(\boldsymbol{u}_G, \boldsymbol{u}_L, s_L, \boldsymbol{u}_\Gamma\ , \boldsymbol{\lambda}_C, \boldsymbol{\lambda}_L)$. In the finite element setting, the continuous primal fields are described based on piecewise polynomial discrete functions, the so-called nodal shape function $N^i(\boldsymbol{\xi})$ associated with the node i. The scalar-valued quantity $\hat{\bullet}^i$ represents the nodal value. For the Global-Local approach, we assume the existence of the partitions $\mathcal{B}_{G,e}$ and $\mathcal{B}_{L,e}$. The solution discretization are given by

$$\boldsymbol{u}_G^h = \sum_i \boldsymbol{N}_{\boldsymbol{u}}^{G,i} \hat{\boldsymbol{u}}_G^i, \quad \boldsymbol{u}_L^h = \sum_i \boldsymbol{N}_{\boldsymbol{u}}^{L,i} \hat{\boldsymbol{u}}_L^i, \quad s_L^h = \sum_i N_s^{L,i} \hat{\boldsymbol{s}}_L^i \ . \tag{4.48}$$

To construct the discretization of the Lagrange multipliers $\boldsymbol{\lambda}_C^h$, $\boldsymbol{\lambda}_L^h$, $\boldsymbol{u}_\Gamma^h$ and the supplementary quantity $\boldsymbol{\lambda}_F^h$ on Γ, we write

$$\begin{aligned} \boldsymbol{\lambda}_C^h &= \sum_i \boldsymbol{N}_{\lambda,i}^{G,i} \hat{\boldsymbol{\lambda}}_C^i, \qquad & \boldsymbol{\lambda}_L^h &= \sum_i \boldsymbol{N}_{\lambda}^{L,i} \hat{\boldsymbol{\lambda}}_L^i, \\ \boldsymbol{u}_\Gamma^h &= \sum_i \boldsymbol{N}_{\boldsymbol{u}}^{\Gamma,i} \hat{\boldsymbol{u}}_\Gamma^i, \qquad & \boldsymbol{\lambda}_F^h &= \sum_i \boldsymbol{N}_{\lambda}^{G,i} \hat{\boldsymbol{\lambda}}_F^i \ , \end{aligned} \tag{4.49}$$

with the following basis functions,

$$\boldsymbol{N}_{\Box}^{\bullet,i} = \begin{bmatrix} N_{\Box}^{\bullet,i} & 0 \\ 0 & N_{\Box}^{\bullet,i} \end{bmatrix}, \quad N_s^{L,i} = \left[N_s^{L,i} \right] . \tag{4.50}$$

Here, $\Box$ is related to $\boldsymbol{\lambda}, \boldsymbol{u}$ and $\bullet$ indicates G, L. Accordingly, its constitutive state variables are represented by $(\boldsymbol{\varepsilon}_G^h, \boldsymbol{\varepsilon}_L^h, \boldsymbol{G}_L^h)$

$$\begin{aligned} \boldsymbol{\varepsilon}_G^h(\boldsymbol{u}_G) &= \nabla_{\boldsymbol{u}}^{sym} \boldsymbol{u}_G^h = \frac{1}{2} \sum_i \left(\hat{\boldsymbol{u}}_G^i \otimes \nabla \boldsymbol{N}_{\boldsymbol{u}}^{G,i} + \nabla \boldsymbol{N}_{\boldsymbol{u}}^{G,i} \otimes \hat{\boldsymbol{u}}_G^i \right) = \sum_i \boldsymbol{B}_{\boldsymbol{u}}^{G,i} \hat{\boldsymbol{u}}_G^i, \\ \boldsymbol{\varepsilon}_L^h(\boldsymbol{u}_L) &= \nabla_{\boldsymbol{u}}^{sym} \boldsymbol{u}_L^h = \frac{1}{2} \sum_i \left(\hat{\boldsymbol{u}}_L^i \otimes \nabla \boldsymbol{N}_{\boldsymbol{u}}^{L,i} + \nabla \boldsymbol{N}_{\boldsymbol{u}}^{L,i} \otimes \hat{\boldsymbol{u}}_L^i \right) = \sum_i \boldsymbol{B}_{\boldsymbol{u}}^{L,i} \hat{\boldsymbol{u}}_L^i, \\ \boldsymbol{G}_L^h(s_L) &= \nabla_{\boldsymbol{x}} s_L^h = \sum_i \hat{s}_L^i . \nabla \boldsymbol{N}_s^{L,i} = \sum_i \boldsymbol{B}_s^{L,i} \hat{s}_L^i \ . \end{aligned} \tag{4.51}$$

Here, $\boldsymbol{B}_{\boldsymbol{u}}^{G,i}$, $\boldsymbol{B}_{\boldsymbol{u}}^{L,i}$, and $\boldsymbol{B}_s^{L,i}$ are the matrix representation for the i^{th} nodal shape function's derivative, corresponding to the global deformation, local deformation and local crack phase-field, respectively. To do so, using the Voigt notation the tensorial constitutive state variables are written in the vectorial form:

$$\boldsymbol{\varepsilon}^h = [\varepsilon_{11}^h, \varepsilon_{22}^h, 2\varepsilon_{12}^h]^T, \quad \boldsymbol{G}^h = [G_1^h, G_2^h]^T, \tag{4.52}$$

in the analogy to (4.51). Hence, the $\boldsymbol{B}^i$ matrix in (4.51) takes the following explicit form in a two-dimensional setting through

$$\boldsymbol{B}_{\boldsymbol{u}}^{G,i} = \begin{bmatrix} N_{\boldsymbol{u},1}^{G,i} & 0 \\ 0 & N_{\boldsymbol{u},2}^{G,i} \\ N_{\boldsymbol{u},2}^{G,i} & N_{\boldsymbol{u},1}^{G,i} \end{bmatrix}, \quad \boldsymbol{B}_{\boldsymbol{u}}^{L,i} = \begin{bmatrix} N_{\boldsymbol{u},1}^{L,i} & 0 \\ 0 & N_{\boldsymbol{u},2}^{L,i} \\ N_{\boldsymbol{u},2}^{L,i} & N_{\boldsymbol{u},1}^{L,i} \end{bmatrix}, \quad \boldsymbol{B}_s^{L,i} = \begin{bmatrix} N_{s,1}^{L,i} \\ N_{s,2}^{L,i} \end{bmatrix}, \tag{4.53}$$

where the subscript j in $N_{\boldsymbol{u},j}^{G,i}$ denotes the first derivatives of the basis function, namely $\hat{\bullet}_{,j} = \partial_{x_j} \hat{\bullet}$, while the superscripted i indicates the nodal point.

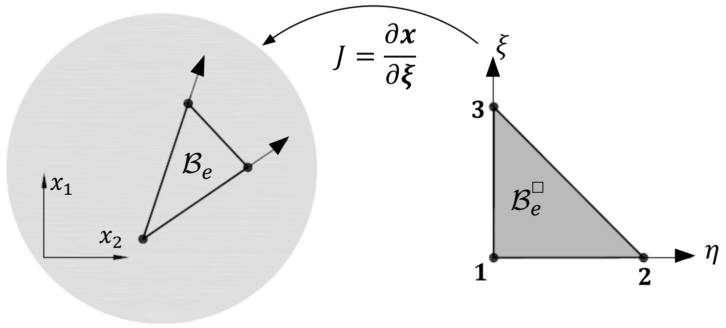

Figure 4.8: Illustration of the isoparametric mapping for the triangular element $\mathcal{B}_e$,

In the finite element setting, the isoparametric coordinate system is typically used rather than the Cartesian coordinate system [135]. Isoparametric transformations preserve the type of elements such as triangular or quadrilateral elements, yet allow numerical integration to be performed more efficiently. Figure 4.8 describes the transformation from physical configuration $\mathcal{B}$ to the isoparametric configuration denoted by $\mathcal{B}^\square$. This mapping is performed by the so-called Jacobi mapping matrix via

$$\boldsymbol{J}_\bullet = \frac{\partial \boldsymbol{x}}{\partial \boldsymbol{\xi}} = \sum_i \hat{\boldsymbol{x}}_\bullet^i \otimes \frac{\partial N_{\boldsymbol{u}}^{\bullet,i}(\boldsymbol{\xi})}{\partial \boldsymbol{\xi}} \ . \tag{4.54}$$

Here, $\bullet$ refers to the G or L, which are correspond to the global and local levels, respectively. Hence, the Jacobian matrix $\boldsymbol{J}$ includes the derivative of the Cartesian coordinate system with respect to the isoparametric coordinate system. The mapping between the gradients of physical configurations to the isoparametric configurations yields,

$$\frac{\partial N_{\boldsymbol{u}}^{\bullet,i}}{\partial \boldsymbol{\xi}} = \boldsymbol{J}_\bullet^T \frac{\partial N_{\boldsymbol{u}}^{\bullet,i}}{\partial \boldsymbol{x}}. \tag{4.55}$$

Piecewise linear basis functions for the triangular element within an isoparametric setting take the following forms

$$N_{\boldsymbol{u}}^{\bullet,1}(\xi,\eta) = 1 - \zeta - \eta, \quad N_{\boldsymbol{u}}^{\bullet,2}(\xi,\eta) = \zeta, \quad N_{\boldsymbol{u}}^{\bullet,3}(\xi,\eta) = \eta, \quad \text{such that} \ \sum_i N_{\boldsymbol{u}}^{\bullet,i}(\xi,\eta) = 1, \tag{4.56}$$

with

$$\boldsymbol{\xi}_1 = (\xi_1,\eta_1) = (0,0), \ \ \boldsymbol{\xi}_2 = (\xi_2,\eta_2) = (1,0), \ \ \boldsymbol{\xi}_3 = (\xi_3,\eta_3) = (0,1).$$

Here, the ordering numbers for the nodal points are anticlockwise within $\mathcal{B}_\square$; see Fig. 4.8.

4.8.1. Global-Local with Dirichlet-Neumann-type boundary conditions

In this section, we provide discretizations of the variational forms given in Algorithm 2. These equations stem from the Global-Local formulation augmented with Dirichlet-Neumann-type boundary conditions, i.e., $g/l - 1$. Thus, the space-discrete variational formulation via finite element approximation for the local and global BVPs are discussed.

- ***Discretization of the local boundary value problem***

Discretization of the local BVP is aimed at determining the primary fields $(\boldsymbol{u}_L, s_L, \boldsymbol{\lambda}_L)$ via finite element approximation. To do so, for each primary field, the set of discretized equilibrium equations based on the *residual* force vector denoted by $\boldsymbol{R}^{\bullet}$ has to be determined. Thus, for the crack phase-field part we have,

$$\begin{aligned}\mathbf{R}_L^s = \bigcup_{e=1} \sum_i \Big(\int_{\mathcal{B}_e} \big(N_s^{L,i}\big)^T \Big[g'(s_+^h)\mathcal{H}(\boldsymbol{\varepsilon}(\boldsymbol{u}_L^h)) + (s_L^h - 1) \Big] \,\mathrm{d}\boldsymbol{x} \\ + \int_{\mathcal{B}_e} \big(\boldsymbol{B}_s^{L,i}\big)^T l^2 \nabla s_L^h \,\mathrm{d}\boldsymbol{x} \Big) = \mathbf{0},\end{aligned} \tag{4.57}$$

with

$$g'(s_+^h) = 2(1-\kappa) s_{L+}^h,$$

and for the local mechanical part, we have

$$\begin{cases} \mathbf{R}_L^{\boldsymbol{u}} = \bigcup_{e=1} \sum_i \int_{\mathcal{B}_e} \Big(\boldsymbol{B}_{\boldsymbol{u}}^{L,i}\Big)^T \boldsymbol{\sigma}_h(\boldsymbol{u}_L, s_L) \,\mathrm{d}\boldsymbol{x} - \mathbf{J}_L^T \hat{\boldsymbol{\lambda}}_L = \mathbf{0}, \\ \mathbf{R}_L^{\mathrm{C}_3} = \mathbf{L}_L \hat{\boldsymbol{u}}_\Gamma^{k-1} - \mathbf{J}_L \hat{\boldsymbol{u}}_L = \mathbf{0}, \end{cases} \tag{4.58}$$

such that the coupling terms are discretized by

$$\mathbf{J}_L = \int_{\mathcal{B}_L} (\boldsymbol{N}_\lambda^L)^T \boldsymbol{N}_u^L \,\mathrm{d}a, \quad \mathbf{L}_L = \int_{\Gamma_L} (\boldsymbol{N}_\lambda^L)^T \boldsymbol{N}_u^\Gamma \,\mathrm{d}a. \tag{4.59}$$

Here, the matrix $\mathbf{B}_{\boldsymbol{u}}^{L,i}$ is given in (4.53).

- ***Discretization of the global boundary value problem***

Discretization of the global BVP is aimed at determining the primary fields $(\boldsymbol{u}_G, \boldsymbol{u}_\Gamma, \boldsymbol{\lambda}_C)$ via finite element approximation. Hence, a nodal residual force vector for the coupling part (C_1) is: for a given $\hat{\boldsymbol{\lambda}}_L^k$, solve for $\hat{\boldsymbol{\lambda}}_C^k$ by

$$\mathbf{R}_G^{\mathrm{C}_1} = \mathbf{L}_G^T \hat{\boldsymbol{\lambda}}_C + \mathbf{L}_L^T \hat{\boldsymbol{\lambda}}_L^k = \mathbf{0}, \tag{4.60}$$

and then by the given $\hat{\boldsymbol{u}}_G^{k-1}$, solve for $\hat{\boldsymbol{\lambda}}_F^k$ in the fictitious domain $\mathcal{B}_F$ through

$$\mathbf{R}_F^{\boldsymbol{u}} = \bigcup_{e=1} \sum_i \int_{\mathcal{B}_e} \Big(\boldsymbol{B}_{\boldsymbol{u}}^{G,i}\Big)^T \boldsymbol{\sigma}_h(\hat{\boldsymbol{u}}_G^{k-1}) \,\mathrm{d}\boldsymbol{x} - \mathbf{J}_F^T \hat{\boldsymbol{\lambda}}_F = \mathbf{0}, \tag{4.61}$$

and afterwards by the given $\hat{\boldsymbol{\lambda}}_F^k$ and $\hat{\boldsymbol{\lambda}}_C^k$, solve for $\hat{\boldsymbol{u}}_G^k$ by

$$\mathbf{R}_G^{\boldsymbol{u}} = \bigcup_{e=1} \sum_i \int_{\mathcal{B}_e} \Big(\boldsymbol{B}_{\boldsymbol{u}}^{G,i}\Big)^T \boldsymbol{\sigma}_h(\boldsymbol{u}_G) \,\mathrm{d}\boldsymbol{x} - \mathbf{J}_F^T \hat{\boldsymbol{\lambda}}_F^k - \mathbf{J}_G^T \hat{\boldsymbol{\lambda}}_C^k - \int_{\Gamma_N} (\boldsymbol{N}_u^G)^T \bar{\boldsymbol{\tau}} \,\mathrm{d}a = \mathbf{0}, \tag{4.62}$$

where $\mathbf{B}_{\boldsymbol{u}}^{G,i}$ is given in (4.53). Now, using the given $\hat{\boldsymbol{u}}_G^k$ from (4.62), solve for $\hat{\boldsymbol{u}}_\Gamma^k$ through

$$\mathbf{R}_G^{\mathrm{C}_2} = \mathbf{L}_G \hat{\boldsymbol{u}}_\Gamma - \mathbf{J}_G \hat{\boldsymbol{u}}_G^k = \mathbf{0}. \tag{4.63}$$

Here, the coupling terms are discretized as follows:

$$\mathbf{J}_G = \int_{\mathcal{B}_G} (\boldsymbol{N}_\lambda^G)^T \boldsymbol{N}_u^G \,\mathrm{d}a, \qquad \mathbf{L}_G = \int_{\Gamma_G} (\boldsymbol{N}_\lambda^G)^T \boldsymbol{N}_u^\Gamma \,\mathrm{d}a. \tag{4.64}$$

4.8.2. Global-Local with Robin-type boundary conditions

In this section, discretizations for the variational formulations given in Algorithm 3 for the $g/l-2$ are further discussed.

- ***Discretization of the local boundary value problem***

Discretization of the local BVP is aimed at determining the primary fields $(\boldsymbol{u}_L, s_L, \boldsymbol{u}_\Gamma, \boldsymbol{\lambda}_L)$ through finite element approximation. Discretization of the crack phase-field part is given in (4.57). Additionally, the local mechanical part is discretized, as follows:

$$\begin{cases} \mathbf{R}_L^{\boldsymbol{u}} = \bigcup\limits_{e=1} \sum\limits_{i} \int_{\mathcal{B}_e} \left(\boldsymbol{B}_{\boldsymbol{u}}^{L,i}\right)^T \boldsymbol{\sigma}_h(\boldsymbol{u}_L, s_L)\ \mathrm{d}\boldsymbol{x} - \mathbf{J}_L^T \hat{\boldsymbol{\lambda}}_L = \mathbf{0}, \\ \mathbf{R}_L^{\widetilde{\mathrm{C}}_1} = \mathbf{L}_L^T \hat{\boldsymbol{\lambda}}_L + \mathbb{A}_L \mathbf{L}_G \hat{\boldsymbol{u}}_\Gamma - \boldsymbol{\Lambda}_L^{k-1} = \mathbf{0}, \\ \mathbf{R}_L^{\widetilde{\mathrm{C}}_2} = \mathbf{L}_L \hat{\boldsymbol{u}}_\Gamma - \mathbf{J}_L \hat{\boldsymbol{u}}_L = \mathbf{0}, \end{cases} \tag{4.65}$$

such that

$$\boldsymbol{\Lambda}_L^{k-1} := \boldsymbol{\Lambda}_L^{k-1}(\hat{\boldsymbol{u}}_G, \hat{\boldsymbol{\lambda}}_C) = \mathbb{A}_L \mathbf{J}_G \hat{\boldsymbol{u}}_G^{k-1} - \mathbf{L}_G^T \hat{\boldsymbol{\lambda}}_C^{k-1}. \tag{4.66}$$

- ***Discretization of the global boundary value problem***

Discretization of the global BVP is aimed at determining the primary fields $(\boldsymbol{u}_G, \boldsymbol{u}_\Gamma, \boldsymbol{\lambda}_C)$ via finite element approximation. Hence, a nodal residual force vector for the global mechanical part reads

$$\begin{cases} \mathbf{R}_G^{\boldsymbol{u}} = \bigcup\limits_{e=1} \sum\limits_{i} \int_{\mathcal{B}_e} \left(\boldsymbol{B}_{\boldsymbol{u}}^{G,i}\right)^T \boldsymbol{\sigma}_h(\boldsymbol{u}_G)\ \mathrm{d}\boldsymbol{x} - \mathbf{J}_F^T \hat{\boldsymbol{\lambda}}_F - \mathbf{J}_G^T \hat{\boldsymbol{\lambda}}_C - \int_{\Gamma_N} (\boldsymbol{N}_{\boldsymbol{u}}^G)^T \bar{\boldsymbol{\tau}} = \mathbf{0}, \\ \mathbf{R}_G^{\widetilde{\mathrm{C}}_3} = \mathbf{L}_G^T \hat{\boldsymbol{\lambda}}_C + \mathbb{A}_G \mathbf{L}_G - \boldsymbol{\Lambda}_G^{k} = \mathbf{0}, \\ \mathbf{R}_G^{\widetilde{\mathrm{C}}_4} = \mathbf{L}_G \hat{\boldsymbol{u}}_\Gamma - \mathbf{J}_G \hat{\boldsymbol{u}}_G = \mathbf{0}, \end{cases} \tag{4.67}$$

such that

$$\boldsymbol{\Lambda}_G^{k} := \boldsymbol{\Lambda}_G^{k}(\hat{\boldsymbol{u}}_L, \hat{\boldsymbol{\lambda}}_L) = \mathbb{A}_G \mathbf{J}_L \hat{\boldsymbol{u}}_L^{k} - \mathbf{L}_L^T \hat{\boldsymbol{\lambda}}_L^{k}. \tag{4.68}$$

4.8.3. Space-discrete linearization of the variational formulation in material configuration

A typical way to solve nonlinear BVPs is to approximate an exact solution through numerical treatment. Some of these techniques are based on variational formulations of the continuous PDE which lead to the discretization of the variational form, in the weak sense. Thus, to solve the set of nonlinear algebraic equations that arises in (4.58), and (4.65), we use an iterative Newton-Raphson method. To this end, the linearization of the discretized residual vector based on the first-order Taylor series expansion yields the following:

$$\text{Lin}\left[\mathbf{R}(\hat{\boldsymbol{u}}_{k+1})\right]_{\boldsymbol{x}=\hat{\boldsymbol{u}}} \approx \mathbf{R}(\hat{\boldsymbol{u}}_k) + D\mathbf{R}(\hat{\boldsymbol{u}}_k)\left[\Delta\hat{\boldsymbol{u}}\right] = \mathbf{0} \ , \tag{4.69}$$

with

$$\hat{\boldsymbol{u}}_{k+1} = \hat{\boldsymbol{u}}_k + \Delta\hat{\boldsymbol{u}} \ . \tag{4.70}$$

A Gateaux derivative or the so-called directional derivative denoted by $D\mathbf{R}(\hat{\boldsymbol{u}}_k)\left[\Delta\hat{\boldsymbol{u}}\right]$ for the vector $\mathbf{R}$ at $\hat{\boldsymbol{u}}_k$ in the direction of $\Delta\hat{\boldsymbol{u}}$ is written as

$$\begin{aligned} D\mathbf{R}(\hat{\boldsymbol{u}}_k)\left[\Delta\hat{\boldsymbol{u}}\right] &= \frac{d}{d\epsilon}\mathbf{R}(\hat{\boldsymbol{u}}_k + \epsilon\Delta\hat{\boldsymbol{u}})\Big|_{\epsilon=0} = \lim_{\epsilon\to 0}\frac{\mathbf{R}(\hat{\boldsymbol{u}}_k + \epsilon\Delta\hat{\boldsymbol{u}}) - \mathbf{R}(\hat{\boldsymbol{u}}_k)}{\epsilon} \\ &= \frac{\partial\mathbf{R}(\hat{\boldsymbol{u}})}{\partial\hat{\boldsymbol{u}}}.\Delta\hat{\boldsymbol{u}} = \boldsymbol{K}.\Delta\hat{\boldsymbol{u}} \ . \end{aligned} \tag{4.71}$$

Here the *tangent stiffness matrix* $\boldsymbol{K}$ is defined by

$$\boldsymbol{K}(\hat{\boldsymbol{u}}) = \frac{\partial\mathbf{R}(\hat{\boldsymbol{u}})}{\partial\hat{\boldsymbol{u}}} \quad \text{with} \quad K_{ij} = \frac{\partial R_i(\hat{\boldsymbol{u}})}{\partial\hat{u}_j} \ . \tag{4.72}$$

This results in the update solution field $\hat{\boldsymbol{u}}_{k+1}$ with

$$\hat{\boldsymbol{u}}_{k+1} = \hat{\boldsymbol{u}}_k - \boldsymbol{K}^{-1}\mathbf{R}(\hat{\boldsymbol{u}}_{\mathbf{k}}) \ . \tag{4.73}$$

4.9. Numerical examples

In this section, to illustrate the proposed Global-Local approach at small deformation, we consider the following benchmark problem. A square specimen with two holes of different diameters is subjected to tension loading (see Fig. 4.9a). The holes are introduced to weaken the structure and to facilitate the specimen cracking in the absence of a stronger singularity such as a pre-existing crack. The holes location is chosen such that prediction of the sub-region where cracking occurs (hence, the local domain for the forthcoming Global-Local analysis) is feasible. Taking a different sizes of holes is intended to obtain a geometrically non-trivial crack pattern, as depicted in Fig. 4.9b. This, moreover, results in a multi-stage crack propagation process manifested in a load-displacement response with two peak points; see Fig. 4.9c for a sketch, and Fig. 4.11 and 4.14 for the actual results. We believe that the present setup, being neither extremely complex, nor trivial, is suitable for the purpose of a qualitative and quantitative comparison between the reference results and results obtained with the proposed Global-Local approach.

As a setup for the numerical investigations, we use:

- **Geometries and parameters:** We set $a = 1\ mm$, $b_1 = 0.197\ mm$, $b_2 = 0.210\ mm$, and $b_3 = 0.490\ mm$ with the hole diameters of $c_1 = 0.247\ mm$ and $c_2 = 0.0806\ mm$.

- **Material parameters:** In this section, the constitutive parameters for the isotropic material are the same as in [93] and given as $\lambda = 121.15$ kN/mm^2, and $\mu = 80.77$ kN/mm^2. Griffith's critical elastic energy release rate is set as $G_c = 2.7 \times 10^{-3}$ kN/mm. We consider the plane-strain situation.

- **Model parameters:** The phase-field parameters are chosen as $\kappa = 10^{-10}$ and $l = 2h$. The characteristic length-scale in the phase-field formulation is $l = 1.5 \times 10^{-2}$ mm.
- **The solution of the nonlinear problems:** An alternate minimzation scheme is used for solving the reference and local BVP in the $g/l-1$ and $g/l-2$. Specifically, the tolerance magnitudes are $\mathtt{TOL}_{\mathrm{NR}} := 10^{-8}$, $\mathtt{TOL}_{\mathrm{Stag}} := 10^{-5}$, and $\widetilde{\mathtt{TOL}}_{\mathrm{GL}} := 10^{-6}$.
- **Software:** The implementation is based on MATLAB R2015b [89] and FORTRAN 90 [29]. The general framework for the Global-Local approach is implemented in MATLAB as a parent/main program such that all subprograms in FORTRAN 90 are called as a MEX-FILE.

In the following numerical example, the displacement control is used with displacement increments $\Delta\bar{u} = 0.06 \times 10^{-5}\ mm$ for 110 time steps. The minimum finite element size in the reference and local domains is 0.004 mm, and the maximum element size in the reference and global domains is $0.1\sqrt{2}$ mm. The former fulfills the heuristic requirement $h < l/2$ for the element size inside the localization zone (i.e., the support) of s. The reference domain partition contains 18,672 elements. The discretizations of the global and local domains contain 200 and 18,552 elements, respectively. That is, in our case, the reference and Global-Local problems have a comparable discretization size, as can be grasped from Fig. 4.10.

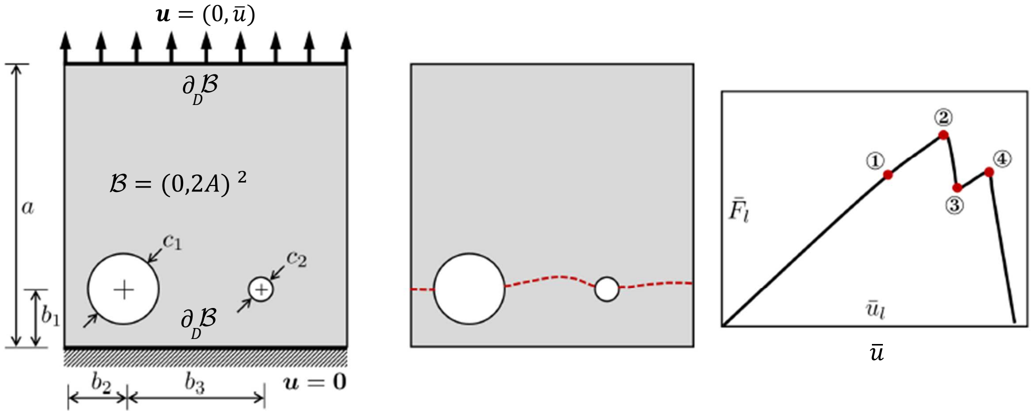

Figure 4.9: (a) Specimen geometry and loading conditions, (b) sketches of the fracture pattern, and (c) the load-displacement curve with the points of interest.

4.9.1. Investigating the references and Global-Local results

We start with the presentation of the quantitative and qualitative reference and Global-Local results and their comparison. As desired, the two load-displacement curves in Fig. 4.11a are identical in the entire range of loading, including in the pre- and post-peak behavior.

Resulting from the slow convergence of the Global-Local procedure, the corresponding accumulative computational time turns out to be high; see Fig. 4.11b, where the time for solving the reference formulation using the staggered scheme is depicted. For the given setup, with a standard machine (Intel(R) Core(TM) i7-3770 OK, CPU 3.5 GHz, RAM

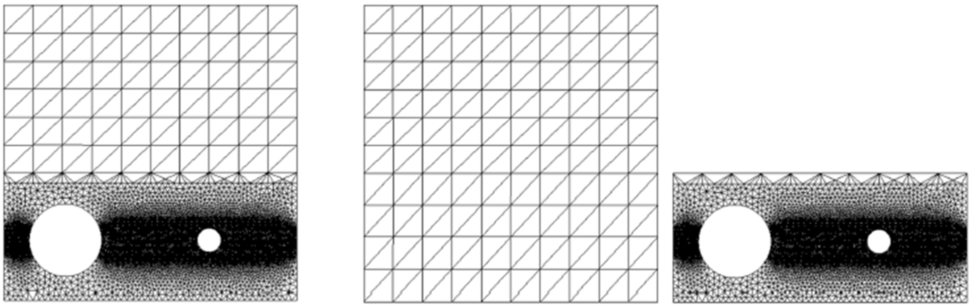

Figure 4.10: Finite element discretization (a) of the reference domain $\mathcal{B}$, (b) of the global and local domains $\mathcal{B}_G$ and $\mathcal{B}_L$, respectively.

16.0 GB) it takes approximated one hour of staggered computations versus the approximately four hours required for the Global-Local approach. (We should note however that our goal was not to gain computational efficiency, but rather to enable computations with legacy codes.) High efforts are not surprising, as the Global-Local problem has a larger discretization size compared with the reference problem, and three nested iterative processes versus two for the reference problem. The latter results in a larger time per loading step, as can be seen in Fig. 4.11c.

It can be grasped that the rapid increase of cumulative time in Fig. 4.11b for both formulations appears at loading steps related to the peak points 2 and 4. Furthermore, regardless of the formulation, the computational time per step in Fig. 4.11c at these points is significantly higher (by almost two orders of magnitude, to be more precise) than at the pre-peak loading steps.

The computed phase-field profiles in Fig. 4.12 are also in very good agreement. This

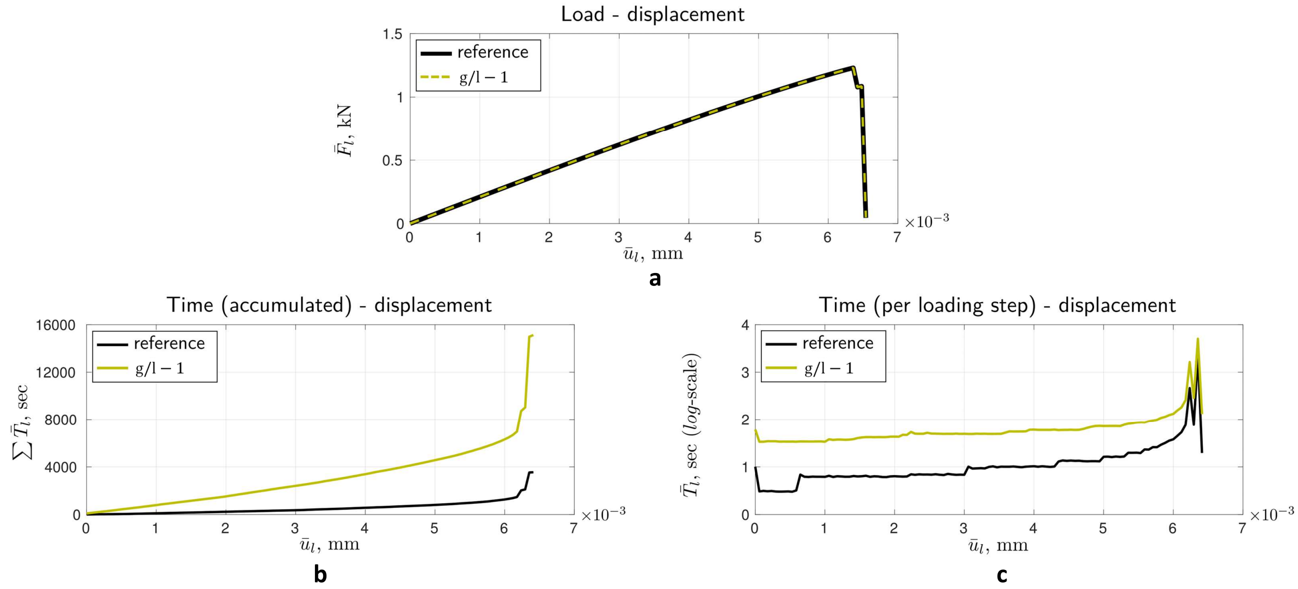

Figure 4.11: Comparison of the reference and the Global-Local solutions. (a) The load-displacement curves, (b) time-displacement curves in terms of 'accumulated time', and (c) time-displacement curves in terms of 'time per loading step'.

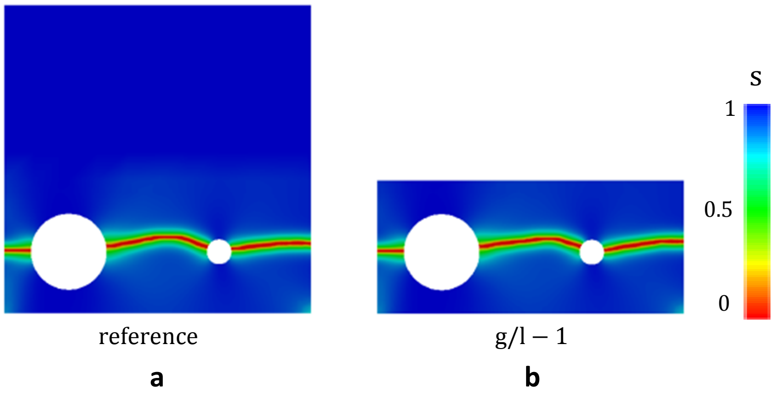

Figure 4.12: Comparison of the crack phase-field response. (a) Reference, and (b) the Global-Local solutions.

is already a good indicator of the potential of the Global-Local approach with application to systems with strong non-linearity and localization.

For deeper insights into the iterative convergence behavior of the Global-Local solution process, in Fig. 4.13 we depict the convergence indicators from Section 4.5 for four given loading steps corresponding to the points 1–4 of our interest sketched in Fig. 4.9c. Thus, we plot the quantities $\eta_{\boldsymbol{u}}$, $\eta_{\boldsymbol{\lambda}}$ and $\eta = \sqrt{\eta_{\boldsymbol{u}}^2 + \eta_{\boldsymbol{\lambda}}^2}$ such that the number of Global-Local iterations required for the solution convergence at the step (also in comparison with other steps) can be detected.

The first important observation is that $\eta_{\boldsymbol{u}}$, which implicitly measures the displacement discontinuity between the solutions of the global and local problem across the interface, is two orders of magnitude less than $\eta_{\boldsymbol{\lambda}}$. Thus, its contribution to η, which is used not only for tracing the convergence of the iterative solution process, but also for the solution accuracy check, is negligible. This means that a stopping criterion based solely on the use of $\eta_{\boldsymbol{u}}$ (what seems typical for the Global-Local approaches for example, plasticity) will yield erroneous results in our case. Secondly, it can be noted that a quite large amount of Global-Local iterations are required, especially at loading steps corresponding to the peak loads of the load-displacement curves in Fig. 4.11a (the points of interest 2 and 4 from Fig. 4.9c).

The non-convexity and non-linearity of the Global-Local formulation, as well as the complicated multi-level iterative nature of the related iterative solution procedure result in a generically slow convergence of the approach. Another impacting factor that should be noted is that the stiffness matrix of the global problem $\mathbf{K}_G$ is never updated within the Global-Local computation process. The incorporation of an incremental update relaxation in this process is thus our next goal, with the objective of obtaining an acceleration of the convergence process.

4.9.2. Reference and $g/l - 1$ augmented with relaxation techniques

In this section, numerical simulation for the Global-Local solution equipped with relaxation/acceleration techniques is provided; see Section 4.6. Accordingly, the convergence performance of $g/l - 1$ is investigated.

The results obtained with the relaxation/acceleration techniques are depicted in Figs.

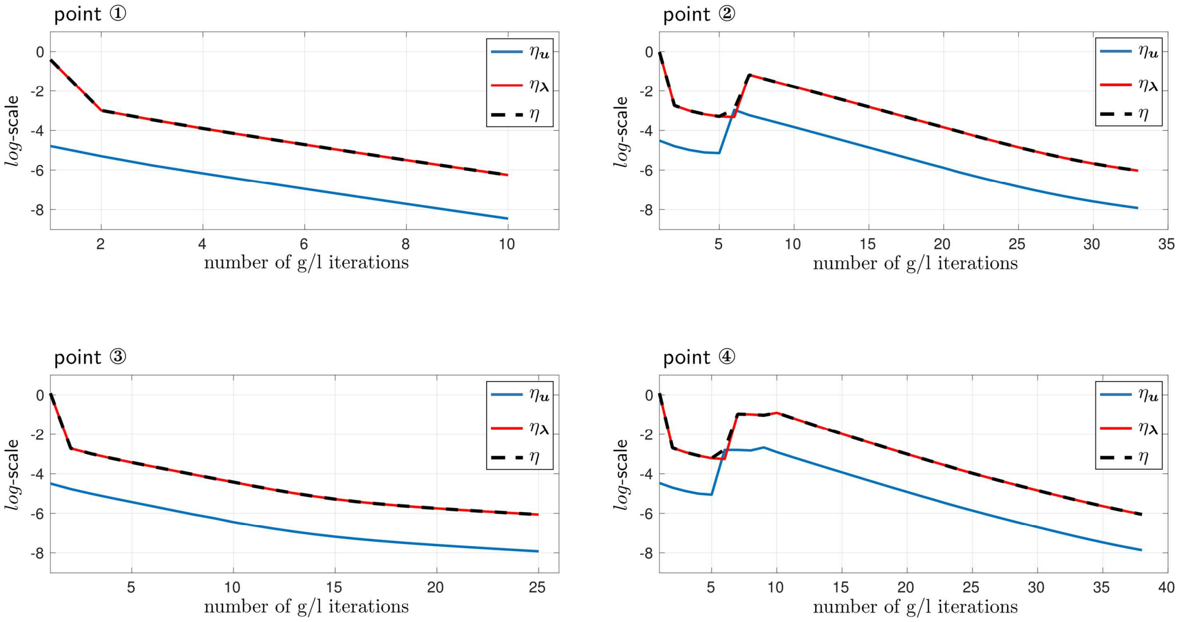

Figure 4.13: Convergence behavior of the Global-Local iterative solution process at four different loading steps (points 1–4 from Fig. 4.9c), illustrated in terms of the indicator η, as well as its ingredients $\eta_{\boldsymbol{u}}$ and $\eta_{\boldsymbol{\lambda}}$.

4.14 to 4.16. As can be seen from Fig. 4.14a, all three considered techniques yield identical load-displacement curves, which are also identical to the curve obtained from the Global-Local procedure with no relaxation/acceleration.

From the time-displacement curves comparison in terms of both 'accumulative time' and 'time per loading step' in Fig. 4.14b,c, it can be concluded that the desired improvement of efficiency of the original procedure has indeed been achieved. However, in the global time scale, all three techniques have a very similar effect, at least for the considered example.

Similar to Fig. 4.13, Fig. 4.15 presents and compares the convergence of the Global-Local iterative procedure and its acceleration/relaxation versions at the four loading steps of interest. Here, we only plot the indicator η and not its ingredients. For a given point, the number of iterations required for the convergence of the solution process in all acceleration/relaxation techniques is similar, but is less (in some cases, significantly) than in the original unaccelerated case.

Figure 4.16 compares the phase-field solutions of the Global-Local formulations computed using the corresponding acceleration/relaxation techniques. It can be observed that even though the load-displacement curves are identical in all cases, the corresponding phase-field profiles are not. This can be explained, first of all, by the solution non-uniqueness of the original reference phase-field formulation, and, secondly, by the fact that the Global-Local formulation is only the approximation of the reference one.

4.9.3. Investigating $g/l-1$ results for different global discretization spaces

In this section, the Global-Local approach for the given setup in Section 4.9.1 is performed, while different global discretizations are considered. Specifically, we aim to quantitatively investigate the convergence performance of the iterative Global-Local formulation

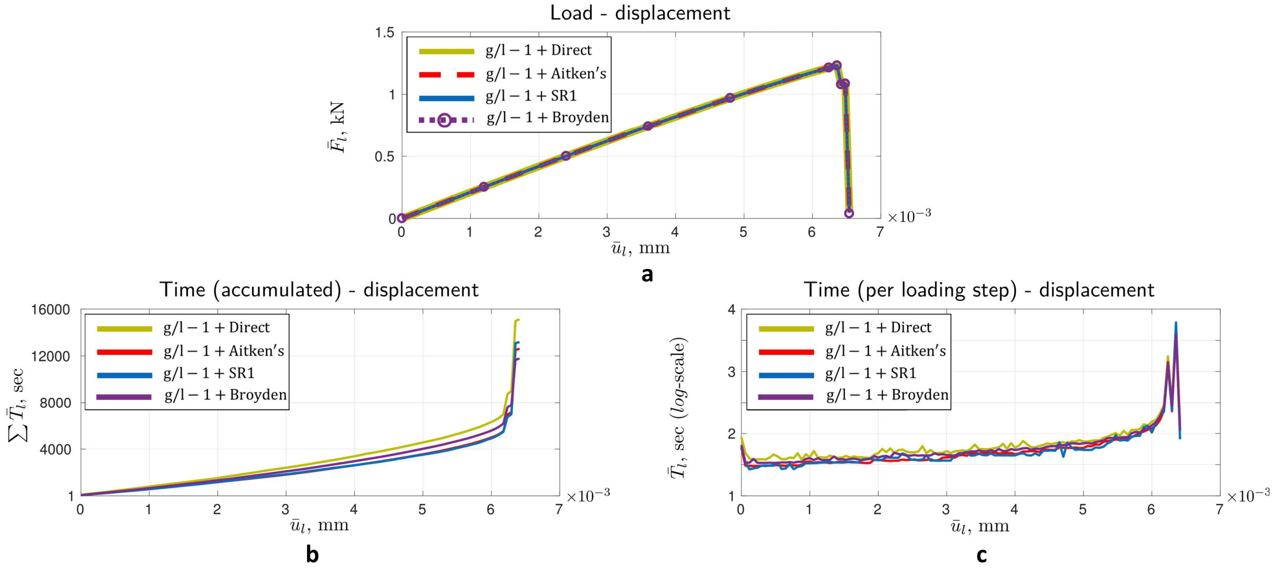

Figure 4.14: Comparison of the reference solution and the Global-Local formulation augmented with relaxation techniques. (a) The load-displacement curves, (b) time-displacement curves in terms of 'accumulated time', and (c) time-displacement curves in terms of 'time per loading step'.

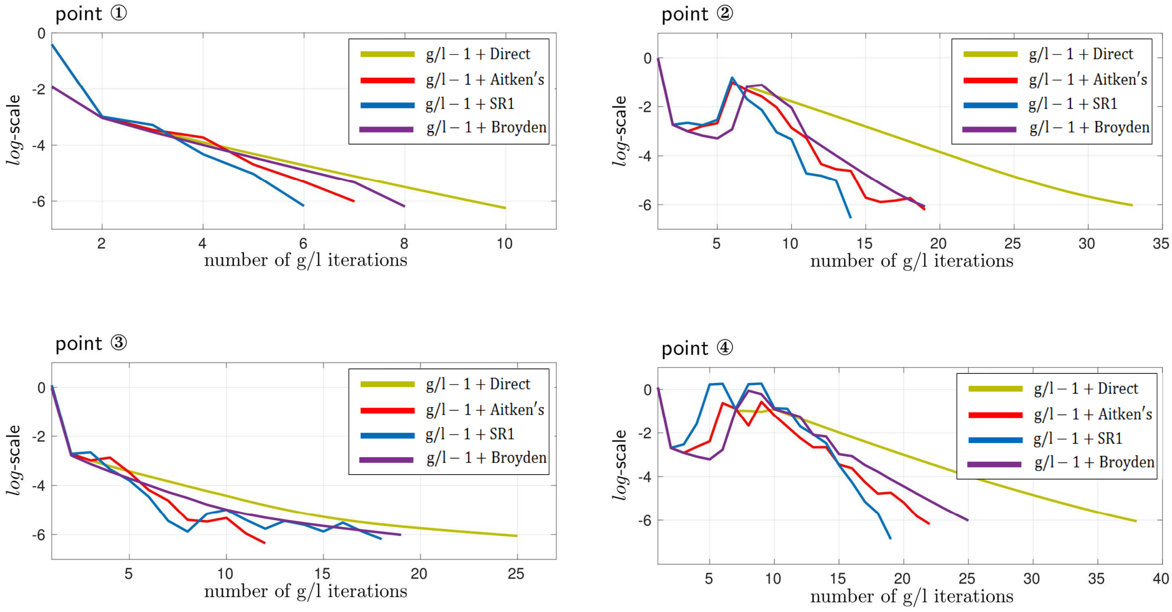

Figure 4.15: Convergence behavior of the different versions of the Global-Local iterative solution process at four different loading steps (points 1–4 in from Fig. 4.9c), illustrated in terms of the indicator η.

through the effect of (i) global discretization space, and (ii) the presence of voids with its coarse representation on the global level (to weaken the global material stiffness). Thus, four more cases are investigated which are shown in Fig. 4.17. These cases are as follows:

- **Case 1.** We set $h_C = h_F$ and $E_C = E_F$ which corresponds to the numerical

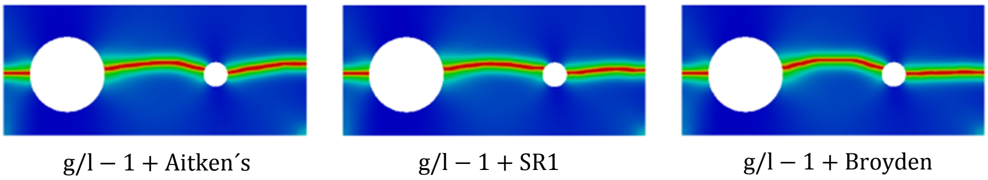

Figure 4.16: Comparison of the phase-field profiles computed with the various acceleration/relaxation versions of the Global-Local approach.

simulation explained in Section 4.9.2.

- **Case 2.** We set $h_C = h_F$ and $E_C \neq E_F = \frac{1}{V(\mathcal{B}_L)} \int_{\mathcal{B}_L} E(\boldsymbol{x}) d\boldsymbol{x}$. Thus, E_F sets as the effective quantity of Young's modulus in the local area.
- **Case 3.** We set $h_C = h_F$ and $E_C = E_F$ including the coarse representation of the left void.
- **Case 4.** We set $h_C = 2h_F$ and $E_C = E_F$ including the coarse representation of the left void; however a finer discretization with respect to Case 3 is used.
- **Case 5.** We set $h_C = 4h_F$ and $E_C = E_F$, including the coarse representation of both left and right voids, thus becoming the finest discretization space among all global domain cases.

Similar to Fig. 4.15 for Case 1, Figs. 4.18-4.21 correspond to Cases 2-5, respectively. These figures present the convergence performance of the Global-Local iterative procedure and its acceleration/relaxation version at four loading steps. Notably, the Global-Local formulation equipped with acceleration/relaxation techniques required fewer iterations to reach the convergence. Additionally, the presence of the void in the global domain (e.g., Case 3) results in fewer iterations (compare with Fig. 4.15 for Case 1). This is mainly because the gap between material stiffness at the fictitious domain and its corresponding local domain becomes drastically smaller. Using this idea, in Case 2, when an effective quantity for Young's modulus is used (still without the presence of the void), we observed that fewer iterations required to reach the convergence.

For a better insight into the iterative convergence behavior through different global discretizations, Table 4.2 is provided. It can be seen that the presence of the void in the global domain results in fewer iterations, while between Cases 4 and 5, there is no significant difference. Hence, the coarse representation of the single left void is quite sufficient to reduce the number of Global-Local iterations.

Accordingly, the resulting global vertical displacement u_y at the complete failure for different case studies are shown in Fig. 4.22. It can be seen that the smaller value for h_F leads to circular-shaped for the voids (i.e., Cases 4, 5), while its coarse representation leads to the polygonal-shaped (i.e., Case 3).

4.9.4. Reference and $g/l-2$ with Robin-type boundary conditions

We continue with the quantitative and qualitative investigation of the Global-Local solutions, namely $g/l-2$, compared with the reference counterpart. Due to the slow con-

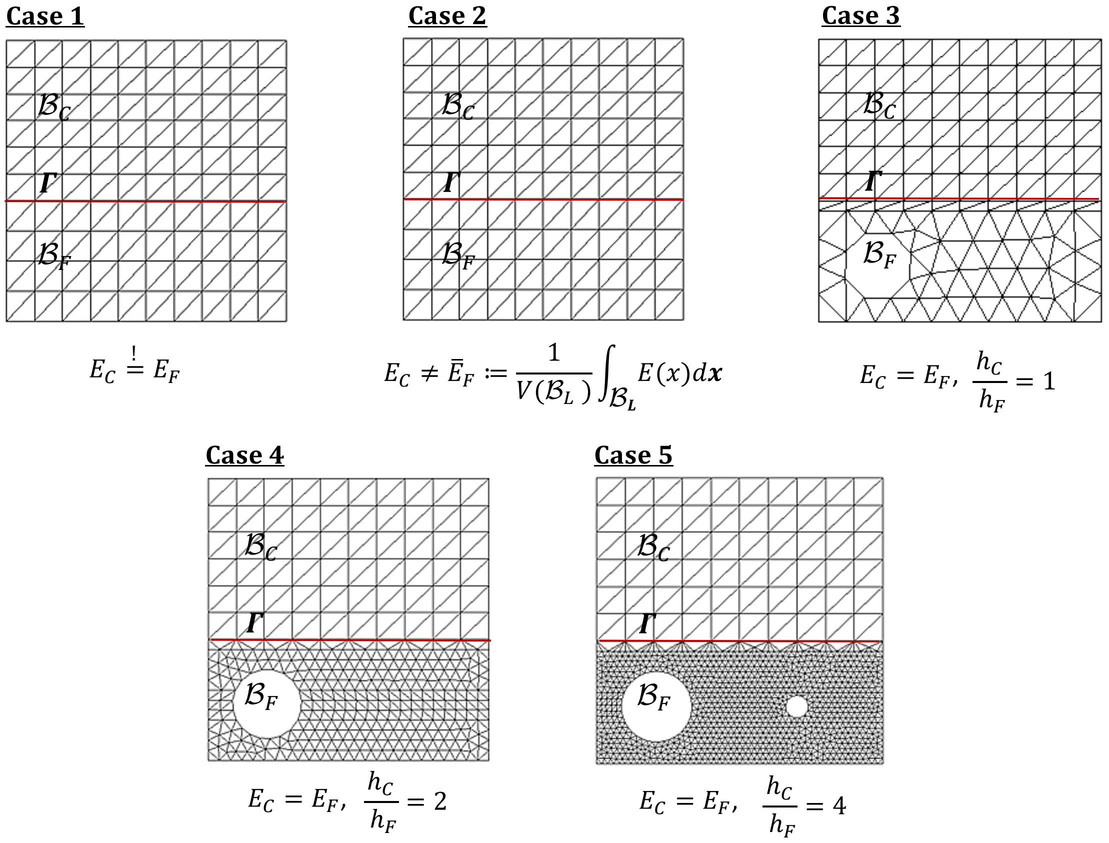

Figure 4.17: Finite element discretization of the global domain $\mathcal{B}_G$ for different case studies.

vergence performance of the Global-Local approach with Dirichlet-Neumann-type boundary conditions in $g/l-1$, the Robin-type boundary conditions is employed. Through $g/l-2$, it is observed that the stiff local response at the global level (due to the local non-linearities) can be removed; hence, the computational time will be reduced. For a better insight into the Global-Local formulation enhanced with Robin-type boundary conditions, the load-displacement curve is depicted in Fig. 4.23a. The important observation is that $g/l-2$ provides an identical response with respect to the reference solution. Next, we examine the computational time between $g/l-1$, and $g/l-2$ with respect to the reference solutions. The corresponding accumulative computational time per prescribed displacement is represented in Fig. 4.23b. The resulting accumulative computational time shows

Table 4.2: The number of Global-Local iterations for different case studies at four different loading steps (points 1–4 from Fig. 4.9c)

$g/l-1+$ Direct	Number of g/l iterations				
	Case 1	Case 2	Case 3	Case 4	Case 5
Point 1	10	9	6	5	5
Point 2	33	31	24	21	20
Point 3	25	23	19	17	16
Point 4	38	34	34	33	33

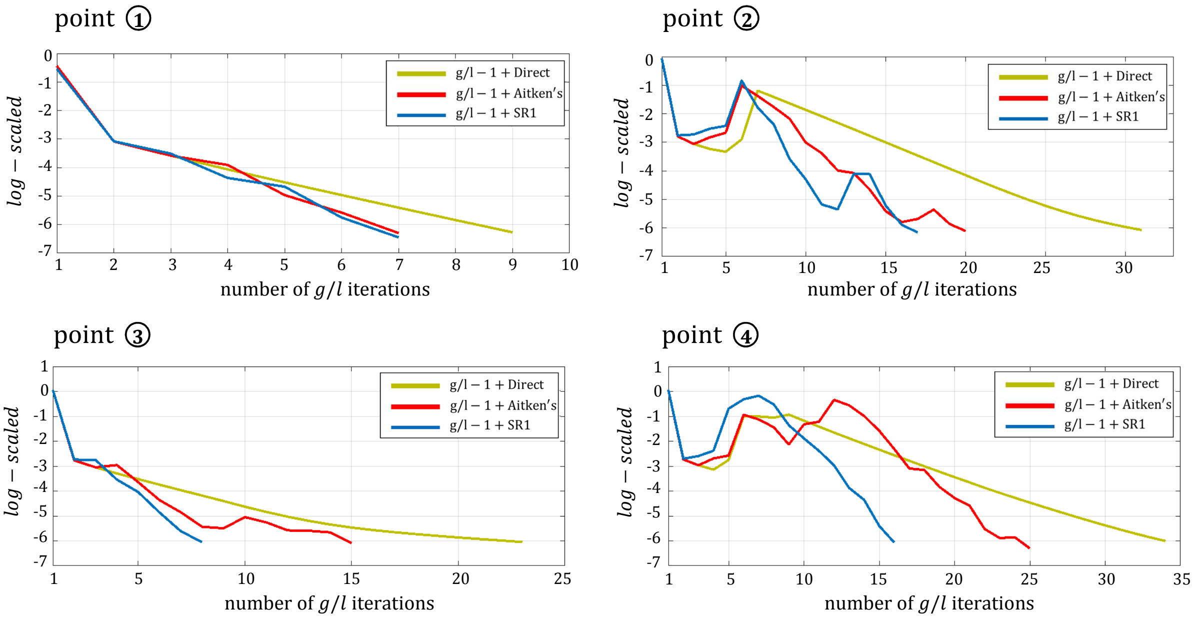

Figure 4.18: Case 2. Convergence behavior of the different versions of the Global-Local iterative solution process at four different loading steps (points 1–4 from Fig. 4.9c), illustrated in terms of the indicator η.

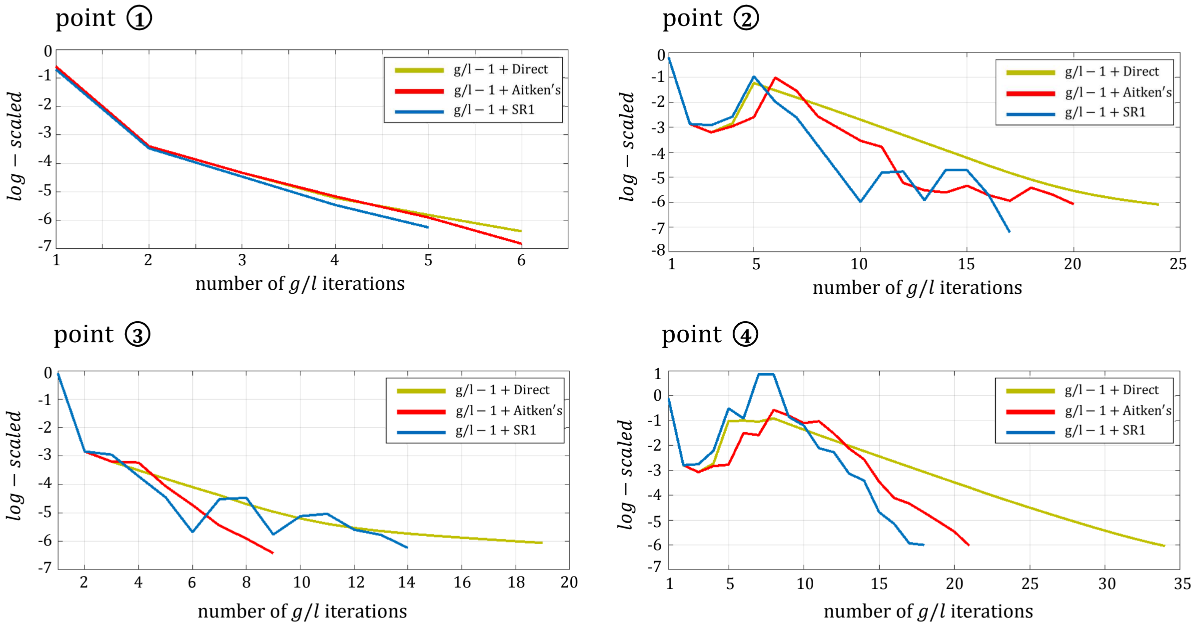

Figure 4.19: Case 3. Convergence behavior of the different versions of the Global-Local iterative solution process at four different loading steps (points 1–4 from Fig. 4.9c), illustrated in terms of the indicator η.

that $g/l - 2$ requires 17% less time compared with the reference solution. By contrast, the computational time for $g/l - 1$ requires four times more than the reference time, but it is strongly non-intrusive, enabling the numerical implementation straightforwardly performed through legacy codes.

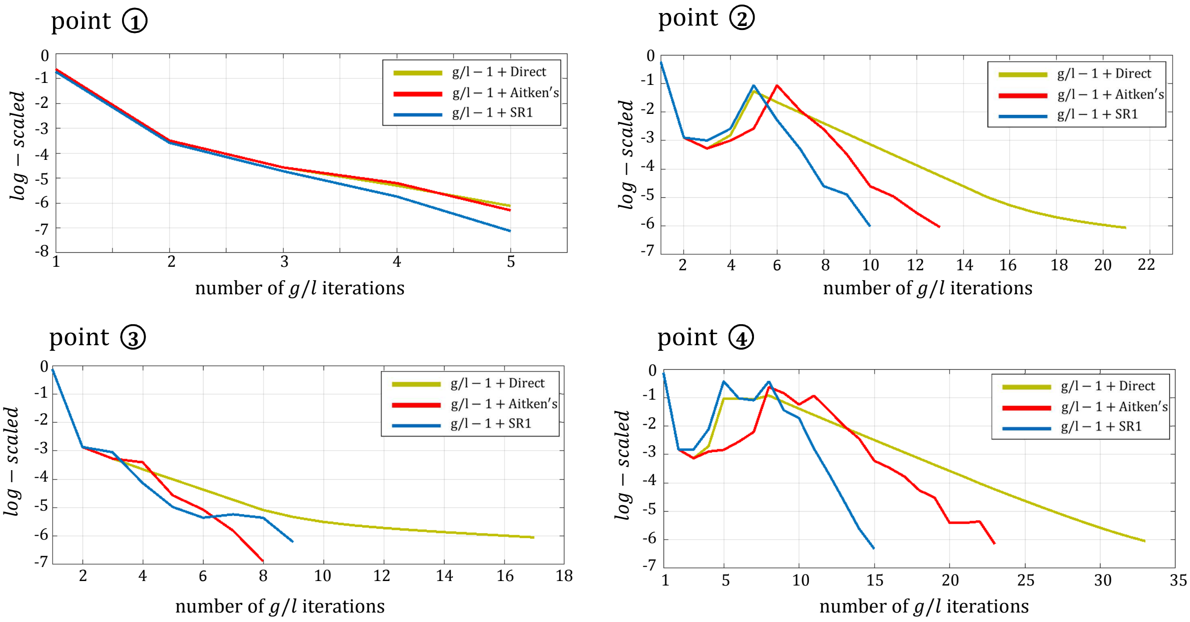

Figure 4.20: Case 4. Convergence behavior of the different versions of the Global-Local iterative solution process at four different loading steps (points 1–4 from Fig. 4.9c), illustrated in terms of the indicator η.

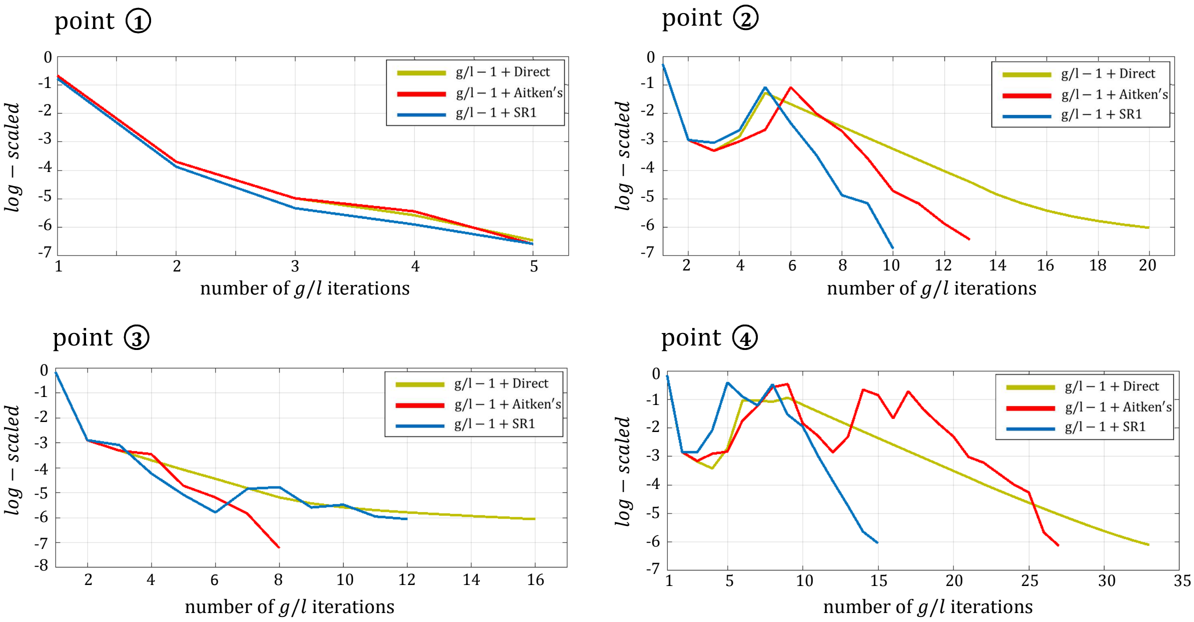

Figure 4.21: Case 5. Convergence behavior of the different versions of the Global-Local iterative solution process at four different loading steps (points 1–4 from Fig. 4.9c), illustrated in terms of the indicator η.

Another impacting factor that should be noted is the computed crack phase-field solution s_L. Figure 4.24 presents the crack profile obtained through $g/l-2$. For the sake of comparison, the crack profile obtained through $g/l-1$ + direct is also provided. It can be grasped that even though the load-displacement curves are identical for both $g/l-1$

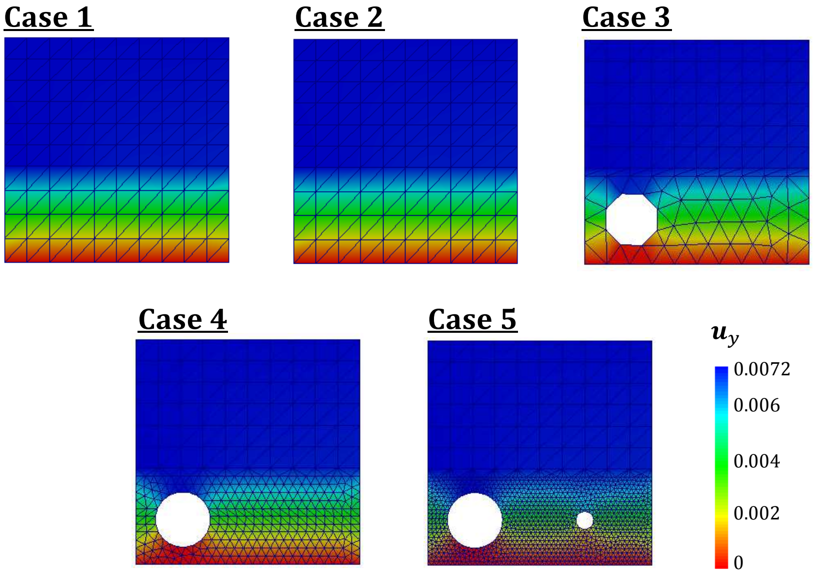

Figure 4.22: The resulting global vertical displacement u_y at the complete failure state for different case studies.

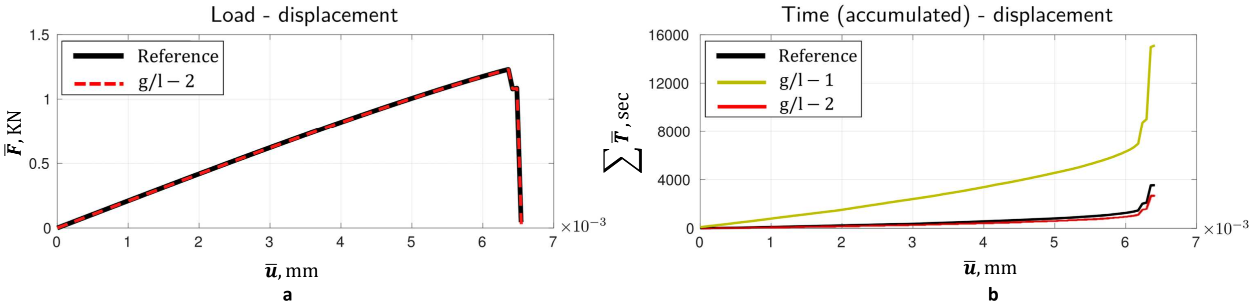

Figure 4.23: Comparison of the reference solution and the Global-Local formulation $g/l-2$. (a) The load-displacement curves, and (b) time-displacement curves in terms of 'accumulated time' compared with $g/l-1$.

and $g/l-2$, the corresponding phase-field profiles are not precisely the same. This is mainly because, the non-uniqueness of the original reference phase-field formulation, and, additionally, the fact that the Global-Local formulation provides an approximation of the reference solution and not an exact solution, namely $s \approx s_L$.

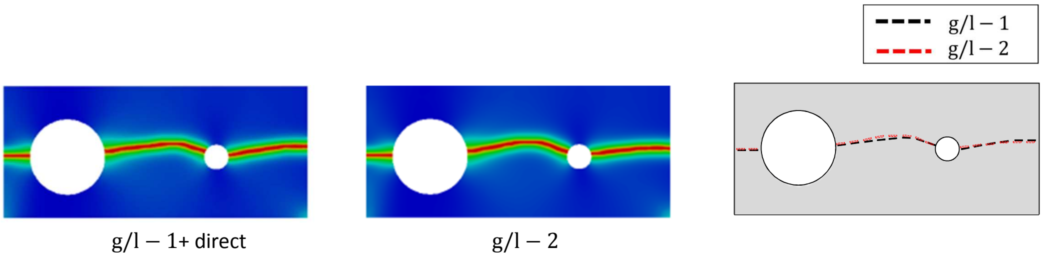

Figure 4.24: Computed crack phase-field solution through $g/l-1+$ direct, $g/l-2$ and their comparison.

Chapter 5

Global-Local Approach Applied to the Phase-Field Fracture at Finite Strain

The phase-field simulation of fracture processes with legacy codes bears several advantages that fit perfectly within the framework of the Global-Local coupling framework using pre-defined fixed meshes. The most obvious advantage is the ability to automatically track a cracking process through the evolution of the smooth crack field on a fixed mesh, which, in the proposed procedure, is the mesh of the local model. For the polymer-like material, of which the structure is subjected to large deformation, its reference treatment is computationally demanding. Additionally, the large deformation of the specimen results in the significant nonlinearity of the constitutive model; hence, the more computational time is required. As a result, the necessity of introducing the Global-Local framework for the high nonlinear setting, such as hyperelastic fracturing material through the phase-field formulation, seems particularly demanding [4].

In this chapter, the Global-Local formulation which has been derived in Chapter 4, is further extended towards large defamation. Thus, the main objective here is to introduce the adoption of the variational phase-field fracture formulation within legacy codes when a finite strain response is observed. The resulting framework is algorithmically described in detail and substantiated with some numerical tests.

5.1. Non-overlapping domain decomposition formulation

Recall, the complementary domain in the undeformed configuration denoted by $\mathcal{B}_C := \mathcal{B}\backslash\mathcal{B}_L \subset \mathcal{B} \in \mathbb{R}^\delta$, $\delta = \{2, 3\}$ corresponds to the intact region, and let $\mathcal{B}_L$ be a bounded open domain, where the fracture surface is approximated in this region; see Fig. 5.1(a). It is assumed the fracture surface in $\mathcal{B}_L$ represents a reasonably small 'fraction' of $\mathcal{B}$ such

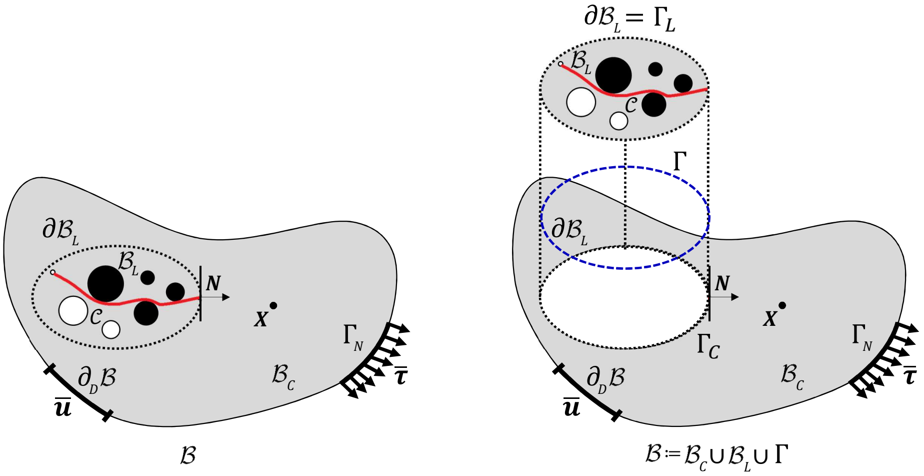

Figure 5.1: Domain decomposition scheme. (*a*) Geometry and loading setup of the reference BVP at the undeformed configuration, and (*b*) non-overlapping domain decomposition setting whereas $\mathcal{B}$ is decomposed into the intact and fracture region denoted as complementary and local domains $\mathcal{B}_C$ and $\mathcal{B}_L$ at the material configuration, respectively.

that $|\mathcal{B}_L| \ll |\mathcal{B}_C|$. We further define an interface between an unbroken domain $\mathcal{B}_C$ and broken domain $\mathcal{B}_L$ by $\Gamma \in \mathcal{R}^{\delta-1} \subset \mathcal{B}$ in the continuum setting to be the interface between $\mathcal{B}_L$ and $\mathcal{B}_C$, such that $\mathcal{B} \equiv \mathcal{B}_L \cup \Gamma \cup \mathcal{B}_C$. We further assume that $\mathcal{B}_L$ is free from any external imposed load and hence we have prescribed load description *only* in $\mathcal{B}_C$.

A domain decomposition with a geometric sketch in Fig. 5.1(b) is applied to the undeformed reference configuration in Fig. 5.1(a). Three functions on $\mathcal{B}_L$ and $\mathcal{B}_C$ are considered, namely $\varphi_L \in \mathbf{V_L}$, $s_L \in W_{L,in}$ and $\varphi_C \in \mathbf{V_C}$, where we introduce additional three sets:

$$\boldsymbol{V}_L := \mathbf{H}^1_0(\mathcal{B}_L)^\delta, \quad \boldsymbol{V}_C := \mathbf{V}(\mathcal{B}_C), \quad \text{and } \; W_{L,in} := W_{in}(\mathcal{B}_L)\ ,$$

referring to the spaces defined in (3.8).

Similar to the small strain setting, Section 4.2, two restrictions in the model are as follows: (*i*) the strong coupling scheme (i.e., the strong displacement continuity condition) which holds along with (*ii*) the predefined interface. To this end, one needs to assume that the discrete interface for both complementary and local domain are exactly coincide together, thus yielding

$$\varphi_L(\boldsymbol{X}, t) \overset{!}{=} \varphi_C(\boldsymbol{X}, t) \quad \text{at} \quad \boldsymbol{X} \in \Gamma = \Gamma_C = \Gamma_L, \tag{5.1}$$

Now, let the *reference deformation map* $\boldsymbol{\varphi}(\boldsymbol{X}, t) \in \mathbf{V}$ to be the solution of the multi-field variational problem in (3.93) whichs is decomposed as

$$\boldsymbol{\varphi}(\boldsymbol{X}, t) := \begin{cases} \varphi_L(\boldsymbol{X}, t) & \text{for } \boldsymbol{X} \in \mathcal{B}_L, \\ \varphi_C(\boldsymbol{X}, t) & \text{for } \boldsymbol{X} \in \mathcal{B}_C. \end{cases} \tag{5.2}$$

Accordingly, as discussed earlier, the fracture surface lives only in the $\mathcal{B}_L$ hence we introduce scalar-valued function $s_L : \mathcal{B}_L \to [0, 1] \in W_{L,in}$. The *reference phase-field* s is then decomposed in the following representation

$$s(\boldsymbol{X}, t) := \begin{cases} s_L & \text{for } \boldsymbol{X} \in \mathcal{B}_L, \\ 1 & \text{for } \boldsymbol{X} \in \mathcal{B}_C. \end{cases} \tag{5.3}$$

By imposing (5.2) and (5.3) to the energy functional indicated in Formulation 3.2.2, thus the following energy functionals corresponding to $\mathcal{B}_C$ and $\mathcal{B}_L$, read:

$$\widehat{\mathcal{E}}_C(\boldsymbol{\varphi}_C) := \int_{\mathcal{B}_C} w(\boldsymbol{C}_C, 1, 0; 1)\,\mathrm{d}\boldsymbol{X} - \int_{\partial_N \mathcal{B}_C} \bar{\boldsymbol{\tau}} \cdot \boldsymbol{\varphi}_C \,\mathrm{d}A, \tag{5.4}$$

and

$$\widehat{\mathcal{E}}_L(\boldsymbol{\varphi}_L, s_L; H_J) := \int_{\mathcal{B}_L} w(\boldsymbol{C}_L, s_L, \nabla_{\boldsymbol{X}} s_L; H_J)\,\mathrm{d}\boldsymbol{X}, \tag{5.5}$$

for the total pseudo-energy density defined in Formulation 3.2.2. Let the strong displacement continuity in (5.1) holds true, this results in

$$\mathcal{E}(\boldsymbol{\varphi}, s; H_J) \equiv \widehat{\mathcal{E}}(\boldsymbol{\varphi}_C, \boldsymbol{\varphi}_L, s_L; H_J) := \widehat{\mathcal{E}}_C(\boldsymbol{\varphi}_C) + \widehat{\mathcal{E}}_L(\boldsymbol{\varphi}_L, s_L; H_J), \tag{5.6}$$

where $\mathcal{E}$ is the original reference functional in Formulation 3.2.2. As a result, the domain decomposition variational formulation, which is *equivalent* to the reference formulation (3.93), reads

$$\{\boldsymbol{\varphi}_C, \boldsymbol{\varphi}_L, s_L\} = \arg\{ \min_{\boldsymbol{\varphi}_C \in \mathbf{V_C}, \boldsymbol{\varphi}_L \in \mathbf{V_L}} \min_{s_L \in W_{L,in}} [\, \widehat{\mathcal{E}}(\boldsymbol{\varphi}_C, \boldsymbol{\varphi}_L, s_L; H_J)\,]\ \}\ . \tag{5.7}$$

Note, the major advantage of using the minimization problem (5.7) instead of the (3.93) is reducing the nonlinearity order of the complementary domain when material undergoing large deformation.

The strong displacement continuity requirement given in (5.1) is too restrictive from the computational standpoint [38], hence we relax (5.1) in a weak sense by introducing the traction-like terms in the corresponding energy functionals (5.4) and (5.5). They read

$$\widehat{\mathcal{E}}_C(\boldsymbol{\varphi}_C, \boldsymbol{\lambda}_C) := \int_{\mathcal{B}_C} w(\boldsymbol{C}_C, 1, 0; 1)\,\mathrm{d}\boldsymbol{X} - \int_{\Gamma_C} \boldsymbol{\lambda}_C \cdot \boldsymbol{\varphi}_C \,\mathrm{d}A - \int_{\Gamma_{N,C}} \bar{\boldsymbol{\tau}} \cdot \boldsymbol{\varphi}_C \,\mathrm{d}A, \tag{5.8}$$

and

$$\widehat{\mathcal{E}}_L(\boldsymbol{\varphi}_L, s_L, \boldsymbol{\lambda}_L; H_J) := \int_{\mathcal{B}_L} w(\boldsymbol{C}_L, s_L, \nabla_{\boldsymbol{X}} s_L; H_J)\,\mathrm{d}\boldsymbol{X} - \int_{\Gamma_L} \boldsymbol{\lambda}_L \cdot \boldsymbol{\varphi}_L \,\mathrm{d}A, \tag{5.9}$$

with $\boldsymbol{\lambda}_C, \boldsymbol{\lambda}_L \in \mathbf{L}^2(\Gamma)$ being the unknown Lagrange multipliers, which represent tractions at the interface. The saddle point problem including complementary and local domains takes the form

$$\widehat{\mathcal{E}}(\boldsymbol{\varphi}_C, \boldsymbol{\varphi}_L, s_L, \boldsymbol{\lambda}_L, \boldsymbol{\lambda}_C; H_J) := \widehat{\mathcal{E}}_C(\boldsymbol{\varphi}_C, \boldsymbol{\lambda}_C) + \widehat{\mathcal{E}}_L(\boldsymbol{\varphi}_L, s_L, \boldsymbol{\lambda}_L; H_J),$$

which is under-determined, since no relation is yet specified between $\boldsymbol{\varphi}_L$ and $\boldsymbol{\varphi}_C$, nor between $\boldsymbol{\lambda}_L$ and $\boldsymbol{\lambda}_C$. The latter is achieved by introducing the functional

$$\widehat{\mathcal{E}}_\Gamma(\boldsymbol{\varphi}_\Gamma, \boldsymbol{\lambda}_C, \boldsymbol{\lambda}_L) := \int_\Gamma \boldsymbol{\varphi}_\Gamma \cdot (\boldsymbol{\lambda}_L + \boldsymbol{\lambda}_C)\,\mathrm{d}A, \tag{5.10}$$

with $\boldsymbol{\varphi}_\Gamma \in \mathbf{H}^1(\Gamma)$ representing the (unknown) Lagrange multiplier, which has the dimension of a displacement and is the so-called displacement interface. Summing $\mathcal{E}_C$ and $\mathcal{E}_L$

with $\mathcal{E}_\Gamma$, we get

$$\widehat{\mathcal{E}}(\boldsymbol{\varphi}_C,\boldsymbol{\varphi}_L,s_L,\boldsymbol{\varphi}_\Gamma,\boldsymbol{\lambda}_C,\boldsymbol{\lambda}_L;H_J):=\int_{\mathcal{B}_C} w(\boldsymbol{C}_C,1,0;1)\,\mathrm{d}\boldsymbol{X}+\int_{\mathcal{B}_L} w(\boldsymbol{C}_L,s_L,\nabla_{\boldsymbol{X}}s_L;H_J)\,\mathrm{d}\boldsymbol{X} \\ +\int_\Gamma \{\boldsymbol{\lambda}_C\cdot(\boldsymbol{\varphi}_\Gamma-\boldsymbol{\varphi}_C)+\boldsymbol{\lambda}_L\cdot(\boldsymbol{\varphi}_\Gamma-\boldsymbol{\varphi}_L)\}\,\mathrm{d}A-\int_{\Gamma_{N,C0}}\bar{\boldsymbol{\tau}}\cdot\boldsymbol{\varphi}_C\,\mathrm{d}A. \tag{5.11}$$

The variational formulation of (5.11) is equivalent to the reference minimization problem in (3.93), such that $\mathcal{E}\approx\widehat{\mathcal{E}}$, yields

$$\boxed{\boldsymbol{s}=\arg\{\min_{\boldsymbol{\varphi}_C\in\boldsymbol{V}_C,\boldsymbol{\varphi}_L\in\boldsymbol{V}_L,\boldsymbol{\varphi}_\Gamma\in\boldsymbol{H}^1(\Gamma),s_L\in W_{L,in}}\ \max_{\boldsymbol{\lambda}_C,\boldsymbol{\lambda}_L\in\mathbf{L}^2(\Gamma)}[\,\widehat{\mathcal{E}}(\boldsymbol{\varphi}_C,\boldsymbol{\varphi}_L,s_L,\boldsymbol{\varphi}_\Gamma,\boldsymbol{\lambda}_C,\boldsymbol{\lambda}_L;H_J)\,]\},} \tag{5.12}$$

where $\boldsymbol{s}:=(\boldsymbol{\varphi}_C,\boldsymbol{\varphi}_L,s_L,\boldsymbol{\varphi}_\Gamma,\boldsymbol{\lambda}_C,\boldsymbol{\lambda}_L)$. Accordingly, the displacement field $\boldsymbol{\varphi}$ as a minimizer of the (3.93) is decomposed as

$$\boldsymbol{\varphi}(\boldsymbol{X},t)=\begin{cases}\boldsymbol{\varphi}_L(\boldsymbol{X},t) & \text{for } \boldsymbol{X}\in\mathcal{B}_L,\\ \boldsymbol{\varphi}_C(\boldsymbol{X},t) & \text{for } \boldsymbol{X}\in\mathcal{B}_C,\\ \boldsymbol{\varphi}_\Gamma(\boldsymbol{X},t) & \text{for } \boldsymbol{X}\in\Gamma,\end{cases} \tag{5.13}$$

which is based on the solution triple $(\boldsymbol{\varphi}_C,\boldsymbol{\varphi}_L,\boldsymbol{\varphi}_\Gamma)$ as a minimizer of the (5.11). Note, the representation for s in terms of s_L which is defined by (4.3) remains also same at finite strain setting.

5.2. Global-Local formulation

In this section, the resulting formulation is extended toward the Global-Local setting. Specifically, we present the Global-Local formulation of the crack phase-field for the quasi-brittle material undergoing finite strain.

Let us define open and bounded fictitious domain $\mathcal{B}_F$ to *recover the space* of $\mathcal{B}$ that is obtained by removing $\mathcal{B}_L$ from its continuum domain; see Fig. 5.2. Indeed, fictitious domain is prolongation of the $\mathcal{B}_C$ towards $\mathcal{B}$. This gives the same constitutive modeling used in $\mathcal{B}_C$ for $\mathcal{B}_F$. Thus, the energy functional of the complementary and fictitious domain is one to one. We also use the identical discretization space for both $\mathcal{B}_F$ and $\mathcal{B}_C$, results $h_F:=h_C$. We further define, open and bounded *global domain* $\mathcal{B}_G$ such that $\mathcal{B}_G=\mathcal{B}_F\cup\Gamma\cup\mathcal{B}_C$. It yields the same energy functional for $\mathcal{B}_C$, $\mathcal{B}_F$ and $\mathcal{B}_G$. Hence, the martial parameters are identical for $\mathcal{B}_C$, $\mathcal{B}_F$ and $\mathcal{B}_G$. Additionally, this unification yields the identical discretization space for global domain compare to $\mathcal{B}_F$ and $\mathcal{B}_C$, results $h_G\approx h_F\approx h_C$, refer to the element size.

The global domain is assumed to be free from any given imperfection. Let us also define, global and local interface denoted as $\Gamma_G\subset\mathcal{B}_G$ and $\Gamma_L\subset\mathcal{B}_L$, such that in the continuum setting we have $\Gamma=\Gamma_G=\Gamma_L$. However in a discrete setting we might have $\Gamma\neq\Gamma_G\neq\Gamma_L$ due to the presence of different meshing scheme (i.e., different element size/type used in $\mathcal{B}_G$ and $\mathcal{B}_L$ such that $h\neq h_L\neq h_G$ on Γ); see Chapter 6 for a detailed discussion.

Furthermore, it is assumed that there exists a continuous prolongation of $\boldsymbol{\varphi}_C$ into $\mathcal{B}_F$. Hence, we introduce a function $\boldsymbol{\varphi}_G \in \mathbf{V}(\mathcal{B}_G)$ such that $\boldsymbol{\varphi}_G|_{\mathcal{B}_C} \equiv \boldsymbol{\varphi}_C$ and $\boldsymbol{\varphi}_G = \boldsymbol{\varphi}_C$ on Γ in the sense of trace on the undeformed configuration. Thus, the boundary conditions for the $\mathcal{B}_G$ is same as $\mathcal{B}_C$, therefore $\boldsymbol{\varphi}_G = \bar{\boldsymbol{\varphi}}$ on $\partial_D\mathcal{B}$ and $\boldsymbol{\tau} = \bar{\boldsymbol{\tau}}$ on $\Gamma_{N,G}$. By means of the fictitious domain, the first term in (5.11) is recast as follows:

$$\begin{aligned}\int_{\mathcal{B}_C} w(\boldsymbol{C}(\boldsymbol{\varphi}_C), 1, 0; 1)\,\mathrm{d}\boldsymbol{X} &= \int_{\mathcal{B}_C} w(\boldsymbol{C}(\boldsymbol{\varphi}_G), 1, 0; 1)\,\mathrm{d}\boldsymbol{X} \\ &= \int_{\mathcal{B}_G} w(\boldsymbol{C}(\boldsymbol{\varphi}_G), 1, 0; 1)\,\mathrm{d}\boldsymbol{X} - \int_{\mathcal{B}_F} w(\boldsymbol{C}(\boldsymbol{\varphi}_G), 1, 0; 1)\,\mathrm{d}\boldsymbol{X}.\end{aligned} \tag{5.14}$$

Note, we substitute $\boldsymbol{\varphi}_G$ for $\boldsymbol{\varphi}_C$ in the second and fourth integrals in (5.14). That is trivial by means of the prolongation concept such that $\boldsymbol{\varphi}_G|_{\mathcal{B}_F} \equiv \boldsymbol{\varphi}_F$ and $\boldsymbol{\varphi}_G = \boldsymbol{\varphi}_F$ on Γ.

This gives the *Global-Local* approximation of the reference energy functional $\mathcal{E}$ indicated in Formulation 3.2.2 by the following Formulation.

Formulation 5.2.1 (Global-Local energy functional applied to the isotropic crack topology)**.** *Let* λ, μ *be given with the initial conditions* $\boldsymbol{\varphi}_0 = \boldsymbol{\varphi}(\boldsymbol{X}, 0)$ *and* $s_0 = s(\boldsymbol{X}, 0)$. *For the loading increments* $n = 1, 2, \dots, N$, *find* $\boldsymbol{\varphi}_G := \boldsymbol{\varphi}_G^n \in \mathbf{V_G}$, $\boldsymbol{\varphi}_L := \boldsymbol{\varphi}_L^n \in \mathbf{V_L}$, $\boldsymbol{\varphi}_\Gamma := \boldsymbol{\varphi}_\Gamma^n \in \mathbf{H}^1(\Gamma)$, $s_L := s_L^n \in W_{L,in}$, $\boldsymbol{\lambda}_C := \boldsymbol{\lambda}_C^n \in \mathbf{L}^2(\Gamma)$ *and* $\boldsymbol{\lambda}_L := \boldsymbol{\lambda}_L^n \in \mathbf{L}^2(\Gamma)$, *such*

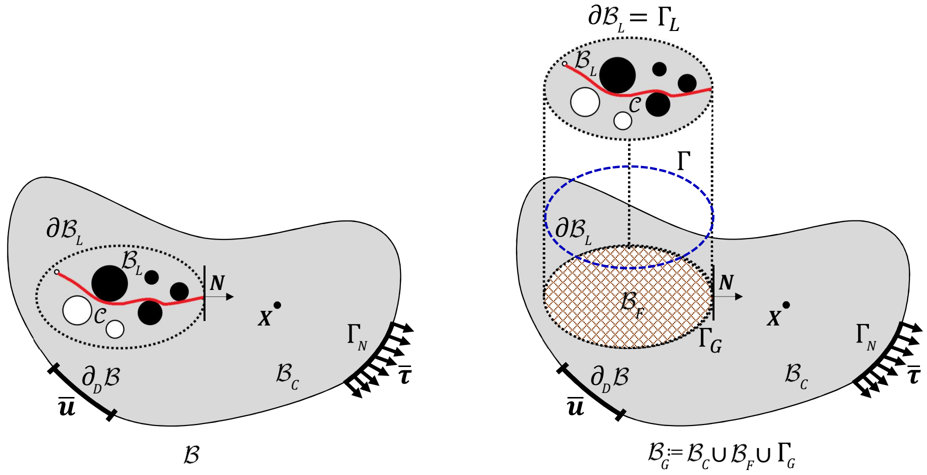

Figure 5.2: Illustration of the (*a*) geometry and loading setup of the reference BVP in the undeformed configuration, and (*b*) Global-Local setting, by the introduction of the fictitious domain $\mathcal{B}_F$ through prolongation of $\mathcal{B}_C$ to the entire domain whereas its unification is so-called global domain $\mathcal{B}_G := \mathcal{B}_C \cup \Gamma_G \cup \mathcal{B}_F$ at the undeformed configuration.

that the functional

$$
\begin{aligned}
\widetilde{\mathcal{E}}(&\boldsymbol{\varphi}_G, \boldsymbol{\varphi}_L, s_L, \boldsymbol{\varphi}_\Gamma, \boldsymbol{\lambda}_C, \boldsymbol{\lambda}_L; H_J) \\
&:= \underbrace{\int_{\mathcal{B}_G} w(\boldsymbol{C}_G, 1, 0; 1)\,\mathrm{d}\boldsymbol{X} - \int_{\mathcal{B}_F} w(\boldsymbol{C}_F, 1, 0; 1)\,\mathrm{d}\boldsymbol{X} - \int_{\Gamma_{N,G}} \bar{\boldsymbol{\tau}} \cdot \boldsymbol{\varphi}_G\,\mathrm{d}A}_{\textit{global terms}} \\
&+ \underbrace{\int_{\mathcal{B}_L} w(\boldsymbol{C}_L, s_L, \nabla_{\boldsymbol{X}} s_L; H_J)\,\mathrm{d}\boldsymbol{X}}_{\textit{local term}} \\
&+ \underbrace{\int_{\Gamma} \{\boldsymbol{\lambda}_C \cdot (\boldsymbol{\varphi}_\Gamma - \boldsymbol{\varphi}_G) + \boldsymbol{\lambda}_L \cdot (\boldsymbol{\varphi}_\Gamma - \boldsymbol{\varphi}_L)\}\,\mathrm{d}A,}_{\textit{coupling terms}}
\end{aligned}
$$

is minimized and the approximation $\mathcal{E} \equiv \widetilde{\mathcal{E}}$ *holds.*

Note, we are not anymore using $\partial_N \mathcal{B}$ for the applied surface load, and hence $\Gamma_{N,G}$ is considered. This is because the global domain is free from any fracture state. The minimization problem for the Global-Local energy functional given in Formulation 5.2.1 that is applied to the isotropic crack topology takes the following compact form,

$$
\boldsymbol{s} = \arg\{ \min_{\boldsymbol{\varphi}_G \in \boldsymbol{V}_G, \boldsymbol{\varphi}_L \in \boldsymbol{V}_L, \boldsymbol{\varphi}_\Gamma \in\, \mathbf{H}^1(\Gamma), s_L \in W_{L,in}} \; \max_{\boldsymbol{\lambda}_C, \boldsymbol{\lambda}_L \in \mathbf{L}^2(\Gamma)} [\, \widetilde{\mathcal{E}}(\boldsymbol{\varphi}_G, \boldsymbol{\varphi}_L, s_L, \boldsymbol{\varphi}_\Gamma, \boldsymbol{\lambda}_C, \boldsymbol{\lambda}_L; H_J)]\} \;, \tag{5.15}
$$

where $\boldsymbol{s} := (\boldsymbol{\varphi}_G, \boldsymbol{\varphi}_L, s_L, \boldsymbol{\varphi}_\Gamma, \boldsymbol{\lambda}_C, \boldsymbol{\lambda}_L)$. The relation between the solution $\boldsymbol{\varphi}$ of the minimization problem in (3.93) and the solution triple $(\boldsymbol{\varphi}_G, \boldsymbol{\varphi}_L, \boldsymbol{\varphi}_\Gamma)$ of (5.15) reads

$$
\boldsymbol{\varphi} = \begin{cases} \boldsymbol{\varphi}_L, & \text{for } \boldsymbol{X} \in \mathcal{B}_L, \\ \boldsymbol{\varphi}_G, & \text{for } \boldsymbol{X} \in \mathcal{B}_C, \\ \boldsymbol{\varphi}_\Gamma, & \text{for } \boldsymbol{X} \in \Gamma_0. \end{cases}
$$

5.3. Variational formulation for the Global-Local coupling system

Now, we consider the weak formulation of (5.15) by directional derivatives of the functional $\widetilde{\mathcal{E}}$, results in:

$$
\begin{aligned}
\widetilde{\mathcal{E}}_{\boldsymbol{\varphi}_G}(\boldsymbol{s}; \delta\boldsymbol{\varphi}_G) := \int_{\mathcal{B}_G} \frac{1}{2}\mathbf{S}(\boldsymbol{C}_G) : \delta\boldsymbol{C}_G\,\mathrm{d}\boldsymbol{X} - \int_{\mathcal{B}_F} \frac{1}{2}\mathbf{S}(\boldsymbol{C}_G) : \delta\boldsymbol{C}_G\,\mathrm{d}\boldsymbol{X} \\
- \int_{\Gamma_G} \boldsymbol{\lambda}_C \cdot \delta\boldsymbol{\varphi}_G\,\mathrm{d}A - \int_{\Gamma_{N,G}} \bar{\boldsymbol{\tau}} \cdot \delta\boldsymbol{\varphi}_G\,\mathrm{d}A = 0,
\end{aligned} \tag{G}
$$

with $\mathbf{S}(\boldsymbol{C}_G) := \partial_{\boldsymbol{C}_G} w(\boldsymbol{C}(\boldsymbol{\varphi}_G), 1, 1; 1)$ and $\delta\boldsymbol{C}_G = 2sym\big(\boldsymbol{\varphi}_G^T \nabla_{\boldsymbol{X}}(\delta\boldsymbol{\varphi}_G)\big)$ such that $\delta\boldsymbol{\varphi}_G \in \{\mathbf{H}^1(\mathcal{B}_G) : \delta\boldsymbol{\varphi}_G = \mathbf{0} \text{ on } \partial_D\mathcal{B}\}$ is the test function, representing the global weak form problem. The local weak formulations take the following form

$$
\begin{cases}
\widetilde{\mathcal{E}}_{\boldsymbol{\varphi}_L}(\boldsymbol{s}; \delta\boldsymbol{\varphi}_L) := \displaystyle\int_{\mathcal{B}_L} \frac{1}{2}\mathbf{S}(\boldsymbol{C}_L, s_L; H_J) : \delta\boldsymbol{C}_L\,\mathrm{d}\boldsymbol{X} - \int_{\Gamma_L} \boldsymbol{\lambda}_L \cdot \delta\boldsymbol{\varphi}_L\,\mathrm{d}A = 0, \\
\widetilde{\mathcal{E}}_{s_L}(\boldsymbol{s}; \delta s_L) := (1-\kappa)\displaystyle\int_{\mathcal{B}_L} 2s_{L+}\mathcal{H}(\boldsymbol{C}; H_J).\delta s_L \mathrm{d}\boldsymbol{X} + \int_{\mathcal{B}_L} (s_L - 1).\delta s_L \mathrm{d}\boldsymbol{X} \\
\qquad + \displaystyle\int_{\mathcal{B}_L} l^2 \nabla_{\boldsymbol{X}} s_L . \nabla_{\boldsymbol{X}}(\delta s_L)\mathrm{d}\boldsymbol{X} = 0,
\end{cases} \tag{L}
$$

where $\boldsymbol{S}(\boldsymbol{\varphi}_L, s_L; H_J) = \partial_{\boldsymbol{C}_L} w(\boldsymbol{C}_L, s_L, \nabla_{\boldsymbol{X}} s_L; H_J)$ defined in (3.85) and $\delta \boldsymbol{C}_L = 2sym\left(\boldsymbol{\varphi}_L^T \nabla_{\boldsymbol{X}}(\delta \boldsymbol{\varphi}_L)\right)$ such that $\delta \boldsymbol{\varphi}_L \in \mathbf{H}^1(\mathcal{B}_L)$ is the local test function and $\delta s_L \in \mathrm{H}^1(\mathcal{B}_L)$ is the local phase-field test function.

The variational derivatives of $\widetilde{\mathcal{E}}$ with respect to $(\boldsymbol{\varphi}_\Gamma, \boldsymbol{\lambda}_C, \boldsymbol{\lambda}_L)$ gives kinematic equations due to weak coupling between them which yields

$$\widetilde{\mathcal{E}}_{\boldsymbol{\varphi}_\Gamma}(\boldsymbol{s}; \delta \boldsymbol{\varphi}_\Gamma) := \int_\Gamma (\boldsymbol{\lambda}_C + \boldsymbol{\lambda}_L) \cdot \delta \boldsymbol{\varphi}_\Gamma \, \mathrm{d}A = 0, \tag{C$_1$}$$

$$\widetilde{\mathcal{E}}_{\boldsymbol{\lambda}_C}(\boldsymbol{s}; \delta \boldsymbol{\lambda}_C) := \int_\Gamma (\boldsymbol{\varphi}_\Gamma - \boldsymbol{\varphi}_G) \cdot \delta \boldsymbol{\lambda}_C \, \mathrm{d}A = 0, \tag{C$_2$}$$

$$\widetilde{\mathcal{E}}_{\boldsymbol{\lambda}_L}(\boldsymbol{s}; \delta \boldsymbol{\lambda}_L) := \int_\Gamma (\boldsymbol{\varphi}_\Gamma - \boldsymbol{\varphi}_L) \cdot \delta \boldsymbol{\lambda}_L \, \mathrm{d}A = 0. \tag{C$_3$}$$

Herein $\delta \boldsymbol{\varphi}_\Gamma \in \mathbf{H}^1(\Gamma)$, and $\delta \boldsymbol{\lambda}_C, \delta \boldsymbol{\lambda}_L \in \mathbf{L}^2(\Gamma)$ are the corresponding test functions.

Let us now focus on the global variational form in (G). The presence of the two domain integrals, namely, over $\mathcal{B}_G$ and $\mathcal{B}_F$ would imply in this case the need to simultaneously access the corresponding stiffness matrices. Avoiding this can be done as follows: We focus on the domain integral over $\mathcal{B}_F$ in (G). The idea is to transform the domain integral in $\mathcal{B}_F$ to the global interface Γ_G. The divergence theorem leads to

$$\int_{\mathcal{B}_F} \frac{1}{2} \mathbf{S}(\boldsymbol{C}_G) : \delta \boldsymbol{C}_G \, \mathrm{d}\boldsymbol{X} = -\int_{\mathcal{B}_F} \mathrm{Div}(\boldsymbol{P}(\boldsymbol{\varphi}_G)) \cdot \delta \boldsymbol{\varphi}_G \, \mathrm{d}\boldsymbol{X} + \int_{\partial \mathcal{B}_F} \boldsymbol{P}(\boldsymbol{\varphi}_G) \cdot \boldsymbol{N}_{\partial \mathcal{B}_F} \cdot \delta \boldsymbol{\varphi}_G \, \mathrm{d}A, \tag{5.16}$$

where $\boldsymbol{n}_{\partial \mathcal{B}_F}$ is the unit outward normal vector to $\partial \mathcal{B}_F$.

The first term in the right-hand side of in (5.16) can be canceled using the divergence-free assumption for the stress (no body forces applied in $\mathcal{B}_F$). Following a detailed argument has been done in Gerasimov et al. [48] (Section 3.3), the second term can be further simplified

$$\int_{\partial \mathcal{B}_F} \boldsymbol{P}(\boldsymbol{\varphi}_G) \cdot \boldsymbol{N}_{\partial \mathcal{B}_F} \cdot \delta \boldsymbol{\varphi}_G \, \mathrm{d}A = \int_{\Gamma_G} \boldsymbol{P}(\boldsymbol{\varphi}_G) \cdot \boldsymbol{N}_\Gamma \cdot \delta \boldsymbol{\varphi}_G \, \mathrm{d}A + \int_{\partial \mathcal{B}_F \cap \Gamma_{N,G}} \bar{\boldsymbol{\tau}} \cdot \delta \boldsymbol{\varphi}_G \, \mathrm{d}A.$$

Here, $\boldsymbol{n}_\Gamma := \boldsymbol{n}_{\partial \mathcal{B}_F}$ denotes the normal vector on Γ_G, outward of $\mathcal{B}_F$, as illustrated in Fig. 5.2. Furthermore, it is possible to choose $\mathcal{B}_L$ and its coarse representation into the global level as $\mathcal{B}_F$ such that $\partial \mathcal{B}_F \cap \Gamma_{N,G} = \emptyset$. This is in line with the assumption introduced in Section 5.1 such that in the local domain $\mathcal{B}_L$ and additionally $\mathcal{B}_F$, is free from any applied external load. Thus, the last surface integral cancels, which finally, (5.16) restated as,

$$\int_{\mathcal{B}_F} \frac{1}{2} \mathbf{S}(\boldsymbol{C}_G) : \delta \boldsymbol{C}_G \, \mathrm{d}\boldsymbol{X} = \int_{\Gamma_G} \boldsymbol{P}(\boldsymbol{\varphi}_G) \cdot \boldsymbol{N}_\Gamma \cdot \delta \boldsymbol{\varphi}_G \, \mathrm{d}A, \tag{5.17}$$

such that there exists fictitious Lagrange multiplier $\boldsymbol{\lambda}_F \in \mathbf{L}^2(\Gamma)$ with

$$\int_{\Gamma_G} \boldsymbol{P}(\boldsymbol{\varphi}_G) \cdot \boldsymbol{N}_\Gamma \cdot \delta \boldsymbol{\varphi}_G \, \mathrm{d}A =: \int_{\Gamma_G} \boldsymbol{\lambda}_F \cdot \delta \boldsymbol{\varphi}_G \, \mathrm{d}A, \tag{5.18}$$

holds. Here, $\boldsymbol{\lambda}_F$ denoted as traction-like quantity to be the outward normal vector on Γ_G. Due to (5.17)−5.18, the *partitioned* representation of equation (G) takes the following form

$$\int_{\mathcal{B}_G} \frac{1}{2} \mathbf{S}(\boldsymbol{C}_G) : \delta \boldsymbol{C}_G \, \mathrm{d}\boldsymbol{X} - \int_{\Gamma_G} \boldsymbol{\lambda}_F \cdot \delta \boldsymbol{\varphi}_G \, \mathrm{d}A - \int_{\Gamma_G} \boldsymbol{\lambda}_C \cdot \delta \boldsymbol{\varphi}_G \, \mathrm{d}A - \int_{\Gamma_{N,G}} \bar{\boldsymbol{\tau}} \cdot \delta \boldsymbol{\varphi}_G \, \mathrm{d}A = 0, \tag{G$_1$}$$

with $\boldsymbol{\lambda}_F$ satisfying

$$\int_{\Gamma_G} \boldsymbol{\lambda}_F \cdot \delta\boldsymbol{\varphi}_G \,\mathrm{d}A = \int_{\mathcal{B}_F} \frac{1}{2}\mathbf{S}(\boldsymbol{C}_G) : \delta\boldsymbol{C}_G \,\mathrm{d}\boldsymbol{X}. \tag{G$_2$}$$

Equations (G_1), (G_2) refers to a global system of equations. The system of equations (L) is called a local variational equation and additionally (C_1), (C_2), (C_3) refer to the coupling terms. The entire system is denoted as the *Global-Local approach* at finite strain.

5.4. $g/l-1$: Dirichlet-Neumann-type boundary conditions

To accommodate a Global-Local computational scheme, instead of finding the stationary solution of the (G_1), (G_2), (L) along with (C_1), (C_2), (C_3) in the monolithic sense, an alternate minimization scheme is used. This is in line with [48], which leads to the Global-Local formulation through the concept of non-intrusive coupling, i.e., global and local level solved in a multiplicative manner according to the idea of Schwarz alternating method [103]. We refer to this type of Global-Local formulation by $g/l-1$ method.

Let $k \geq 0$ be the Global-Local iteration index at a fixed loading step n. The summary of the solution operations to be performed at any iteration k of the procedure, is as follows:

- Dirichlet local problem: solution of local problem (L) coupled with (C_3),
- Pre-processing global level: recovery phase using (C_1) and (G_2),
- Neumann global problem: solution of global problem (G_1),
- Post-processing global level: recovery phase using (C_2).

The detailed procedure scheme including the iteration $k=0$, is depicted in Algorithm 4. Accordingly, Fig. 5.3a depicts one iteration of the Global-Local approach by means of the Dirichlet-Neumann-type boundary conditions.

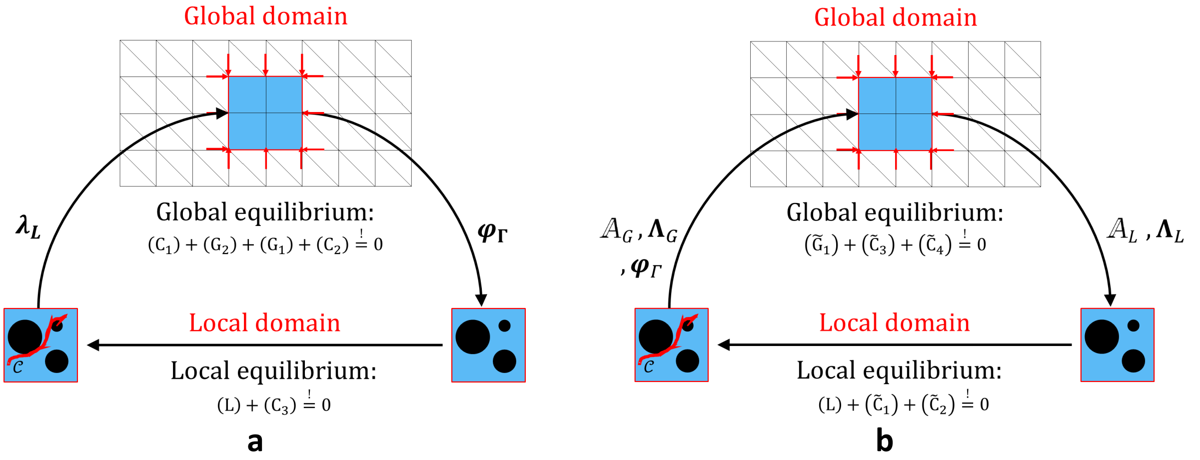

Figure 5.3: Global-Local scheme at finite strain. (*a*) Dirichlet-Neumann-type boundary conditions $g/l-1$, and (*b*) Robin-type boundary conditions $g/l-2$.

5.5. Accuracy/convergence check

Derivation of the convergence and stopping criteria for the Global-Local iterative solution process in Algorithm 4 is similar to the small deformation setting. In fact, at any iteration $k \geq 1$, the solution outcome is denoted as $(\boldsymbol{\varphi}_G^k, \boldsymbol{\varphi}_L^k, s_L^k, \boldsymbol{\varphi}_\Gamma^k, \boldsymbol{\lambda}_C^k, \boldsymbol{\lambda}_L^k)$. Plugging this in equations (G_1), (G_2), (L), (C_1), (C_2), (C_3), the imbalanced quantities reads,

$$\int_\Gamma (\boldsymbol{\varphi}_\Gamma^k - \boldsymbol{\varphi}_L^k) \cdot \delta\boldsymbol{\lambda}_L \neq 0 \quad \texttt{and} \quad \int_\Gamma \boldsymbol{\lambda}_F^k \cdot \delta\boldsymbol{\varphi}_G \neq \int_{\mathcal{B}_F} \frac{1}{2}\mathbf{S}(\boldsymbol{C}_G^k) : \delta\boldsymbol{C}_G \,\mathrm{d}\boldsymbol{X}. \tag{5.19}$$

Therefore, the solution accuracy at iteration k is measured by the quantity

$$\mathrm{Res}_{\mathrm{GL}}^k := \mathrm{Res}_{\mathrm{Stag}}^{\text{'last } k\text{'}} + |\int_\Gamma (\boldsymbol{\varphi}_\Gamma^k - \boldsymbol{\varphi}_L^k) \cdot \delta\boldsymbol{\lambda}_L| + |\int_\Gamma (\boldsymbol{\lambda}_F^k - \boldsymbol{\lambda}_F^{k+1}) \cdot \delta\boldsymbol{\varphi}_G|, \quad \forall\, \delta\boldsymbol{\lambda}_L, \delta\boldsymbol{\varphi}_G. \tag{5.20}$$

The stopping criterion for the Global-Local loop can then be defined as

$$\mathrm{Res}_{\mathrm{GL}}^k \leq \texttt{TOL}_{\mathrm{GL}}, \tag{5.21}$$

with $\texttt{TOL}_{\mathrm{GL}}$ to be prescribed. Owing to the 'nested in' nature of the staggered process, it has to be $\texttt{TOL}_{\mathrm{Stag}} < \texttt{TOL}_{\mathrm{GL}}$. Recalling that $\texttt{TOL}_{\mathrm{Stag}} = 10^{-5}$, we set $\texttt{TOL}_{\mathrm{GL}} := 10^{-4}$. In our computations (i.e., Algorithm 4), we use a more convenient form of the stopping criterion. Setting

$$\eta_{\boldsymbol{\varphi}}^k := \left\|\boldsymbol{\varphi}_\Gamma^k - \boldsymbol{\varphi}_L^k\right\|_{\mathbf{L}^2(\Gamma)}, \quad \eta_{\boldsymbol{\lambda}}^k := \left\|\boldsymbol{\lambda}_F^k - \boldsymbol{\lambda}_F^{k+1}\right\|_{\mathbf{L}^2(\Gamma)},$$

we define $\eta^k := \sqrt{(\eta_{\boldsymbol{\varphi}}^k)^2 + (\eta_{\boldsymbol{\lambda}}^n)^2}$, and use this quantity to now check

$$\eta^k \leq \widetilde{\texttt{TOL}}_{\mathrm{GL}} := 10^{-6}.$$

This choice of $\widetilde{\texttt{TOL}}_{\mathrm{GL}}$ fulfills the requirement $\eta^k \overset{!}{<} \texttt{TOL}_{\mathrm{GL}} - \texttt{TOL}_{\mathrm{Stag}}$, which is stipulated by (5.20), (5.21).

Algorithm 4 *Global-Local iterative scheme combined with Dirichlet-Neumann-type boundary conditions namely g/l − 1.*

```
Input: loading data $(\bar{\boldsymbol{\varphi}}_n, \bar{\boldsymbol{\tau}}_n)$ on $\partial_D\mathcal{B}$ and $\Gamma_N$, respectively;
       solution $(\boldsymbol{\varphi}_{G,n-1}, \boldsymbol{\varphi}_{L,n-1}, s_{L,n-1}, \boldsymbol{\varphi}_{\Gamma,n-1}, \boldsymbol{\lambda}_{C,n-1}, \boldsymbol{\lambda}_{L,n-1})$ and $\mathcal{H}_{L,n-1}$ from step $n-1$.

    Initialization, $k = 0$:
      • given $\boldsymbol{\lambda}_{C,n-1}$, set $\boldsymbol{\lambda}_{C,n-1} =: \boldsymbol{\lambda}_C^0$,
      • given $\boldsymbol{\varphi}_{G,n-1}$, solve
            $\int_{\Gamma_G} \boldsymbol{\lambda}_F \cdot \delta\boldsymbol{\varphi}_G \, \mathrm{d}A = \int_{\mathcal{B}_F} \frac{1}{2}\mathbf{S}(\boldsymbol{C}_{G,n-1}) : \delta\boldsymbol{C}_G \, \mathrm{d}\boldsymbol{X},$
        for $\boldsymbol{\lambda}_F$, set $\boldsymbol{\lambda}_F =: \boldsymbol{\lambda}_F^0$,
      • given $\boldsymbol{\lambda}_F^0$ and $\boldsymbol{\lambda}_C^0$, solve
            $\int_{\mathcal{B}_G} \frac{1}{2}\mathbf{S}(\boldsymbol{C}_G) : \delta\boldsymbol{C}_G \, \mathrm{d}\boldsymbol{X} - \int_{\Gamma_G} \boldsymbol{\lambda}_F^0 \cdot \delta\boldsymbol{\varphi}_G \, \mathrm{d}A - \int_{\Gamma_G} \boldsymbol{\lambda}_C^0 \cdot \delta\boldsymbol{\varphi}_G \, \mathrm{d}A - \int_{\Gamma_{N,G}} \bar{\boldsymbol{\tau}} \cdot \delta\boldsymbol{\varphi}_G \, \mathrm{d}A = 0,$
        for $\boldsymbol{\varphi}_G$, set $\boldsymbol{\varphi}_G =: \boldsymbol{\varphi}_G^0$,
      • given $\boldsymbol{\varphi}_G^0$, solve
            $\int_{\Gamma} (\boldsymbol{\varphi}_\Gamma - \boldsymbol{\varphi}_G^0) \cdot \delta\boldsymbol{\lambda}_C \, \mathrm{d}A = 0$
        for $\boldsymbol{\varphi}_\Gamma$, set $\boldsymbol{\varphi}_\Gamma =: \boldsymbol{\varphi}_\Gamma^0$.

Global-Local iteration $k \geq 1$:
    Local boundary value problem:
        • given $\boldsymbol{\varphi}_\Gamma^{k-1}, \mathcal{H}_{L,n-1}$, solve
              phase-field part:
                $(1-\kappa) \int_{\mathcal{B}_L} 2s_{L+}\mathcal{H}(\boldsymbol{C}_L; H_J).\delta s_L \mathrm{d}\boldsymbol{X} + \int_{\mathcal{B}_L} (s_L - 1).\delta s_L \mathrm{d}\boldsymbol{X}$
                  $+ \int_{\mathcal{B}_L} l^2 \nabla_{\boldsymbol{X}} s_L . \nabla_{\boldsymbol{X}}(\delta s_L) \mathrm{d}\boldsymbol{X} = 0,$
              mechanical part:
                $\begin{cases} \int_{\mathcal{B}_L} \frac{1}{2}\mathbf{S}(\boldsymbol{C}_L, s_L; H_J) : \delta\boldsymbol{C}_L \, \mathrm{d}\boldsymbol{X} - \int_{\Gamma_L} \boldsymbol{\lambda}_L \cdot \delta\boldsymbol{\varphi}_L \, \mathrm{d}A = 0, \\ \int_{\Gamma} (\boldsymbol{\varphi}_\Gamma^{k-1} - \boldsymbol{\varphi}_L) \cdot \delta\boldsymbol{\lambda}_L \, \mathrm{d}A = 0, \end{cases}$
          set $(\boldsymbol{\varphi}_L, s_L, \boldsymbol{\lambda}_L) =: (\boldsymbol{\varphi}_L^k, s_L^k, \boldsymbol{\lambda}_L^k)$,
    Global boundary value problem:
        • given $\boldsymbol{\lambda}_L^k$, solve
              $\int_{\Gamma} (\boldsymbol{\lambda}_C + \boldsymbol{\lambda}_L^k) \cdot \delta\boldsymbol{\varphi}_\Gamma \, \mathrm{d}A = 0$
          for $\boldsymbol{\lambda}_C$, set $\boldsymbol{\lambda}_C =: \boldsymbol{\lambda}_C^k$,
      • given $\boldsymbol{\varphi}_G^{k-1}$, solve
            $\int_{\Gamma_G} \boldsymbol{\lambda}_F \cdot \delta\boldsymbol{\varphi}_G \, \mathrm{d}A = \int_{\mathcal{B}_F} \frac{1}{2}\mathbf{S}(\boldsymbol{C}_G(\boldsymbol{\varphi}_G^{k-1})) : \delta\boldsymbol{C}_G \, \mathrm{d}\boldsymbol{X},$
        for $\boldsymbol{\lambda}_F$, set $\boldsymbol{\lambda}_F =: \boldsymbol{\lambda}_F^k$,
      • given $\boldsymbol{\lambda}_F^k$ and $\boldsymbol{\lambda}_C^k$, solve
            $\int_{\mathcal{B}_G} \frac{1}{2}\mathbf{S}(\boldsymbol{C}_G) : \delta\boldsymbol{C}_G \, \mathrm{d}\boldsymbol{X} - \int_{\Gamma_G} \boldsymbol{\lambda}_F^k \cdot \delta\boldsymbol{\varphi}_G \, \mathrm{d}A - \int_{\Gamma_G} \boldsymbol{\lambda}_C^k \cdot \delta\boldsymbol{\varphi}_G \, \mathrm{d}A - \int_{\Gamma_{N,G}} \bar{\boldsymbol{\tau}} \cdot \delta\boldsymbol{\varphi}_G \, \mathrm{d}A = 0,$
        for $\boldsymbol{\varphi}_G$, set $\boldsymbol{\varphi}_G =: \boldsymbol{\varphi}_G^k$,
      • given $\boldsymbol{\varphi}_G^k$, solve
            $\int_{\Gamma} (\boldsymbol{\varphi}_\Gamma - \boldsymbol{\varphi}_G^k) \cdot \delta\boldsymbol{\lambda}_C \, \mathrm{d}A = 0$
        for $\boldsymbol{\varphi}_\Gamma$, set $\boldsymbol{\varphi}_\Gamma =: \boldsymbol{\varphi}_\Gamma^k$.

      • Accuracy/convergence check: $\eta^k \leq \widetilde{\mathtt{TOL}}_{\mathrm{GL}}$,
      • if fulfilled, set $(\boldsymbol{\varphi}_G^k, \boldsymbol{\varphi}_L^k, s_L^k, \boldsymbol{\varphi}_\Gamma^k, \boldsymbol{\lambda}_C^k, \boldsymbol{\lambda}_L^k) =: (\boldsymbol{\varphi}_{G,n}, \boldsymbol{\varphi}_{L,n}, s_{L,n}, \boldsymbol{\varphi}_{\Gamma,n}, \boldsymbol{\lambda}_{C,n}, \boldsymbol{\lambda}_{L,n})$ and stop;
        else $k+1 \to k$.

Output: solution $(\boldsymbol{\varphi}_{G,n}, \boldsymbol{\varphi}_{L,n}, s_{L,n}, \boldsymbol{\varphi}_{\Gamma,n}, \boldsymbol{\lambda}_{C,n}, \boldsymbol{\lambda}_{L,n})$.
```

5.6. $g/l-2$: Robin-type boundary conditions

This section presents the Global-Local formulation, which is enhanced with Robin-type boundary conditions toward the large deformation setting. Using the Robin-type boundary conditions, we aim to relax the stiff local response, which is observed at the global level. Additionally, this helps resolve the imbalanced quantities mentioned in (5.19) and accelerate the Global-Local computational iterations. We refer to this type of Global-Local formulation by $g/l-2$ method.

Similar to the Global-Local formulation at small deformation, we introduce the Robin-type boundary conditions for the local and global levels.

- ***Robin-type boundary conditions at the local level***

At the local level, the new coupling term is introduced as a linear combination of (C$_1$) and (C$_2$), through

$$\widetilde{\mathcal{E}}_{\boldsymbol{\varphi}_\Gamma}(\boldsymbol{s};\delta\boldsymbol{\varphi}_\Gamma)+\mathbb{A}_L\widetilde{\mathcal{E}}_{\boldsymbol{\lambda}_C}(\boldsymbol{s};\delta\boldsymbol{\lambda}_C):=\int_\Gamma(\boldsymbol{\lambda}_C+\boldsymbol{\lambda}_L)\cdot\delta\boldsymbol{\varphi}_\Gamma\,\mathrm{d}A+\mathbb{A}_L\int_\Gamma(\boldsymbol{\varphi}_\Gamma-\boldsymbol{\varphi}_G)\cdot\delta\boldsymbol{\lambda}_C\,\mathrm{d}A=0. \tag{5.22}$$

We write this for the iteration k, as follows:

$$\int_\Gamma(\boldsymbol{\lambda}_C^{k-1}+\boldsymbol{\lambda}_L^{k})\cdot\delta\boldsymbol{\varphi}_\Gamma\,\mathrm{d}A+\mathbb{A}_L\int_\Gamma(\boldsymbol{\varphi}_\Gamma^{k,\frac{1}{2}}-\boldsymbol{\varphi}_G^{k-1})\cdot\delta\boldsymbol{\lambda}_C\,\mathrm{d}A=0. \tag{5.23}$$

Herein, $\mathbb{A}_L$ is a local augmented stiffness matrix applied at the interface. By means of (5.23) at iteration k, the local system of equation is equipped through the following boundary conditions,

$$\int_\Gamma\boldsymbol{\lambda}_L^{k}\cdot\delta\boldsymbol{\varphi}_\Gamma\,\mathrm{d}A+\mathbb{A}_L\int_\Gamma\boldsymbol{\varphi}_\Gamma^{k,\frac{1}{2}}\cdot\delta\boldsymbol{\lambda}_C\,\mathrm{d}A=\boldsymbol{\Lambda}_L^{k-1}, \tag{$\widetilde{\mathrm{C}}_1$}$$

$$\int_\Gamma(\boldsymbol{\varphi}_\Gamma^{k,\frac{1}{2}}-\boldsymbol{\varphi}_L^{k})\cdot\delta\boldsymbol{\lambda}_L\,\mathrm{d}A=0, \tag{$\widetilde{\mathrm{C}}_2$}$$

with

$$\boldsymbol{\Lambda}_L^{k-1}:=\boldsymbol{\Lambda}_L(\boldsymbol{\lambda}_C^{k-1},\boldsymbol{\varphi}_G^{k-1};\mathbb{A}_L)=\mathbb{A}_L\int_\Gamma\boldsymbol{\varphi}_G^{k-1}\cdot\delta\boldsymbol{\lambda}_C\,\mathrm{d}A-\int_\Gamma\boldsymbol{\lambda}_C^{k-1}\cdot\delta\boldsymbol{\varphi}_\Gamma\,\mathrm{d}A. \tag{5.24}$$

Along with (L), the local system of equations has to be solved for $(\boldsymbol{\varphi}_L^{k},\boldsymbol{\lambda}_L^{k},\boldsymbol{\varphi}_\Gamma^{k,\frac{1}{2}})$ for a given local Robin-type parameters $(\boldsymbol{\Lambda}_L^{k-1},\mathbb{A}_L)$.

- ***Robin-type boundary conditions at the global level***

Accordingly, at the global level, the new coupling term is stated as a linear combination of (C$_1$) and (C$_3$) yields,

$$\widetilde{\mathcal{E}}_{\boldsymbol{\varphi}_\Gamma}(\boldsymbol{s};\delta\boldsymbol{\varphi}_\Gamma)+\mathbb{A}_G\widetilde{\mathcal{E}}_{\boldsymbol{\lambda}_L}(\boldsymbol{s};\delta\boldsymbol{\lambda}_L):=\int_\Gamma(\boldsymbol{\lambda}_C+\boldsymbol{\lambda}_L)\cdot\delta\boldsymbol{\varphi}_\Gamma\,\mathrm{d}A+\mathbb{A}_G\int_\Gamma(\boldsymbol{\varphi}_\Gamma-\boldsymbol{\varphi}_L)\cdot\delta\boldsymbol{\lambda}_L\,\mathrm{d}A=0. \tag{5.25}$$

We write this for the iteration k, as follows:

$$\int_\Gamma (\boldsymbol{\lambda}_C^k + \boldsymbol{\lambda}_L^k) \cdot \delta\boldsymbol{\varphi}_\Gamma \,\mathrm{d}A + \mathbb{A}_G \int_\Gamma (\boldsymbol{\varphi}_\Gamma^k - \boldsymbol{\varphi}_L^k) \cdot \delta\boldsymbol{\lambda}_L \,\mathrm{d}A = 0.$$

Where, $\mathbb{A}_G$ is a global augmented stiffness matrix applied at the interface. Additionally, through (5.25) at iteration k, the Robin-type boundary condition at the global level takes the following form,

$$\int_\Gamma \boldsymbol{\lambda}_C^k \cdot \delta\boldsymbol{\varphi}_\Gamma \,\mathrm{d}A + \mathbb{A}_G \int_\Gamma \boldsymbol{\varphi}_\Gamma^k \cdot \delta\boldsymbol{\lambda}_L \,\mathrm{d}A = \boldsymbol{\Lambda}_G^k, \tag{$\widetilde{\mathrm{C}}_3$}$$

$$\int_\Gamma (\boldsymbol{\varphi}_\Gamma^{k,\frac{1}{2}} - \boldsymbol{\varphi}_G^k) \cdot \delta\boldsymbol{\lambda}_C \,\mathrm{d}A = 0, \tag{$\widetilde{\mathrm{C}}_4$}$$

with

$$\boldsymbol{\Lambda}_G^k := \boldsymbol{\Lambda}_G(\boldsymbol{\lambda}_L^k, \boldsymbol{\varphi}_L^k; \mathbb{A}_G) = \mathbb{A}_G \int_\Gamma \boldsymbol{\varphi}_L^k \cdot \delta\boldsymbol{\lambda}_L \,\mathrm{d}A - \int_\Gamma \boldsymbol{\lambda}_L^k \cdot \delta\boldsymbol{\varphi}_\Gamma \,\mathrm{d}A. \tag{5.26}$$

Together with (G_1) and (G_2), the global system of equations has to be solved for $(\boldsymbol{\varphi}_G^k, \boldsymbol{\lambda}_C^k, \boldsymbol{\varphi}_\Gamma^k)$ for a given $(\boldsymbol{\Lambda}_G^k, \mathbb{A}_G, \boldsymbol{\varphi}_\Gamma^{k,\frac{1}{2}})$. Here, $\mathbb{A}_G$ and $\boldsymbol{\Lambda}_G^k$ stand for a global Robin-type parameters.

Note, based on the new boundary conditions provided in ($\widetilde{\mathrm{C}}_1$), ($\widetilde{\mathrm{C}}_2$), ($\widetilde{\mathrm{C}}_3$) and ($\widetilde{\mathrm{C}}_4$) the imbalanced quantities in the Global-Local iterations read as follows:

$$\int_\Gamma (\boldsymbol{\varphi}_\Gamma^k - \boldsymbol{\varphi}_\Gamma^{k,\frac{1}{2}}) \cdot \delta\boldsymbol{\lambda}_L \,\mathrm{d}A \neq 0 \quad \texttt{and} \quad \int_\Gamma \boldsymbol{\lambda}_F^k \cdot \delta\boldsymbol{\varphi}_G \neq \int_{\mathcal{B}_F} \frac{1}{2}\mathbf{S}(\boldsymbol{C}_G^k) : \delta\boldsymbol{C}_G \,\mathrm{d}\boldsymbol{X}. \tag{5.27}$$

For the specific Robin-type boundary conditions, we can resolve $(5.27)_1$ such that this term is not produced an error in the iterative procedure. To do so, following Appendix A, the global and local augmented stiffness matrix within Robin-type boundary conditions take the following forms

$$\boxed{\mathbb{A}_G = \boldsymbol{L}_L^T \boldsymbol{T}_L^{-T} \boldsymbol{\mathcal{S}}_L \quad \text{and} \quad \mathbb{A}_L := \boldsymbol{\mathcal{S}}_C.} \tag{5.28}$$

Additionally, to achieve a balanced state of $(5.27)_2$, we recall the global weak formulation in (G_1) which we aim to solve for $\boldsymbol{u}_G$, with

$$\int_{\mathcal{B}_G} \frac{1}{2}\mathbf{S}(\boldsymbol{C}_G) : \delta\boldsymbol{C}_G \,\mathrm{d}\boldsymbol{X} - \int_{\Gamma_G} \boldsymbol{\lambda}_F \cdot \delta\boldsymbol{\varphi}_G \,\mathrm{d}A - \int_{\Gamma_G} \boldsymbol{\lambda}_C \cdot \delta\boldsymbol{\varphi}_G \,\mathrm{d}A - \int_{\Gamma_{N,G}} \bar{\boldsymbol{\tau}} \cdot \delta\boldsymbol{\varphi}_G \,\mathrm{d}A = 0, \tag{$\widetilde{\mathrm{G}}_1$}$$

(to distinguish our solver with $g/l-1$, we named it as $\widetilde{\mathrm{G}}_1$ for $g/l-2$ setting) is now equipped with a linearized $\Delta\boldsymbol{\lambda}_F$ satisfying

$$\int_\Gamma \Delta\boldsymbol{\lambda}_F \cdot \delta\boldsymbol{\varphi}_G \,\mathrm{d}A = \int_\Gamma \boldsymbol{\mathcal{S}}_F \Delta\boldsymbol{\varphi}_G \cdot \delta\boldsymbol{\varphi}_G \,\mathrm{d}A, \tag{$\widetilde{\mathrm{G}}_2$}$$

such that (A.7) in Appendix A is used with $\boldsymbol{\varphi}_F = \boldsymbol{\varphi}_G$ on Γ. Notably, we are not solving for $\boldsymbol{\lambda}_F$, and in the linearized setting of ($\widetilde{\mathrm{G}}_1$), the corresponding term (i.e., the second term) is replaced by ($\widetilde{\mathrm{G}}_2$).

The detailed Global-Local formulation by Robin-type boundary conditions is depicted in Algorithm 5. Accordingly, Fig. 5.3b depicts one iteration of the Global-Local coupling scheme namely $g/l-2$.

Algorithm 5 *Global-Local iterative scheme combined with Robin-type boundary conditions namely $g/l-2$.*

```
Input: loading data $(\bar{\boldsymbol{\varphi}}_n, \bar{\boldsymbol{\tau}}_n)$ on $\partial_D\mathcal{B}$ and $\Gamma_{N0}$, respectively;
       solution $(\boldsymbol{\varphi}_{G,n-1}, \boldsymbol{\varphi}_{L,n-1}, s_{L,n-1}, \boldsymbol{\varphi}_{\Gamma,n-1}, \boldsymbol{\lambda}_{C,n-1}, \boldsymbol{\lambda}_{L,n-1})$ and $\mathcal{H}_{L,n-1}$ from step $n-1$.
Global-Local iteration $k \geq 1$:
    Local boundary value problem:
        • given $\mathbb{A}_L, \boldsymbol{\Lambda}_L^{k-1}, \mathcal{H}_{L,n-1}$, solve
              phase-field part:
              $(1-\kappa)\int_{\mathcal{B}_L} 2s_{L+}\mathcal{H}(\boldsymbol{C}_L; H_J).\delta s_L \mathrm{d}\boldsymbol{X} + \int_{\mathcal{B}_L}(s_L-1).\delta s_L \mathrm{d}\boldsymbol{X}$
                $+ \int_{\mathcal{B}_L} l^2 \nabla_{\boldsymbol{X}} s_L . \nabla_{\boldsymbol{X}}(\delta s_L)\mathrm{d}\boldsymbol{X} = 0,$
              mechanical part:
              $\begin{cases} \int_{\mathcal{B}_L} \frac{1}{2}\mathbf{S}(\boldsymbol{C}_L, s_L; H_J) : \delta\boldsymbol{C}_L \,\mathrm{d}\boldsymbol{X} - \int_{\Gamma_L} \boldsymbol{\lambda}_L \cdot \delta\boldsymbol{\varphi}_L \,\mathrm{d}A = 0, \\ \int_\Gamma \boldsymbol{\lambda}_L \cdot \delta\boldsymbol{\varphi}_\Gamma \,\mathrm{d}A + \mathbb{A}_L \int_\Gamma \boldsymbol{\varphi}_\Gamma \cdot \delta\boldsymbol{\lambda}_C \,\mathrm{d}A = \boldsymbol{\Lambda}_L^{k-1}, \\ \int_\Gamma (\boldsymbol{\varphi}_\Gamma - \boldsymbol{\varphi}_L) \cdot \delta\boldsymbol{\lambda}_L \,\mathrm{d}A = 0, \end{cases}$
          set $(\boldsymbol{\varphi}_L, s_L, \boldsymbol{\varphi}_\Gamma, \boldsymbol{\lambda}_L) =: (\boldsymbol{\varphi}_L^k, s_L^k, \boldsymbol{\varphi}_\Gamma^{k,\frac{1}{2}}, \boldsymbol{\lambda}_L^k)$,
        • given $(\boldsymbol{\varphi}_L^k, \boldsymbol{\lambda}_L^k; \mathbb{A}_G)$, set
              $\boldsymbol{\Lambda}_G^k = \mathbb{A}_G \int_\Gamma \boldsymbol{\varphi}_L^k \cdot \delta\boldsymbol{\lambda}_L \,\mathrm{d}A - \int_\Gamma \boldsymbol{\lambda}_L^k \cdot \delta\boldsymbol{\varphi}_\Gamma \,\mathrm{d}A.$
    Global boundary value problem:
        • given $\mathbb{A}_G, \boldsymbol{\Lambda}_G^k, \boldsymbol{\varphi}_\Gamma^{k,\frac{1}{2}}$, solve
              $\begin{cases} \int_{\mathcal{B}_G} \frac{1}{2}\mathbf{S}(\boldsymbol{C}_G) : \delta\boldsymbol{C}_G \,\mathrm{d}\boldsymbol{X} - \int_{\Gamma_G} \boldsymbol{\lambda}_F \cdot \delta\boldsymbol{\varphi}_G \,\mathrm{d}A - \int_{\Gamma_G} \boldsymbol{\lambda}_C \cdot \delta\boldsymbol{\varphi}_G \,\mathrm{d}A \\ \qquad - \int_{\Gamma_{N,G}} \bar{\boldsymbol{\tau}} \cdot \delta\boldsymbol{\varphi}_G \,\mathrm{d}A = 0, \\ \int_\Gamma \boldsymbol{\lambda}_C \cdot \delta\boldsymbol{\varphi}_\Gamma \,\mathrm{d}A + \mathbb{A}_G \int_\Gamma \boldsymbol{\varphi}_\Gamma \cdot \delta\boldsymbol{\lambda}_C \,\mathrm{d}A = \boldsymbol{\Lambda}_G^k, \\ \int_\Gamma (\boldsymbol{\varphi}_\Gamma^{k,\frac{1}{2}} - \boldsymbol{\varphi}_G) \cdot \delta\boldsymbol{\lambda}_C \,\mathrm{d}A = 0, \end{cases}$
          set $(\boldsymbol{\varphi}_G, \boldsymbol{\varphi}_\Gamma, \boldsymbol{\lambda}_C) =: (\boldsymbol{\varphi}_G^k, \boldsymbol{\varphi}_\Gamma^k, \boldsymbol{\lambda}_C^k)$,
        • given $(\boldsymbol{\varphi}_G^k, \boldsymbol{\lambda}_C^k; \mathbb{A}_L)$, set
              $\boldsymbol{\Lambda}_L^k = \mathbb{A}_L \int_\Gamma \boldsymbol{\varphi}_G^k \cdot \delta\boldsymbol{\lambda}_C \,\mathrm{d}A - \int_\Gamma \boldsymbol{\lambda}_C^k \cdot \delta\boldsymbol{\varphi}_\Gamma \,\mathrm{d}A.$
        • if fulfilled, set $(\boldsymbol{\varphi}_G^k, \boldsymbol{\varphi}_L^k, s_L^k, \boldsymbol{\varphi}_\Gamma^k, \boldsymbol{\lambda}_C^k, \boldsymbol{\lambda}_L^k) =: (\boldsymbol{\varphi}_{G,n}, \boldsymbol{\varphi}_{L,n}, s_{L,n}, \boldsymbol{\varphi}_{\Gamma,n}, \boldsymbol{\lambda}_{C,n}, \boldsymbol{\lambda}_{L,n})$ and stop;
          else $k+1 \to k$.
Output: solution $(\boldsymbol{\varphi}_{G,n}, \boldsymbol{\varphi}_{L,n}, s_{L,n}, \boldsymbol{\varphi}_{\Gamma,n}, \boldsymbol{\lambda}_{C,n}, \boldsymbol{\lambda}_{L,n})$.
```

5.7. Finite Element Discretization

An equivalent variational setting at finite strain of the continuous differential equation leads to the minimization problem within a continuous setting by

$$\textit{Find } (\boldsymbol{\varphi}, s) \in \boldsymbol{V} \text{ such that } F(\boldsymbol{\varphi}, s) \leq F(\boldsymbol{v}, g) \;\; \forall(\boldsymbol{v}, g) \in \boldsymbol{V}. \tag{5.29}$$

Here, $(\boldsymbol{\varphi}, s)$ are primary fields that corresponds to the deformation and crack phase-field, respectively, $\boldsymbol{V}$ is a given set of admissible continuous functions such that a functional $F : \boldsymbol{V} \to \mathbb{R}^\delta$ is subjected to minimization. Through finite element discretization techniques (5.29) is rewritten to the finite-dimensional minimization problem in a discrete space through

$$\textit{Find}\ \ (\boldsymbol{\varphi}_h, s_h) \in \boldsymbol{V}_h \ \text{ such that }\ F(\boldsymbol{\varphi}_h, s_h) \leq F(\boldsymbol{v}_h, g_h)\ \ \forall (\boldsymbol{v}_h, g_h) \in \boldsymbol{V}_h, \tag{5.30}$$

for the unknown quantity fields $(\boldsymbol{\varphi}_h, s_h)$. Additionally, $\boldsymbol{V}_h \subset \boldsymbol{V}$ is a given set of admissible discrete functions such that a functional $F : \boldsymbol{V}_h \to \mathbb{R}^\delta$ is subjected to minimization.

Recall, a continuous domain $\mathcal{B}$ is approximated to $\mathcal{B}_h$ such that $\mathcal{B} \approx \mathcal{B}_h$ with non-overlapping finite numbers of elements $\mathcal{B}_e \subset \mathcal{B}_h$; see Fig. 4.7. Both global and local subproblems are discretized with a Galerkin finite element method using H^1-conforming bilinear (2D) elements. Consequently, the discrete spaces have the property $\boldsymbol{V}_h \subset \boldsymbol{V}$ and $W_h \subset W$.

Recall, the continuous primal fields used in the Global-Local formulation, namely $(\boldsymbol{\varphi}_G, \boldsymbol{\varphi}_L,\ s_L, \boldsymbol{\varphi}_\Gamma\ , \boldsymbol{\lambda}_C, \boldsymbol{\lambda}_L)$. In the finite element setting, the continuous primal fields are described based on piecewise polynomial discrete functions, the so-called nodal shape function $N^i(\boldsymbol{\xi})$, associated with node i. The scalar-valued quantity $\hat{\bullet}^i$ represents the nodal value. For the Global-Local approach, we assume the existence of the partitions $\mathcal{B}_{G,e}$ and $\mathcal{B}_{L,e}$. The solution discretizations are given by

$$\boldsymbol{\varphi}^h_G = \sum_i \boldsymbol{N}^{G,i}_{\boldsymbol{\varphi}} \hat{\boldsymbol{\varphi}}^{\,i}_G, \quad \boldsymbol{\varphi}^h_L = \sum_i \boldsymbol{N}^{L,i}_{\boldsymbol{\varphi}} \hat{\boldsymbol{\varphi}}^{\,i}_L, \quad s^h_L = \sum_i N^{L,i}_s \hat{\boldsymbol{s}}^{\,i}_L. \tag{5.31}$$

To construct the discretization of the Lagrange multipliers $\boldsymbol{\lambda}^h_C$, $\boldsymbol{\lambda}^h_L$, $\boldsymbol{\varphi}^h_\Gamma$ and the supplementary quantity $\boldsymbol{\lambda}^h_F$ on Γ, we write

$$\begin{aligned} \boldsymbol{\lambda}^h_C &= \sum_i \boldsymbol{N}^{G,i}_{\lambda,i} \hat{\boldsymbol{\lambda}}^{\,i}_C, \qquad & \boldsymbol{\lambda}^h_L &= \sum_i \boldsymbol{N}^{L,i}_{\lambda} \hat{\boldsymbol{\lambda}}^{\,i}_L, \\ \boldsymbol{\varphi}^h_\Gamma &= \sum_i \boldsymbol{N}^{\Gamma,i}_{\boldsymbol{\varphi}} \hat{\boldsymbol{\varphi}}^{\,i}_\Gamma, \qquad & \boldsymbol{\lambda}^h_F &= \sum_i \boldsymbol{N}^{G,i}_{\lambda} \hat{\boldsymbol{\lambda}}^{\,i}_F, \end{aligned} \tag{5.32}$$

with the following basis function:

$$\boldsymbol{N}^{\bullet,i}_{\square} = \begin{bmatrix} N^{\bullet,i}_{\square} & 0 \\ 0 & N^{\bullet,i}_{\square} \end{bmatrix}, \quad N^{L,i}_s = \begin{bmatrix} N^{L,i}_s \end{bmatrix}. \tag{5.33}$$

Here, $\square$ is related to $\boldsymbol{\lambda}, \boldsymbol{\varphi}$ and $\bullet$ indicates G, L. Accordingly, its constitutive state variables are represented by $(\boldsymbol{F}^h_G, \boldsymbol{F}^h_L, \boldsymbol{G}^h_L)$, through

$$\begin{aligned} \boldsymbol{F}^h_G(\boldsymbol{X}_G) &= \nabla_{\boldsymbol{X}} \boldsymbol{\varphi}^h_G = \sum_i \hat{\boldsymbol{\varphi}}^{\,i}_G \otimes \nabla_0 \boldsymbol{N}^{G,i}_{\boldsymbol{\varphi}} = \sum_i \boldsymbol{B}^{G,i}_{\boldsymbol{\varphi}} \hat{\boldsymbol{\varphi}}^{\,i}_G, \\ \boldsymbol{F}^h_L(\boldsymbol{X}_L) &= \nabla_{\boldsymbol{X}} \boldsymbol{\varphi}^h_{L,i} = \sum_i \hat{\boldsymbol{\varphi}}^{\,i}_L \otimes \nabla_0 \boldsymbol{N}^{L,i}_{\boldsymbol{\varphi}} = \sum_i \boldsymbol{B}^{L,i}_{\boldsymbol{\varphi}} \hat{\boldsymbol{\varphi}}^{\,i}_L, \\ \boldsymbol{G}^h_L(\boldsymbol{X}_L) &= \nabla_{\boldsymbol{X}} s^h_L = \sum_i \hat{s}^{\,i}_L . \nabla_0 \boldsymbol{N}^{L,i}_s = \sum_i \boldsymbol{B}^{L,i}_s \hat{s}^{\,i}_L. \end{aligned} \tag{5.34}$$

Here, $\boldsymbol{B}^{G,i}_{\boldsymbol{\varphi}}$, $\boldsymbol{B}^{L,i}_{\boldsymbol{\varphi}}$, and $\boldsymbol{B}^{L,i}_s$ are the matrix representation for the i^{th} nodal shape function's derivative, corresponding to the global deformation, local deformation and local crack

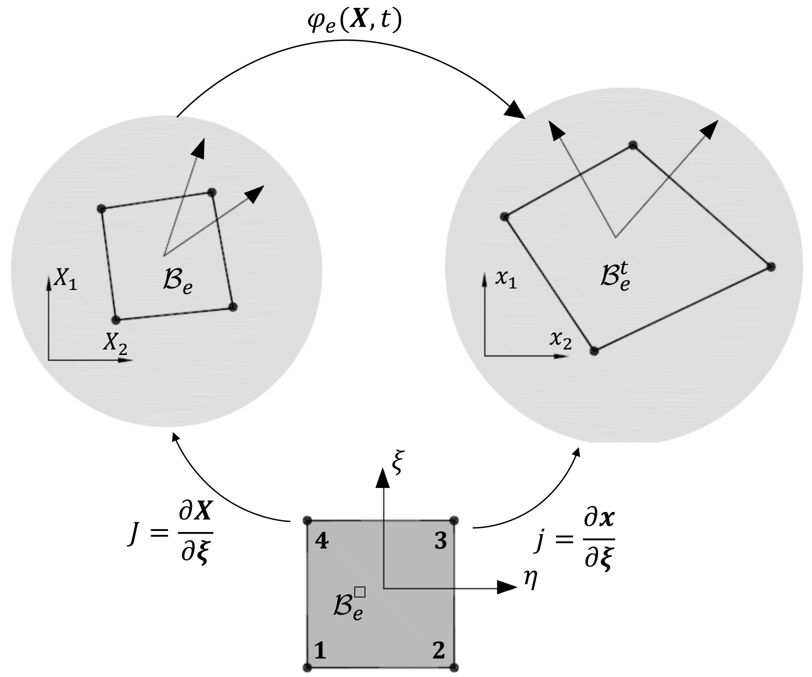

Figure 5.4: Illustration of the isoparametric mapping for the quadrilateral element $\mathcal{B}_e$.

phase-field, respectively. By using the Voigt notation the tensorial constitutive state variables are written in the vectorial form:

$$\boldsymbol{F}^h = [F^h_{11}, F^h_{12}, F^h_{21}, F^h_{22}]^T, \quad \boldsymbol{G}^h = [G^h_1, G^h_2]^T, \tag{5.35}$$

in an analogy to the (5.34). Hence, the $\boldsymbol{B}^i$ matrix in (5.34) takes the following explicit form in a two-dimensional setting through

$$\boldsymbol{B}^{G,i}_{\boldsymbol{\varphi}} = \begin{bmatrix} N^{G,i}_{\boldsymbol{\varphi},1} & 0 \\ N^{G,i}_{\boldsymbol{\varphi},2} & 0 \\ 0 & N^{G,i}_{\boldsymbol{\varphi},1} \\ 0 & N^{G,i}_{\boldsymbol{\varphi},2} \end{bmatrix}, \quad \boldsymbol{B}^{L,i}_{\boldsymbol{\varphi}} = \begin{bmatrix} N^{L,i}_{\boldsymbol{\varphi},1} & 0 \\ N^{L,i}_{\boldsymbol{\varphi},2} & 0 \\ 0 & N^{L,i}_{\boldsymbol{\varphi},1} \\ 0 & N^{L,i}_{\boldsymbol{\varphi},2} \end{bmatrix}, \quad \boldsymbol{B}^{L,i}_{s} = \begin{bmatrix} N^{L,i}_{s,1} \\ N^{L,i}_{s,2} \end{bmatrix}. \tag{5.36}$$

Where the subscript j in $N^{G,i}_{\boldsymbol{\varphi},j}$ denotes the material derivatives of the basis function, namely $\hat{\bullet}_{,j} = \partial_{X_j}\hat{\bullet}$ while superscript i indicates the nodal value.

Figure 5.4 describes the transformation from martial configuration $\mathcal{B}$ and spatial configuration $\mathcal{B}^t$ to the isoparametric configuration denoted by $\mathcal{B}^{\square}$. These mapping performed by the so-called Jacobi mapping matrix via

$$\boldsymbol{J}_{\bullet} = \frac{\partial \boldsymbol{X}}{\partial \boldsymbol{\xi}} = \sum_i \hat{\boldsymbol{X}}^{\;i}_{\bullet} \otimes \frac{\partial N^{\bullet,i}_{\boldsymbol{\varphi}}(\boldsymbol{\xi})}{\partial \boldsymbol{\xi}}, \quad \text{and} \quad \boldsymbol{j}_{\bullet} = \frac{\partial \boldsymbol{\varphi}}{\partial \boldsymbol{\xi}} = \sum_i \hat{\boldsymbol{\varphi}}^{\;i}_{\bullet} \otimes \frac{\partial N^{\bullet;i}_{\boldsymbol{\varphi}}(\boldsymbol{\xi})}{\partial \boldsymbol{\xi}}. \tag{5.37}$$

such that

$$\boldsymbol{F}^h_{\bullet}(\boldsymbol{X}_{\bullet}) = \boldsymbol{j}\boldsymbol{J}^{-1}, \quad \text{with} \quad det\ \boldsymbol{F} = \frac{det\ \boldsymbol{j}}{det\ \boldsymbol{J}}\ . \tag{5.38}$$

Using (5.37), the mapping between the gradients of material and spatial configurations to the isoparametric configurations reads,

$$\frac{\partial N^{\bullet,i}_{\boldsymbol{\varphi}}}{\partial \boldsymbol{\xi}} = \boldsymbol{J}^T_{\bullet} \frac{\partial N^{\bullet,i}_{\boldsymbol{\varphi}}}{\partial \boldsymbol{X}} \quad \text{and} \quad \frac{\partial N^{\bullet,i}_{\boldsymbol{\varphi}}}{\partial \boldsymbol{\xi}} = \boldsymbol{j}^T_{\bullet} \frac{\partial N^{\bullet,i}_{\boldsymbol{\varphi}}}{\partial \boldsymbol{x}} \ . \tag{5.39}$$

Here, • refers to the G or L, which corresponds to the global and local levels. Piecewise linear basis functions for the linear quadrilateral element within an isoparametric setting takes the following form

$$N^{\bullet,i}_{\boldsymbol{\varphi}}(\xi,\eta) = \frac{1}{2}(1+\xi_i\xi)\frac{1}{2}(1+\eta_i\eta), \tag{5.40}$$

with

$$\begin{aligned} \boldsymbol{\xi}_1 &= (\xi_1,\eta_1) = (-1,-1), \qquad & \boldsymbol{\xi}_2 &= (\xi_2,\eta_2) = (1,-1), \\ \boldsymbol{\xi}_3 &= (\xi_3,\eta_3) = (1,1), & \boldsymbol{\xi}_4 &= (\xi_4,\eta_4) = (-1,1). \end{aligned}$$

Here, the ordering numbers for the nodal points are anticlockwise within $\mathcal{B}_\square$; see Fig. 5.4.

5.7.1. Global-Local with Dirichlet-Neumann-type boundary conditions

This section provides the discretizations of the variational forms given in Algorithm 4. These equations stem from the Global-Local formulation augmented with Dirichlet-Neumann-type boundary conditions; see Section 5.4. Thus, the space-discrete variational formulations in material configuration via finite element approximation for the local and global BVPs at finite strain are discussed.

- ***Discretization of the local boundary value problem***

Discretization of the local BVP is aimed at determining the primary fields $(\boldsymbol{\varphi}_L, s_L, \boldsymbol{\lambda}_L)$ via finite element approximation. For the crack phase-field part, we have

$$\begin{aligned} \mathbf{R}^s_L = \bigcup_{e=1} \sum_i \Big(\int_{\mathcal{B}_e} \big(N^{L,i}_s\big)^T \Big[g'(s^h_+)\mathcal{H}(\boldsymbol{C}^h_L; H_J) + (s^h_L - 1) \Big] \, \mathrm{d}\boldsymbol{X} \\ + \int_{\mathcal{B}_e} \big(\boldsymbol{B}^{L,i}_s\big)^T l^2 \nabla s^h_L \, \mathrm{d}\boldsymbol{X} \Big) = \mathbf{0}, \end{aligned} \tag{5.41}$$

with

$$g'(s^h_+) = 2(1-\kappa)s^h_{L+},$$

and for the local mechanical part, we have

$$\begin{cases} \mathbf{R}^{\boldsymbol{\varphi}}_L = \bigcup_{e=1} \sum_i \int_{\mathcal{B}_e} \Big(\mathbf{B}^{L,i}_{\boldsymbol{E}}\Big)^T \mathbf{S}_h(\boldsymbol{C}_L, s_L; H_J) \, \mathrm{d}\boldsymbol{X} - \mathbf{J}^T_L \hat{\boldsymbol{\lambda}}_L = \mathbf{0}, \\ \\ \mathbf{R}^{\mathrm{C}_3}_L = \mathbf{L}_L \hat{\boldsymbol{\varphi}}^{k-1}_\Gamma - \mathbf{J}_L \hat{\boldsymbol{\varphi}}_L = \mathbf{0}, \end{cases} \tag{5.42}$$

such that the coupling terms are discretized by

$$\mathbf{J}_L = \int_{\mathcal{B}_L} (\boldsymbol{N}^L_\lambda)^T \boldsymbol{N}^L_u \, \mathrm{d}A, \quad \mathbf{L}_L = \int_{\Gamma_L} (\boldsymbol{N}^L_\lambda)^T \boldsymbol{N}^\Gamma_u \, \mathrm{d}A. \tag{5.43}$$

The matrix $\mathbf{B}_{\boldsymbol{E}}^{\bullet,i}$ has the explicit form by,

$$\mathbf{B}_{\boldsymbol{E}}^{\bullet,i} = \begin{bmatrix} F_{11}^{\bullet} N_{\boldsymbol{\varphi},1}^{\bullet,i} & F_{21}^{\bullet} N_{\boldsymbol{\varphi},1}^{\bullet,i} \\ F_{12}^{\bullet} N_{\boldsymbol{\varphi},2}^{\bullet,i} & F_{22}^{\bullet} N_{\boldsymbol{\varphi},2}^{\bullet,i} \\ F_{11}^{\bullet} N_{\boldsymbol{\varphi},2}^{\bullet,i} + F_{12}^{\bullet} N_{\boldsymbol{\varphi},1}^{\bullet,i} & F_{21}^{\bullet} N_{\boldsymbol{\varphi},2}^{\bullet,i} + F_{22}^{\bullet} N_{\boldsymbol{\varphi},1}^{\bullet,i} \end{bmatrix} . \tag{5.44}$$

Here, $\bullet$ can be set for the G or L corresponds to the global and local level, respectively.

- ***Discretization of the global boundary value problem***

Discretization of the global BVP is aimed at determining the primary fields $(\boldsymbol{\varphi}_G, \boldsymbol{\varphi}_\Gamma, \boldsymbol{\lambda}_C)$ via finite element approximation. Hence, a nodal residual force vector for the coupling part (C_1) is: for a given $\hat{\boldsymbol{\lambda}}_L^k$, solve for $\hat{\boldsymbol{\lambda}}_C^k$ by

$$\mathbf{R}_G^{\mathrm{C}_1} = \mathbf{L}_G^T \hat{\boldsymbol{\lambda}}_C + \mathbf{L}_L^T \hat{\boldsymbol{\lambda}}_L^{k-1} = \mathbf{0}, \tag{5.45}$$

and then by using the given $\hat{\boldsymbol{\varphi}}_G^{k-1}$, solve for $\hat{\boldsymbol{\lambda}}_F^k$ within the fictitious domain $\mathcal{B}_F$ through

$$\mathbf{R}_F^{\boldsymbol{\varphi}} = \bigcup_{e=1} \sum_i \int_{\mathcal{B}_e} \Big(\mathbf{B}_{\boldsymbol{E}}^{G,i}\Big)^T \mathbf{S}_h\Big(\boldsymbol{C}_G(\hat{\boldsymbol{\varphi}}_G^{k-1})\Big)\, \mathrm{d}\boldsymbol{X} - \mathbf{J}_F^T \hat{\boldsymbol{\lambda}}_F = \mathbf{0}, \tag{5.46}$$

and afterwards by the given $\hat{\boldsymbol{\lambda}}_F^k$ and $\hat{\boldsymbol{\lambda}}_C^k$, solve for $\hat{\boldsymbol{\varphi}}_G^k$ by

$$\mathbf{R}_G^{\boldsymbol{\varphi}} = \bigcup_{e=1} \sum_i \int_{\mathcal{B}_e} \Big(\mathbf{B}_{\boldsymbol{E}}^{G,i}\Big)^T \mathbf{S}_h(\boldsymbol{C}_G)\, \mathrm{d}\boldsymbol{X} - \mathbf{J}_F^T \hat{\boldsymbol{\lambda}}_F^k - \mathbf{J}_G^T \hat{\boldsymbol{\lambda}}_C^k - \int_{\Gamma_N} (\boldsymbol{N}_u^G)^T \bar{\boldsymbol{\tau}}\, \mathrm{d}A = \mathbf{0}. \tag{5.47}$$

Here, $\mathbf{B}_{\boldsymbol{E}}^{G,i}$ is used from (5.44). Now, using the given $\hat{\boldsymbol{\varphi}}_G^k$, solve for $\hat{\boldsymbol{\varphi}}_\Gamma^k$ through

$$\mathbf{R}_G^{\mathrm{C}_2} = \mathbf{L}_G \hat{\boldsymbol{\varphi}}_\Gamma - \mathbf{J}_G \hat{\boldsymbol{\varphi}}_G^k = \mathbf{0}. \tag{5.48}$$

Here, the coupling terms are discretized by

$$\mathbf{J}_G = \int_{\mathcal{B}_G} (\boldsymbol{N}_\lambda^G)^T \boldsymbol{N}_u^G\, \mathrm{d}A, \qquad \mathbf{L}_G = \int_{\Gamma_G} (\boldsymbol{N}_\lambda^G)^T \boldsymbol{N}_u^\Gamma\, \mathrm{d}A. \tag{5.49}$$

5.7.2. Global-Local with Robin-type boundary conditions

In this section, discretizations for the variational formulations given in Algorithm 5 for the $g/l-2$ are further discussed.

- ***Discretization of the local boundary value problem***

Discretization of the local BVP is aimed at determining the primary fields $(\boldsymbol{\varphi}_L, s_L, \boldsymbol{\varphi}_\Gamma, \boldsymbol{\lambda}_L)$ through finite element approximation. Discretization of the crack phase-field part is given in (5.41), and for the local mechanical part, we have

$$\begin{cases} \mathbf{R}_L^{\boldsymbol{\varphi}} = \bigcup_{e=1} \sum_i \int_{\mathcal{B}_e} \Big(\mathbf{B}_{\boldsymbol{E}}^{L,i}\Big)^T \mathbf{S}_h(\boldsymbol{C}_L, s_L; H_J)\, \mathrm{d}\boldsymbol{X} - \mathbf{J}_L^T \hat{\boldsymbol{\lambda}}_L = \mathbf{0}, \\[2ex] \mathbf{R}_L^{\widetilde{\mathrm{C}}_1} = \mathbf{L}_L^T \hat{\boldsymbol{\lambda}}_L + \mathbb{A}_L \mathbf{L}_G \hat{\boldsymbol{\varphi}}_\Gamma - \boldsymbol{\Lambda}_L^{k-1} = \mathbf{0}, \\[2ex] \mathbf{R}_L^{\widetilde{\mathrm{C}}_2} = \mathbf{L}_L \hat{\boldsymbol{\varphi}}_\Gamma - \mathbf{J}_L \hat{\boldsymbol{\varphi}}_L = \mathbf{0}, \end{cases} \tag{5.50}$$

such that

$$\boldsymbol{\Lambda}_L^{k-1} := \boldsymbol{\Lambda}_L^{k-1}(\hat{\boldsymbol{\varphi}}_G, \hat{\boldsymbol{\lambda}}_C) = \mathbb{A}_L \mathbf{J}_G \hat{\boldsymbol{\varphi}}_G^{k-1} - \mathbf{L}_G^T \hat{\boldsymbol{\lambda}}_C^{k-1}. \tag{5.51}$$

- ***Discretization of the global boundary value problem***

Discretization of the global BVP is aimed at determining the primary fields $(\boldsymbol{\varphi}_G, \boldsymbol{\varphi}_\Gamma, \boldsymbol{\lambda}_C)$ via finite element approximation. Hence, a nodal residual force vector for the mechanical part reads

$$\begin{cases} \mathbf{R}_G^{\boldsymbol{\varphi}} = \bigcup\limits_{e=1} \sum\limits_i \displaystyle\int_{\mathcal{B}_e} \left(\mathbf{B}_{\boldsymbol{E}}^{G,i}\right)^T \mathbf{S}_h(\boldsymbol{C}_G)\,\mathrm{d}\boldsymbol{X} - \mathbf{J}_F^T \hat{\boldsymbol{\lambda}}_F - \mathbf{J}_G^T \hat{\boldsymbol{\lambda}}_C - \displaystyle\int_{\Gamma_N} (\boldsymbol{N}_u^G)^T \bar{\boldsymbol{\tau}}\,\mathrm{d}A = \mathbf{0}, \\ \mathbf{R}_G^{\widetilde{\mathrm{C}}_3} = \mathbf{L}_G^T \hat{\boldsymbol{\lambda}}_C + \mathbb{A}_G \mathbf{L}_G - \boldsymbol{\Lambda}_G^k = \mathbf{0}, \\ \mathbf{R}_G^{\widetilde{\mathrm{C}}_4} = \mathbf{L}_G \hat{\boldsymbol{\varphi}}_\Gamma - \mathbf{J}_G \hat{\boldsymbol{\varphi}}_G = \mathbf{0}, \end{cases} \tag{5.52}$$

such that

$$\boldsymbol{\Lambda}_G^{k} := \boldsymbol{\Lambda}_G^{k}(\hat{\boldsymbol{\varphi}}_L, \hat{\boldsymbol{\lambda}}_L) = \mathbb{A}_G \mathbf{J}_L \hat{\boldsymbol{\varphi}}_L^{k} - \mathbf{L}_L^T \hat{\boldsymbol{\lambda}}_L^{k}. \tag{5.53}$$

5.7.3. Space-discrete linearization of the variational formulation in material configuration

In order to solve the set of nonlinear algebraic equations which arises in (5.42), (5.46), (5.47), (5.50), and (5.52), we use an iterative Newton-Raphson method. To this end, the linearization of the discretized residual vector based on the first-order Taylor series expansion reads the following:

$$\mathrm{Lin}\left[\mathbf{R}(\hat{\boldsymbol{\varphi}}_{k+1})\right]_{\boldsymbol{X}=\hat{\boldsymbol{\varphi}}} \approx \mathbf{R}(\hat{\boldsymbol{\varphi}}_k) + D\mathbf{R}(\hat{\boldsymbol{\varphi}}_k)\left[\Delta\hat{\boldsymbol{\varphi}}\right] = \mathbf{0}, \tag{5.54}$$

with

$$\hat{\boldsymbol{\varphi}}_{k+1} = \hat{\boldsymbol{\varphi}}_k + \Delta\hat{\boldsymbol{\varphi}}. \tag{5.55}$$

A Gateaux derivative denoted by $D\mathbf{R}(\hat{\boldsymbol{\varphi}}_k)\left[\Delta\hat{\boldsymbol{\varphi}}\right]$ for the vector $\mathbf{R}$ at $\hat{\boldsymbol{\varphi}}_k$ in the direction of $\Delta\hat{\boldsymbol{\varphi}}$ is written as

$$\begin{aligned} D\mathbf{R}(\hat{\boldsymbol{\varphi}}_k)\left[\Delta\hat{\boldsymbol{\varphi}}\right] &= \frac{d}{d\epsilon}\mathbf{R}(\hat{\boldsymbol{\varphi}}_k + \epsilon\Delta\hat{\boldsymbol{\varphi}})\Big|_{\epsilon=0} = \lim_{\epsilon\to 0} \frac{\mathbf{R}(\hat{\boldsymbol{\varphi}}_k + \epsilon\Delta\hat{\boldsymbol{\varphi}}) - \mathbf{R}(\hat{\boldsymbol{\varphi}}_k)}{\epsilon} \\ &= \frac{\partial\mathbf{R}(\hat{\boldsymbol{\varphi}})}{\partial\hat{\boldsymbol{\varphi}}}.\Delta\hat{\boldsymbol{\varphi}} = \boldsymbol{K}.\Delta\hat{\boldsymbol{\varphi}}, \end{aligned} \tag{5.56}$$

here, the *tangent stiffness matrix* $\boldsymbol{K}$ is defined by

$$\boldsymbol{K}(\hat{\boldsymbol{\varphi}}) = \frac{\partial\mathbf{R}(\hat{\boldsymbol{\varphi}})}{\partial\hat{\boldsymbol{\varphi}}} \quad \text{with} \quad K_{ij} = \frac{\partial R_i(\hat{\boldsymbol{\varphi}})}{\partial\hat{\varphi}_j}. \tag{5.57}$$

This results in the update solution field $\hat{\boldsymbol{\varphi}}_{k+1}$ with

$$\hat{\boldsymbol{\varphi}}_{k+1} = \hat{\boldsymbol{\varphi}}_k - \boldsymbol{K}^{-1}\mathbf{R}(\hat{\boldsymbol{\varphi}}_{\mathbf{k}}). \tag{5.58}$$

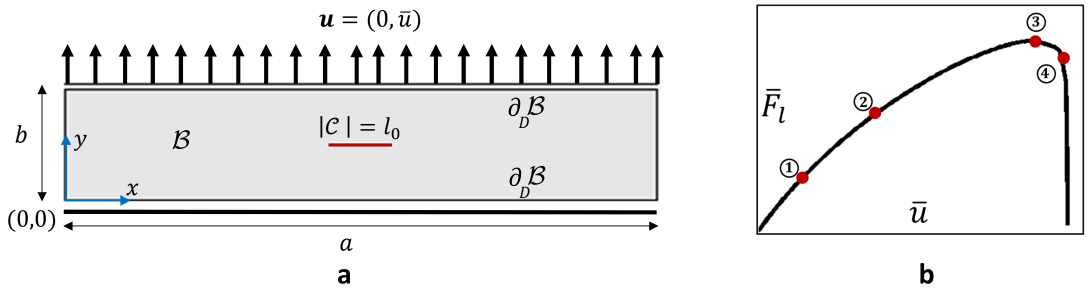

Figure 5.5: Example 1. Penny-shaped pre-cracked test (a) Specimen geometry and loading conditions, and (b) the load-displacement curve with the points of interest.

5.8. Numerical examples

This section demonstrates the performance of the proposed Global-Local approach at finite strain, with two numerical model problems. These include a penny-shaped pre-cracked test and a de-bonding test undergoing finite strain. The large deformation of the specimen results in the significant nonlinearity of the constitutive model; hence, more gap is observed between the material stiffness of the global and local models. Thus, we aim to demonstrate the modeling capabilities of the proposed approach for the high nonlinear setting (e.g., a hyperelastic fracturing material). Specifically, we consider the hyperelastic Neo-Hookean model with a volumetric-isochoric split given in (3.82). Qualitative and quantitative comparisons with a reference phase-field solution for the quasi-brittle fracture are also provided.

5.8.1. Example 1: Penny-shaped pre-cracked test at finite strain

In the following numerical example, a BVP is applied to the rectangular plate shown in Fig. 5.5. We set $a = 2\ mm$, $b = 0.4\ mm$, and hence $\mathcal{B} = (0,2) \times (0,0.4)$, which includes a predefined single notch $\mathcal{C}$ of length $l_0 = 0.2\ mm$ in the body center as depicted in Fig. 5.5a. At the lower edge, the vertical displacement is set to zero while at the upper edge vertical displacement is uniformly imposed on the Dirichlet boundary. Following [96] the elastic material property is set for the hyperelastic Neo-Hookean model, such that shear modulus $\mu = 5$ N/mm^2 and Poisson's ration $\nu = 0.45$ for a weakly compressible material are used. The phase-field parameters are chosen as $\kappa = 10^{-10}$, and $l = 2h$. The characteristic length-scale in the phase-field formulation is $l = 1 \cdot 10^{-2}$ mm. The Griffith's critical elastic energy release rate is set as $G_c = 2.4 \times 10^{-3}$ N/mm. We consider the plane-strain situation.

The reference domain partition contains 10,714 elements. The discretizations of the global and local domains contain 998 and 9,734 elements, respectively. That is, in our case, the reference and Global-Local problems have a comparable discretization size, as can be grasped from Fig. 5.6. In the following numerical example, the displacement control is used with displacement increments $\Delta\bar{u} = 1.0 \times 10^{-4}\ mm$. With respect to the solution of the nonlinear problems, the tolerance magnitudes are $\texttt{TOL}_{\text{NR}} := 10^{-8}$, $\texttt{TOL}_{\text{Stag}} := 10^{-5}$, and $\widetilde{\texttt{TOL}}_{\text{GL}} := 10^{-5}$.

Investigating the reference and Global-Local results. In the following, we illustrate the quantitative and qualitative reference and Global-Local results and their comparison. Evidently through Fig. 5.7, the two load-displacement curves are identical in the entire range of loading, including the pre- and post-peak behavior. The good agreement between the reference and Global-Local response demonstrates the capability of the proposed Global-Local framework for the high nonlinear setting.

The crack phase-field profiles shown in Fig. 5.8 are also in very good agreement. This is a good indicator for evaluating the down-scaling procedure (i.e., the transition of external loading increments from the global level to the local one). Next, we evaluate the iterative convergence behavior of the Global-Local solution process, as shown in Fig. 5.9. Here, we depict the convergence indicators for the four interest points given in Fig. 5.5b. Through the convergence behavior shown in Fig. 5.9, in the pre-cracked state (i.e., points 1–2), the Global-Local formulation is required a fewer number of iterations to reach convergence versus the post-peak stage (i.e., points 3–4).

In the following, we investigate the possible influence of the different (i) global discretization space, and (ii) Global-Local tolerance indicator (i.e., $\widetilde{\texttt{TOL}}_{\text{GL}}$) on the Global-Local iterative process. These are accordingly discussed.

Investigating $g/l-1$ results for different global discretization spaces. We perform the Global-Local framework for the given setup in Section 5.1, whereas different global discretization spaces are considered. Specifically, we quantitatively investigate the convergence performance of the iterative Global-Local formulation through the effect of (i) global discretization space, and (ii) the presence of a single notch-shaped located in the center of the global domain. Thus, four more cases are shown in Fig. 5.10, are accordingly investigated. These cases include:

- **Case 1.** We set $h_C = 2h_F$ without considering a predefined single notch.
- **Case 2.** We set $h_C = h_F$ but considering predefined single notch at the center of the global domain.
- **Case 3.** We set $h_C = 2h_F$, including a predefined single notch at the center of the global domain. This has a similar discretization space to Case 1 but includes predefined notch.
- **Case 4.** We set $h_C = 4h_F$, including a predefined single notch at the center of the

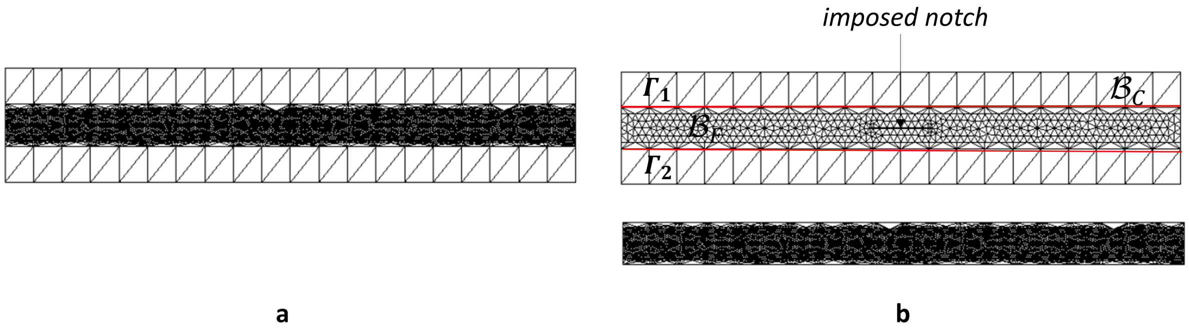

Figure 5.6: Example 1. Finite element discretization (a) of the reference domain $\mathcal{B}$, and (b) of the global and local domains $\mathcal{B}_G$ and $\mathcal{B}_L$, respectively.

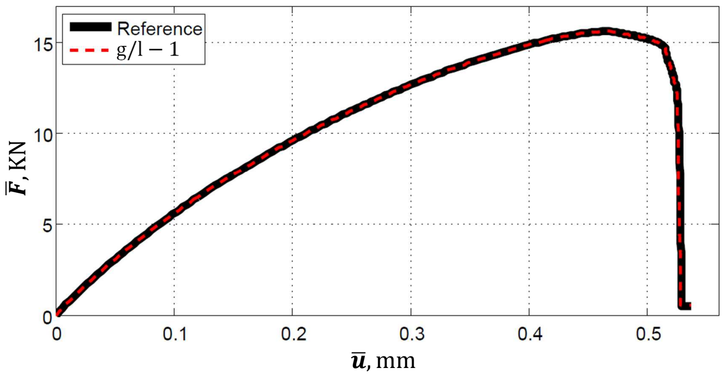

Figure 5.7: Example 1. Comparison of the load-displacement curves between the reference and the Global-Local solutions.

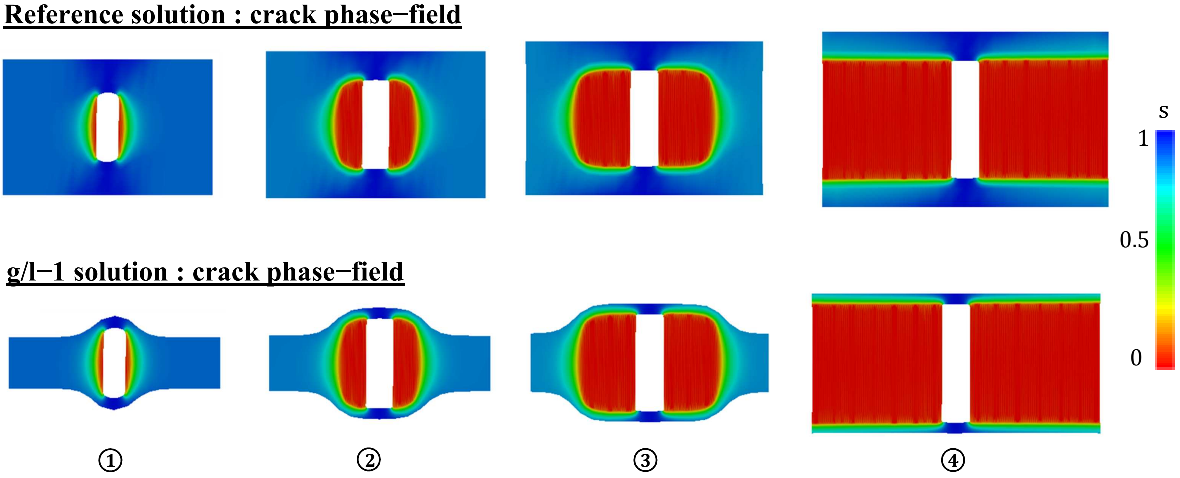

Figure 5.8: Example 1. Comparison of the crack phase-field response on the deformed configuration. First row: the reference, and second row: the Global-Local solutions on the deformed configuration, at $\bar{u} = [0.042, 0.147, 0.474, 0.5148]$ mm.

global domain. This has the finest discretization space that is used for the global domain.

The load-displacement curves for all case studies are depicted in Fig. 5.10. All case studies exhibit an excellent agreement with the reference solution. Thus, the Global-Local formulation enables a consistent transition procedure of the local non-linearity to the upper level; while preserving accuracy. Figure 5.12 compares the crack phase-field solutions of the Global-Local formulation computed from different case studies. It can be observed that the crack profiles are almost identical in all cases.

Similar to Fig. 5.9, Fig. 5.13 presents and compares the convergence performance of the Global-Local iterative procedure at the four loading steps of interest (points 1–4 from Fig. 5.5b). This is illustrated in terms of the indicator η. From Fig. 5.10, it can be grasped that the existence of the predefined single notch at the global domain, even with its coarse representation, leads to fewer iterations for the convergence of the solution. This is mainly because, the traction jump that appears along the predefined notch between

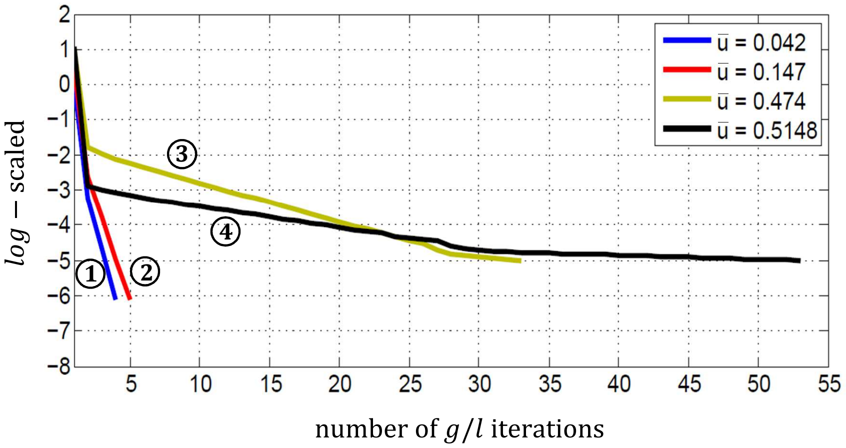

Figure 5.9: Example 1. Convergence behavior of the Global-Local iterative solution process at four different loading steps (the points 1–4 from Fig. 5.5b), illustrated in terms of the indicator η.

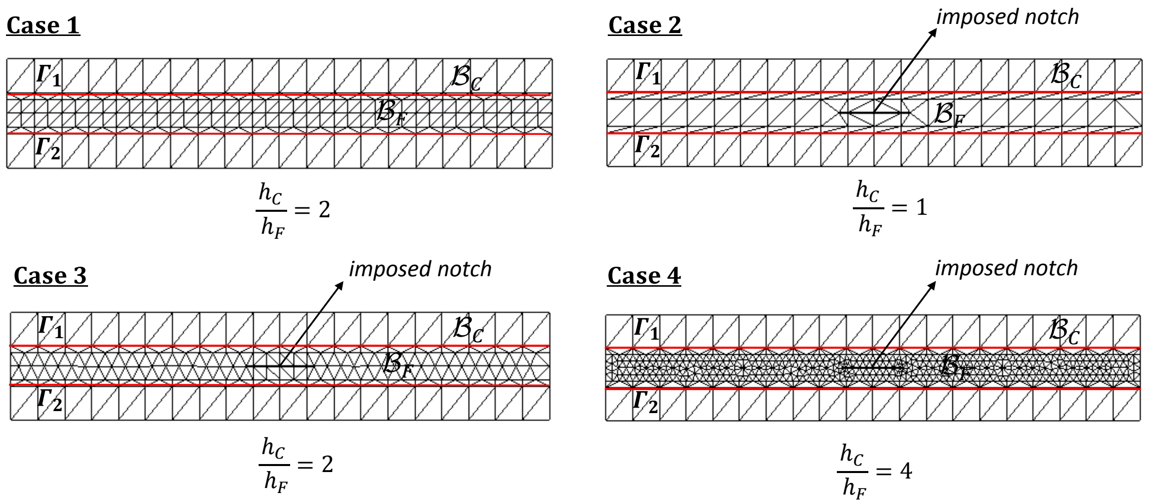

Figure 5.10: Example 1. Finite element discretization of the global domain $\mathcal{B}_G$ for different case studies.

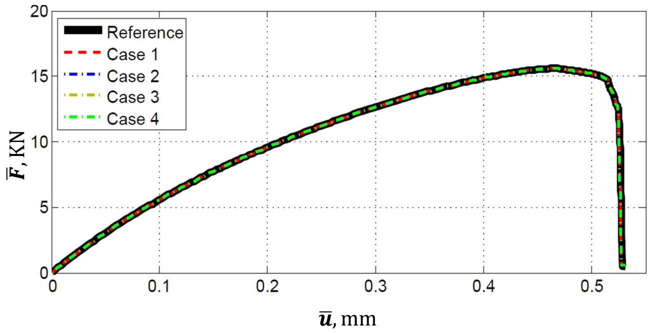

Figure 5.11: Example 1. The load-displacement curves for the different case studies shown in Fig. 5.10

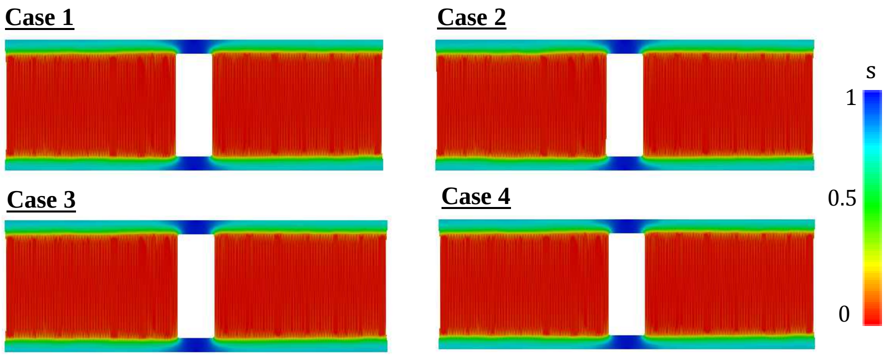

Figure 5.12: Example 1. Comparison of the crack phase-field solution (at the complete failure) on the deformed configuration for different case studies shown in Fig. 5.10.

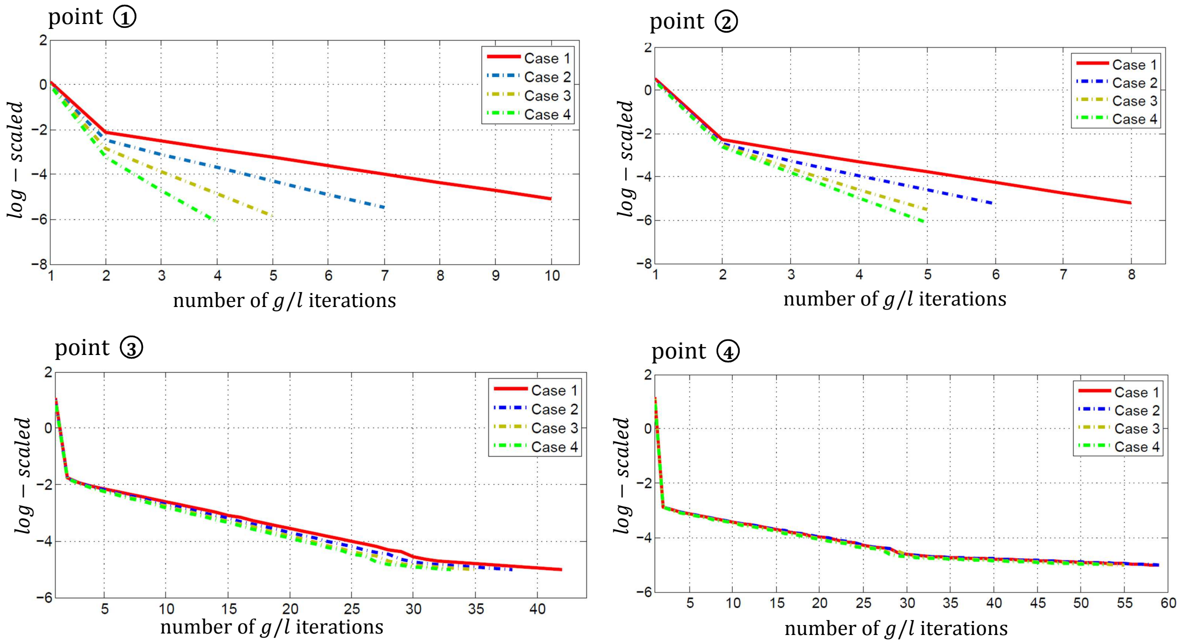

Figure 5.13: Example 1. Convergence behavior of the different case studies of the Global-Local iterative solution process at four different loading steps (points 1–4 from Fig. 5.5b), illustrated in terms of the indicator η.

the global and local domains becomes drastically less, and thus requires less iterations for the convergence.

For deeper insights, into the presence of a predefined notch within the global domain, the resulting global vertical displacement u_y at complete failure for different case studies are shown in Fig. 5.14. Evidently, a coarse representation of the predefined notch in the global domain (i.e., Case 2) leads to the singular deformed shape while in the finer mesh (i.e., Case 4), it leads to the piecewise-smooth deformed shape.

Investigating the effect of $\widetilde{\mathtt{TOL}}_{\mathrm{GL}}$ on the Global-Local iterative process. Here, the effect of $\widetilde{\mathtt{TOL}}_{\mathrm{GL}}$ is investigated on the Global-Local iterative process. To do so, we study the BVP described in Section 5.1 with its discretization given in Fig. 5.6. In the following, we consider three different case studies:

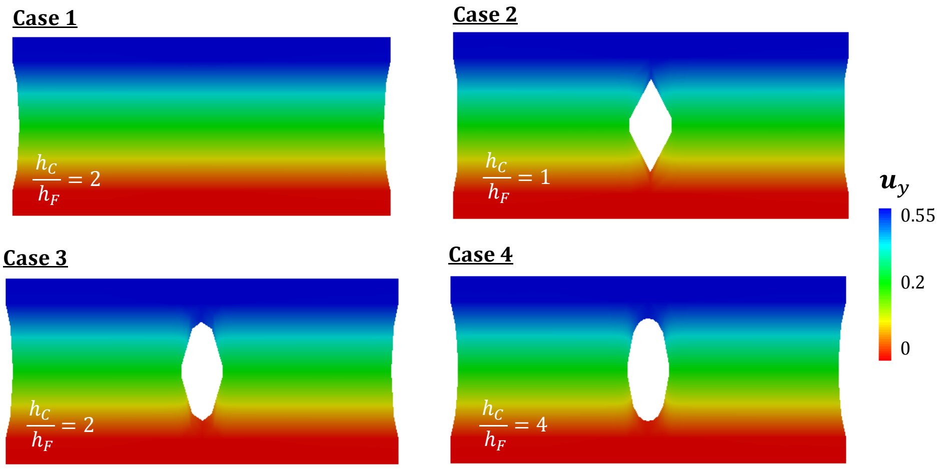

Figure 5.14: Example 1. The resulting global vertical displacement u_y (at the complete failure) for different case studies on the deformed configuration.

- **Case 1.** We set $\widetilde{\mathtt{TOL}}_{\mathrm{GL}} := 10^{-3}$ and $\mathtt{TOL}_{\mathrm{Stag}} := 10^{-3}$.
- **Case 2.** We set $\widetilde{\mathtt{TOL}}_{\mathrm{GL}} := 10^{-4}$ and $\mathtt{TOL}_{\mathrm{Stag}} := 10^{-4}$.
- **Case 3.** We set $\widetilde{\mathtt{TOL}}_{\mathrm{GL}} := 10^{-5}$ and $\mathtt{TOL}_{\mathrm{Stag}} := 10^{-5}$.

The load-displacement curves for these three case studies are depicted in Fig. 5.15. All case studies exhibit an excellent agreement with the reference solution. Accordingly, Fig. 5.16 compares the phase-field solutions of the Global-Local formulation for different case studies. Thus, even through low specified $\widetilde{\mathtt{TOL}}_{\mathrm{GL}}$ (i.e., Case 1), we can achieve a good agreement with the reference solution, while it requires less computational cost compared to other case studies.

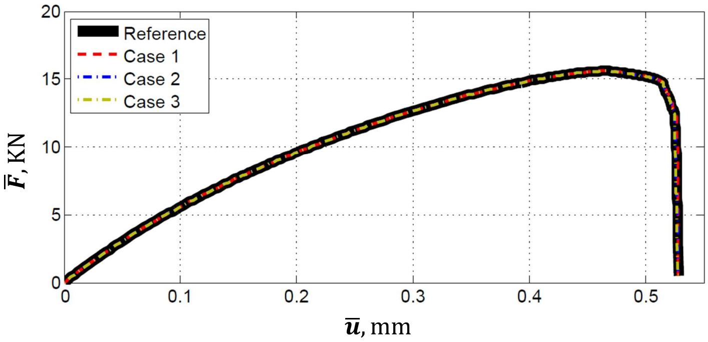

Figure 5.15: Example 1. The load-displacement curves for different case studies used to observe the effect of $\widetilde{\mathtt{TOL}}_{\mathrm{GL}}$ on the Global-Local iterative process.

***g/l* − 2 with Robin-type boundary conditions.** Here, we continue to study the quantitative and qualitative comparison between the reference and Global-Local results equipped with Robin-type boundary conditions, namely $g/l-2$. The main objective of

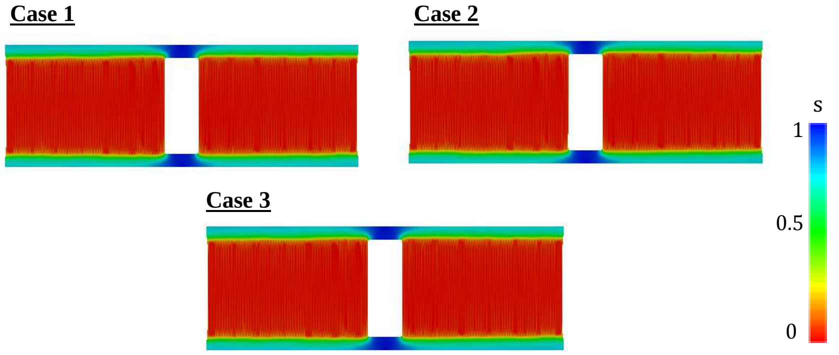

Figure 5.16: Example 1. Comparison of the crack phase-field profile (at the complete failure) to investigate the effect of $\widetilde{\mathtt{TOL}}_{\mathrm{GL}}$ on the Global-Local iterative process, for different case studies.

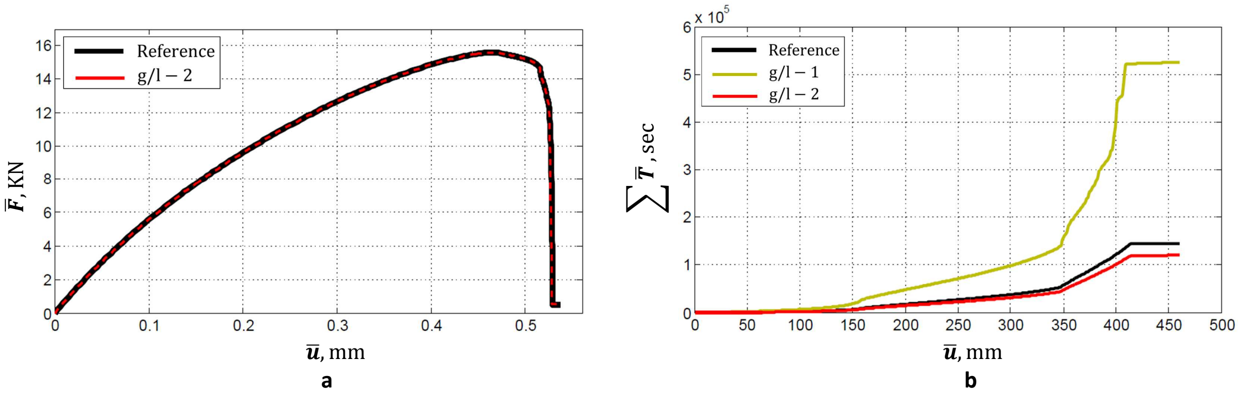

Figure 5.17: Example 1. Comparison of the reference solution and the Global-Local formulation $g/l-2$. (a) The load-displacement curves, and (b) time-displacement curves in terms of 'accumulated time' compared with $g/l-1$.

using $g/l-2$ is computational efficiency for coupling the two-nested models denoted by the local and global domains rather than strong non-intrusive coupling.

The load-displacement curve corresponds to the $g/l-2$ is depicted in Fig. 5.17a. The resulting Global-Local curve via $g/l-2$ is in very good agreement with the reference solution. Accordingly, Fig. 5.17b represents the corresponding accumulative computational time (i.e., CPU simulation time) per prescribed displacement through $g/l-2$ as well as $g/l-1$ and its comparison versus the reference time. The resulting accumulative computational time illustrates that $g/l-2$ requires 17% less time than the reference computational time, which underlines the efficiency of using Robin-type boundary conditions. However, the accumulative computational time through $g/l-1$ is accordingly presented in Fig. 5.17b which shows the high computational time versus $g/l-2$. Thus, depending on the application's interest, one could either choose between $g/l-1$ (to be computationally non-intrusive) or $g/l-2$ (to gain computational efficiency).

Additionally, the computed crack phase-field profiles through $g/l-2$ are presented in Fig. 5.18 at $\bar{u} = [0.042, 0.147, 0.474, 0.5148]\ mm$. The crack resolution for different time steps are also in very good agreement with the reference solution (see Fig. 5.8) which demonstrates the consistent transition between global and local BVPs.

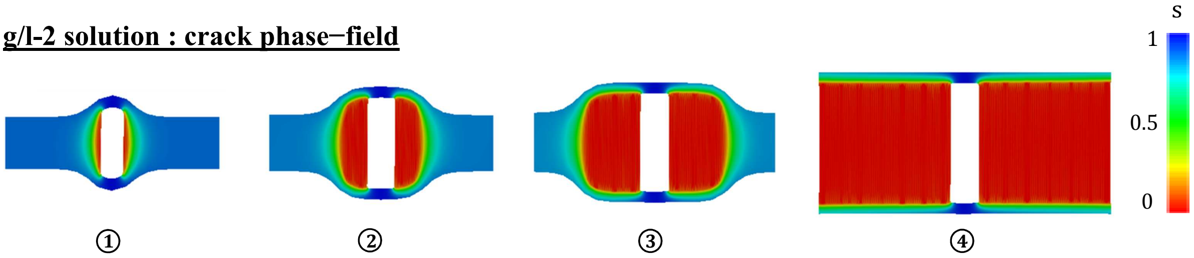

Figure 5.18: Example 1. Computed crack phase-field solution through $g/l-2$ with Robin-type boundary conditions, on the deformed configuration at $\bar{u} = [0.042, 0.147, 0.474, 0.5148]$ *mm*.

5.8.2. Example 2: Debonding test undergoing finite strain

The second example is concerned with a debonding test at finite strain through phase-field modeling. In the following, a BVP is applied to the rectangular plate shown in Fig. 5.19. We set $a = 2.5$ *mm*, $b = 9$ *mm*, and $c = 1$ *mm* hence $\mathcal{B} = (0, 2.5) \times (0, 10)$ that includes a predefined single notch $\mathcal{C}$ of length $l_0 = 1$ *mm* and width $s = 0.1$ *mm* in the top edge; as depicted in Fig. 5.19a. The lower edge is fixed in both x and y directions and set to zero while at the upper edge horizontal displacement is imposed around the predefined notch. Here, the elastic material property is set for the hyperelastic Neo-Hookean model, such that Young's modulus $E = 100$ N/mm^2 and Poisson's ration $\nu = 0.3$ for a weakly compressible material are used. The characteristic length in the phase-field formulation is $l = 25 \times 10^{-2}$ mm. The Griffith's critical elastic energy release rate is set as $G_c = 1$ N/mm. We consider the plane-strain situation. The reference domain partition contains 8,213 elements. The discretizations of the global and local domains contain 857 and 7,377 elements, respectively. In our case, the reference and Global-Local problems have a comparable discretization size, as can be grasped from Fig. 5.19. In the following numerical example, the displacement control is used with displacement increments $\Delta\bar{u} = 1.0 \times 10^{-3}$ *mm*.

First, we start with the presentation of the reference and Global-Local results $g/l-1$ and their comparison. The load-displacement curve for the Global-Local formulation with Dirichlet-Neumann-type boundary conditions $g/l-1$ is depicted in Fig. 5.20a. Accordingly, Fig. 5.20b demonstrates the corresponding accumulative computational time per prescribed displacement through $g/l-1$ and its comparison versus the reference time. As mentioned earlier, we should note that our goal for the $g/l-1$ formulation was not to gain computational efficiency but rather to enable computations with legacy codes.

The iterative convergence behavior of the Global-Local solution process $g/l-1$ is depicted in Fig. 5.21. We plot the quantity η such that the amount of Global-Local iterations required for the solution convergence can be detected. The results show that as the crack propagates in the post-peak stage (i.e., point 3–4), the Global-Local iterative process required more iterations for the convergence of solutions than crack initiation stage (i.e., point 1).

Next, we continue with the presentation of the reference and Global-Local results $g/l-2$ and their comparison. The load-displacement curve corresponds to the $g/l-2$ solution is depicted in Fig. 5.22a. The resulting Global-Local curve via $g/l-2$ solution is in very good agreement with the reference solution. Accordingly, Fig. 5.22b represents the corresponding accumulative computational time, per prescribed displacement through $g/l-2$ and its comparison versus the reference time. The resulting accumulative computational time through $g/l-2$ demonstrates that the Global-Local formulation with Robin-type boundary conditions requires 18% less time compared with the reference computational time which underlines the efficiency of $g/l-2$.

The evolution of the crack phase-field for different prescribed displacements are depicted in Fig. 5.23. The first row represents the reference s solution, the second row corresponds to the solution of s_L through $g/l-1$, and the third row is the solution of s_L through $g/l-2$ at $\bar{u}=[0.4,1,3,6]\ mm$. Regardless of the formulation, the crack phase-field profile initiates at the tip of the notch and then continues to propagate downwards until the end of the computation. The deformed shapes in Fig. 5.23 are not magnified. Notably, the crack phase-field profiles are obtained from the Global-Local formulations, namely $g/l-1$ and $g/l-2$, which are also in good agreement with the reference solution. Thus, the proposed method is also applicable to the problems which exhibit strong non-linearity and localization response.

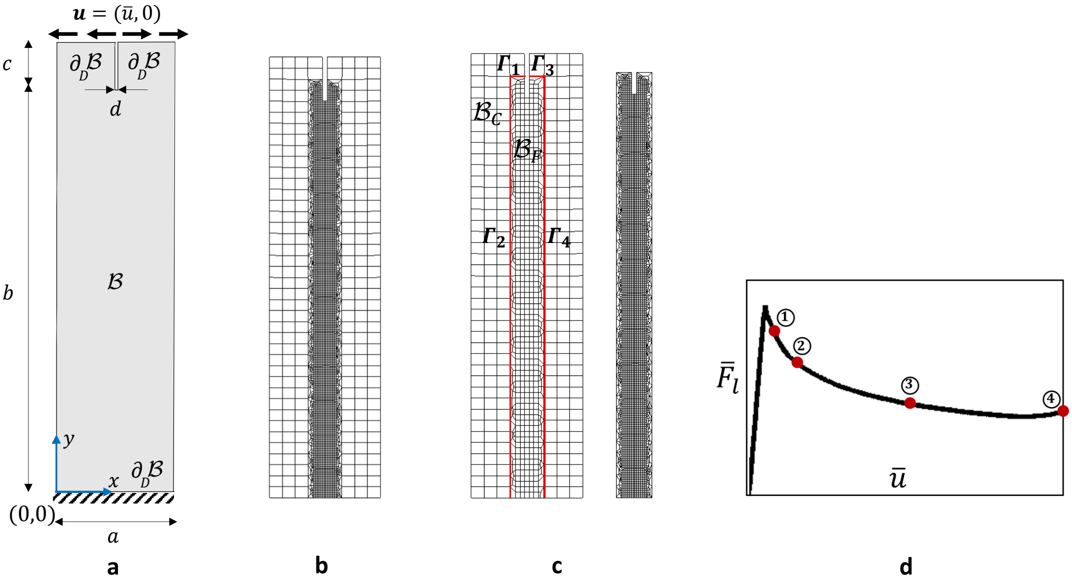

Figure 5.19: Example 2. Debonding test at finite strain. (a) Specimen geometry and loading conditions. Finite element discretization of the (b) reference domain $\mathcal{B}$, (c) global and local domains $\mathcal{B}_G$ and $\mathcal{B}_L$, respectively, and (d) the load-displacement curve with the points of interest.

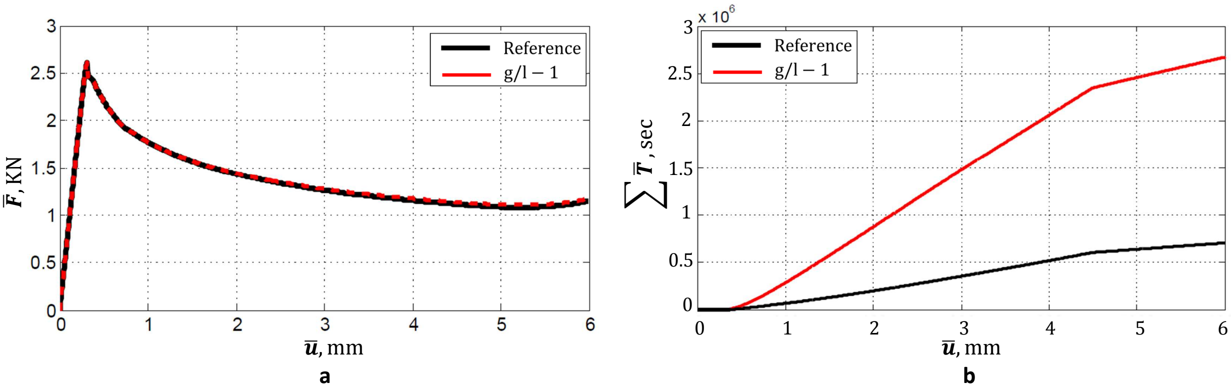

Figure 5.20: Example 2. Comparison of the reference solution and the Global-Local formulation $g/l-1$. (a) The load-displacement curves, and (b) time-displacement curves in terms of 'accumulated time'.

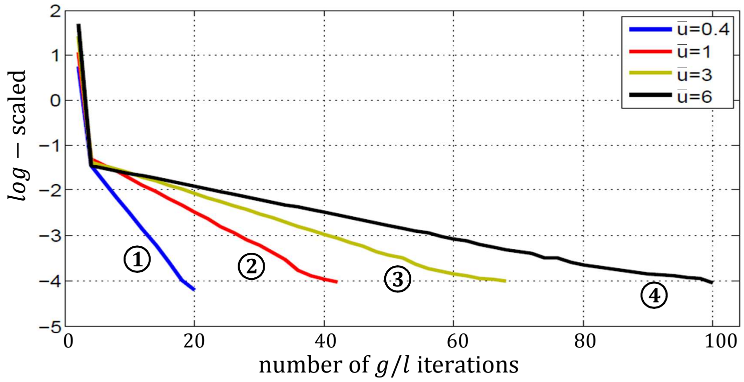

Figure 5.21: Example 2. Convergence behavior of the Global-Local iterative solution process $g/l-1$ at four different loading steps (points 1–4 from Fig. 5.19d), illustrated in terms of the indicator η.

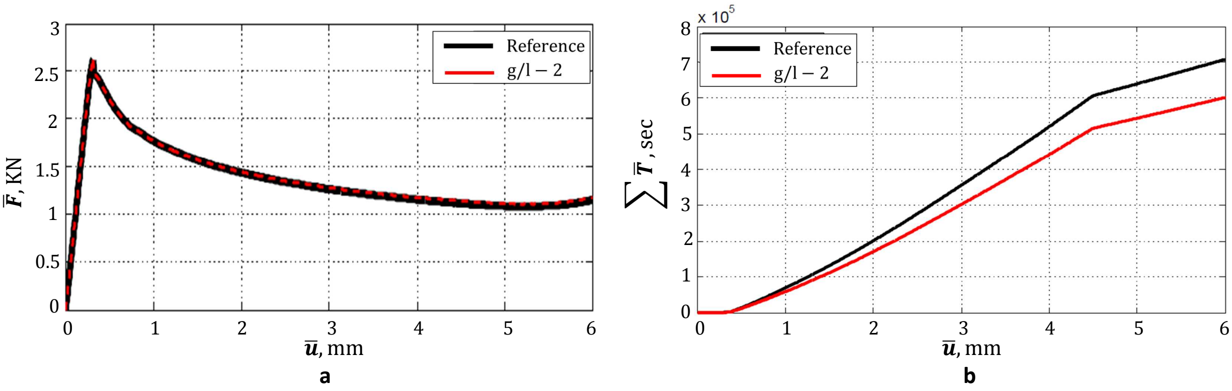

Figure 5.22: Example 2. Comparison of the reference solution and the Global-Local formulation $g/l-2$. (a) The load-displacement curves, and (b) time-displacement curves in terms of 'accumulated time'.

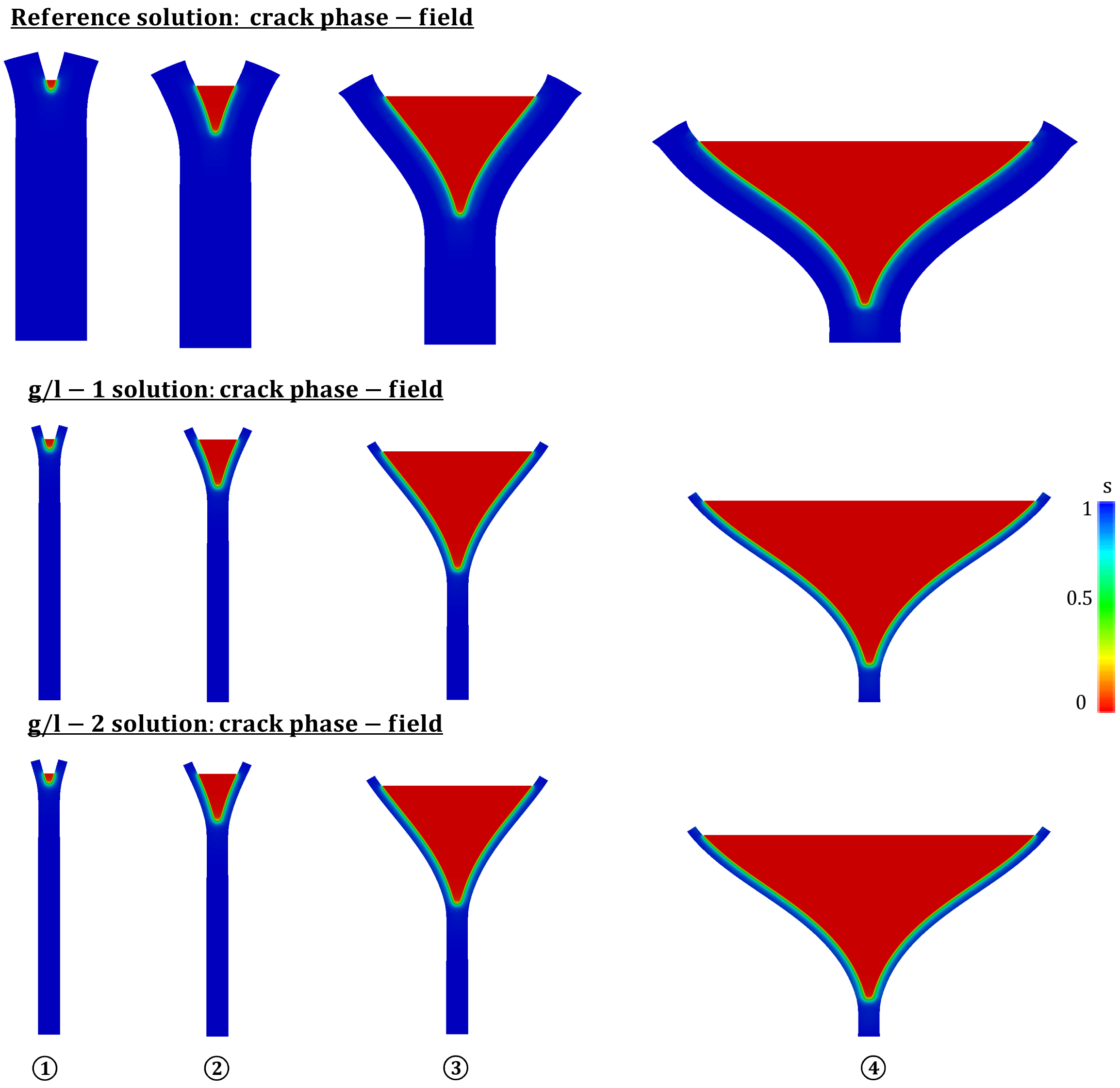

Figure 5.23: Example 2. Comparison of the crack phase-field response. First row: reference s solution, second row: the solution of s_L through $g/l-1$, and third row: the solution of s_L through $g/l-2$ on the deformed configuration at $\bar{u} = [0.4, 1, 3, 6]\ mm$.

Chapter 6

Global-Local Approach for Non-conforming Finite Element Discretization

This chapter aims to describe a mathematical framework to glue global and local domains through their common interface. Hence, the Global-Local framework formulated in Chapters 4 and 5 is further extended to non-conforming discretization. The main advantage here is to achieve more regularity at the interface and adopting the local domain without taking the global discretization space into account. Thus, through the non-conforming discrete interface, we can have an arbitrary mesh at the local domain (including interface) without any given interface conditions from the global discretization space (thus avoiding to have distorted mesh between fine and coarse discretization). Here, the MORTAR METHOD [15], the DUAL MORTAR METHOD [133], and the LOCALIZED MORTAR METHOD [110] are adopted. To conclude, two numerical examples are conducted to substantiate our algorithmic developments.

6.1. Non-conforming discrete interfaces between global and local domains

To resolve the crack phase-field problem, one requires $h_L \ll h_G$ (to have a sufficiently small characteristic length-scale at the local domain versus global one). By contrast, if the global and local discretization has to be matched across the interface, this results in $h_L = h_G$ on Γ, which contradicts with $h_L \ll h_G$. This could be a significant problem when the crack reaches an interface. Hence, further development is performed through the extension of the proposed Global-Local formulation toward the non-conforming finite element discretization across the common interface. Let $\mathcal{B}_G$ and $\mathcal{B}_L \in \mathbb{R}^\delta$ be two polygonal sub-domains as shown in Fig. 6.1 with an outer interface denoted by Γ_G and $\Gamma_L \in \mathcal{R}^{\delta-1}$, respectively. Two sub-domains share an interface $\Gamma \in \mathcal{R}^{\delta-1}$ where $\boldsymbol{u}_\Gamma$ is located there.

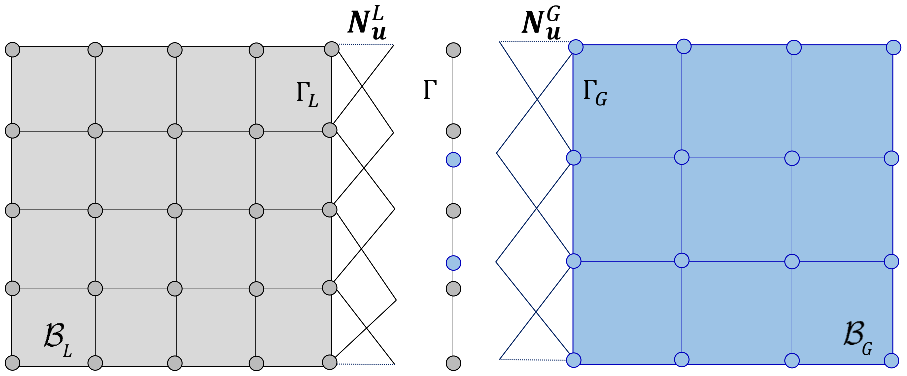

Figure 6.1: Setup of the notation used for the non-conforming discretization techniques for the $\mathcal{B}_G$, $\mathcal{B}_L$, and Γ.

We have the following:

- In a continuum setting: $\Gamma_L \equiv \Gamma_G \equiv \Gamma$,
- In a discrete setting: $\Gamma_L \neq \Gamma_G \neq \Gamma$ thus yielding $\boldsymbol{N}_u^L \neq \boldsymbol{N}_u^G \neq \boldsymbol{N}_u^\Gamma$.

More specifically, this section aims at determining the following coupling terms:

$$\begin{aligned} \mathbf{J}_G &= \int_{\mathcal{B}_G} (\boldsymbol{N}_\lambda^G)^T \boldsymbol{N}_u^G \,\mathrm{d}\boldsymbol{x}, \qquad & \mathbf{J}_L &= \int_{\mathcal{B}_L} (\boldsymbol{N}_\lambda^L)^T \boldsymbol{N}_u^L \,\mathrm{d}\boldsymbol{x}, \\ \mathbf{L}_G &= \int_{\Gamma_G} (\boldsymbol{N}_\lambda^G)^T \boldsymbol{N}_u^\Gamma \,\mathrm{d}a, \qquad & \mathbf{L}_L &= \int_{\Gamma_L} (\boldsymbol{N}_\lambda^L)^T \boldsymbol{N}_u^\Gamma \,\mathrm{d}a \;, \end{aligned} \tag{6.1}$$

such that these coupling terms are used in the Global-Local formulation; see Chapters 4 and 5. To overcome the non-conforming finite element discretized setting, the mortar method, the dual mortar method, and the localized mortar method are explained. Accordingly, in the following sections, the type of basis functions for the $\boldsymbol{\lambda}_L$, $\boldsymbol{\lambda}_C$ and $\boldsymbol{u}_\Gamma$ (i.e., $\boldsymbol{N}_\lambda^G$, $\boldsymbol{N}_\lambda^L$ and $\boldsymbol{N}_u^\Gamma$) are discussed.

6.1.1. Mortar method

The mortar method was proposed by Bernardi et al. [15] for the coupling of the spectral elements within multi-physics frameworks. The mortar method aims to use the weak coupling continuity condition between two sub-domains instead of the strong point-wise continuity condition. This type of coupling method is further developed in the finite element setting in [131, 130, 76], and also toward domain decomposition approach, which is the so-called finite element tearing and interconnecting method, i.e., FETI method [39].

To accommodate the mortar method in the Glocal-Local framework, let the basis function for the Lagrange multiplier at the global level, i.e., $\boldsymbol{N}_\lambda^G$, is set by Dirac delta function, as

$$N_{\lambda i}^G(x) = \delta(x - x_i) \quad \text{with} \quad \delta(x - x_i) = \begin{cases} +\infty & x = x_i \\ 0 & x \neq x_i \end{cases} , \tag{6.2}$$

for the collocation point x_i; see [116, 120]. The following properties hold for Dirac delta function:

- $\displaystyle\int_{-\infty}^{\infty} \delta(x)\,dx = 1,$
- $\displaystyle\int_{-\infty}^{\infty} \delta(x) f(x)\,dx = f(0),$ (6.3)
- $\displaystyle\int_{-\infty}^{\infty} \delta(x - x_i) f(x)\,dx = f(x_i).$

thus, we have

$$\int_{-\infty}^{\infty} N^G_{\lambda i}(x) f(x)\,dx = f(x_i) \;\; \rightarrow \;\; \int_{-a}^{a} N^G_{\lambda i}(x) f(x)\,dx = f(x_i) \qquad -\infty \leq -a \leq x_i \leq a \leq \infty,$$

if $x_i \in (-a, a)$ is bounded [74]. We further assume $\boldsymbol{N}^G_u = \boldsymbol{N}^\Gamma_u$ and $\boldsymbol{N}^L_\lambda = \boldsymbol{N}^L_u$ are the linear Lagrange interpolation polynomial functions. This type of discretization for the Lagrange multipliers satisfies the *inf-sup* condition; see for example [133, 132]. Accordingly, these choice of basis functions within the mortar method are shown in Fig. 6.2a.

6.1.2. Mortar method with a dual basis function for the local Lagrange multiplier

The dual mortar method is an alternative to the mortar method and differs in terms of the local Lagrange multiplier basis function [133, 132]. Let us define the coupling non-mortar mass matrix $\mathbf{T}_L := \mathbf{J}_L|_{\Gamma_L}$ which is a restriction of $\mathbf{J}_L$ from $\mathcal{B}_L$ to Γ_L. The dual mortar method denoted by $\widehat{\mathbf{T}}_L$ is based on a "diagonal structure" of the $\mathbf{T}_L$ such that a dual shape function is formulated to satisfy the so-called biorthogonality condition in addition to the Babuska-Brezzi condition [118]; thus we have

$$\widehat{\mathbf{T}}_L = \int_{\Gamma_L} (\widehat{\boldsymbol{N}}^L_\lambda)^T \boldsymbol{N}^L_u \;\mathrm{d}a = \delta_{ij} \int_{\Gamma_L} \boldsymbol{N}^L_u \;\mathrm{d}a. \tag{6.4}$$

Here, δ_{ij} represents the Kronecker delta function. The main objective of the dual mortar method is to determine the unknown dual basis function (i.e., $\widehat{\boldsymbol{N}}^L_\lambda$) such that (6.4) satisfies. To do so, we assume that the dual basis function $\widehat{\boldsymbol{N}}^L_\lambda$ at point ξ is defined through a linear combination of $\boldsymbol{N}^L_\lambda$, thus reads

$$\widehat{N}^L_{\lambda\,i}(\xi) = \sum_{j=1}^{n_{\Gamma_L}} b_{ij} N^L_{\lambda\,j}(\xi), \tag{6.5}$$

where, n_{Γ_L} represents the degrees of freedom for the local interface Γ_L. Here, b_{ij} is an unknown quantity (which has to be determined) within square matrix $\boldsymbol{B}$ with dimensions $(n_{\Gamma_L} \times n_{\Gamma_L})$. To do so, we can re-write (6.4) by using (6.5), thus yielding

$$\widehat{T}^{ij}_L = \int_{\Gamma_L} \Big(\sum_{j=1}^{n_{\Gamma_L}} b_{ik} N^L_{\lambda\,k}(\xi)\Big)^T N^L_{u\,j} \;\mathrm{d}a = \delta_{ij} \int_{\Gamma_L} N^L_u \;\mathrm{d}a =: D_{ij}, \tag{6.6}$$

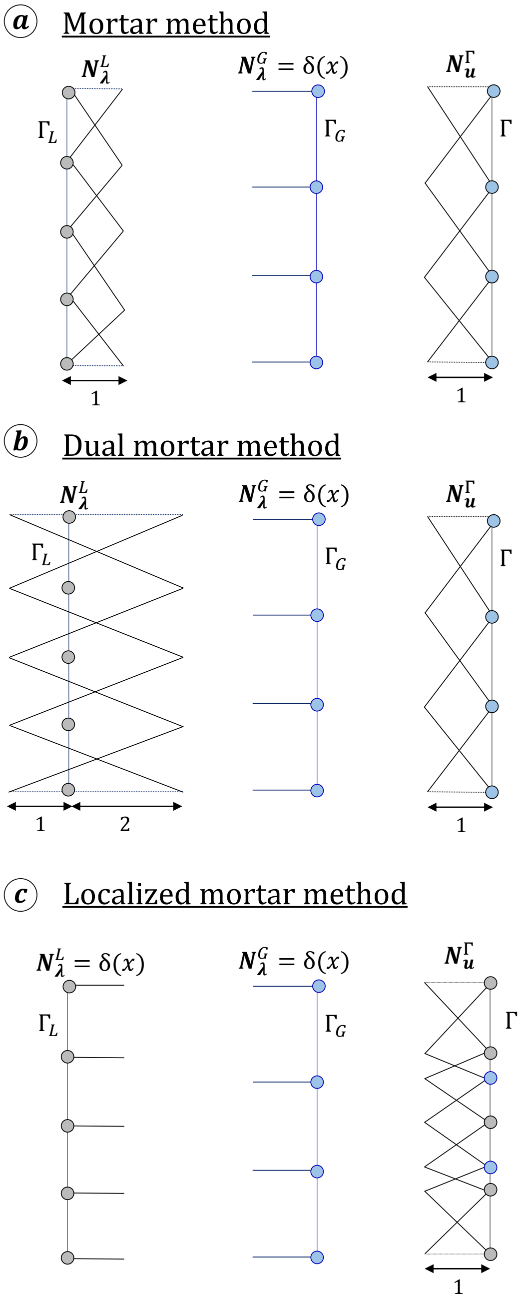

Figure 6.2: Two-dimensional linear 'hat' basis function for the $\boldsymbol{\lambda}_L$, $\boldsymbol{\lambda}_C$, and $\boldsymbol{u}_\Gamma$. (a) A mortar method, (b) a dual mortar method, and (c) a localized mortar method.

thus

$$\begin{aligned}\sum_{j=1}^{n_{\Gamma_L}} b_{ik} \int_{\Gamma_L} \left(N^L_{\lambda\,k}(\xi)\right)^T N^L_{u\,j}\ \mathrm{da} &= \sum_{j=1}^{n_{\Gamma_L}} b_{ik}\left(T_L^{kj}\right) \\ &= \left[\boldsymbol{B}\mathbf{T}_L\right]_{ij}(\xi) = \left[\boldsymbol{D}\right]_{ij}(\xi),\end{aligned} \tag{6.7}$$

with diagonal non-mortar mass matrix given by

$$D_{ij} = \delta_{ij} \int_{\Gamma_L} \boldsymbol{N}_u^L \ da. \tag{6.8}$$

An unknown square matrix $\boldsymbol{B}$, includes the mapping coefficients for determining a dual basis function, thus eventually obtained through:

$$\boldsymbol{B} = \boldsymbol{D}\mathbf{T}_L^{-1}.$$

In the two-dimensional setting, which results in the one-dimensional interface with linear basis functions, dual basis functions $\widehat{\boldsymbol{N}}_\lambda^L$ are given in Table 6.1. Note, $\widehat{\boldsymbol{N}}_\lambda^L$ is not strictly positive (see Fig. 6.2b) because two $\boldsymbol{N}_\lambda^L$ are strictly positive, yet two strictly positive functions cannot be orthogonal [133].

Notably, the resulting solution fields through the mortar method and a dual mortar method are identical. But the non-mortar coupling mass matrix in the dual mortar method $\widehat{\mathbf{T}}_L$ is a diagonal matrix; hence, less effort is required for the inversing problem of $\widehat{\mathbf{T}}_L$ while $\mathbf{T}_L$ is a sparse non-diagonal squared matrix.

Remark 6.1.1. *Following our discretization for the set of basis functions* $(\boldsymbol{\lambda}_C, \boldsymbol{u}_\Gamma, \boldsymbol{u}_G)$, *namely* $(\boldsymbol{N}_\lambda^G, \boldsymbol{N}_u^\Gamma, \boldsymbol{N}_u^G)$, *in the mortar method (as well as the dual mortar method), the coupling global mass matrix* $\mathbf{J}_G : \mathcal{B}_G \to \Gamma_G$ *becomes signed Boolean mappings [13]. This mapping is used to project the entire domain to interface contributions. Hence,* $\hat{\boldsymbol{u}}_{G,b} := \mathbf{J}_G \hat{\boldsymbol{u}}_G$, *in which, b denotes as interface nodes. Additionally,* $\mathbf{L}_G$ *becomes an identity tensor with a dimension of the* Γ_G *degrees of freedom. As a result, the main challenge here is to determine* $(\mathbf{J}_L, \mathbf{L}_L)$, *which is explained in the following section.*

Table 6.1: Dual interpolation basis functions for a two-dimensional setting.

Linear Segment $\xi, \zeta \in [-1, 1]$	$N_1^\bullet$	$\boldsymbol{N}_2^\bullet$
Local displacement field $\boldsymbol{u}_L$	$\widehat{N}_{u1}^L(\xi) = \frac{1}{2}(1-\xi)$	$\widehat{N}_{u2}^L(\xi) = \frac{1}{2}(1+\xi)$
Local Lagrange parameter $\boldsymbol{\lambda}_L$	$\widehat{N}_{\lambda 1}^L(\xi) = \frac{1}{2}(1-3\xi)$	$\widehat{N}_{\lambda 2}^L(\xi) = \frac{1}{2}(1+3\xi)$
Intermediate displacement field $\boldsymbol{u}_\Gamma$	$\widehat{N}_{u1}^\Gamma(\zeta) = \frac{1}{2}(1-\zeta)$	$\widehat{N}_{u2}^\Gamma(\zeta) = \frac{1}{2}(1+\zeta)$

6.1.3. Numerical integration for non-mortar/mortar integrals

In this section, we evaluate the local coupling matrices $\mathbf{L}_L$ and $\mathbf{J}_L$ using a numerical integration procedure called the Gaussian quadrature rule. Here, the numerical integration procedure relies on the definition of the *intermediate interface* denoted by Γ_{int}; see Fig. 6.3a. The intermediate interface Γ_{int} results from the projection of the both discretized Γ_L and Γ onto the unique line surface Γ_{int}; hence, we have

$$n_{\Gamma_{int}} = n_\Gamma \oplus n_{\Gamma_L} - n_0. \tag{6.9}$$

Here, $(n_{\Gamma_{int}}, n_\Gamma, n_{\Gamma_L}, n_0)$ represent the degrees of freedom of the intermediate interface Γ_{int}, interface Γ, local interface Γ_L, and overlapping collocated nodes n_0, respectively.

Notably, one should not confuse Γ_{int} and Γ, such that Γ_{int} is *only* virtually defined to calculate coupling quantity, while in Γ we have a solution field denoted as $\boldsymbol{u}_\Gamma$. Once Γ_{int} is made from the summation of Γ_L and Γ interfaces, the numerical integration for $\mathbf{L}_L$ and $\mathbf{J}_L$ is performed on the Γ_{int}. To evaluate the numerical integration through the Gaussian quadrature rule, a local coordinate system based on the isoparametric coordinate

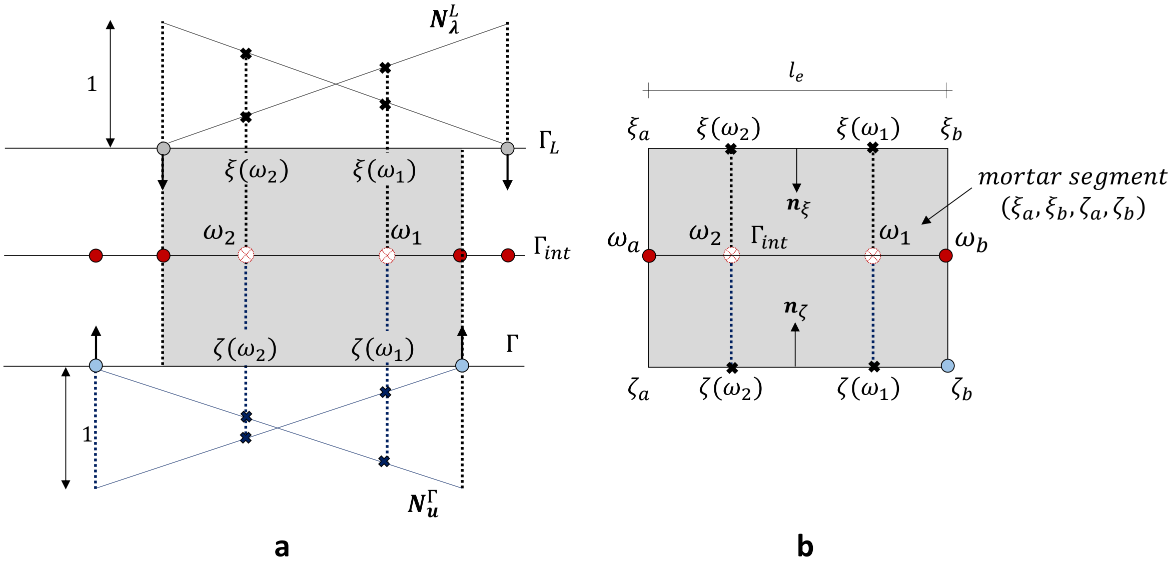

Figure 6.3: Setup of the notation for a schematic illustration of the (a) projected segment strategy to be used in numerical integration for the non-mortar/mortar integrals, and (b) mortar segment $(\xi_a, \xi_b, \zeta_a, \zeta_b)$ inclduing $\Gamma_{int}^{seg} = (\omega_a, \omega_b) \subset \Gamma_{int}$.

$\omega \in [-1, +1]$ is defined for every *segment* within Γ_{int}. We refer the segment to each discretized elements within Γ_{int} denoted by $\Gamma_{int}^{seg} \subset \Gamma_{int}$; see Fig. 6.3b. In the following, the number segments is shown with n_{seg}.

Notably, for the one-dimensional linear element, using only two Gauss quadrature points is sufficient for achieving an exact integration; hence, two Gauss quadrature points are used herein. Let $(\xi, \zeta, \omega) \in [-1, +1]$ be Gauss quadrature points that corresponds to the Γ_L, Γ and Γ_{int}, respectively. Accordingly, we define the mortar segment with four nodes including $(\xi_a, \xi_b) \in \Gamma_L$ and $(\zeta_a, \zeta_b) \in \Gamma$; see Fig. 6.3b.

To evaluate the corresponding points $\omega \in \Gamma_{int}$ within Γ_L and Γ, the following linear interpolation holds:

$$\xi(\omega) = N_1(\omega)\xi_a + N_2(\omega)\xi_b \quad \text{and} \quad \zeta(\omega) = N_1(\omega)\zeta_a + N_2(\omega)\zeta_b, \tag{6.10}$$

such that

$$N_1(\omega) = \frac{1}{2}(1 - \omega), \quad N_2 = \frac{1}{2}(1 + \omega) \quad \text{with} \quad N_1 + N_2 = 1. \tag{6.11}$$

Next, the coupling mortar mass matrix $\mathbf{L}_L$ is evaluated on Γ_{int} based on the Gaussian quadrature rule through

$$\mathbf{L}_L = \int_{\Gamma_L} (\boldsymbol{N}_\lambda^L)^T \boldsymbol{N}_u^\Gamma \, \mathrm{d}a = \int_{\Gamma_{int}} (\boldsymbol{N}_\lambda^L)^T \boldsymbol{N}_u^\Gamma \, \mathrm{d}a = \bigcup_{e}^{n_{seg}} \mathbf{L}_L^e, \tag{6.12}$$

with,

$$\mathbf{L}_L^e = \int_{\Gamma_{int}^{seg}} (\boldsymbol{N}_\lambda^L)^T \boldsymbol{N}_u^\Gamma \, \mathrm{d}a = \int_{-1}^{1} \Big(\boldsymbol{N}_\lambda^L(\xi)\Big)^T \boldsymbol{N}_u^\Gamma(\zeta) J_p \, \mathrm{d}\xi. \tag{6.13}$$

To perform a numerical integration for the $\mathbf{L}_L^e$ in (6.13), a mapping between physical Cartesian to the isoparametric coordinates is performed using the *Jacobian*, denoted by J_p. Because numerical integration is evaluated within Γ_{int}, mapping first from the physical coordinate to the ξ and then from ξ to ω is performed. Thus, we have

$$J_p = J_\xi J_\omega \quad \text{with} \quad J_p = \left|\frac{\partial \boldsymbol{x}}{\partial \boldsymbol{\omega}}\right|, \; J_\xi = \left|\frac{\partial \boldsymbol{x}}{\partial \boldsymbol{\xi}}\right|, \quad \text{and} \quad J_\omega = \left|\frac{\partial \boldsymbol{\xi}}{\partial \boldsymbol{\omega}}\right|, \tag{6.14}$$

that is

$$J_\xi = \left|\frac{\partial \boldsymbol{x}}{\partial \boldsymbol{\xi}}\right| = \frac{1}{2} l_e, \quad \text{and} \quad J_\omega = \left|\frac{\partial \boldsymbol{\xi}}{\partial \boldsymbol{\omega}}\right| = \frac{1}{2}\left|\xi_b - \xi_a\right|, \tag{6.15}$$

where, l_e is the length of local element (i.e., $|x_b - x_a|$) on Γ_L; see Fig. 6.3. Accordingly, $|\xi_b - \xi_a|$ is the length of the segment in Γ_{int} projected to the Γ_L through isoparametric coordinates; see Fig. 6.3. Following the above mentioned formulations, $(i,j)^{th}$ components of the $\mathbf{L}_L^e$, associated with $N_{\lambda\, i}^L$ and $N_{u\, j}^\Gamma$, reads

$$\begin{aligned}(L_L^e)^{ij} &= \sum_{p=1}^{n_{gp}} N_{\lambda\, i}^L\Big(\xi(\omega_p)\Big) N_{u\, j}^\Gamma\Big(\zeta(\omega_p)\Big) W_p J_p \\ &= \sum_{p=1}^{n_{gp}} N_{\lambda\, i}^L\Big(\xi(\omega_p)\Big) N_{u\, j}^\Gamma\Big(\zeta(\omega_p)\Big) \frac{1}{4} l_e \left|\xi_b - \xi_a\right| W_p.\end{aligned} \tag{6.16}$$

Here, W_p represents the Gaussian weight factor for the numerical integration, and ω_p stands for the Gauss quadrature points in Γ_{int}^{seg}. Notably, the local Lagrange multiplier basis function $\boldsymbol{N}_\lambda^L$ is determined based on the projection of the Gauss quadrature point $\omega \in \Gamma_{int}$ to the Γ_L while $\boldsymbol{N}_u^\Gamma$ is determined based on the projection of the Gauss quadrature point $\omega \in \Gamma_{int}$ to the Γ. Accordingly, for the coupling non-mortar mass matrix $\mathbf{T}_L$, we have

$$\mathbf{T}_L = \int_{\Gamma_L} (\boldsymbol{N}_\lambda^L)^T \boldsymbol{N}_u^L \; \mathrm{d}a = \int_{\Gamma_{int}} (\boldsymbol{N}_\lambda^L)^T \boldsymbol{N}_u^L \; \mathrm{d}a = \bigcup_e^{n_{seg}} \mathbf{T}_L^e. \tag{6.17}$$

with,

$$\mathbf{T}_L^e = \int_{\Gamma_{int}^{seg}} (\boldsymbol{N}_\lambda^L)^T \boldsymbol{N}_u^L \; \mathrm{d}a = \int_{-1}^{1} \Big(\boldsymbol{N}_\lambda^L(\xi)\Big)^T \boldsymbol{N}_u^L(\xi) J_p \; \mathrm{d}\xi. \tag{6.18}$$

The $(i,j)^{th}$ components of the $\mathbf{T}_L^e$ associated with the $N_{\lambda\, i}^L$ and $N_{u\, j}^L$, respectively, reads as follows:

$$\begin{aligned}(T_L^e)^{ij} &= \sum_{p=1}^{n_{gp}} N_{\lambda\, i}^L\Big(\xi(\omega_p)\Big) N_{u\, j}^L\Big(\xi(\omega_p)\Big) W_p J_p \\ &= \sum_{p=1}^{n_{gp}} N_{\lambda\, i}^L\Big(\xi(\omega_p)\Big) N_{u\, j}^L\Big(\xi(\omega_p)\Big) \frac{1}{4} l_e \left|\xi_b - \xi_a\right| W_p.\end{aligned} \tag{6.19}$$

Here, both basis functions $\boldsymbol{N}_\lambda^L$ and $\boldsymbol{N}_u^L$ are determined based on the projection of the Gauss quadrature point $\omega \in \Gamma_{int}$ to the local interface Γ_L. Once the assembly procedure through all segments in Γ_{int} is performed, the so-called dependency matrix denoted by $\boldsymbol{\alpha}_{GL}$ is obtained through $\mathbf{L}_L$ and $\mathbf{T}_L$

$$\hat{\boldsymbol{u}}_{L,b} = \boldsymbol{\alpha}_{GL}\hat{\boldsymbol{u}}_{G,b} \quad \text{with} \quad \boldsymbol{\alpha}_{GL} := \mathbf{L}_L^{-1}\mathbf{T}_L. \tag{6.20}$$

Here, b denotes interface nodes. Dependency matrix $\boldsymbol{\alpha}_{GL}$ relates the local displacement field $\hat{\boldsymbol{u}}_{L,b}$ with the global displacement field $\hat{\boldsymbol{u}}_{G,b}$ at the interface. The detailed numerical framework for the integration of coupling terms based on the mortar method is illustrated in Algorithm 6. Accordingly, Fig. 6.4 depicts numerical integration through the mortar method.

Remark 6.1.2. *Recall,* $\mathbf{T}_L := \mathbf{J}_L|_{\Gamma_L}$ *which, is a restriction of* $\mathbf{J}_L$ *from* $\mathcal{B}_L$ *to* Γ_L*. Hence, by having* $\mathbf{T}_L$ *through Algorithm 6 and thus by using the prolongation operator defined on* $\Gamma_L \to \mathcal{B}_L$*, we could simply obtain* $\mathbf{J}_L$*. By prolongation operator, we mean* $\mathbf{J}_L := [\mathbf{0}_{\mathcal{B}_L\setminus\Gamma_L}\ , \mathbf{T}_L]^T$*, whereas* $\mathbf{0}_{\mathcal{B}_L\setminus\Gamma_L}$ *is the null tensor that stands for the interior degrees of freedom, and* $\mathbf{T}_L$ *is the coupling non-mortar mass matrix for the interface degrees of freedom.*

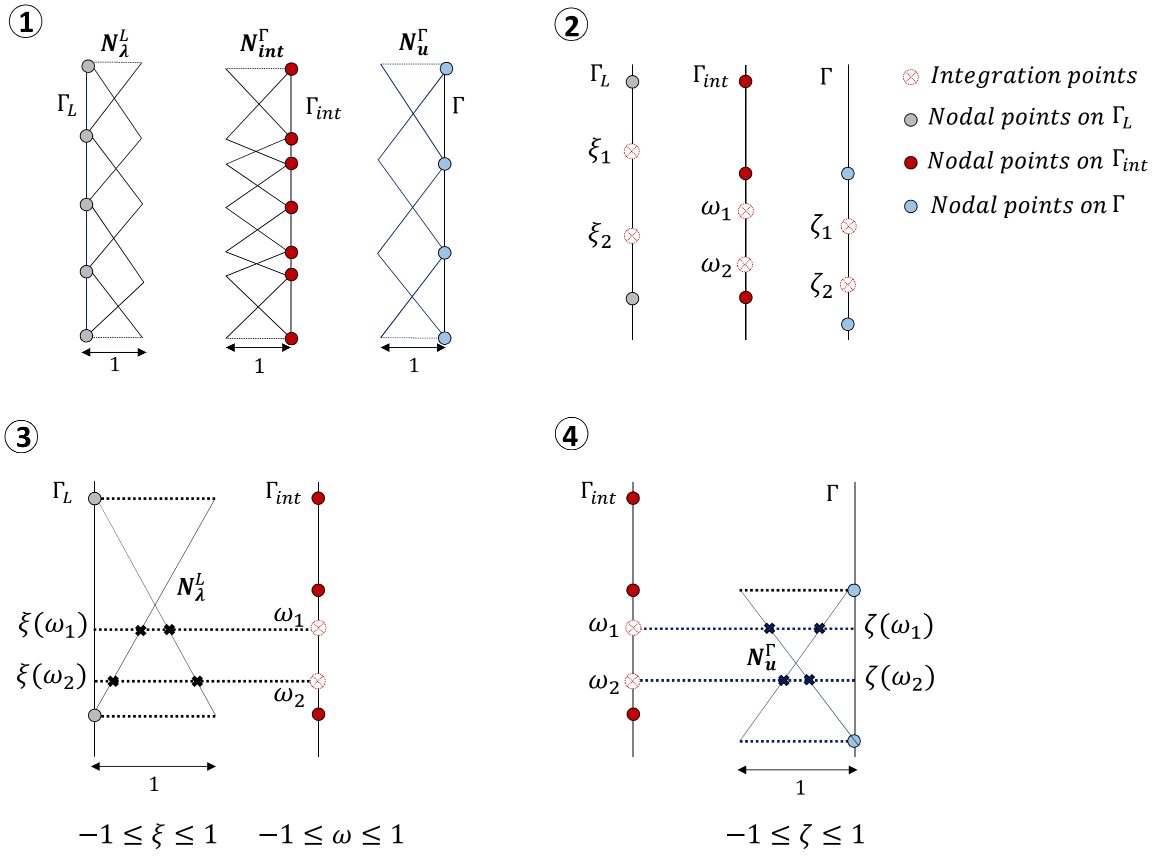

Figure 6.4: Numerical steps to compute the numerical integration scheme for the non-mortar/mortar integrals through the projected segment strategy.

Algorithm 6 *Numerical integration framework for the mortar method*

```
• Create $\Gamma_{int}$ by projecting non-mortar nodes in $\Gamma_L$ and mortar nodes in $\Gamma$ (Fig. 6.3).
• Discretize intermediate interface thus $\Gamma_{int} = \bigcup_{e}^{n_{seg}} \Gamma_{int}^{seg}$ (Fig. 6.4(1)).
• Loop over segments $\Gamma_{int}^{seg}$: $k = 1,\, n_{seg}$
    I. For each $\Gamma_{int}^{seg}$ locate $n_{gp}$ Gauss quadrature points $\omega_p$ (Fig. 6.4(2))
    II. Loop over non-mortar side to find an element $\Gamma_L^e \subset \Gamma_L$ such that $\Gamma_{int}^{seg} \subset \Gamma_L^e$.
    III. Loop over mortar side to find an element within $\Gamma^e \subset \Gamma$ such that $\Gamma_{int}^{seg} \subset \Gamma^e$.
    IV. Loop over Gauss points in $\Gamma_{int}^{seg}$: $p = 1,\, n_{gp}$
        V. Calculate the physical coordinates of the integration points $w_p$ thus
            $w_p \to x_G : \quad x_G = \sum_{i=1}^{2} N_i(w_p)\bar{w}_i,$
           where $(\bar{w}_1, \bar{w}_2) := (\bar{w}_a, \bar{w}_b)$ is nodal coordinates within $\Gamma_{int}^{seg}$ (Fig. 6.3).
        VI. Perform *inverse mapping* to determine the isoparametric coordinates
            $\xi_p = \xi(w_p) \subset \Gamma_L^e, \quad \text{and} \quad \zeta_p = \zeta(w_p) \subset \Gamma^e,$
            associated with the physical coordinate $x_G$ (Fig. 6.4(3-4)).
        VII. Evaluate the $(i,j)^{th}$ component of the mortar/non-mortar mass matrices
            $(L_L^e)^{ij} = \sum_{p=1}^{n_p} N_{\lambda\, i}^{L}(\xi_p) N_{u\, j}^{\Gamma}(\zeta_p) \tfrac{1}{4} l_e \,|\xi_b - \xi_a|\, W_p,$
            $(T_L^e)^{ij} = \sum_{p=1}^{n_p} N_{\lambda\, i}^{L}(\xi_p) N_{u\, j}^{L}(\xi_p) \tfrac{1}{4} l_e \,|\xi_b - \xi_a|\, W_p.$
        VIII. Update the coupling mortar/non-mortar mass matrices: $\mathbf{L}_L^e$ and $\mathbf{T}_L^e$
    End loop for integration points
    • Assemble the contributions of mortar/non-mortar elements
        $\mathbf{L}_L = \bigcup_{e}^{n_{seg}} \mathbf{L}_L^e, \quad \text{and} \quad \mathbf{T}_L = \bigcup_{e}^{n_{seg}} \mathbf{T}_L^e\ .$
End
```

6.1.4. Localized mortar method

To formulate the non-conforming discrete interfaces based on the localized mortar method, following [110, 120] *the maximally collocated frame node* approach is used. Thus, an interface Γ results from the projection of the both discretized Γ_L and Γ_G onto the unique line surface Γ (see Fig. 6.2c); hence, we have

$$n_{\Gamma} = n_{\Gamma_G} \oplus n_{\Gamma_L} - n_0. \tag{6.21}$$

Here, $(n_{\Gamma}, n_{\Gamma_G}, n_{\Gamma_L}, n_0)$ represent the degrees of freedom of an interface Γ, global interface Γ_G, local interface Γ_L, and overlapping collocated nodes n_0, respectively.

- ***Interpolating the global and local interface solution to the intermediate interface solution***

The choice of basis functions for the Lagrange multipliers within the localized mortar method (i.e., $\boldsymbol{N}_\lambda^G$ and $\boldsymbol{N}_\lambda^L$), are based on the Dirac delta function, through

$$N_{\lambda i}^G(x) = N_{\lambda i}^L(x) = \delta(x - x_i) \quad \text{with} \quad \delta(x - x_i) = \begin{cases} +\infty & x = x_i \\ 0 & x \neq x_i \end{cases}, \tag{6.22}$$

for the collocation point x_i. We further assume $\boldsymbol{N}_u^G$, $\boldsymbol{N}_u^\Gamma$, $\boldsymbol{N}_\lambda^L$ and $\boldsymbol{N}_u^L$ are the linear Lagrange interpolation polynomial functions.

Following our discretization, $\mathbf{J}_G : \mathcal{B}_G \to \Gamma_G$ and $\mathbf{J}_L : \mathcal{B}_L \to \Gamma_L$ become signed Boolean mappings [13, 120] which are used to project the entire domain to interface contributions, thus yielding

$$\hat{\boldsymbol{u}}_{G,b} := \mathbf{J}_G \hat{\boldsymbol{u}}_G \quad \text{and} \quad \hat{\boldsymbol{u}}_{L,b} := \mathbf{J}_L \hat{\boldsymbol{u}}_L. \tag{6.23}$$

Here, b denotes the interface nodes. Next, we aim to obtain $\mathbf{L_L}$ and $\mathbf{L_G}$.

By the given continuous function $\boldsymbol{u}_{G,b}$ in Γ_G, we define the linear interpolation operator $\boldsymbol{\pi}_G : \Gamma_G \to \Gamma$ through

$$\hat{\boldsymbol{u}}_\Gamma(\boldsymbol{x}) := \boldsymbol{\pi}_G \hat{\boldsymbol{u}}_{G,b} = \boldsymbol{N}_u^G(\boldsymbol{x}) \hat{\boldsymbol{u}}_{G,b} \quad \text{for } \boldsymbol{x} \in \Gamma, \tag{6.24}$$

and additionally with a given continuous function $\boldsymbol{u}_{L,b}$ in Γ_L, we define the linear interpolation operator $\boldsymbol{\pi}_L : \Gamma_L \to \Gamma$ by

$$\hat{\boldsymbol{u}}_\Gamma(\boldsymbol{x}) := \boldsymbol{\pi}_L \hat{\boldsymbol{u}}_{L,b} = \boldsymbol{N}_u^L(\boldsymbol{x}) \hat{\boldsymbol{u}}_{L,b} \quad \text{for } \boldsymbol{x} \in \Gamma, \tag{6.25}$$

and duality to the global and local displacement fields yields,

$$\hat{\boldsymbol{\lambda}}_G = \boldsymbol{\pi}_G^T \hat{\boldsymbol{\lambda}}_\Gamma \quad \text{and} \quad \hat{\boldsymbol{\lambda}}_L = \boldsymbol{\pi}_L^T \hat{\boldsymbol{\lambda}}_\Gamma. \tag{6.26}$$

Following [67, 120], the coupling matrix $\mathbf{L_G}$ and $\mathbf{L_L}$ have to be computed by the pseudo-inverse transformation through

$$\mathbf{L_G} = \boldsymbol{\pi}_\mathbf{G}^+ \quad \text{and} \quad \mathbf{L_L} = \boldsymbol{\pi}_\mathbf{L}^+, \tag{6.27}$$

such that the identity

$$\mathbf{I_G} = \mathbf{L_G} \boldsymbol{\pi}_\mathbf{G} \quad \text{and} \quad \mathbf{I_L} = \mathbf{L_L} \boldsymbol{\pi}_\mathbf{L}, \tag{6.28}$$

holds. Hence, we have

$$\mathbf{L_G} = (\boldsymbol{\pi}_\mathbf{G}^\mathbf{T} \boldsymbol{\pi}_\mathbf{G})^{-\mathbf{1}} \boldsymbol{\pi}_\mathbf{G}^\mathbf{T} \quad \text{and} \quad \mathbf{L_L} = (\boldsymbol{\pi}_\mathbf{L}^\mathbf{T} \boldsymbol{\pi}_\mathbf{L})^{-\mathbf{1}} \boldsymbol{\pi}_\mathbf{L}^\mathbf{T}. \tag{6.29}$$

- ***To determine dependency matrix***

In line with the mortar method, we are able to relate $\hat{\boldsymbol{u}}_{G,b}$ and $\hat{\boldsymbol{u}}_{L,b}$ through dependency matrix. To do so, if Γ_G (i.e., coarser mesh) is explicitly chosen as the mortar side, using (4.58)2, (6.23) and (6.24), we have

$$\mathbf{L}_L \hat{\boldsymbol{u}}_\Gamma - \mathbf{J}_L \hat{\boldsymbol{u}}_L = \mathbf{L}_L \boldsymbol{\pi}_G \hat{\boldsymbol{u}}_{G,b} - \mathbf{J}_L \hat{\boldsymbol{u}}_L = \mathbf{L}_L \boldsymbol{\pi}_G \hat{\boldsymbol{u}}_{G,b} - \hat{\boldsymbol{u}}_{L,b} = \mathbf{0}, \tag{6.30}$$

results in,

$$\hat{\boldsymbol{u}}_{L,b} = \boldsymbol{\alpha}_{GL} \hat{\boldsymbol{u}}_{G,b} \quad \text{with} \quad \boldsymbol{\alpha}_{GL} := \mathbf{L}_L \boldsymbol{\pi}_G. \tag{6.31}$$

Additionally, if Γ_L (i.e., finer mesh) is explicitly chosen as mortar side, using (4.63), (6.23) and (6.25), we have

$$\mathbf{L}_G \hat{\boldsymbol{u}}_\Gamma - \mathbf{J}_G \hat{\boldsymbol{u}}_G = \mathbf{L}_G \boldsymbol{\pi}_L \hat{\boldsymbol{u}}_{L,b} - \mathbf{J}_G \hat{\boldsymbol{u}}_G = \mathbf{L}_G \boldsymbol{\pi}_L \hat{\boldsymbol{u}}_{L,b} - \hat{\boldsymbol{u}}_{G,b} = \mathbf{0}, \tag{6.32}$$

results in,

$$\hat{\boldsymbol{u}}_{G,b} = \boldsymbol{\alpha}_{LG} \hat{\boldsymbol{u}}_{L,b} \quad \text{with} \quad \boldsymbol{\alpha}_{LG} := \mathbf{L}_G \boldsymbol{\pi}_L. \tag{6.33}$$

6.1.5. Effect of the type of basis function for the $\boldsymbol{N}_\lambda^L$ on $\mathbf{L}_L$

In this section, the effects of Lagrange multiplier basis function $\boldsymbol{N}_\lambda^L$ on the $\mathbf{L}_L$, which could be Kronecker delta function (e.g., the localized mortar method, see Fig. 6.2c) or linear basis function (e.g., the mortar method, see Fig. 6.2a), are investigated.

Recall the linear discretizations which are used for Γ_L and Γ in Fig. 6.2. To evaluate $\mathbf{L}_L$, we specifically consider the $\boldsymbol{N}_{\lambda 2}^L$ shown in Fig. 6.5. It turns out that if a Dirac delta function is chosen for the $\boldsymbol{N}_{\lambda 2}^L$, it simplifies the mortar mass matrix $\mathbf{L}_L$; see Fig. 6.5(right column). By Contrast, if a linear basis function is chosen, the mortar integration results in the entire gray area shown in Fig. 6.5(left column). Hence, the localized mortar method is computationally faster yet it preserves the computational accuracy (for the numeircal examples see Section 6.2). For a further detailed discussion, see [116].

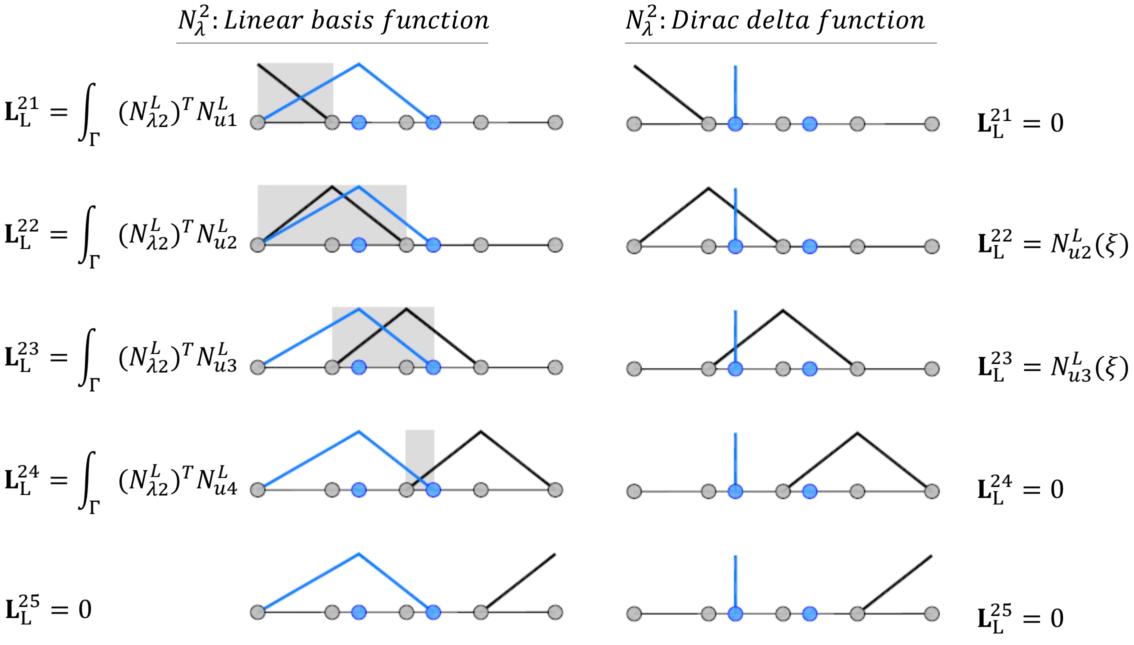

Figure 6.5: Integration of the $\mathbf{L}_L$ based on different $\boldsymbol{N}_\lambda^L$. First, as a piecewise linear function on the left side, and second as a Dirac delta function on the right side.

6.2. Benchmark numerical problems

This section verifies the performance of the non-matching formulation described earlier for the elasticity problem. Two numerical benchmark tests are investigated. In these examples, the constitutive parameters for the isotropic material are considered to be fixed with $\lambda = 121.15$ kN/mm^2 and $\mu = 80.77$ kN/mm^2. Additionally, sub-domains are discretized using bilinear quadrilateral $Q1$ finite elements. The performance of the different non-matching formulations for the elasticity problem is accordingly provided.

6.2.1. Contact patch test

In the first numerical example, a well-known contact patch test is considered. A BVP is shown in Fig. 6.6. The numerical problem is divided into two sub-domains, namely $\mathcal{B}_1$ and $\mathcal{B}_2$, which are shared on the interface Γ. Domain $\mathcal{B}_2$ is in contact at uniform traction and thus we set $\bar{F} = 1000$. The contour plot of the vertical displacement are shown in Fig. 6.7 for the mortar method (left), the dual mortar method(middle), and the localized mortar method (right). Regarding u_y, all methods provide an identical deformation resolution, yet the localized mortar method is much easier to implement and more efficient in terms of computational cost. In terms of the vertical stress distribution σ_y, the mortar and dual mortar methods give the exact results, whereas the localized mortar method is not as precise as other methods; see Fig. 6.7. The result could be accepted depending on the accuracy we require (in this method, the computational stress error is approximately 0.16%).

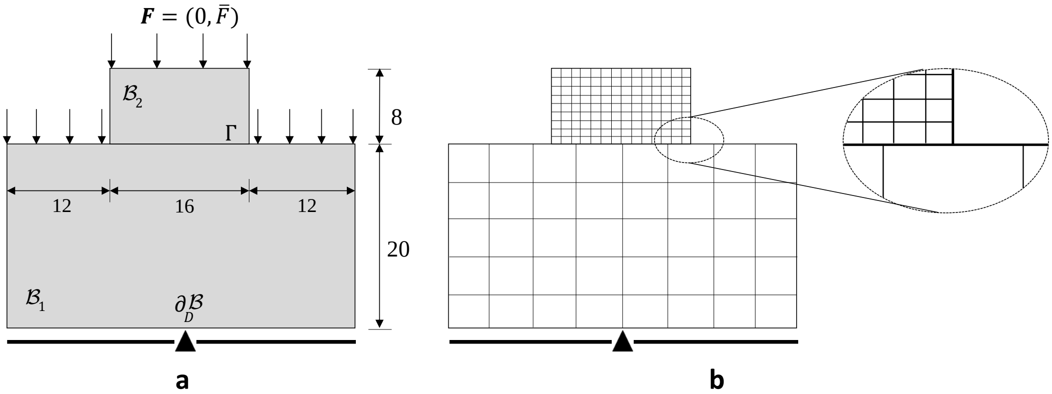

Figure 6.6: Benchmark numerical example 1. Contact patch test. (a) Geometry and loading setup, and (b) non-conforming finite element discretization.

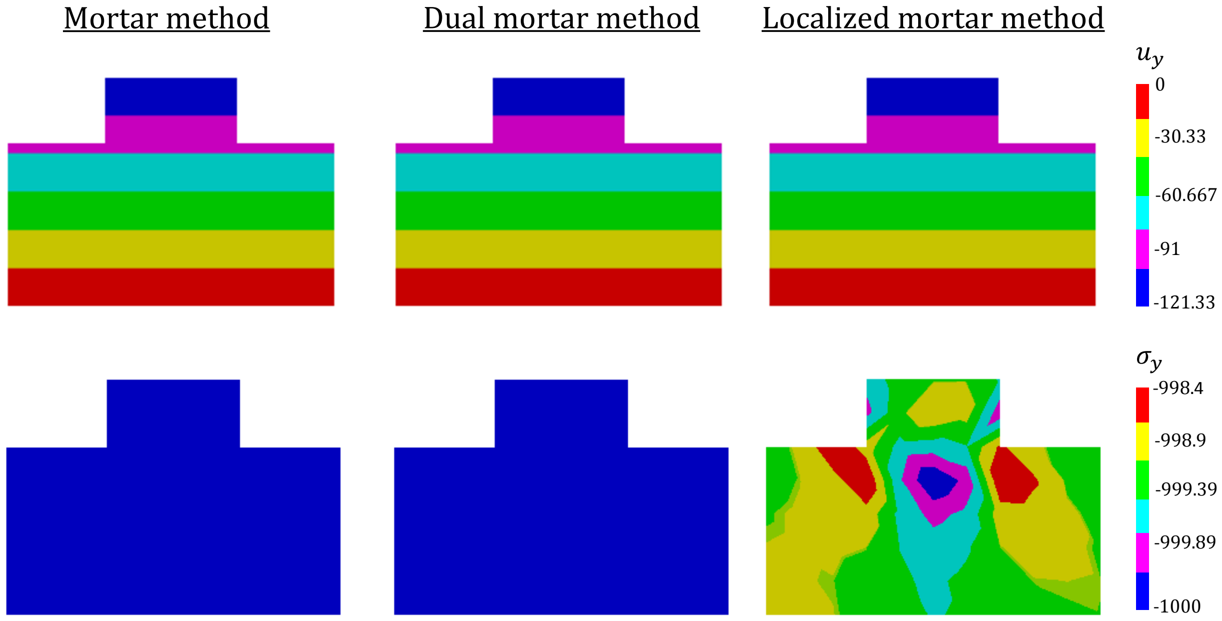

Figure 6.7: Benchmark numerical example 1. First row represents vertical displacement field, and second row indicates vertical stress distribution.

6.2.2. Two-dimensional elasticity squared problem

Next, in the second example, different methods are also investigated for dealing with non-conforming discretization. The boundary value problem is given in Fig. 6.8. A single domain is divided into two sub-domains $\mathcal{B}_1$ and $\mathcal{B}_2$ with a common interface Γ, where $\mathcal{B}_2$ is subjected to the uniform traction. We set $\bar{F} = 1$ and $A = 0.5$, and hence $\mathcal{B} = (0,1)^2$. Displacement contours for the vertical quantity u_y of different methods are shown in Fig. 6.9 (first row). It is evident that all these methods produce an excellent agreement with exact results, yet the localized mortar method does so with less computational cost. Regarding the stress continuity across the interface, the localized mortar method leads to small oscillation; however, this stress error distribution is approximately 0.025% (because of the discretization).

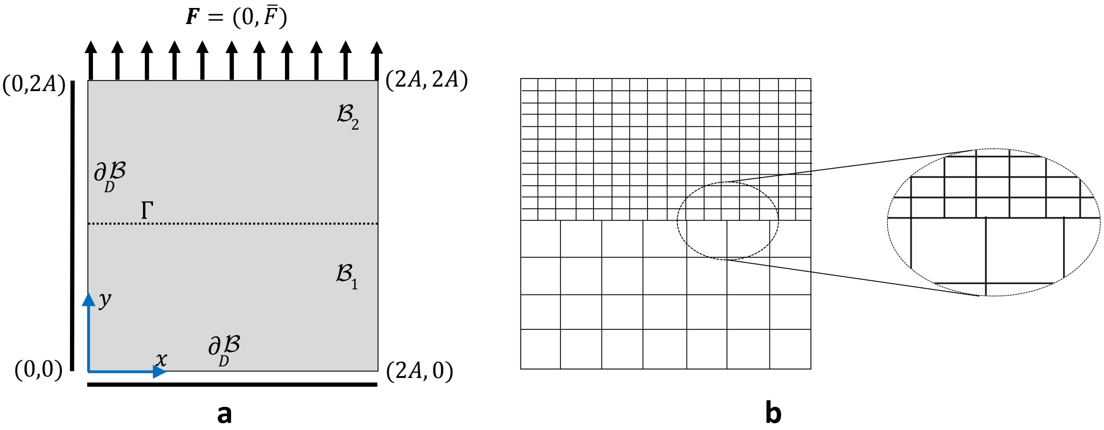

Figure 6.8: Benchmark numerical example 2. Tensile elasticity patch test. (a) Geometry and loading setup, and (b) non-conforming finite element discretization.

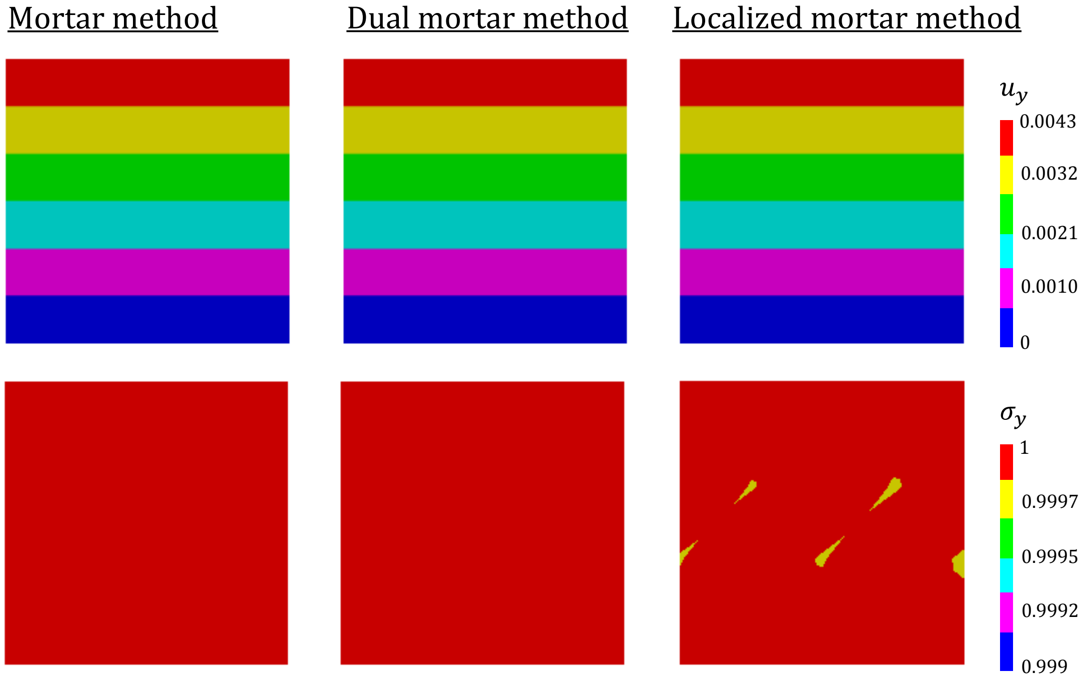

Figure 6.9: Benchmark numerical example 2. The first row represents the vertical displacement field, and the second row indicates vertical stress distribution.

6.3. Numerical examples

This section demonstrates the performance of the proposed Global-Local formulation for the non-conforming finite element discretization in the Global-Local framework. The main advantage here is to discretize the local domain, independently of the global mesh, thereby gaining more freedom in terms of the numerical implementation. Another impacting factor is achieving more regularity at the interface. Hence, if the crack path reaches to the local boundary, we would still have a sufficiently small number of elements, resulting in the small characteristic length-scale l to resolve the crack phase-field. Additionally, using the non-conforming finite element discretization, we can use hybrid finite element discretization, meaning that the local discretization element type is not necessarily identical to the global level. Thus, we gain more freedom from a numerical implementation point of view. In the following, two numerical examples are investigated and explained in detail.

6.3.1. Example 1: Tensile test including voids and fibers at small deformation

In the first example, we investigate the effects of the different non-conforming finite element discretization on the Global-Local framework. These include the dual mortar method and the localized mortar method. Specifically, $g/l - 2$ in Algorithm 3 (Section 4.7) is considered here for the solid material undergoing small deformation. Here, a BVP is applied to the square plate with three voids and four hard inclusions, which is shown in Fig. 6.10. We set $A = 0.5\ mm$ and hence $\mathcal{B} = (0,1)^2\ mm^2$ with voids and inclusions of diameter $0.0806\ mm$, which are uniformly located in the centerline of the specimen. The voids' locations are chosen such that prediction of the sub-region where cracking occurs (hence, the local domain for the forthcoming Global-Local analysis) is feasible, as depicted in Fig. 6.10b. Here, a non-matching discrete interface with the predefined local domain is used, meaning $\Gamma_G \neq \Gamma_L$. The elastic material properties are set for the linear elastic material model, which is identical to the numerical example in Section 4.9. Additionally, the mismatch ratio $\chi = \frac{E_{fiber}}{E_{matrix}}$ is set as $\chi = 10$, which is a ratio between the inclusions and matrix Young's modules. In the next, qualitative and quantitative comparisons with a reference solution are provided.

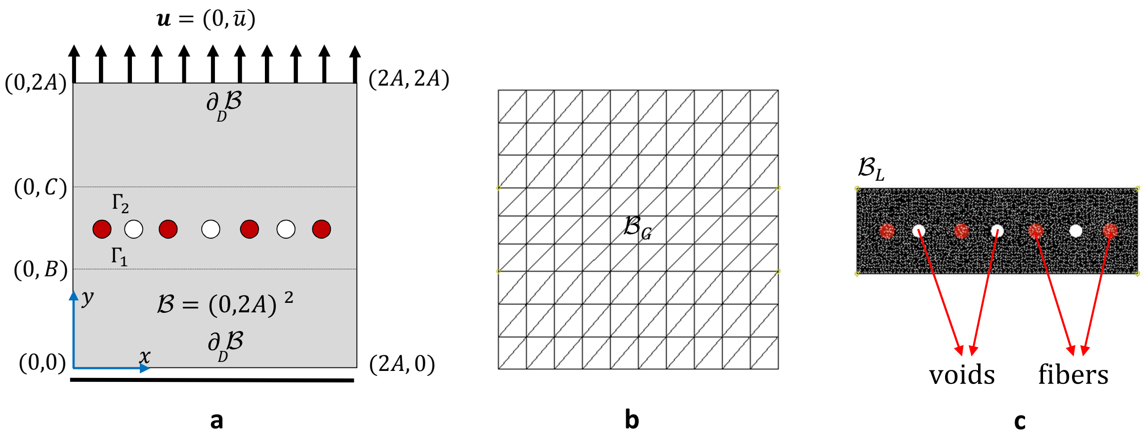

Figure 6.10: Example 1. Tensile test with voids and inclusions at small deformation. (a) Specimen geometry and loading conditions. Finite element discretization (b) of the global domain $\mathcal{B}_G$, and (c) the local domain $\mathcal{B}_L$.

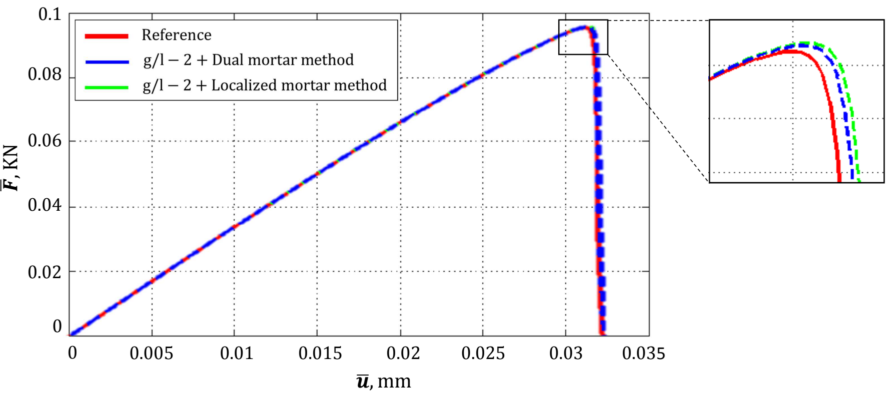

Figure 6.11: Example 1. Comparison of load-displacement curves between the reference solution and the Global-Local formulation $g/l-2$ with different non-conforming discretization techniques (left); zoomed in framed region of the left plot (right).

Figure 6.11 provides the resulting load-displacement curves, which correspond to the dual mortar method and the localized mortar method while comparing it with the reference response. As desired, the three load-displacement curves in Fig. 6.11 are nearly identical in the entire range of loading, including the pre- and post-peak behavior. Through zooming into the area close to the peak point, it can be observed that $g/l-2+$ the dual mortar method performs slightly better; however, it is not significant.

For a deeper insight into non-matching coupling techniques, the convergence performance of the Global-Local solution $g/l-2$ equipped with the dual mortar method, and the localized mortar method is evaluated which are depicted in Fig. 6.12a-b, respectively. This is illustrated in terms of the indicator η. Following Fig. 6.12a, it can be grasped $g/l-2+$ the dual mortar method results in the convergence error about $\eta \approx 10^{-13}$ which performs significantly better compared with $g/l-2+$ the localized mortar method's with the convergence error about $\eta \approx 10^{-6}$; see Fig. 6.12b. The highest value in these figures corresponds to the peak point in Fig. 6.11. This is mainly because, in the dual mortar

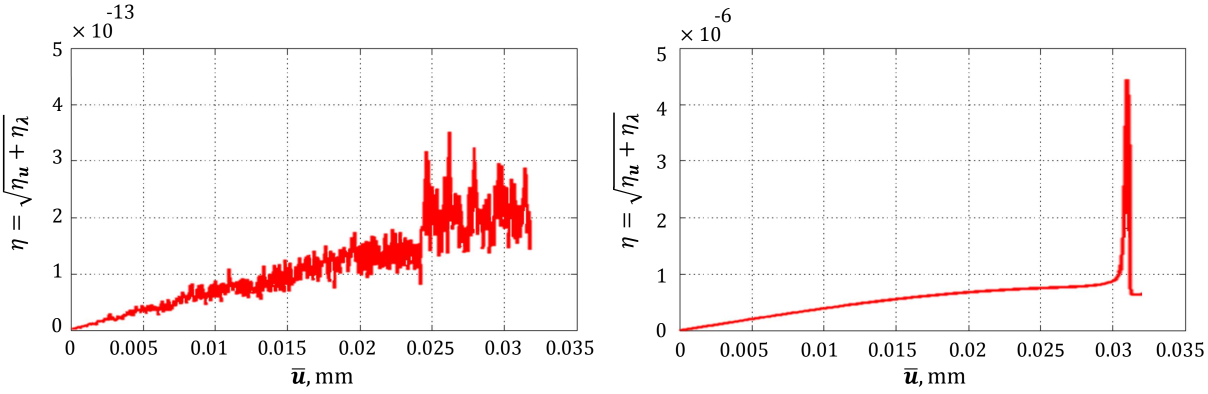

a **b**

Figure 6.12: Example 1. Convergence behavior of the Global-Local solution process $g/l-2$ during loading time equipped with (a) the dual mortar method, and (b) the localized mortar method.

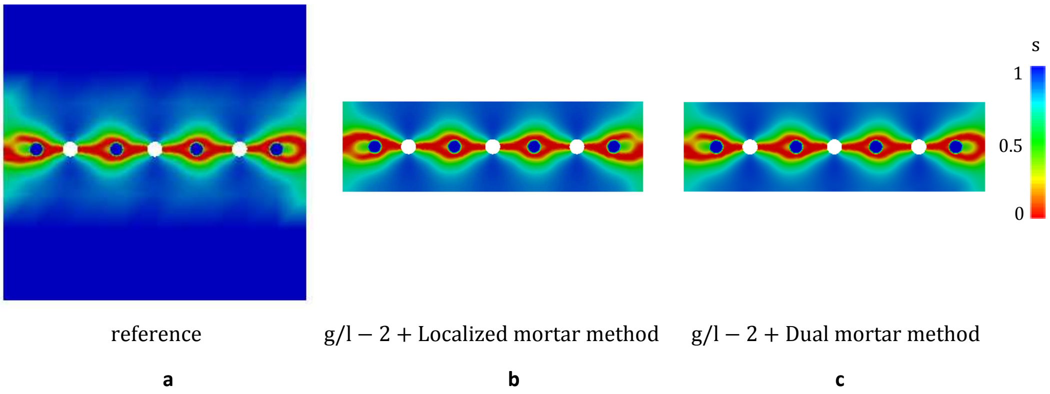

Figure 6.13: Example 1. Comparison of the crack phase-field pattern (at the complete failure). (a) Reference, (b) $g/l-2+$ localized mortar method, and (c) $g/l-2+$dual mortar method solutions.

method, a Lagrange multiplier is assigned with a dual basis function versus the Dirac delta function for the localized mortar method; see Fig. 6.5. Remarkably, the result for the $g/l - 2 +$ localized mortar method, depending on the accuracy is required, could be accepted; because of the ease of numerical implantation compared with the dual mortar method.

Accordingly, the computed crack phase-field profiles for the reference and the Global-Local solutions at the complete fracture state are shown in Fig. 6.13. It can be observed the corresponding crack phase-field profiles are not precisely identical close to the boundary. However, the crack profile for the $g/l - 2 +$ dual mortar method is closer to the reference solution. First of all, this can be explained by the solution non-uniqueness of the reference phase-field formulation, and, secondly by the fact that the Global-Local formulation is only the approximation of the reference solution. Hence, according to the results illustrated here, in the next example, we used the $g/l - 2 +$ dual mortar method because of its superior performance.

6.3.2. Example 2: I-shaped specimen at finite strain

To gain deeper insights into the performance of the Global-Local formulation equipped with non-conforming discretization techniques, a tensile test on the I-shaped specimen undergoing large deformation is performed. Here, the dual mortar method is used, which its computational efficiency has been demonstrated in the previous example. Following [6, 97], a BVP is applied to the specimen, which is depicted in Fig. 6.14. The main challenge here is to demonstrate the efficiency of the Global-Local formulation from a computational standpoint. In particular, (i) we aim to fix the large global domain in terms of the geometry and modeling, while *different* local domains are introduced at the region of interest. Thus, for the simulation standpoint, the large structure at $\mathcal{B}_G$ (which typically comes from industry) is kept fixed, and only the geometry of $\mathcal{B}_L$ will be changed; (ii) Furthermore, we aim to use non-conforming finite element discretization, and hybrid finite element discretization. Specifically, this means that the local discretization element's type is $T1$ (triangular isoparametric element) while the global mesh is set with $Q1$ (i.e., quadrilateral isoparametric element); see Fig. 6.15.

Here, for the global domain, we set $l_1 = 25\ mm$, $l_2 = 18.8\ mm$, $l_3 = 22.4\ mm$,

$H_1 = 110\ mm$, and $w_1 = 22\ mm$ with a quarter circular notched shape with a radius of $r_1 = 3.625\ mm$. The discretizations of the global domain contains 532 $Q1$ elements. For the local BVP in $\mathcal{B}_L$, we consider three different case studies:

- **Case 1.** The local domain includes double notched at the left and right edges, as shown in Fig. 6.14b. Here, we set $H_2 = 22.4\ mm$, $w_2 = 14.8\ mm$, $l_4 = 13\ mm$, $l_5 = 3.7\ mm$, and $r_2 = 2.5\ mm$. The discretizations of the local domain contain 16,484 $T1$ elements.
- **Case 2.** The local domain includes voids to weaken the specimen and facilitate the material cracking. Here, dimensions of the domain are identical to Case 1. Three types of voids are considered: small, medium, and big voids, which are distributed randomly with radius $r = (0.94, 1.58, 3.15)\ mm$, respectively. The discretizations of the local domain contain 12,155 $T1$ elements.
- **Case 3.** The local domain includes hard inclusions to stiffen the specimen, and thus more time is required to initiate the cracking. Here, dimensions of the domain are identical to Case 1. Three types of hard inclusion are considered: small, medium, and big inclusions which are distributed randomly with radius $r = (1.28, 1.98, 2.8)\ mm$, respectively. The local domain partition contains 18,074 $T1$ elements.

Here, the elastic material property is set for the hyperelastic Neo-Hookean model identical to the numerical example given in Section 5.8.2. For Case 3, the mismatch ratio

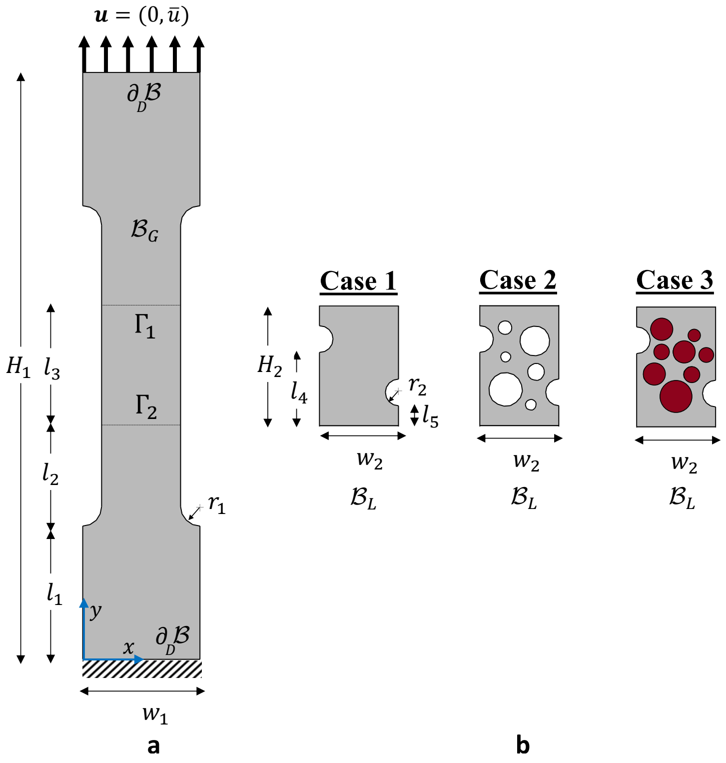

Figure 6.14: Example 2. I-shaped fracture test at finite strain. (a) Specimen geometry and loading conditions for the global domain $\mathcal{B}_G$, and (b) the local domains $\mathcal{B}_L$ for different case studies.

$\chi = \frac{E_{fiber}}{E_{matrix}}$ is set to $\chi = 10$, which is a ratio between the inclusions and matrix Young's modules.

The overall response of the Global-Local approach in terms of accuracy/robustness and efficiency for the two nested finite element models is verified using a reference problem. The reference domain is made from simultaneously considering $\mathcal{B}_G$, including $\mathcal{B}_L$ within a single geometry. In the reference domain, a single type of finite element is used by the $Q1$ quadrilateral isoparametric element.

The load-displacement curves that correspond to Cases 1, 2, and 3 are depicted in Figs. 6.16a, 6.17a, and 6.18a, respectively. Accordingly, a comparison of the reference solution and the Global-Local formulations $g/l-1$ and $g/l-2$ are presented. The resulting Global-Local curve for both $g/l-1$ and $g/l-2$ in all examples are in very good agreement with the reference solution. Hence, the transition of local non-linearity and heterogeneity responses to the global level (through the up-scaling procedure) for all the numerical case studies is consistently performed. Notably, the fracturing process in Case 3 takes longer to initiate due to the hard inclusions (see Fig. 6.18a), while in Case 2, crack initiates earlier compared with the others because of voids being used in the $\mathcal{B}_L$ to weaken the material stiffness; see Fig. 6.17a.

Next, we evaluate the corresponding accumulative computational time, that is the CPU simulation time per the prescribed displacement. The corresponding accumulative computational time for Cases 1, 2, and 3 are depicted in 6.16b, 6.17b and 6.18b, respectively. It can be grasped that the resulting accumulative computational times through $g/l-2$ is required 13%, 13.3% and 16% less time compared to the reference computational time for the Cases 1, 2, and 3, respectively. Additionally, the accumulative computational time through $g/l-1$ shows higher computational time compared with $g/l-2$. But, as

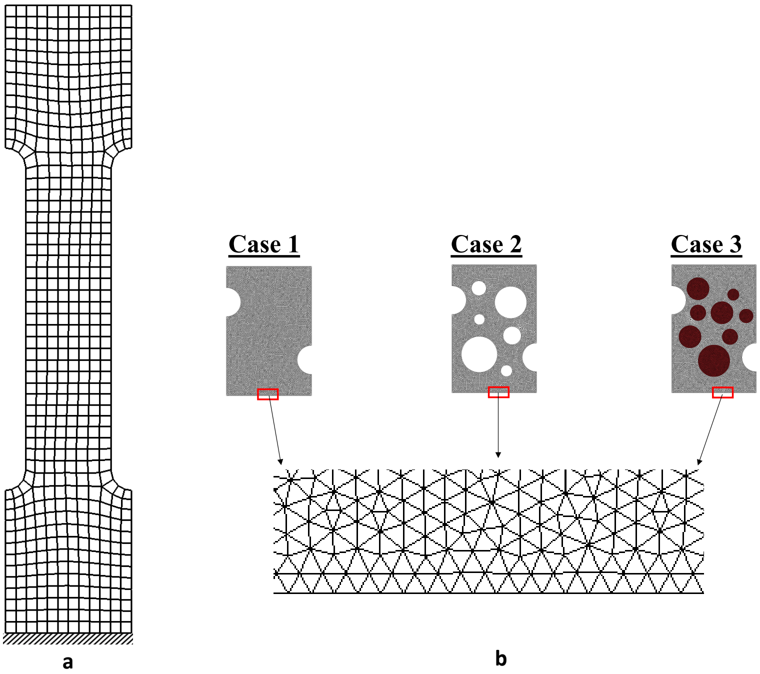

Figure 6.15: Example 2. Finite element discretization of (a) the global domain $\mathcal{B}_G$, and (b) the local domains $\mathcal{B}_L$ for different case studies with the non-matching discrete interface, i.e., $\Gamma_G \neq \Gamma_L$.

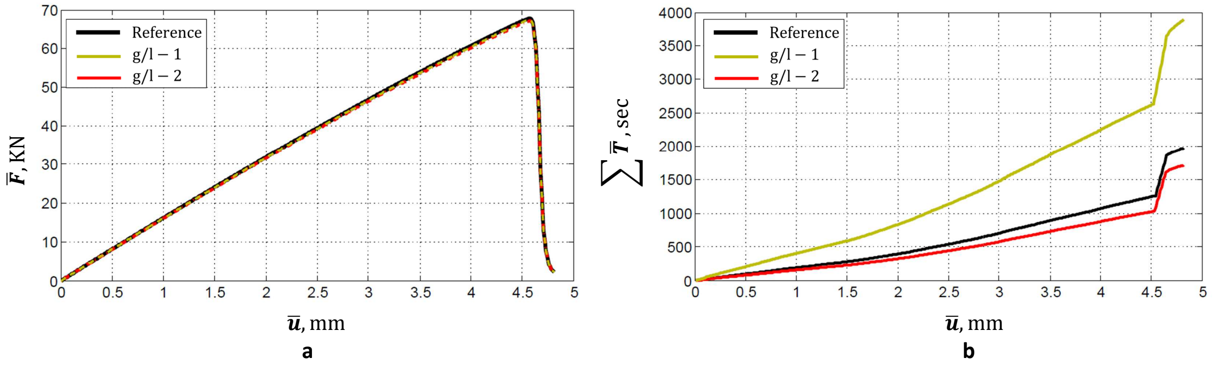

Figure 6.16: Example 2 (Case 1). Comparison of the reference solution and the Global-Local formulation $g/l-1$, and $g/l-2$. (a) Load-displacement curves, and (b) time-displacement curves in terms of 'accumulated time'.

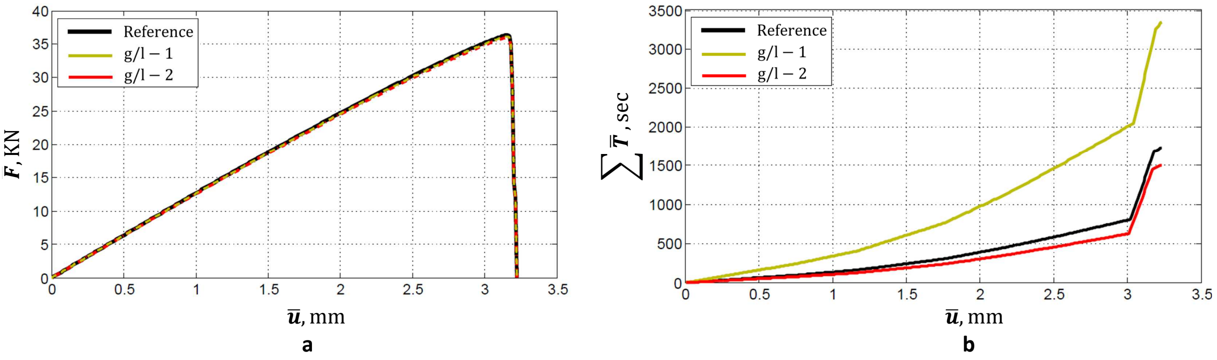

Figure 6.17: Example 2 (Case 2). Comparison of the reference solution and the Global-Local formulation $g/l-1$, and $g/l-2$. (a) Load-displacement curves, and (b) time-displacement curves in terms of 'accumulated time'.

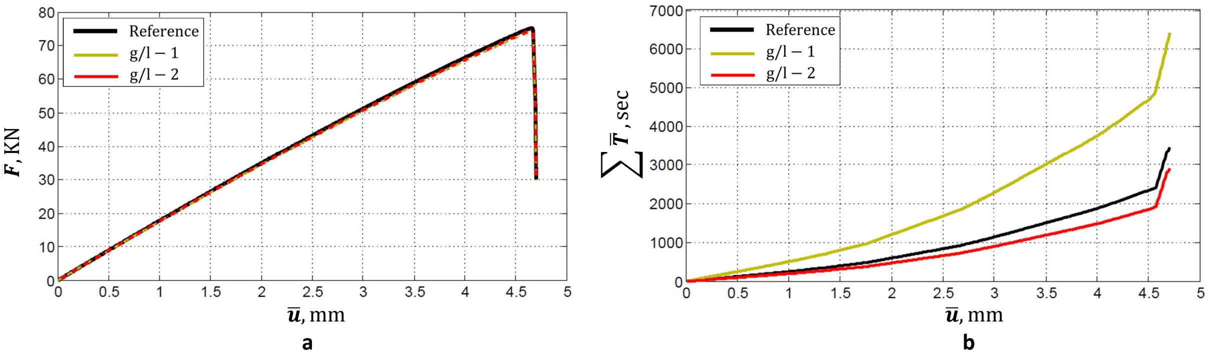

Figure 6.18: Example 2 (Case 3). Comparison of the reference solution and the Global-Local formulation $g/l-1$, and $g/l-2$. (a) Load-displacement curves, and (b) time-displacement curves in terms of 'accumulated time'.

already mentioned, the advantage of using $g/l-1$ is being strongly non-intrusive for the coupling $\mathcal{B}_G$ and $\mathcal{B}_L$ and not computational efficiency (as observed for $g/l-2$).

Furthermore, we investigate the energy response when solving a reference problem and a Global-Local approximation. Recall, the consistency of the energy functional (the departing point of the Global-Local approximation; see Section 5.2)

$$\mathcal{E}(\boldsymbol{\varphi}, s) \equiv \widetilde{\mathcal{E}}(\boldsymbol{\varphi}_G, \boldsymbol{\varphi}_L, s_L, \boldsymbol{\varphi}_\Gamma, \boldsymbol{\lambda}_C, \boldsymbol{\lambda}_L),$$

between reference $\mathcal{E}$ and the Global-Local $\widetilde{\mathcal{E}}$ functional which are indicated in Formulation 3.2.2 and 5.2.1, respectively. We investigate this approximation by means of the evolution of the total stored elastic strain energy plotted in Fig. 6.19 for different case studies, and zooming into the framed region of the left plot. An important observation is that the $g/-1$ gives an overestimate energy response compared with the reference energy for all the numerical examples; see. Fig 6.19. This observation holds when Dirichlet boundary condition being used for the coupling of the global and local domains. This is similar to the computational homogenization when linear displacement boundary conditions are used; see [42]. In summary, the Global-Local simulation results for both $g/l-1$ and $g/l-2$ show very good agreement with the reference solution, for all case studies.

The computed crack phase-field is a good indicator for evaluating the down-scaling procedure (i.e., the transition of external loading increments from the global level to the local one). To this end, the crack phase-field profiles are presented in Fig. 6.20, Fig. 6.21, and Fig. 6.22 on the deformed configuration for Case 1, Case 2, and Case 3, respectively. A qualitative crack profile from the Global-Local formulation are compared with the reference solution. For visualization purposes, the elements where $s_L < 0.05$ are removed from the contour plots. Notably, the deformed shapes are not magnified. Due to the different local structures used for $\mathcal{B}_L$, different crack patterns are observed. In Case 1, the crack initiates at the tip of the circular notched at the both left and right edges and continues to propagate straight till the end of the computation; see Fig. 6.20. In Case 2, the crack initiates from the void near the left circular notch, and after merging to that, it continues to propagate to the right edge till the end of the computation, see Fig. 6.21. In the last case, the crack initiates between two fibers, as depicted in Fig. 6.22, and after merging to the left circular notch continues to propagate to the right edge until the end of the computation.

As a result, the crack phase-field profiles, for different time steps, are in very good agreement with the reference solution, which demonstrates the consistent transition between the global and local BVPs. Thus, the feasibility/efficiency of using the proposed Global-Local approach equipped with non-matching discretization techniques are observed for these complicated local structures.

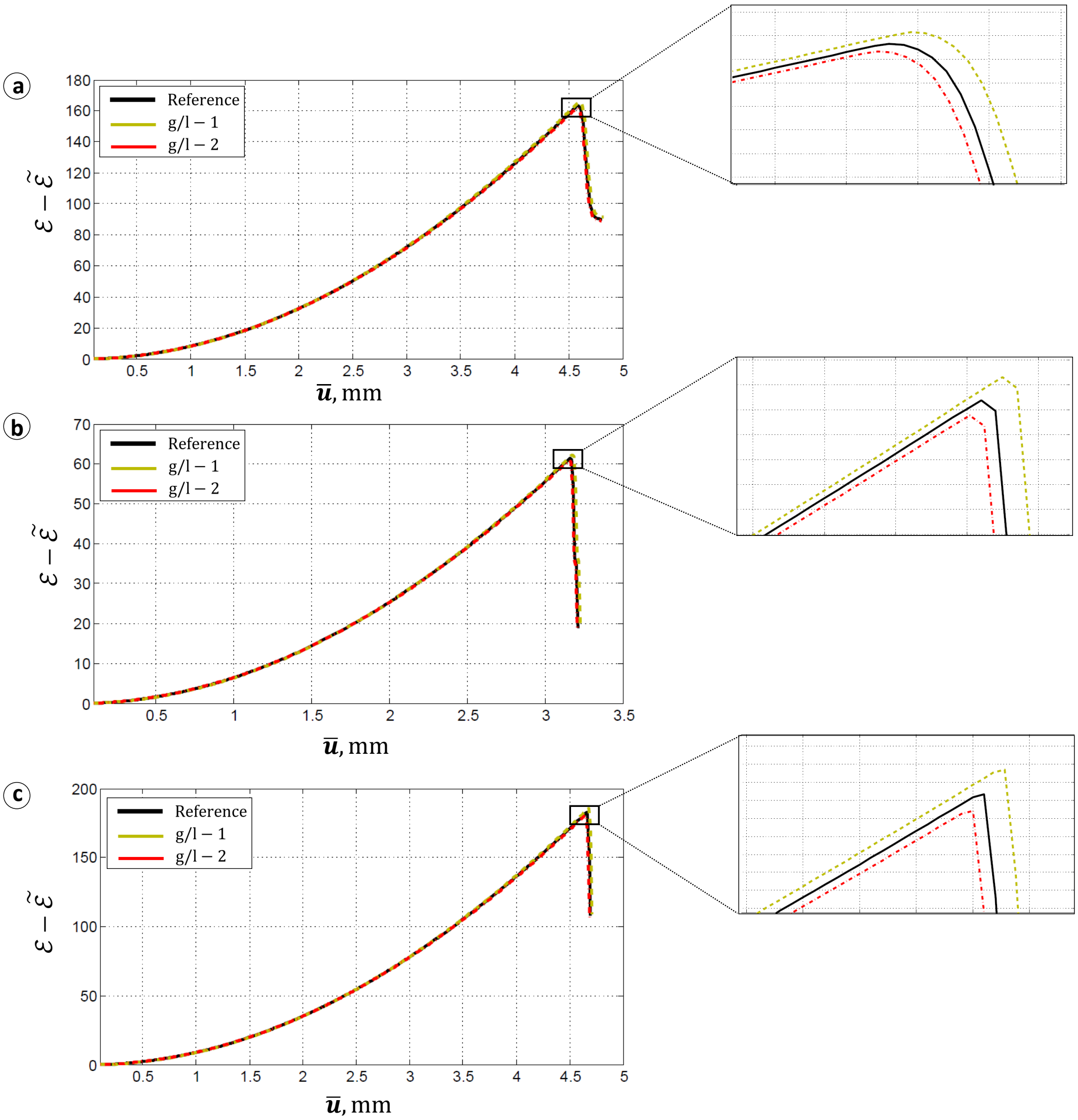

Figure 6.19: Example 2. Comparison of the total free-energy functional between the reference solution $\mathcal{E}$ and the Global-Local approach $\widetilde{\mathcal{E}}$ in (a) Case 1, (b) Case 2, and (c) Case 3 (left); zooming into the framed region of the left plot (right).

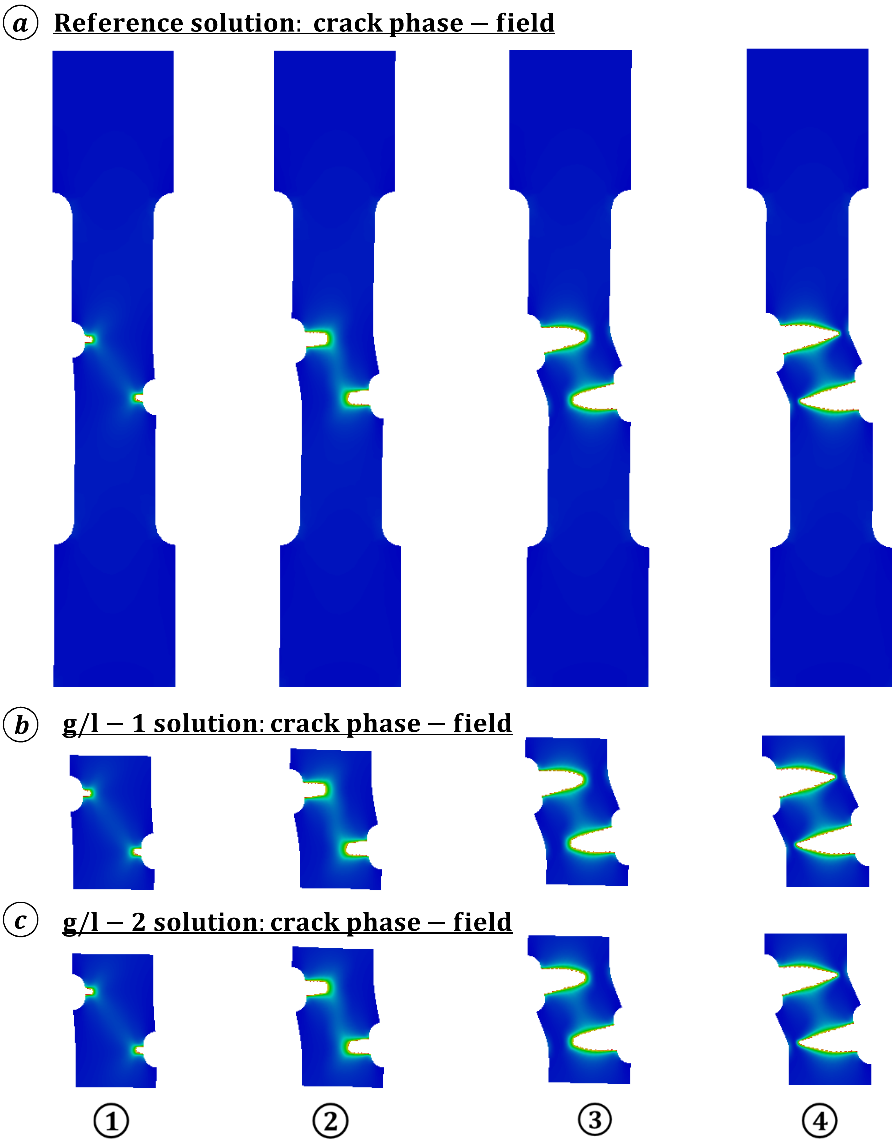

Figure 6.20: Example 2 (Case 1). Comparison of the crack phase-field profiles. (a) The reference solution s. The local solution s_L through (b) $g/l-1$, and (c) $g/l-2$ on the deformed configuration at $\bar{u} = [4.61, 4.65, 4.7, 4.84]$ mm.

ⓐ **Reference solution: crack phase − field**

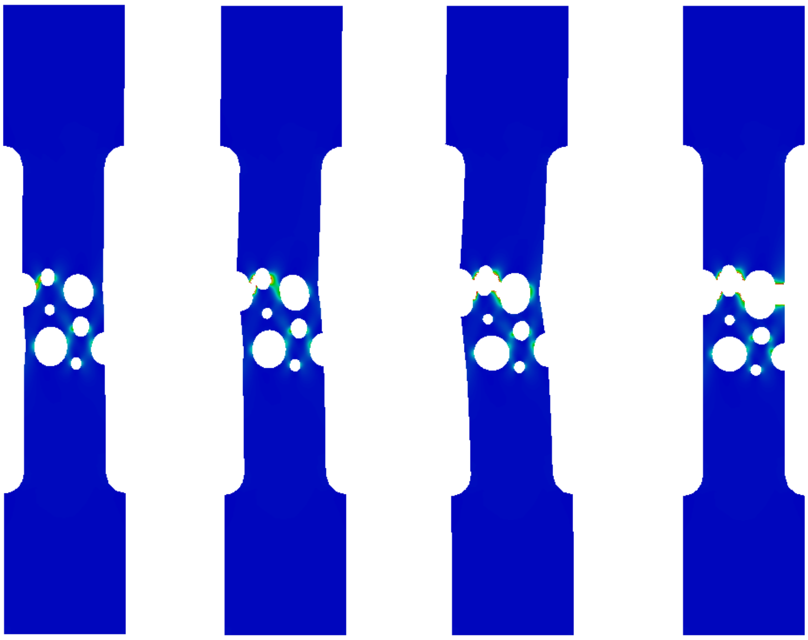

ⓑ **g/l − 1 solution: crack phase − field**

ⓒ **g/l − 2 solution: crack phase − field**

Figure 6.21: Example 2 (Case 2). Comparison of the crack phase-field profiles. (a) The reference solution s. The local solution s_L through (b) $g/l-1$, and (c) $g/l-2$ on the deformed configuration at $\bar{u} = [3.17, 3.18, 3.19, 3.21]$ mm.

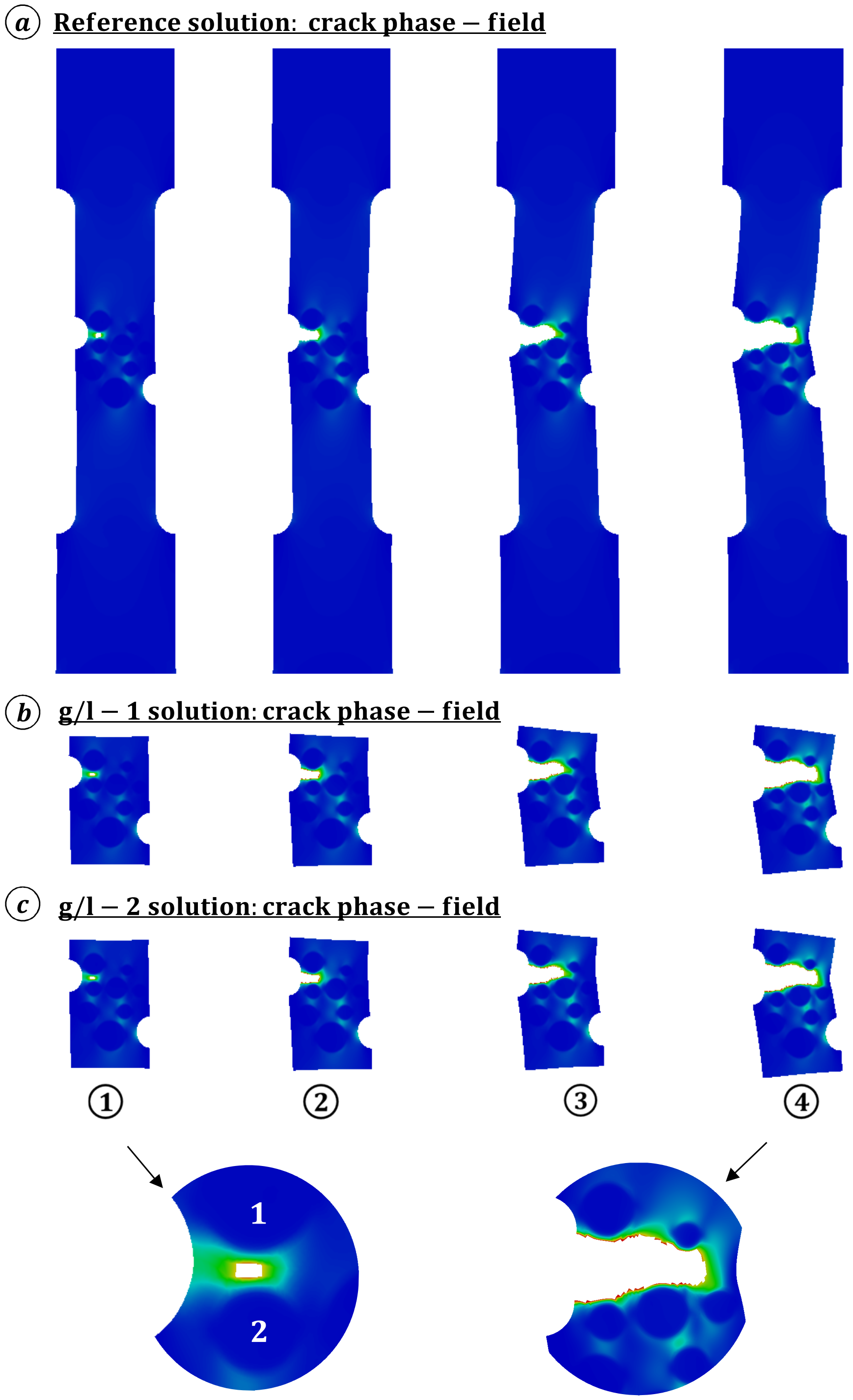

Figure 6.22: Example 2 (Case 3). Comparison of the crack phase-field profiles. (a) The reference solution s. The local solution s_L through (b) $g/l-1$, and (c) $g/l-2$ on the deformed configuration at $\bar{u} = [4.66, 4.67, 4.68, 4.69]\ mm$.

Chapter 7

Conclusion and Future Research

7.1. Conclusion

Variational phase-field modeling is the regularized fractured formulation with a strong capability to simulate complicated failure processes. These include crack initiation (also in the absence of a crack tip singularity), propagation, coalescence, and branching without additional ad-hoc criteria. This feature is particularly attractive for industrial applications, as it minimizes the need for time-consuming and expensive calibration tests. In contrast to these advantages, the finite element treatment of the phase-field formulation is known to be computationally demanding, mainly due to the non-convexity of the energy functional to be minimized with respect to the displacement and the phase-field [46, 58, 128]. Other challenges for the phase-field fracturing formulation is two-fold.

First, that is a regularized-based formulation which is strongly linked to the element discretization size h due to the principal parameters: a small residual scalar κ and characteristic length-scale l. Specifically, $\kappa := \kappa(h)$ and $l := l(h)$ hold such that $h \ll l$ and $h \ll \kappa$ through discretization error estimates [85]. Hence, the equations to be minimized for the variational phase-field formulation are strongly related to the element size h. Thus, for resolving the crack phase-field, a sufficiently small h is chosen to obtain the experimental resolution.

The second challenge is to use the phase-field fracture approach for structures of industrial complexity. This has been the subject of limited investigations, and further studies in this direction will pave the way for the wide adoption of phase-field modeling within legacy codes for industrial applications.

In fact, when dealing with large structures, the failure behavior is solely analyzed in a (small) local region, whereas in the surrounding medium, a simplified and linearized system of equations can be solved. Thus, the idea of a two-scale formulation, in which the full displacement/phase-field problem is solved on a lower(local) scale while dealing with a purely elastic problem on an upper(global) level, is particularly appealing. These features lead us to use the Global-Local approaches as they make it possible first to compute the global model elastically, and then to determine the critical areas to be re-analyzed, while storing the factorization of the structural stiffness decomposition. The local model is then iteratively substituted within the unchanged/fixed global one, which avoids the reconstruction of the global mesh. Here, we proposed an efficient *variational-based Global-Local approach for a phase-field formulation of a fracturing material at small and large deformations.*

In this thesis, two types of Global-Local formulation were adopted for the phase-field brittle fracture. These Global-Local formulations are based on Dirichlet-Neumann-type boundary conditions and Robin-type boundary conditions, namely $g/l-1$ and $g/l-2$, respectively.

The first type, $g/l-1$, is strongly non-intrusive in the computational aspect enabling the formulation to be performed within legacy codes. Due to the extreme difference in stiffness between the global counterpart of the zone to be analyzed locally and its actual response when undergoing extensive cracking, relaxation/acceleration techniques are used. These include the Aitken's Δ^2-method, the SR1, and Broyden's methods. Our findings showed that the iterative convergence could be improved significantly, and to a similar extent for all investigated methods. We observed that Aitken's Δ^2-method is the most convenient choice for the implementation of the approach within legacy codes, as this method needs only tools already available for the so-called sub-modeling approach, which is well-known and widely used in industrial contexts.

The second type, $g/l-2$, has the advantage of computational efficiency. In contrast to the Dirichlet boundary conditions (being used in $g/l-1$), Robin-type boundary conditions (is used in $g/l-2$) did not lead to a stiff local response, particularly in a softening regime; thus no "extra efforts" were required (e.g., relaxation/acceleration procedures).

Here, the proposed framework for the Global-Local approach was first used for the material undergoing small deformation. A successful extension of the Global-Local approach was further extended towards large defamation for both $g/l-1$ and $g/l-2$. Here, the performance of the Global-Local formulation was demonstrated in a quantitatively and qualitatively manner, as follows:

- Crack patterns at the local scale at the complete failure state to evaluate the down-scaling procedure (i.e., the transition of external loading increments from the global level to the local one).
- Load-displacement curve for evaluating the up-scaling procedure during the Global-Local coupling approach (i.e., the transition of local non-linearity and heterogeneity responses to the global level).
- Investigations of the thermodynamical consistency between the reference energy and its Global-Local energy functional.

Accordingly, the overall response of the Global-Local approach in terms of accuracy and efficiency for the two nested finite element models was verified using a reference problem. The resulting crack phase-field patterns and load-displacement curves for both $g/l-1$ and $g/l-2$ showed very good agreement with the reference solution. This is observed for all case studies in the entire range of loading, including the pre- and post-peak behavior. Furthermore, the consistency of the energy functional (the departing point of the Global-Local approximation) between the reference and the approximated Global-Local energy functional were investigated. An important observation was that the $g/-1$ gave an overestimated energy response compared with the reference energy due to the Dirichlet boundary condition, whereas $g/l-2$ showed very good agreement with the reference solution.

For deeper insight into the Global-Local formulation, we quantitatively investigated convergence performance based on the newly proposed indicator for the stopping criterion of the iterative process. Another evaluated factor is the corresponding accumulative computational time (i.e., CPU simulation time) per prescribed displacement. An important observation was that $g/l-2$ required fewer iterations for the convergence of the solution. The required accumulative computational time through $g/l-2$ was approximately 14% less than the reference computational time which underlines the efficiency of using Robin-type boundary conditions. Additionally, the accumulative computational time through $g/l-1$ shows the high computational time versus $g/l-2$. Yet, the advantage of using the $g/l-1$ is being strongly non-intrusive way of coupling (and not computational efficiency). High efforts within $g/l-1$ are not surprising because the Global-Local problem has a larger discretization size than the reference problem and three nested iterative processes versus two for the reference problem.

Because the strong displacement continuity through the matching discretized interface is too restrictive (from the computational standpoint), the Global-Local formulation was further extended toward the non-conforming finite element discretization. The main advantage here is to achieve more regularity at the interface. Another impacting factor is to discretize the local domain independently from the global mesh, thereby gaining more freedom in terms of implementation. In this study, we investigated the mortar method, the dual mortar method, and the localized mortar method. Our findings showed that the mortar method and dual mortar method gave exact results, while the localized mortar method was not precise as other methods. On the other hand, the localized mortar method was computationally faster, yet preserved computational accuracy with some order of approximation. The reason is that a Lagrange multiplier is assigned with a dual basis function in a dual mortar method, whereas in the localized mortar method is set with Dirac delta function. For all numerical examples, the excellent performance of the proposed framework in terms of accuracy for both $g/l-1$ and $g/l-2$ were observed.

7.2. Future research

Possible extensions of the Global-Local formulation for the fracturing material are as follows:

- In practical applications, when the evolving localization areas are not known á-priori, the Global-Local approach must be supplied with the possibility of the adaptive choice of the local domain. The adaptive procedure has two goals: (*i*) to adjust the local domain when fractures are propagating dynamically; and (*ii*) to reduce the total computational cost because the local domains are tailored to á-priori unknown fracture path.

- To approximate the Robin-type boundary conditions rather than using the exact representation. For instance, a two-scale approximation of the Schur complement within the Global-Local formulation is a possibility to reduce the computational effort, yet preserving accuracy; see [44].
- The careful investigation of the error evolution during an iterative Global-Local process to evaluate the decay of the iterative coupling error.
- A further application of the proposed framework which needs to be investigated is the phase-field modeling of ductile fracture undergoing small/large strains toward the efficient Global-Local approach.
- An extension of phase-field modeling within a multi-physics framework towards the Global-Local approach. For instance, hydraulic phase-field fracture, and thermo-elastic solids.
- Global-Local approaches easily allow different numerical techniques to be used for the global and local domains. In this regard, a flexible choice of the discretization scheme can be employed on each domain, individually, such as FEM [135], IGA [66], and VEM [3], among other numerical treatments.
- To extend the Global-Local formulation toward a three-dimensional setting. Thus, a rigorous numerical analysis must be left for future work.

Appendix A

Derivation of Robin-Type Boundary Conditions

In this section, we investigate the relationship between $\Delta\hat{\boldsymbol{u}}$ and $\Delta\hat{\boldsymbol{\lambda}}$ (in the incremental sense) for the complementary, fictitious and local domains at the converged solution state. We aim to derive the Robin-type boundary conditions such that all coupling terms given in (C_1), (C_2), and (C_3) are satisfied, simultaneously, at the Global-Local iteration k.

Recall, the complementary term used in (5.11), and let $\boldsymbol{u}_C$ and $\boldsymbol{\lambda}_C$ be the stationary of the following functional:

$$\mathcal{L} = \mathcal{L}(\boldsymbol{u}_C, \boldsymbol{\lambda}_C) := \int_{\mathcal{B}_C} w(\boldsymbol{\varepsilon}_C, 1, 1)\,\mathrm{d}\boldsymbol{x} + \int_{\Gamma} \boldsymbol{\lambda}_C \cdot (\boldsymbol{u}_\Gamma - \boldsymbol{u}_C)\,\mathrm{d}s - \int_{\Gamma_{N,C}} \bar{\boldsymbol{\tau}} \cdot \boldsymbol{u}_C\,\mathrm{d}s. \tag{A.1}$$

Here, $\Gamma \in \mathcal{R}^{\delta-1} \subset \mathcal{B}_C$ is denoted as an interface, and $\boldsymbol{u}_\Gamma := \mathrm{tr}\ \boldsymbol{u}_C \in \mathbf{H}^{1/2}(\Gamma)$ can be given implicitly, i.e., ($\widetilde{\mathrm{C}}_1$)+($\widetilde{\mathrm{C}}_2$), or explicitly, i.e., ($\widetilde{\mathrm{C}}_4$). Recall that (A.1) lives in $\mathcal{B}_C$ (the following description holds true for $\mathcal{B}_F$ except $\bar{\boldsymbol{\tau}} = \mathbf{0}$). In the discrized setting, the stationary points of the energy functional for the $\mathcal{L}$ is characterized by the first-order necessary conditions through $\mathcal{L}_{\mathbf{1}} = \mathcal{L}_{\boldsymbol{u}}(\boldsymbol{u}_C, \boldsymbol{\lambda}_C; \delta\boldsymbol{u}) = \mathbf{0}$ and $\mathcal{L}_{\mathbf{2}} = \mathcal{L}_{\boldsymbol{\lambda}}(\boldsymbol{u}_C, \boldsymbol{\lambda}_C; \delta\boldsymbol{\lambda}) = \mathbf{0}$. Here, $\delta\boldsymbol{u}$ and $\delta\boldsymbol{\lambda}$ are test functions. We split $\mathcal{L}_{\mathbf{1}}$ into inner nodes and interface nodes denoted as, $\{a,\ b\}$, respectively, by

$$\begin{aligned}
&\mathcal{L}_1^a(\boldsymbol{u}) = \mathtt{f}^{\,a} - \bar{\mathbf{F}} \overset{!}{=} \mathbf{0} && \boldsymbol{x} \in \mathcal{B}\backslash\Gamma,\\
&\mathcal{L}_1^b(\boldsymbol{u}) = \mathtt{f}^{\,b} - \mathbf{L}_G^T\hat{\boldsymbol{\lambda}}_C \overset{!}{=} \mathbf{0} && \boldsymbol{x} \in \Gamma,\\
&\mathcal{L}_{\mathbf{2}} = \mathbf{L}_G\hat{\boldsymbol{u}}_\Gamma - \mathbf{J}_G\hat{\boldsymbol{u}}_C \overset{!}{=} \mathbf{0} && \boldsymbol{x} \in \Gamma.
\end{aligned} \tag{A.2}$$

Here, $\mathtt{f} = \int_{\mathcal{B}_C} (\boldsymbol{B}_u^G)^T \boldsymbol{\sigma}(\boldsymbol{u}_C)\,\mathrm{d}\boldsymbol{x}$ is an internal nodal force vector and $\bar{\mathbf{F}} = \int_{\Gamma_N} (\boldsymbol{N}_u^G)^T \bar{\boldsymbol{\tau}}\,\mathrm{d}s$ stands for the external force vector. It is trivial that the Lagrange multiplier acts as an external force at the interface. A Newton-type solution for the residual-based system of equations for $(\boldsymbol{u}_C, \boldsymbol{\lambda}_C)$ is provided by the following linearization

$$
\begin{aligned}
&(\mathtt{f}^{\,a} - \bar{\mathbf{F}}) + \mathbf{K}_{aa}\Delta\hat{\boldsymbol{u}}_{C,a} + \mathbf{K}_{ab}\Delta\hat{\boldsymbol{u}}_{C,b} = \mathbf{0},\\
&(\mathtt{f}^{\,b} - \mathbf{L}_G^T\hat{\boldsymbol{\lambda}}_C) + \mathbf{K}_{ba}\Delta\hat{\boldsymbol{u}}_{C,a} + \mathbf{K}_{bb}\Delta\hat{\boldsymbol{u}}_{C,b} - \mathbf{L}_G^T\Delta\hat{\boldsymbol{\lambda}}_C = \mathbf{0},\\
&(\mathbf{L}_G\hat{\boldsymbol{u}}_\Gamma - \mathbf{L}_G\Delta\hat{\boldsymbol{u}}_b) + \mathbf{L}_G\Delta\hat{\boldsymbol{u}}_\Gamma - \mathbf{L}_G\Delta\hat{\boldsymbol{u}}_{C,b} = \mathbf{0},
\end{aligned}
\tag{A.3}
$$

where $\mathbf{K} := \partial\mathtt{f}/\partial\hat{\boldsymbol{u}}_C$ is the standard tangent stiffness matrix. Thus yielding the following iterative update

$$
\hat{\boldsymbol{u}}_{C,a} \leftarrow \hat{\boldsymbol{u}}_{C,a} + \Delta\hat{\boldsymbol{u}}_{C,a}, \quad \hat{\boldsymbol{u}}_{C,b} \leftarrow \hat{\boldsymbol{u}}_{C,b} + \Delta\hat{\boldsymbol{u}}_{C,b}, \quad \text{and} \quad \hat{\boldsymbol{\lambda}}_C \leftarrow \hat{\boldsymbol{\lambda}}_C + \Delta\hat{\boldsymbol{\lambda}}_C. \tag{A.4}
$$

Let us now assume that the equilibrium state is achieved such that $\mathcal{L}_1^a = \mathbf{0}, \mathcal{L}_1^b = \mathbf{0}$, and $\mathcal{L}_{\mathbf{2}} = \mathbf{0}$. Through further algebraic analysis, (A.3) is reduced to the interface which takes the following form

$$
\boldsymbol{\mathcal{S}}_C\Delta\hat{\boldsymbol{u}}_{C,b} = \boldsymbol{\mathcal{S}}_C\Delta\hat{\boldsymbol{u}}_\Gamma = \mathbf{L}_G^T\Delta\hat{\boldsymbol{\lambda}}_C \quad \text{with} \quad \boldsymbol{\mathcal{S}}_C := \boldsymbol{\mathcal{S}}(\mathbf{K}_C) = \mathbf{K}_{bb} - \mathbf{K}_{bba}\mathbf{K}_{aa}^{-1}\mathbf{K}_{ab}, \tag{A.5}
$$

where $\boldsymbol{\mathcal{S}}$ refers to the *Steklov-Poincaré mapping* [70]. By means of (A.5), a displacement field $\hat{\boldsymbol{u}}_{C,b}$ is extracted from the interface Γ and then through the Poincaré-Steklov mapping $\boldsymbol{\mathcal{S}}$ returns the outward normal stress derivative with respect to the trace of the displacement. This is called Dirichlet-to-Neumann mapping [33, 52]. Notably, because an identity $\boldsymbol{u}_G = \boldsymbol{u}_C$ holds on Γ in the sense of a trace (see Section 4.2), then (A.5) can be written as,

$$
\boldsymbol{\mathcal{S}}_C\Delta\hat{\boldsymbol{u}}_{G,b} = \mathbf{L}_G^T\Delta\hat{\boldsymbol{\lambda}}_C. \tag{A.6}
$$

Similarly, we have the following identities:

$$
\boldsymbol{\mathcal{S}}_L\Delta\hat{\boldsymbol{u}}_{L,b} = \mathbf{T}_L^T\Delta\hat{\boldsymbol{\lambda}}_L \quad \text{and} \quad \boldsymbol{\mathcal{S}}_F\Delta\hat{\boldsymbol{u}}_{F,b} = \mathbf{L}_G^T\Delta\hat{\boldsymbol{\lambda}}_F. \tag{A.7}
$$

Here, $\mathbf{T}_L := \mathbf{J}_L|_{\Gamma_L}$ is the restriction of $\mathbf{J}_L$ from $\mathcal{B}_L$ to Γ_L. Furthermore, we define $\boldsymbol{\mathcal{S}}_L := \boldsymbol{\mathcal{S}}(\mathbf{K}_L)$, and $\boldsymbol{\mathcal{S}}_F := \boldsymbol{\mathcal{S}}(\mathbf{K}_F)$ in (A.7).

Proposition 1. *Let the global solutions be at the converged state and let the following identity holds true:*

$$
\boldsymbol{u}_\Gamma^{k,\frac{1}{2}} = \boldsymbol{u}_\Gamma^k \;\in\; \Gamma, \tag{A.8}
$$

then, the Global-Local formulation is converged. In addition, (A.8) holds true if and only if

$$
\Delta\boldsymbol{\Lambda}_L = \boldsymbol{\Lambda}_L^k - \boldsymbol{\Lambda}_L^{k-1} = 0. \tag{A.9}
$$

Proof. Let we are at the converged solution of the $g/l-2$ at iteration k. The proof comprises two parts:

a. The Global-Local procedure is in the convergence state *if all* the coupling terms, (C_1), (C_2), and (C_3) holds true at iteration k. We assume that the condition $\boldsymbol{u}_\Gamma^{k,\frac{1}{2}} = \boldsymbol{u}_\Gamma^k \;\in\; \Gamma$

holds. Then, it is evident that (C_2) and (C_3) are satisfied at iteration k; see $(\widetilde{\mathrm{C}}_2)$ and $(\widetilde{\mathrm{C}}_4)$. Accordingly, replacing (4.42) in $(\widetilde{\mathrm{C}}_3)$ yields

$$\int_\Gamma (\boldsymbol{\lambda}_C^k + \boldsymbol{\lambda}_L^k) \cdot \delta \boldsymbol{u}_\Gamma \, \mathrm{d}s + \mathbb{A}_G \int_\Gamma (\boldsymbol{u}_\Gamma^k - \boldsymbol{u}_L^k) \cdot \delta \boldsymbol{\lambda}_L \, \mathrm{d}s = 0. \tag{A.10}$$

The second term in (A.10) due to $(\widetilde{\mathrm{C}}_2)$ and the identity of $\boldsymbol{u}_\Gamma^{k,\frac{1}{2}} = \boldsymbol{u}_\Gamma^k$ becomes zero. Hence, this results in the continuity of tractions at iteration k; that is (C_1). Therefore, all the coupling terms are satisfied at iteration k and thus we are in the convergence state.

b. Let $\Delta \boldsymbol{\Lambda}_L = \boldsymbol{\Lambda}_L^k - \boldsymbol{\Lambda}_L^{k-1} = 0$ holds, then (4.40) restated as

$$\boldsymbol{\Lambda}_L^{k-1} = \boldsymbol{\Lambda}_L^k = \mathbb{A}_L \int_\Gamma \boldsymbol{u}_G^k \cdot \delta \boldsymbol{\lambda}_C \, \mathrm{d}s - \int_\Gamma \boldsymbol{\lambda}_C^k \cdot \delta \boldsymbol{u}_\Gamma \, \mathrm{d}s, \tag{A.11}$$

and therefore $(\widetilde{\mathrm{C}}_1)$ becomes

$$\int_\Gamma (\boldsymbol{\lambda}_C^k + \boldsymbol{\lambda}_L^k) \cdot \delta \boldsymbol{u}_\Gamma \, \mathrm{d}s + \mathbb{A}_L \int_\Gamma (\boldsymbol{u}_\Gamma^{k,\frac{1}{2}} - \boldsymbol{u}_G^k) \cdot \delta \boldsymbol{\lambda}_C \, \mathrm{d}s = \int_\Gamma (\boldsymbol{\lambda}_C^k + \boldsymbol{\lambda}_L^k) \cdot \delta \boldsymbol{u}_\Gamma \, \mathrm{d}s = 0, \tag{A.12}$$

where $(\widetilde{\mathrm{C}}_4)$ is used. Subtracting (A.12) from $(\widetilde{\mathrm{C}}_3)$ yields

$$\mathbb{A}_G \int_\Gamma (\boldsymbol{u}_\Gamma^k - \boldsymbol{u}_L^k) \cdot \delta \boldsymbol{\lambda}_L \, \mathrm{d}s = \mathbb{A}_G \int_\Gamma (\boldsymbol{u}_\Gamma^k - \boldsymbol{u}_\Gamma^{k,\frac{1}{2}}) \cdot \delta \boldsymbol{\lambda}_L \, \mathrm{d}s = 0, \tag{A.13}$$

herein, $(\widetilde{\mathrm{C}}_2)$ is used. Thus, (A.13) results in $\boldsymbol{u}_\Gamma^k = \boldsymbol{u}_\Gamma^{k,\frac{1}{2}}$. Reciprocally, if $\boldsymbol{u}_\Gamma^{k,\frac{1}{2}} = \boldsymbol{u}_\Gamma^k \in \Gamma$ satisfied then $\Delta \boldsymbol{\Lambda}_L = 0$ holds. The proof is left for the readers. ■

We now determine specific Robin-type boundary conditions such that $\Delta \boldsymbol{\Lambda}_L = 0$ holds. Satisfying this condition results in $\boldsymbol{u}_\Gamma^k = \boldsymbol{u}_\Gamma^{k,\frac{1}{2}}$ through Proposition 1, and thus yielding the Global-Local iterative process being in the convergence state.

Recall (4.40), we now aim to find $\mathbb{A}_L$ such that $\Delta \boldsymbol{\Lambda}_L = \boldsymbol{\Lambda}_L^k - \boldsymbol{\Lambda}_L^{k-1} = 0$ holds. Hence we have,

$$\Delta \boldsymbol{\Lambda}_L = \mathbb{A}_L \int_\Gamma \Delta \boldsymbol{u}_G \cdot \delta \boldsymbol{\lambda}_C \, \mathrm{d}s - \int_\Gamma \Delta \boldsymbol{\lambda}_C \cdot \delta \boldsymbol{u}_\Gamma \, \mathrm{d}s = 0, \tag{A.14}$$

resulting in

$$\mathbb{A}_L \int_\Gamma \Delta \boldsymbol{u}_G \cdot \delta \boldsymbol{\lambda}_C \, \mathrm{d}s = \int_\Gamma \Delta \boldsymbol{\lambda}_C \cdot \delta \boldsymbol{u}_\Gamma \, \mathrm{d}s \quad \rightarrow \quad \mathbb{A}_L \mathbf{J}_G \Delta \hat{\boldsymbol{u}}_G = \mathbf{L}_G^T \Delta \hat{\boldsymbol{\lambda}}_C. \tag{A.15}$$

By means of (A.6) and considering $(6.23)_1$, this equality holds if $\mathbb{A}_L := \boldsymbol{\mathcal{S}}_C$, which is the Dirichlet-to-Neumann operator assigned to $\Gamma_G \in \mathcal{B}_C$.

In a similar manner, let us to find $\mathbb{A}_G$ such that $\Delta \boldsymbol{\Lambda}_G = \boldsymbol{\Lambda}_G^k - \boldsymbol{\Lambda}_G^{k-1} = 0$ holds. This yields

$$\mathbb{A}_G \int_\Gamma \Delta \boldsymbol{u}_L \cdot \delta \boldsymbol{\lambda}_L \, \mathrm{d}s = \int_\Gamma \Delta \boldsymbol{\lambda}_L \cdot \delta \boldsymbol{u}_\Gamma \, \mathrm{d}s \quad \rightarrow \quad \mathbb{A}_G \mathbf{J}_L \Delta \hat{\boldsymbol{u}}_L = \mathbf{L}_L^T \Delta \hat{\boldsymbol{\lambda}}_L. \tag{A.16}$$

By means of $(\mathrm{A}.7)_1$ and $(6.23)_2$, we have $\mathbb{A}_G = \boldsymbol{L}_L^T \boldsymbol{T}_L^{-T} \boldsymbol{\mathcal{S}}_L$.

Based on Proposition 1, the converged state of the Global-Local iteration is independent of the choice of $\mathbb{A}_G$, and hence one can simply replace $\boldsymbol{\mathcal{S}}_L$ with the identity tensor. Thus, there is no need to access $\boldsymbol{\mathcal{S}}_L$ at the global level.

Bibliography

[1] Abbaszadeh, M.; Dehghan, M.; Khodadadian, A.; Noii, N.; Heitzinger, C.; Wick, T. [2021]: *A reduced-order variational multiscale interpolating element free galerkin technique based on proper orthogonal decomposition for solving navier–stokes equations coupled with a heat transfer equation: Nonstationary incompressible boussinesq equations.* Journal of Computational Physics, 426: 109875.

[2] Aldakheel, F.; Mauthe, S.; Miehe, C. [2014]: *Towards phase field modeling of ductile fracture in gradient-extended elastic-plastic solids.* Proceedings in Applied Mathematics and Mechanics, 14: 411–412.

[3] Aldakheel, F.; Hudobivnik, B.; Wriggers, P. [2019]: *Virtual element formulation for phase-field modeling of ductile fracture.* International Journal for Multiscale Computational Engineering, 17(2): 181–200.

[4] Aldakheel, F.; Noii, N.; Wick, T.; Wriggers, P. [2020]: *A global–local approach for hydraulic phase-field fracture in poroelastic media.* Computers & Mathematics with Applications.

[5] Ambati, M.; Gerasimov, T.; De Lorenzis, L. [2015]: *A review on phase-field models of brittle fracture and a new fast hybrid formulation.* Computational Mechanics, 55(2): 383–405.

[6] Ambati, M.; Kruse, R.; De Lorenzis, L. [2016]: *A phase-field model for ductile fracture at finite strains and its experimental verification.* Computational Mechanics, 57(1): 149–167.

[7] Ambrosio, L.; Tortorelli, V. [1990]: *Approximation of functionals depending on jumps by elliptic functionals via* Γ*-convergence.* Communications on Pure and Applied Mathematics, 43: 999–1036.

[8] Ambrosio, L.; Tortorelli, V. [1992]: *On the approximation of free discontinuity problems.* Bollettino dell'Unione Matematica Italiana, 6: 105–123.

[9] Artina, M.; Fornasier, M.; Micheletti, S.; Perotto, S. [2015]: *Anisotropic mesh adaptation for crack detection in brittle materials.* SIAM Journal on Scientific Computing, 37(4): B633–B659.

[10] A.S.N. [2008]: *Damaged for Kalitta Air Boeing 747-209F.* `https://aviation-safety.net/database/record.php?id=20080525-0`.

[11] Ball, J. M. [1976]: *Convexity conditions and existence theorems in nonlinear elasticity.* Archive for Rational Mechanics and Analysis, 63(4): 337–403.

[12] Bangerth, W.; Hartmann, R.; Kanschat, G. [2007]: *deal.II – a general purpose object oriented finite element library.* ACM Transactions on Mathematical Software, 33(4): 24/1–24/27.

[13] BELYTSCHKO, T.; LIU, W. K.; MORAN, B.; ELKHODARY, K. [2014]: *Nonlinear Finite Elements for Continua and Structure.* John Wiley and Sons, Ltd., United Kingdom.

[14] BENDER, K. J.; DALEY, H. [2017]: *Bridge closure.* `https://www.spokesman.com/stories/2017/mar/21/bridge-closure-leaves-californias-big-sur-communit`.

[15] BERNARDI, C. [1989]: *A new nonconforming approach to domain decomposition: the mortar element method.* Nonlinear Partial Equations and Their Applications.

[16] BETTINOTTI, O.; ALLIX, O.; MALHERBE, B. [2014]: *A coupling strategy for adaptive local refinement in space and time with a fixed global model in explicit dynamics.* Computational Mechanics, 53(4): 561–574.

[17] BETTINOTTI, O.; ALLIX, O.; PEREGO, U.; OANCEA, V.; MALHERBE, B. [2014]: *A fast weakly intrusive multiscale method in explicit dynamics.* International Journal for Numerical Methods in Engineering, 100(8): 577–595.

[18] BETTINOTTI, O.; ALLIX, O.; PEREGO, U.; OANCEA, V.; MALHERBE, B. [2017]: *Simulation of delamination under impact using a global–local method in explicit dynamics.* Finite Elements in Analysis and Design, 125: 1–13.

[19] BONET, J.; WOOD, R. D. [1997]: *Nonlinear continuum mechanics for finite element analysis.* Cambridge University Press.

[20] BOURDIN, B. [1999]: *Image segmentation with a finite element method.* Mathematical Modelling and Numerical Analysis, 33(2): 229–244.

[21] BOURDIN, B. [2007]: *Numerical implementation of the variational formulation for quasi-static brittle fracture.* Interfaces and Free Boundaries, 9: 411–430.

[22] BOURDIN, B. [2007]: *The variational formulation of brittle fracture: numerical implementation and extensions.* In *IUTAM Symposium on discretization methods for evolving discontinuities*, pp. 381–393. Springer.

[23] BOURDIN, B.; FRANCFORT, G.; MARIGO, J.-J. [2000]: *Numerical experiments in revisited brittle fracture.* Journal of the Mechanics and Physics of Solids, 48(4): 797–826.

[24] BOURDIN, B.; FRANCFORT, G. A.; MARIGO, J.-J. [2008]: *The variational approach to fracture.* Journal of Elasticity, 91: 5–148.

[25] BRAIDES, A. [1998]: *Approximation of free-discontinuity problems.* Number 1694. Springer Science & Business Media.

[26] BRUN, M. K.; WICK, T.; BERRE, I.; NORDBOTTEN, J. M.; RADU, F. A. [2020]: *An iterative staggered scheme for phase field brittle fracture propagation with stabilizing parameters.* Computer Methods in Applied Mechanics and Engineering, 361: 112752.

[27] BURKE, S.; ORTNER, C.; SÜLI, E. [2010]: *An adaptive finite element approximation of a variational model of brittle fracture.* SIAM Journal on Numerical Analysis, 48(3): 980–1012.

[28] BURKE, S.; ORTNER, C.; SÜLI, E. [2013]: *An adaptive finite element approximation of a generalized Ambrosio-Tortorelli functional.* M3AS, 23(9): 1663–1697.

[29] CHAPMAN, S. J. [2003]: *Fortran 90/95 for Scientists and Engineers.* McGraw-Hill, Inc., New York, NY, USA, 2 Edition.

[30] CHEVREUIL, M.; NOUY, A.; SAFATLY, E. [2013]: *A multiscale method with patch for the solution of stochastic partial differential equations with localized uncertainties.* Computer Methods in Applied Mechanics and Engineering, 255: 255–274.

[31] Ciarlet, P. G. [1987]: *The finite element method for elliptic problems.* North-Holland, Amsterdam [u.a.], 2. pr. Edition.

[32] Conn A. R.; Gould N. I. M.; Toint Ph. L. [1991]: *Convergence of quasi-newton matrices generated by the symmetric rank one update.* Mathematical Programming, 50(1): 177–195.

[33] Deparis, S.; Discacciati, M.; Fourestey, G.; Quarteroni, A. [2007]: *Heterogeneous domain decomposition methods for fluid-structure interaction problems.* Domain Decomposition Methods in Science and Engineering XVI. Lecture Notes in Computational Science and Engineering, 55: 41–52.

[34] Dittmann, M.; Aldakheel, F.; Schulte, J.; Wriggers, P.; Hesch, C. [2018]: *Variational phase-field formulation of non-linear ductile fracture.* Computer Methods in Applied Mechanics and Engineering, 342: 71–94.

[35] Dolbow, J.; Moës, N.; Belytschko, T. [2001]: *An extended finite element method for modeling crack growth with frictional contact.* Computer Methods in Applied Mechanics and Engineering, 190(51-52): 6825–6846.

[36] Duval, M.; Passieux, J.-C.; Salaün, M.; Guinard, S. [2016]: *Non-intrusive coupling: recent advances and scalable nonlinear domain decomposition.* Archives of Computational Methods in Engineering, 23(1): 17–38.

[37] Erbts, P.; DüSter, A. [2012]: *Accelerated staggered coupling schemes for problems of thermoelasticity at finite strains.* Computers & Mathematics with Applications, 64(8): 2408–2430.

[38] Farhat, C.; Roux, F. [1991]: *A method of finite element tearing and interconnecting and its parallel solution algorithm.* International Journal for Numerical Methods in Engineering, 32: 1205–1227.

[39] Farhat, C.; Roux, F.-X. [1991]: *A method of finite element tearing and interconnecting and its parallel solution algorithm.* International Journal for Numerical Methods in Engineering, 32(6): 1205–1227.

[40] Farrell, P. E.; Maurini, C. [2017]: *Linear and nonlinear solvers for variational phase-field models of brittle fracture.* International Journal for Numerical Methods in Engineering, 109: 648–667.

[41] Fish, J.; Wagiman, A. [1993]: *Multiscale finite element method for a locally nonperiodic heterogeneous medium.* Computational Mechanics, 12(3): 164–180.

[42] Fish, J. [2014]: *Practical Multiscaling.* John Wiley and Sons, Ltd., United Kingdom.

[43] Francfort, G.; Marigo, J.-J. [1998]: *Revisiting brittle fracture as an energy minimization problem.* Journal of the Mechanics and Physics of Solids, 46(8): 1319–1342.

[44] Gendre, L.; Allix, O.; Gosselet, P. [2011]: *A two-scale approximation of the schur complement and its use for non-intrusive coupling.* International Journal for Numerical Methods in Engineering, 87: 889–905.

[45] Gendre, L.; Allix, O.; Gosselet, P.; Comte, F. [2009]: *Non-intrusive and exact global/local techniques for structural problems with local plasticity.* Computational Mechanics, 44(2): 233–245.

[46] Gerasimov, T.; Lorenzis, L. D. [2016]: *A line search assisted monolithic approach for phase-field computing of brittle fracture.* Computer Methods in Applied Mechanics and Engineering, 312: 276–303.

[47] Gerasimov, T.; De Lorenzis, L. [2019]: *On penalization in variational phase-*

field models of brittle fracture. Computer Methods in Applied Mechanics and Engineering, 354: 990–1026.

[48] Gerasimov, T.; Noii, N.; Allix, O.; De Lorenzis, L. [2018]: *A non-intrusive global/local approach applied to phase-field modeling of brittle fracture.* Advanced Modeling and Simulation in Engineering Sciences, 5(1): 14.

[49] Girault, V.; Wheeler, M. F.; Almani, T.; Dana, S. [2019]: *A priori error estimates for a discretized poro-elastic–elastic system solved by a fixed-stress algorithm.* Oil & Gas Science and Technology–Revue d'IFP Energies nouvelles, 74: 24.

[50] González-Velázquez, J. L. [2019]: *Mechanical behavior and fracture of engineering materials.* Springer.

[51] Gosselet, P.; Rey, C. [2006]: *Non-overlapping domain decomposition methods in structural mechanics.* Archives of Computational Methods in Engineering, 13: 515–572.

[52] Greer, N.; Loisel, S. [2015]: *The optimised schwarz method and the two-lagrange multiplier method for heterogeneous problems in general domains with two general subdomains.* Numerical Algorithms, 69: 737–762.

[53] Guguin, G.; Allix, O.; Gosselet, P.; Guinard, S. [2016]: *On the computation of plate assemblies using realistic 3d joint model: a non-intrusive approach.* Advanced Modeling and Simulation in Engineering Sciences, 3(1): 1–18.

[54] Gurtin, M. E.; Fried, E.; Anand, L. [2010]: *The mechanics and thermodynamics of continua.* Cambridge University Press.

[55] Haupt, P. [2013]: *Continuum mechanics and theory of materials.* Springer Science & Business Media.

[56] Hautefeuille, M.; Colliat, J.-B.; Ibrahimbegovic, A.; Matthies, H.; Villon, P. [2012]: *A multi-scale approach to model localized failure with softening.* Computers & Structures, 94-95: 83–95.

[57] Hecht, F.; Lozinski, A.; Pironneau, O. [2009]: *Numerical zoom and the schwarz algorithm.* Domain Decomposition Methods in Science and Engineering XVIII, 70: 63–73.

[58] Heister, T.; Wheeler, M. F.; Wick, T. [2015]: *A primal-dual active set method and predictor-corrector mesh adaptivity for computing fracture propagation using a phase-field approach.* Computer Methods in Applied Mechanics and Engineering, 290: 466 – 495.

[59] Heister, T.; Wick, T. [2018]: *Parallel solution, adaptivity, computational convergence, and open-source code of 2d and 3d pressurized phase-field fracture problems.* PAMM, 18(1): e201800353.

[60] Hesch, C.; Weinberg, K. [2014]: *Thermodynamically consistent algorithms for a finite-deformation phase-field approach to fracture.* International Journal for Numerical Methods in Engineering, 99: 906–924.

[61] Hill, R. [1965]: *A self-consistent mechanics of composite materials.* Journal of the Mechanics and Physics of Solids, 13(4): 213–222.

[62] Hinojosa, J.; Allix, O.; Guidault, P.-A.; Cresta, P. [2014]: *Domain decomposition methods with nonlinear localization for the buckling and post-buckling analyses of large structures.* Advances in Engineering Software, 70: 13–24.

[63] Holzapfel, A. G. [2000]: *Nonlinear Solid Mechanics: A Continuum Approach for Engineering.* John Wiley & Sons, Inc.

[64] Hughes, T. J. [2012]: *The finite element method: linear static and dynamic finite element analysis.* Courier Corporation.

[65] Hughes, T. J.; Feijóo, G. R.; Mazzei, L.; Quincy, J.-B. [1998]: *The variational multiscale method-a paradigm for computational mechanics.* Computer Methods in Applied Mechanics and Engineering, 166(1): 3–24. Advances in Stabilized Methods in Computational Mechanics.

[66] Hughes, T.; Cottrell, J.; Bazilevs, Y. [2005]: *Isogeometric analysis: Cad, finite elements, nurbs, exact geometry and mesh refinement.* Computer Methods in Applied Mechanics and Engineering, 194(39): 4135 – 4195.

[67] Jeong, G.-E.; Song, Y.-U.; Youn, S.-K.; Park, K. [2020]: *A new approach for nonmatching interface construction by the method of localized lagrange multipliers.* Computer Methods in Applied Mechanics and Engineering, 361: 112728.

[68] Johnson, C. [2012]: *Numerical solution of partial differential equations by the finite element method.* Courier Corporation.

[69] Khodadadian, A.; Noii, N.; Parvizi, M.; Abbaszadeh, M.; Wick, T.; Heitzinger, C. [2020]: *A bayesian estimation method for variational phase-field fracture problems.* Computational Mechanics, 66(4): 827–849.

[70] Khoromskij, B.; Wittum, G. [1998]: *Robust Interface Reduction for Highly Anisotropic Elliptic Equations.* Springer-Verlag Berlin Heidelberg.

[71] Kikuchi, N.; Oden, J. [1988]: *Contact problems in elasticity.* Studies in Applied Mathematics. Society for Industrial and Applied Mathematics (SIAM), Philadelphia, PA.

[72] Kim, J.; Duarte, C. A. [2015]: *A new generalized finite element method for two-scale simulations of propagating cohesive fractures in 3-d.* International Journal for Numerical Methods in Engineering, 104(13): 1139–1172.

[73] Kinderlehrer, D.; Stampacchia, G. [2000]: *An Introduction to Variational Inequalities and Their Applications.* Classics in Applied Mathematics. Society for Industrial and Applied Mathematics.

[74] Kreyszig, E. [2009]: *Advanced engineering mathematics, 10th eddition.*

[75] Küttler, U.; Wall, W. A. [2008]: *Fixed-point fluid–structure interaction solvers with dynamic relaxation.* Computational Mechanics, 43(1): 61–72.

[76] Lamichhane, B. P.; Wohlmuth, B. I. [2004]: *Mortar finite elements for interface problems.* Computing, 72(3-4): 333–348.

[77] Le Tallec, P. [1994]: *Domain decomposition methods in computational mechanics.* Computational Mechanics Advances, 1(2): 121–220.

[78] Lee, S.; Wheeler, M. F.; Wick, T. [2016]: *Pressure and fluid-driven fracture propagation in porous media using an adaptive finite element phase field model.* Computer Methods in Applied Mechanics and Engineering, 305: 111 – 132.

[79] Liu, Y.; Sun, Q.; Fan, X. [2014]: *A non-intrusive global/local algorithm with non-matching interface: derivation and numerical validation.* Computer Methods in Applied Mechanics and Engineering, 277: 81–103.

[80] Lloberas-Valls, O.; Rixen, D. J.; Simone, A.; Sluys, L. J. [2012]: *Multiscale domain decomposition analysis of quasi-brittle heterogeneous materials.* International Journal for Numerical Methods in Engineering, 83: 1337–1366.

[81] Loehnert, S.; Belytschko, T. [2007]: *A multiscale projection method for macro/microcrack simulations.* International Journal for Numerical Methods in Engineering, 71(12): 1466–1482.

[82] Maday, Y.; Magoulés, F. [2006]: *Absorbing interface conditions for domain decomposition methods: A general presentation.* International Journal for Numerical Methods in Fluids, 195: 3880–3900.

[83] Magoules, F.; Roux, F. X.; Series, L. [2006]: *Algebraic approximation of dirichlet-to-neumann maps for the equations of linear elasticity.* Computer Methods in Applied Mechanics and Engineering, 195: 3742–3759.

[84] Mandel, J. [1993]: *Balancing domain decomposition.* Communications in Applied Numerical Methods, 9(4): 233–241.

[85] Mang, K.; Wick, T. [2019]: *Numerical methods for variational phase-field fracture problems.* Lecture notes at Leibniz University Hannover, doi: https://doi.org/10.15488/5129.

[86] Mang, K.; Walloth, M.; Wick, T.; Wollner, W.: *Mesh adaptivity for quasi-static phase-field fractures based on a residual-type a posteriori error estimator.* GAMM-Mitteilungen, 0(0): e202000003.

[87] Marigo, J.-J.; Maurini, C.; Pham, K. [2016]: *An overview of the modelling of fracture by gradient damage models.* Meccanica, 51(12): 3107–3128.

[88] Markovic, D.; Ibrahimbegovic, A. [2004]: *On micro-macro interface conditions for micro scale based fem for inelastic behavior of heterogeneous materials.* Computer Methods in Applied Mechanics and Engineering, 193(48): 5503–5523. Advances in Computational Plasticity.

[89] *MATLAB version 8.5.0.197613 (R2015a).* The Mathworks, Inc., Natick, Massachusetts.

[90] Michel, J.; Moulinec, H.; Suquet, P. [1999]: *Effective properties of composite materials with periodic microstructure: a computational approach.* Computer Methods in Applied Mechanics and Engineering, 172(1): 109–143.

[91] Miehe, C.; Bayreuther, C. [2007]: *On multiscale fe analyses of heterogeneous structures: from homogenization to multigrid solvers.* International Journal for Numerical Methods in Engineering, 71: 1135–1180.

[92] Miehe, C.; Hofacker, M.; Welschinger, F. [2010]: *A phase field model for rate-independent crack propagation: Robust algorithmic implementation based on operator splits.* Computer Methods in Applied Mechanics and Engineering, 199: 2765–2778.

[93] Miehe, C.; Welschinger, F.; Hofacker, M. [2010]: *Thermodynamically consistent phase-field models of fracture: Variational principles and multi-field fe implementations.* International Journal for Numerical Methods in Engineering, 83: 1273–1311.

[94] Miehe, C.; Hofacker, M.; Schänzel, L.-M.; Aldakheel, F. [2015]: *Phase field modeling of fracture in multi-physics problems. Part II. brittle-to-ductile failure mode transition and crack propagation in thermo-elastic-plastic solids.* Computer Methods in Applied Mechanics and Engineering, 294: 486–522.

[95] Miehe, C.; Schänzel, L.; Ulmer, H. [2015]: *Phase field modeling of fracture in multi-physics problems. Part I. balance of crack surface and failure criteria for brittle crack propagation in thermo-elastic solids.* Computer Methods in Applied Mechanics and Engineering, 294: 449–485.

[96] Miehe, C.; Schänzel, L.-M. [2014]: *Phase field modeling of fracture in rubbery polymers. part i: Finite elasticity coupled with brittle failure.* Journal of the Mechanics and Physics of Solids, 65: 93–113.

[97] Miehe, C.; Kienle, D.; Aldakheel, F.; Teichtmeister, S. [2016]: *Phase field modeling of fracture in porous plasticity: A variational gradient-extended eulerian framework for the macroscopic analysis of ductile failure.* Computer Methods in Applied Mechanics and Engineering, 312: 3–50.

[98] Mikelić, A.; Wheeler, M. F.; Wick, T. [2015]: *A quasi-static phase-field approach to pressurized fractures.* Nonlinearity, 28(5): 1371–1399.

[99] Mikelić, A.; Wheeler, M.; Wick, T. [2019]: *Phase-field modeling through iterative splitting of hydraulic fractures in a poroelastic medium.* GEM-International Journal on Geomathematics, 10(1): 2.

[100] Minami, S.; Yoshimura, S. [2010]: *Performance evaluation of nonlinear algorithms with line-search for partitioned coupling techniques for fluid–structure interactions.* International Journal for Numerical Methods in Fluids, 64(10-12): 1129–1147.

[101] Moës, N.; Dolbow, J.; Belytschko, T. [1999]: *A finite element method for crack growth without remeshing.* International Journal for Numerical Methods in Engineering, 46(1): 131–150.

[102] Mooney, M. [1940]: *A theory of large elastic deformation.* Journal of Applied Physics, 11(9): 582–592.

[103] Mota, A.; Tezaur, I.; Alleman, C. [2017]: *The Schwarz alternating method in solid mechanics.* Computer Methods in Applied Mechanics and Engineering, 319: 19–51.

[104] Noii, N.; Wick, T. [2019]: *A phase-field description for pressurized and non-isothermal propagating fractures.* Computer Methods in Applied Mechanics and Engineering, 351: 860 – 890.

[105] Noii, N.; Aldakheel, F.; Wick, T.; Wriggers, P. [2020]: *An adaptive global–local approach for phase-field modeling of anisotropic brittle fracture.* Computer Methods in Applied Mechanics and Engineering, 361: 112744.

[106] Noii, N.; Khodadadian, A.; Wick, T. [2020]: *Bayesian inversion for anisotropic hydraulic phase-field fracture.* arXiv preprint arXiv:2007.16038.

[107] Noii, N.; Khodadadian, A.; Ulloa, J.; Aldakheel, F.; Wick, T.; Francois, S.; Wriggers, P. [2021]: *Bayesian inversion for unified ductile phase-field fracture.* arXiv preprint arXiv:2104.11114.

[108] Ogden, R. W. [1972]: *Large deformation isotropic elasticity–on the correlation of theory and experiment for incompressible rubberlike solids.* Proceedings of the Royal Society of London. A. Mathematical and Physical Sciences, 326(1567): 565–584.

[109] Park, K.; Felippa, C. [2000]: *A variational principle for the formulation of partitioned structural systems.* International Journal for Numerical Methods in Engineering, 47: 395–418.

[110] Park, K.; Felippa, C.; Rebel, G. [2002]: *A simple algorithm for localized construction of non-matching structural interfaces.* International Journal for Numerical Methods in Engineering, 53(9): 2117–2142.

[111] Park, K.; Paulino, G. H. [2011]: *Cohesive zone models: a critical review of traction-separation relationships across fracture surfaces.* Applied Mechanics Reviews, 64(6).

[112] Passieux, J.-C.; Réthoré, J.; Gravouil, A.; Baietto, M.-C. [2013]: *Local/global non-intrusive crack propagation simulation using a multigrid x-fem solver.* Computational Mechanics, 52(6): 1381–1393.

[113] Plews, J.; Duarte, C. A.; Eason, T. [2012]: *An improved nonintrusive global–local approach for sharp thermal gradients in a standard fea platform.* International Journal for Numerical Methods in Engineering, 91(4): 426–449.

[114] Rice, J. [1968]: *Mathematical analysis in the mechanics of fracture.* Academic Press, New York, chapter 3 of fracture: An advanced treatise edition, 3: 191–311.

[115] Rivlin, R. [1948]: *Large elastic deformations of isotropic materials iv. further developments of the general theory.* Philosophical Transactions of the Royal Society of London. Series A, Mathematical and Physical Sciences, 241(835): 379–397.

[116] Ross, M. R. [2006]: *Coupling and simulation of acoustic fluid-structure interaction systems using localized Lagrange multipliers.* Ph.D. Thesis.

[117] Schlüter, A.; Willenbücher, A.; Kuhn, C.; Müller, R. [2014]: *Phase field approximation of dynamic brittle fracture.* Computational Mechanics, 54(5): 1141–1161.

[118] Seitz, A.; Farah, P.; Kremheller, J.; Wohlmuth, B. I.; Wall, W. A.; Popp, A. [2016]: *Isogeometric dual mortar methods for computational contact mechanics.* Computer Methods in Applied Mechanics and Engineering, 301: 259–280.

[119] Sherman, J.; Morrison, W. J. [1950]: *Adjustment of an inverse matrix corresponding to a change in one element of a given matrix.* The Annals of Mathematical Statistics, 21(1): 124–127.

[120] Song, Y.-U.; Youn, S.-K.; Park, K. [2015]: *A gap element for treating non-matching discrete interfaces.* Computational Mechanics, 56(3): 551–563.

[121] Treloar, L. R. G. [1975]: *The physics of rubber elasticity.* Oxford University Press, USA.

[122] Truesdell, C.; Noll, W. [2004]: *The non-linear field theories of mechanics.* In *The non-linear field theories of mechanics*, pp. 1–579. Springer.

[123] Wheeler, J.; Wheeler, M. [2019]: *IPARS, A New Generation Framework for Petroleum Reservoir Simulation, Technical Reference.* http://csm.ices.utexas.edu/ipars/.

[124] Wheeler, M.; Wick, T.; Wollner, W. [2014]: *An augmented-lagrangian method for the phase-field approach for pressurized fractures.* Computer Methods in Applied Mechanics and Engineering, 271: 69–85.

[125] Wick, T. [2016]: *Goal functional evaluations for phase-field fracture using PU-based DWR mesh adaptivity.* Computational Mechanics, 57(6): 1017–1035.

[126] Wick, T. [2017]: *Modified Newton methods for solving fully monolithic phase-field quasi-static brittle fracture propagation.* Computer Methods in Applied Mechanics and Engineering, 325: 577 – 611.

[127] Wick, T. [2017]: *An error-oriented Newton/inexact augmented Lagrangian approach for fully monolithic phase-field fracture propagation.* SIAM Journal on Scientific Computing, 39(4): B589–B617.

[128] Wick, T. [2017]: *Modified newton methods for solving fully monolithic phase-field quasi-static brittle fracture propagation.* Computer Methods in Applied Mechanics and Engineering, 325: 577–611.

[129] Wick, T.; Singh, G.; Wheeler, M. F., et al. [2016]: *Fluid-filled fracture propagation with a phase-field approach and coupling to a reservoir simulator.* SPE Journal, 21(03): 981–999.

[130] Wohlmuth, B. I. [1999]: *Hierarchical a posteriori error estimators for mortar finite element methods with lagrange multipliers.* SIAM Journal on Numerical Anal-

ysis, 36(5): 1636–1658.

[131] Wohlmuth, B. I. [2001]: *Iterative solvers based on domain decomposition.* pp. 85–176.

[132] Wohlmuth, B. I. [2002]: *A comparison of dual lagrange multiplier spaces for mortar finite element discretizations.* ESAIM: Mathematical Modelling and Numerical Analysis, 36(6): 995–1012.

[133] Wohlmuth, B. [2000]: *A mortar finite element method using dual spaces for the lagrange multiplier.* SIAM Journal on Numerical Analysis, 38.

[134] Wriggers, P.; Aldakheel, F.; Hudobivnik, B. [2019]: *Application of the virtual element method in mechanics.* GAMM-Rundbriefe, pp. 4–10. ISSN: 2196-3789.

[135] Wriggers, P. [2008]: *Nonlinear finite element methods.* Springer Science & Business Media.

[136] Zhang, S.; Oskay, C. [2015]: *Variational multiscale enrichment method with mixed boundary conditions for elasto-viscoplastic problems.* Computational Mechanics, 55(4): 771–787.

[137] Zienkiewicz, O. C.; Taylor, R. L.; Zhu, J. Z. [2005]: *The finite element method: its basis and fundamentals.* Elsevier.